The University of Nottingham

UNITED KINGDOM · CHINA · MALAYSIA

Studies of Self-Assembled Metal-Organic Nanostructures and the MBE Growth of Graphene

Alex Summerfield MSci (Hons.)

supervised by Professor Peter H. Beton

Thesis submitted to the University of Nottingham
for the degree of Doctor of Philosophy
March 2016

The School of Physics and Astronomy

Abstract

This thesis discusses the formation of metal-organic and organic structures grown on surfaces using bottom-up self-assembly techniques. Three systems are investigated primarily using scanning probe microscopy techniques.

The growth of metal-organic frameworks (MOFs) on functionalised surfaces is investigated using high resolution atomic force microscopy (AFM). The earliest stages of MOF crystal nucleation are imaged using a layer-by-layer (LBL) growth technique and the ability to track the growth of individual nanocrystallites throughout the LBL process is demonstrated. This LBL method has been suggested as a route to fabricating epitaxially grown, oriented thin-films of MOFs. However, results from these studies indicate that, rather than a uniform crystalline layer, the morphology is that of a preferentially oriented but laterally polycrystalline film and the growth rates of the individual nanocrystallites exceed those expected for a LBL growth mode. This has significant implications for the fabrication of novel devices that incorporate MOFs due to the presence of domain boundaries and defects.

Self-assembled monolayers of light-harvesting porphyrin nanorings are investigated with scanning tunnelling microscopy (STM) and AFM. The nanorings are found to form large supramolecular networks in ambient conditions on graphite and boron nitride surfaces. The size and order of these networks is found to be dependent on the number of porphyrin macrocycles that make up each ring. In addition, simulations of isolated nanorings are

also performed using Monte Carlo methods to model the distortion previously been observed for isolated nanorings on gold surfaces. These are discussed in the context of spectroscopic measurements which suggest that both size dependent and thermally induced distortion affects the lifetime and delocalisation of excited states in these molecules.

Graphene is grown on hexagonal boron nitride surfaces using high-temperature molecular beam epitaxy. Large domains of monolayer graphene are successfully grown and are investigated using AFM and Raman spectroscopy. These domains are found to exhibit hexagonal moiré patterns on the graphene surface which is suggestive of orientational alignment with the underlying boron nitride substrate. Regions with high period and distorted moiré patterns are also observed which suggest that the graphene is under tensile strain which is attributed to the high growth temperatures used. The strain is found to significantly affect the Raman spectrum of graphene and a relationship between the strain and the shifting of Raman spectral peaks is determined. Successful attempts are also made to modify the strain in the graphene monolayer using an AFM tip which is observed to relax when defects are introduced in a controlled manner to the graphene monolayer. These results represent new approaches to the introduction and control of strain in graphene which may be useful for the fabrication of high-performance graphene devices.

Peer Reviewed Publications

- **Alex Summerfield**, Andrew Davies, Tin S. Cheng, Yongjin Cho, Christopher J. Mellow, C. Thomas Foxon, Kenji Watanbe, Takashi Taniguchi, Laurence Eaves, Sergei Novikov and Peter H. Beton. *"Strain-Engineered Graphene Grown on Hexagonal Boron Nitride by Molecular Beam Epitaxy"*. Scientific Reports, 6, (2016), 22440.

- T.S. Cheng, A. Davies, **A. Summerfield**, Y.J. Cho, C.J. Mellor, A.N. Khlobystov, T. Taniguchi, K. Watanabe, P.H. Beton, C.T. Foxon, L. Eaves, S.V. Novikov. *"High temperature MBE of graphene on sapphire and hexagonal boron nitride flakes on sapphire"*, Journal of Vacuum Science and Technology B, 34, (2016), 02L101.

- **Alex Summerfield**, Izabela Cebula, Martin Schröder and Peter H. Beton. *"Nucleation and Early Stages of Layer-by-Layer Growth of Metal Organic Frameworks on Surfaces"*. The Journal of Physical Chemistry C, 119, no 41, (2015), p. 23544–23551.

- Vladimir V. Korolkov, Simon A. Svatek, **Alex Summerfield**, James Kerfoot, Lixu Yang, Takashi Taniguchi, Kenji Watanabe, Neil R. Champness, Nicholas A. Besley, Peter H. Beton. *"van der Waals-Induced Chromatic Shifts in Hydrogen-Bonded Two-Dimensional Porphyrin Arrays on Boron Nitride"*. ACS Nano, 9, no 10, (2015), p. 10347–10355.

- Chaw-Keong Yong, Patrick Parkinson, Dmitry V. Kondratuk, Wei-Hsin Chen, Andrew Stannard, **Alex Summerfield**, Johannes K. Sprafke, Melanie C. O'Sullivan, Peter H. Beton, Harry L. Anderson and Laura M. Herz. *"Ultrafast delocalization of excitation in synthetic light-harvesting nanorings"*. Chemical Science, 6, no 1, (2015), p. 181–189.

Acknowledgments

The completion of a experimental PhD in any scientific field is by no means a solitary effort and there are many people who I owe thanks to for their help over the last few years.

Firstly I would like to thank my supervisor Peter Beton for his support, encouragement and guidance. Having a supervisor who has the ability to explain often abstract concepts in a straightforward manner can never be understated. I would like to thank the following colleagues past and present for their help and contribution to my understanding of the often frustrating and time consuming world of nanoscience, making really tiny things and the occasional bit of chemistry; Izabela Cebula, Vladimir Korolkov, Simon Svatek, Maria Wieland, Simon Taylor, Rob Temperton, Karsten Handrup, Adam Sweetman, Peter Sharp, Sam Jarvis, Philipp Rahe, Julian Stirling, Andrew Davies, Tin Cheng, James Kerfoot, Philip Moriarty, Tim Easun, Martin Schröder, Florian Moreau and Tamoghna Mitra. I would also like to thank Sergei Novikov for giving me the chance to continue my foray into the world of academia and the Engineering and Physical Sciences Research Council for funding my PhD.

The following people have made an extra contribution to my life over the last few years. Dave Farmer, Nikki Threlfall, Alexander of the Allens, Faris Sinjab, Ken Duncan and Emma Bradshaw, you have been part of the most surreal and painfully funny conversations that I have had. I wouldn't trade five minutes of it for the world.

I would also like to thank my parents Paul and Gaynor for their never ending encouragement and for giving me the freedom to do whatever took my interest throughout my formative years.

Thank you Gini for your love and support since we met a fantastic two and a half years ago. It only seems like five minutes ago that I was awkwardly trying to explain nanoscience to you on that hill in Bradgate Park. I promise I'll do the washing up more often when this is handed in.

The endless sight of a blinking cursor on a screen accompanied by the same view out of the window day after day is not pleasant, no matter how much coffee or hummous is ingested to mitigate the experience. Sometimes having company, no matter how annoying, loud or scratchy it can be is a welcome relief. Thank you Teddy for being persistently at my side every day I have spent working at home during the last few months. Your uncanny ability to reach up and tap me for attention, walk over my keyboard or just meow loudly at my face every time I manage to get into the swing of writing brings a level of normality to the caffeine induced psychosis that is writing a PhD thesis. Meow Ted... Meow.

Acronyms

AFM Atomic Force Microscope

AM-AFM Amplitude Modulated Atomic Force Microscopy

cBN Cubic Boron Nitride

CCD Charge-Coupled Device

CLS Classical Least Squares

CVD Chemical Vapour Deposition

DOS Density of States

EBL Electron Beam Lithography

ESD Electrospray Deposition

FFT Fast Fourier Transform

FM-AFM Frequency Modulated Atomic Force Microscopy

hBN Hexagonal Boron Nitride

HOMO Highest Occupied Molecular Orbital

HOPG Highly-Ordered Pyrolytic Graphite

IRMOF Isoreticular Metal Organic Framework

ITO Indium Tin Oxide

LBL Layer-By-Layer

LDOS Local Density of States

LUMO Lowest Unoccupied Molecular Orbital

MBE Molecular Beam Epitaxy

MEMS Microelectromechanical Systems

MLG Multi-Layer Graphene

MOF Metal Organic Framework

MWCNT Multi-Walled Carbon Nanotube

PCP Porous Coordination Polymer

PID Proportional Integral Derivative

PL Photoluminescence

QCM Quartz Crystal Microbalance

RT Room Temperature

SAM Self-Assembled Monolayer

SEM Scanning Electron Microscope

S.H.O Simple Harmonic Oscillator

SLG Single-Layer Graphene

SPM Scanning Probe Microscopy

STM Scanning Tunnelling Microscope

SURMOF Surface-Mounted Metal Organic Framework

SWCNT Single-Walled Carbon Nanotube

UHV Ultra-High Vacuum

TCSPC Time-Correlated Single Photon Counting

TH Tersoff Hamann

vdW van der Waals

XRD X-Ray Diffraction

μCP Microcontact Printing

Contents

Chapter 1

Introduction

"Start it!"

Julian, The Chin Review, episode 2

2009

Investigating structures at the nanometre scale (10^{-9}m) opens a window on the physical processes that drive the formation of bulk materials at the atomic and molecular level. The invention of the scanning tunnelling microscope (STM) [1] and the development of the wider field of scanning probe microscopy (SPM) has enabled unprecedented investigation of the properties of structure in real space at the this scale. The first structures to be investigated using these techniques were the surfaces of ordered bulk materials such as silicon and metallic crystal surfaces, for example, the 7 x 7 reconstruction of Si atoms as shown in Fig 1.1a and b [1]. However, it was not long before attention turned towards manipulating structures at this length scale.

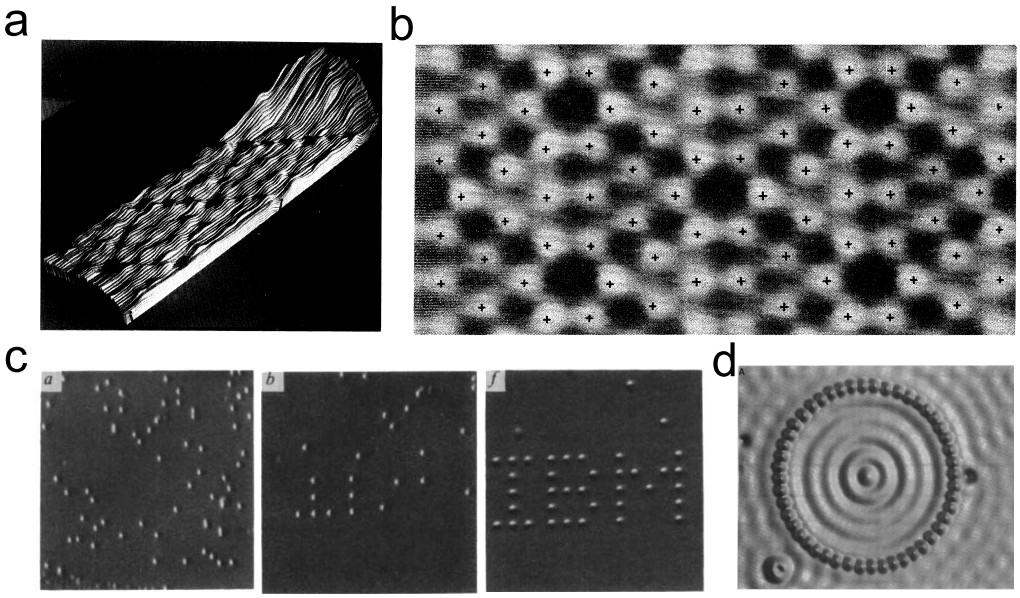

Figure 1.1: Early images of structures taken using a scanning tunnelling microscope. a-b) First images of the 7 x 7 reconstruction of Si atoms [2]. c) Manipulation of Xe atoms into the IBM logo [3]. d) Quantum corral formed by Fe atoms on a Cu(111) surface [4].

By considering a material as an ensemble of building blocks, either atoms or molecules, one can imagine manipulating these 'blocks' into new structures. Indeed some of the earliest work using STM by Eigler et al. involved manipulation of single xenon atoms [3] and the creation of the 'quantum-corral' in which the standing electron waves produced by an ordered structure of Fe atoms on a Cu surface are visible as shown in Fig 1.1c and d [4].

1.1 Top-Down Versus Bottom-Up Assembly

However, before discussing the details of fabrication and imaging of materials at the nanoscale in detail, it is useful to define two important terms when discussing the fabrication of structures on surfaces, the so-called *top-down* and *bottom-up* approaches.

Top-Down

Conventional techniques used to form structures on surfaces form the top-down approach. Pieces are removed from a larger piece of material to form a structure on its surface. For example, a top-down approach is used in the fabrication of microstructures and has been critical to the development of microelectronic devices. A starting material, typically a bulk material such as a wafer of crystalline Si is patterned by a photosensitive resist. This pattern allows the surface to be selectively etched to form permanent features in the surface as shown in Fig 1.2.

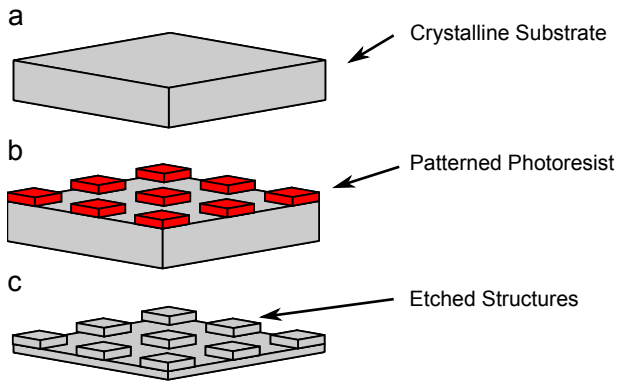

Figure 1.2: Schematic of top-down assembly. a) A single crystal substrate. b) Application of a pattern via photoresist (red) protects specific regions from the effects of etching. c) After etching and removal of the photoresist the final structure is formed in the surface.

As the number of features required on a surface has become ever higher, the space available to fit these features on a surface goes down and down. In the case of photolithography this has meant using smaller and smaller wavelengths of light. However, there are limits on the size of features that can be reliably produced using these techniques despite many remarkable engineering advancements in the semiconductor industry that have kept this as the method used in the fabrication of almost all electronic devices.

Bottom-Up

The creation of structures by using smaller components, such as individual atoms and molecules, to form larger assemblies describes the bottom-up approach. By either manually positioning atoms or molecules or exploiting intermolecular interactions to promote the formation of ordered networks, it is possible to direct the formation of structures in a controlled manner down to the atomic level.

The concept of manipulating matter at this scale is often associated with Richard Feynman's lecture more than 20 years prior to the invention of the STM titled, *"There's plenty of room at the bottom"* [5]. In this talk Feynman discusses the idea of creating new materials and structures by manipulating on an atom-by-atom basis. Whilst the breakthrough work of Eigler et al. demonstrated the realisation of this dream, this approach is often impractical on account of the highly specialised conditions and large amount of time required to make even simple yet delicate structures on an atom-by-atom basis.

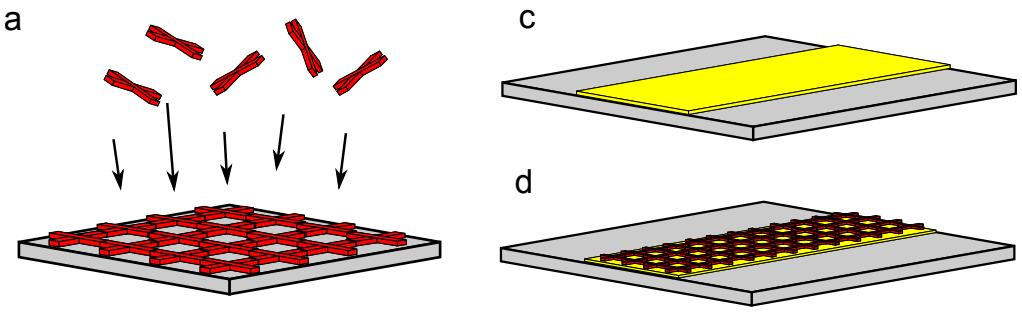

Figure 1.3: Bottom-up assembly of nanostructures. a) Deposition of molecules onto a surface results in the formation of periodic structures through self-assembly. b) Tailoring the surface energy or chemistry in a specific region (yellow) of a surface allows spatial control over the placement of self-assembled nanostructures. c) This allows ordered structures to be formed on a specific region of a substrate.

An alternative to this is the idea of allowing matter to 'self-assemble' using the local interactions between the 'building blocks' to form ordered structures as shown in Fig 1.3a. This also overcomes the problem of fabricating structures with a thickness of a monolayer of molecules or atoms since a material may be 'designed' in way that allows it to be deposited over a surface and form into a desired structure. In addition, changing the properties of a surface allows for the self-assembly of ordered networks to be directed in to specific regions as shown in Fig 1.3b.

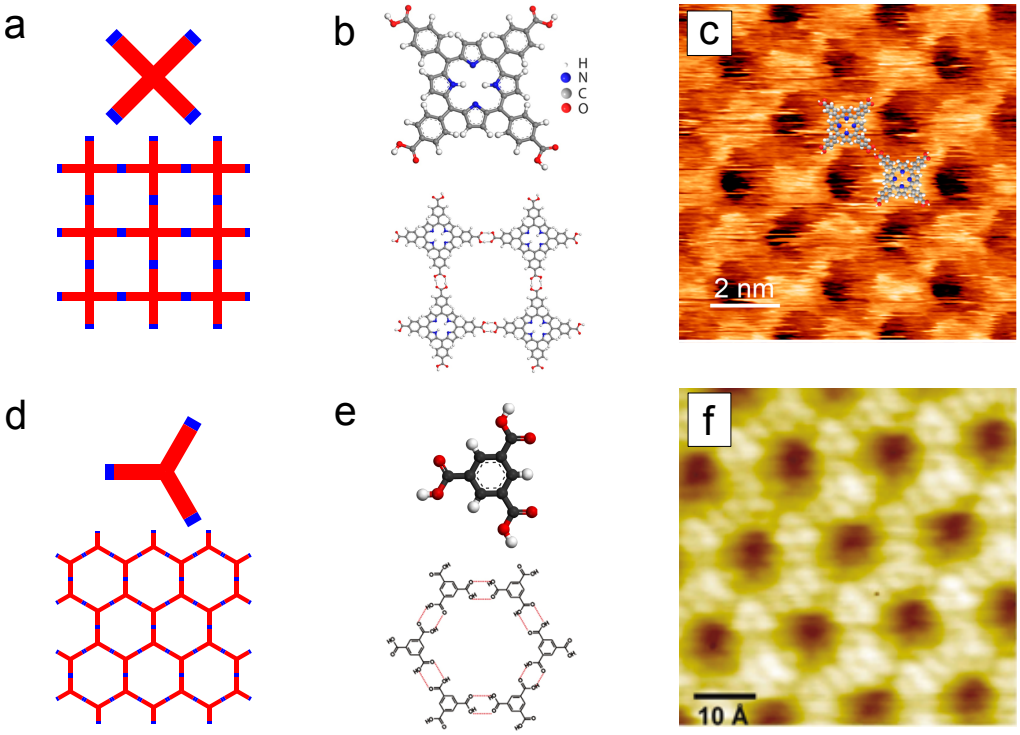

Figure 1.4: Self assembly of molecules into hydrogen bonded structures. a) and d) show two different molecular geometries and the ordered structures that they can form due to intermolecular bonding (blue). b) and e) show examples of the molecular geometries shown in a and d for real molecules and; e) and f) show real-space imaging of these structures using SPM techniques. b and c are adapted from [6]. e and f are adapted from [7] and [8] respectively.

One way to do this is by synthesising molecules with particular geometries and controlling the placement of functional groups. This means that bonding can be directed and allows the formation of long range order in two dimensions on a surface. This is typically achieved through interactions such as hydrogen [9] or coordination [10] bonds to form *supramolecular* assemblies or even the formation of covalent bonds between surface adsorbed molecules [11]. Figure 1.4 shows how molecules with differing symmetries can be used to form square and hexagonal lattices in two dimensions along with some examples from the literature of these structures. These self-assembled structures also allow the investigation of supramolecular structures in ambient conditions since they often do not require the tightly controlled conditions required for atom-by-atom manipulation.

It is this bottom-up self-assembly approach to structure formation that is explored in this thesis. Three different systems are investigated, the growth of three dimensional thin-films, ordered molecular monolayers and the growth of an atomically thin material. The following is a content summary of the theory and experimental chapters.

1.2 Scope of Thesis

Firstly, chapter 2 discusses the theoretical concepts behind the techniques used in the later experimental chapters. The physical effects behind the operation of equipment that has been used to acquire data are introduced at a level sufficient to understand the data that is presented in the experimental chapters. The structure of materials commonly used as substrates in the field of scanning probe microscopy are also discussed as an understanding

of these is often critical to interpreting images of molecular networks and other nm-scale structures.

Chapter 3 describes an investigation of a class of porous coordination polymers known as metal-organic frameworks (MOFs) using high resolution atomic force microscopy (AFM). These materials are promising candidates for a wide range of gas separation, catalytic and storage applications on account of their high porosity, tailorable geometry and chemical functionality. In particular, the epitaxial growth of MOFs on substrates may provide a route to the fabrication of highly responsive coatings and sensor devices. The current literature on this is contradictory and unclear with regards to the nm-scale quality of these films when grown using a 'layer-by-layer' (LBL) growth technique [12].

Growth of a well known MOF, HKUST-1, on gold surfaces using this LBL method is investigated experimentally. Repeated imaging of the same sub-micron area on the surface with AFM has been performed which allows repeated measurement of individual nanocrystallites. The data acquired suggests a model consistent with a polycrystalline growth mode in which small crystallites seed the growth of a laterally polycrystalline film. This has significant implications for some proposed applications of thin MOF films when compared with the epitaxial growth mode that current literature suggests is achievable using the LBL technique.

In addition, early work investigating the surface structure of a newly synthesised family of solvothermally grown MOFs is presented. These crystals grow in a sheet like geometry with known crystallographic faces that may allow integration with devices using micro-positioning and transfer techniques.

Looking to nature for inspiration is often employed when conceiving of novel new materials. In particular, the creation of new materials for applications such as solar power generation can benefit hugely by investigating the structures in photosynthetic complexes [13]. Whilst the properties of artificially synthesised materials for this purpose show promising results in spectroscopic measurements of their light absorption properties [14, 15, 16], integration of these novel materials into practical devices may place limits on their performance. As a result it is useful to study how these materials behave when adsorbed on a surface.

In chapter 4 the deposition of porphyrin-based nanorings on surfaces is investigated. Experimental observations of highly-ordered networks of these nanorings on graphite and hexagonal boron nitride (hBN) surfaces imaged using both liquid STM and high resolution AFM are presented. The formation of long-range order in nanoring networks is found to be affected by changes in the size of the nanorings. This has implications for the fabrication of devices using these materials where long-range order may be desirable.

The bottom-up approach to assembly is taken to the extreme when considering the fabrication of a useful structure from a single layer of atoms to produce a truly two dimensional material. Since the isolation of the most well-known and widely studied of these, graphene, by Geim and Novoselov [17], a huge volume of work has been devoted to the study and potential applications of graphene and related two dimensional materials in the last ten years. Despite many reports of the remarkable properties that graphene exhibits, devices using graphene as an active component typically require time-consuming and laborious top-down assembly techniques.

Attempts to produce graphene using bottom-up methods have had mixed success. Whilst it has become possible to grow large amounts of graphene on an industrial-scale on various metallic surfaces [18], to use this material in an electronic device requires transfer onto a highly-ordered insulating substrate [19]. As a result, several different approaches to the growth of graphene directly onto an insulating substrates are being investigated by various groups.

Chapter 5 presents promising results on the growth of graphene using a bottom-up epitaxial approach to solve this problem. Existing literature on epitaxial approaches to the growth of graphene are discussed and the growth of graphene on hBN using high temperature molecular beam epitaxy (MBE) is investigated experimentally. Initial experiments are performed on bare sapphire substrates in order to calibrate the carbon flux rates at the high substrate temperatures used. Following this, growth onto the hBN surface is investigated. Both island growth and complete coverage of monolayer graphene is observed with ambient AFM and confirmed with Raman spectroscopy which makes these results the first reported growth of large $\sim$10 μm-scale graphene domains using MBE. Highly regular moiré patterns in the graphene surface are observed suggesting an epitaxial relationship between the two lattices.

In addition, highly distorted and large period moiré patterns have been observed which suggests that the graphene is strained. Spatially correlated measurements of the moiré period and Raman signature of this material have been taken which allow the change in Raman spectra to be determined relative to the strain in the graphene lattice. This enables comparisons to be made with existing studies on the strain dependence of the Raman

spectrum of graphene and suggested mechanisms for the formation of strain at these high growth temperatures are proposed. In addition, early results on attempts to modify the strain using an AFM probe are presented which suggest the strain can be manipulated by a local probe.

Finally, chapter 6 presents conclusions from the results in this thesis. In addition, suggestions for further investigation of the systems in chapters 3-5 are discussed.

Chapter 2

Techniques and Theory

The study of atomic and molecular ordering at surfaces requires the use of several imaging and spectroscopic techniques. The following is a discussion of the theory behind the experimental techniques used in this thesis.

Scanning probe microscopy (SPM) is discussed in detail as it is used in all the experimental chapters as the primary tool for imaging surface structures. A theoretical background to scanning tunnelling microscopy and atomic force microscopy is presented along with an explanation of how these techniques are implemented. In addition, image processing steps are discussed as they have been extensively used throughout this thesis to correct for issues commonly encountered such as thermal drift, sample tilt and system noise when working at the nanoscale. The structures of materials commonly used as SPM substrates and the steps required to prepare them are also discussed. Fluorescence microscopy and Raman spectroscopy are also discussed since they are used to acquire data presented in chapters 4 and 5 respectively.

2.1 Scanning Probe Microscopy

Scanning probe microscopy (SPM) is arguably the most useful and widely used tool for the study of atomic surface states and the structures formed by molecular networks on surfaces both in ultra-high vacuum (UHV) and under ambient conditions. In all cases the tip-sample interaction defines the type of SPM and ultimately dictates the maximum resolution possible. Despite this there are many technical aspects common to all SPM instruments, particularly with regard to the movement of the probe relative to the surface being studied. In general a sharp tip (down to a single atom) is moved close to a surface in three dimensions using piezoelectric actuators.

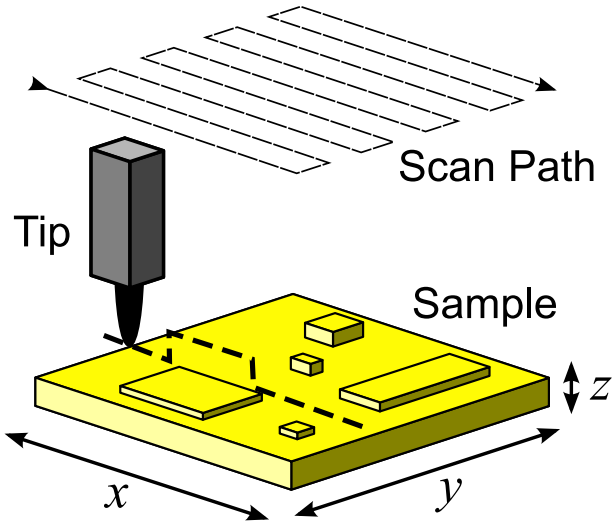

Figure 2.1: Overview of SPM operation, a tip in close proximity to a sample with various topographic features traces a path line by line to build up an image of a surface whilst x, y and z coordinates are recorded to build up a height map of a surface.

An overview of SPM operation is shown in Fig 2.1. A parameter dependent on the interaction between the tip and sample (referred to as a set point from here on) at these distances is constantly fed back into the SPM control system. By monitoring this parameter as the tip is moved in the x

and y direction, the tip z position (height) relative to the surface is kept constant. This is implemented by a feedback loop so that the measured interaction strength at the set point is maintained. As the tip is raster scanned across the sample the height is recorded at each x and y position so that a 3D height map of the surface can be generated.

To a first approximation on a uniform atomic surface this gives the topography of the surface, revealing the atomic arrangement of the surface, crystal-step edges and the arrangement of adsorbed molecules on the surface. However, this assumption does not hold when the state (either electronic or chemical) of the surface is modified or if it varies across the surface (and ultimately the tip-sample interaction is changed) by the adsorption of molecules on to the surface, or the presence of defects in the surface.

An alternative mode of operation is possible known as *constant height* mode in which the tip is kept at a fixed distance above the surface and then scanned in x and y whilst the interaction between the tip and sample is measured. A risk of constant height mode is that, as the tip height is not adjusted, the presence of a feature on the surface might cause the tip to crash into the surface, potentially ruining the sharpness of the tip and ultimately degrading the quality of the image. However, all data presented in this thesis was acquired using constant set point imaging and therefore constant height mode is not discussed further.

2.2 Scanning Tunnelling Microscopy

Since the invention of the scanning tunnelling microscope (STM) by Gerd Binnig and Heinrich Rohrer in 1982 [1] the STM has enabled the first images of individual atomic surfaces [2], the quantum corral [4] and self-assembled molecular networks [20]. The invention of the STM resulted in Binnig and Rohrer being awarded the 1986 Nobel prize in physics for *"their design of the scanning tunnelling microscope"* [21].

The feedback parameter used in STM is the current due to electrons quantum tunnelling through a potential barrier. The barrier in this case is a gap between a sharp tip of width z_t and a sample. Figure 2.2 shows an electron of energy E tunnelling through a 1D barrier of height V_0.

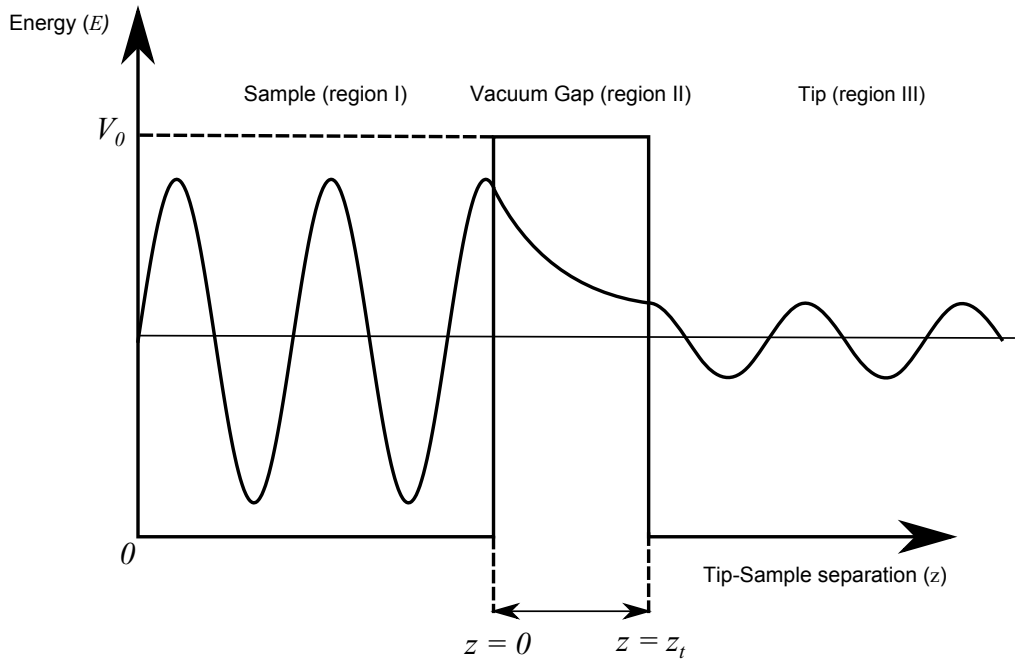

Figure 2.2: Illustration of tunnelling through potential barrier of width, z_t.

Tunnelling can be described by starting with time independent Schrödinger

equation,

$$\mathcal{H}\psi(z) = E\psi(z) \tag{2.1}$$

which for a particle in one dimension is;

$$\frac{\hbar^2}{2m}\frac{d^2\psi(z)}{dz^2} + V(z)\psi(z) = E\psi(z) \tag{2.2}$$

In the regions I-III in Fig 2.2, the wavefunctions ($\psi_{I-III}(z)$ respectively) have the form,

$$\psi_I(z) = Ae^{ikz} + Be^{-ikz} \tag{2.3}$$

$$\psi_{II}(z) = Ce^{-\mu z} + De^{\mu z} \tag{2.4}$$

$$\psi_{III}(z) = Fe^{\pm ikz} \tag{2.5}$$

A and B are the incident and reflected wave function amplitudes, similarly C and D are the amplitudes inside the barrier. Since an electron with a high energy, or for a narrow barrier, is more likely to be found on the left side of the barrier ($z = 0$) than on the right ($z = z_t$), therefore $D = 0$. The wave vector of the electron, k, is given by,

$$k = \sqrt{\frac{2mE}{\hbar^2}} \tag{2.6}$$

where E is the energy of the electron. μ is the decay constant inside the potential barrier ($0 < z < z_t$),

$$\mu = \sqrt{\frac{2m}{\hbar^2}(V_0 - E)} \tag{2.7}$$

where, V_0, is the height of the potential barrier, in this case the vacuum

level, and as a result, the quantity, $V_0 - E$ is the work function of the sample for electrons at the Fermi level. Since the electron has a finite probability of tunnelling through this barrier given by T, the tunnelling coefficient. This is defined as the ratio between the probability fluxes of the transmitted wave (region III) and the incident wave (region I) i.e.

$$T = \left| \frac{F^2}{A^2} \right| \tag{2.8}$$

Since the probability that an electron will cross the barrier decays exponentially with the barrier width (z_t) and T is directly proportional to the tunnelling current, I_t, the following relation can be deduced,

$$T \propto I_t \propto \exp\left(-2\mu z_t\right) \tag{2.9}$$

which implies that to a first approximation; the tunnelling current will decay exponentially with the barrier size (i.e. the tip-sample separation) [22]. Assuming a work function of ∼4-6 eV (an approximate value for many materials) means that increasing the barrier width by 0.1 nm gives approximately an order of magnitude reduction in the tunnelling current. This allows for an extremely high spatial resolution since the main contribution to the tunnelling current will be from small tip-features such as a cluster of atoms at the tip apex close to the sample.

As the absence of a voltage would result in no net electron flow (and zero tunnelling current), a bias voltage is required between the tip and sample. Figure 2.3 shows a tip-vacuum barrier-sample junction system in one dimension. For zero applied bias, the Fermi level of the tip and sample, E_{fT} and E_{fS} respectively, are aligned.

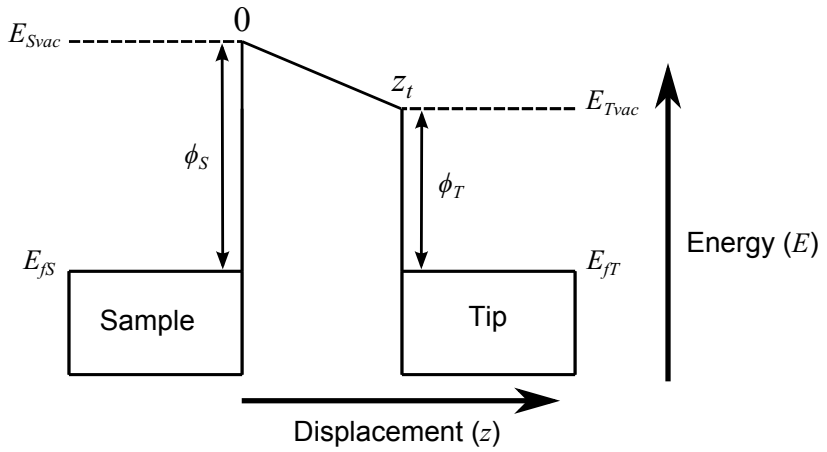

Figure 2.3: STM tunnel junction under zero bias showing the aligned Fermi levels of the tip and sample and the work functions for the tip and sample, ϕ_T and ϕ_S respectively.

In the finite voltage regime, a bias voltage, V, is applied to the tip (or sample) and the energy levels are shifted upwards or downward by an amount eV where, e is the elementary unit of charge. The electron flow is therefore dependent on whether the sample bias is positive or negative [23]. If the sample is positively-biased then electrons tunnel from occupied states in the tip to unoccupied states in the sample (Fig 2.4a) and vice versa for a negatively-biased sample (Fig 2.4b).

This simple exponentially decaying dependence of the tunnelling current on tip-sample separation is typically sufficient to understand basic operation of the STM for uniform metallic substrates. However, in order to understand bias dependent effects and image contrasts caused by adsorbed molecules, a more detailed consideration of the tunnelling effect in STM is required.

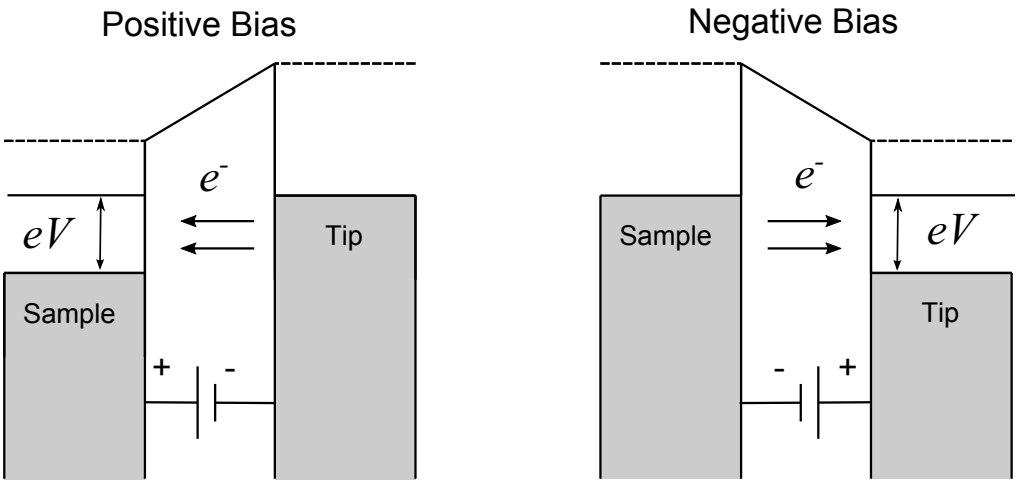

Figure 2.4: Tunnelling when, a) the sample is positively biased, electrons tunnel from the tip to sample and b) when the sample is negatively biased, electrons tunnel from sample to tip.

2.3 Further Analysis of Tunneling

Beyond the simple exponentially decay approximation, further analysis of the tunnelling current becomes non-trivial since it involves detailed consideration of the electronic states of the tip and the sample. For large features (i.e. >1 nm), treating the surface as a topographic representation of the surface is found to be a reasonable approximation (neglecting any large local changes in the work function of the surface being imaged). However, on the atomic scale and particularly for semiconductors, the assumption that constant current operation yields the topography of a substrate often fails.

A useful approach to explaining the contrast in STM imaging was proposed by Tersoff and Hamann [24]. Starting from Bardeen's earlier work, a first-order time-dependent perturbation theory approach gives the tun-

nelling current [25];

$$I = \frac{2\pi e}{\hbar} \sum_{\mu,\nu} \left[f(E_\mu) - f(E_\nu) \right] |M_{\mu\nu}|^2 \, \delta(E_\mu + V - E_\nu) \tag{2.10}$$

where, $f(E)$ is the Fermi function, V is the applied voltage between the tip and sample, $M_{\mu\nu}$ is the tunnelling matrix between states ψ_μ (the tip) and ψ_ν (the surface). E_μ and E_ν are the unperturbed energies of states ψ_μ and ψ_ν respectively. The delta function, $\delta(E_\mu + V - E_\nu)$, ensures the conservation of energy for the case of elastic tunnelling [23]. The main problem in calculating the tunnelling current is the determination of the tunnelling matrix, $M_{\nu\mu}$. According to Bardeen, $M_{\nu\mu}$ is given by;

$$M_{\nu\mu} = \frac{\hbar^2}{2m} \int d\mathbf{S}.(\psi_\mu^* \nabla \psi_\nu - \psi_\nu \nabla \psi_\mu^*) \tag{2.11}$$

The integral in equation 2.11 is evaluated over the surface of the tip which is non-trivial since the atomic structure of the tip is typically not known [23]. Tersoff and Hamann (TH) used the simplest (ideal) model to approximate the STM tip, a spherical symmetric single atom known as an s-wave ($l = 0$) ground state representing ψ_μ [24]. The tip is assumed to be symmetric with a radius of curvature R and centre of curvature r_0. The distance between the surface and the nearest part of the tip is z as shown in Fig 2.5.

For most situations, the Fermi functions can be replaced by the zero temperature values (i.e. unit step functions) and, in the limit of small voltages, equation 2.10 can be simplified to [26];

$$I = \frac{2\pi}{\hbar} e^2 V \sum_{\mu,\nu} |M_{\mu\nu}|^2 \delta(E_\nu - E_F) \delta(E_\mu - E_F) \tag{2.12}$$

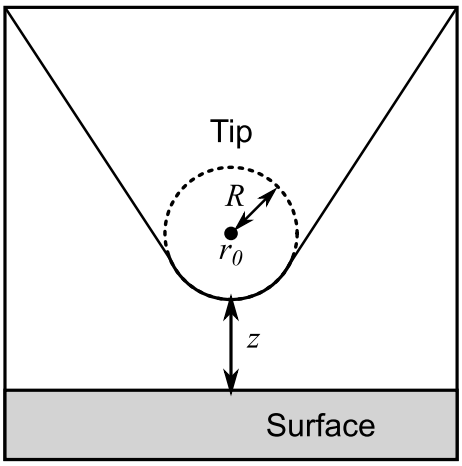

Figure 2.5: Schematic for the Tersoff-Hamann s-wave tip model. Adapted from [23].

where E_F is the Fermi energy. Using the TH model, the relation for the tunnelling current can be determined and the following relation can be made;

$$I \propto \sum_{\nu} |\psi_\nu(r_0)|^2 \delta(E_\nu - E_F) \tag{2.13}$$

Since,

$$\sum_{\nu} |\psi_\nu(r_0)|^2 \delta(E_\nu - E_F) = n_s(E_F, r_0) \tag{2.14}$$

where, $n_s(E_F, r_0)$ is the local density of states (LDOS) at the Fermi level of the surface at the position of the tip [23, 24]. Hence,

$$I \propto n_s(E_F, r_0) \tag{2.15}$$

Therefore using the TH model, STM images at low sample bias in constant current mode image the constant contour LDOS at E_F evaluated at the centre of the radius of the tip r_0 of a surface. As a result this does not necessarily correspond to the spatial arrangement of surface atoms or atomic structure of surface adsorbed molecules. This means that significant differ-

ences in surface topography may be observed depending on the electronic states of the surface. Images of semiconductors such as the GaAs(110) surface illustrate this point and display a strong voltage dependence. In this case the positive contrast changing between either the Ga or As atoms for positive and negative sample bias respectively, as shown in Fig 2.6a and b [27].

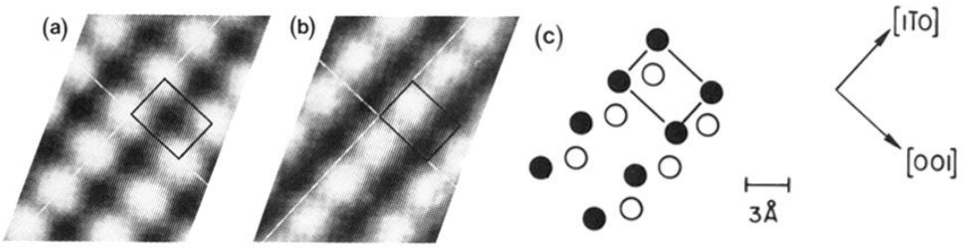

Figure 2.6: Constant current STM images of the GaAs(110) surface at sample voltages of a) +1.9V and b) -1.9V. c) Top view of the surface atomic structure. As atoms are represented by open circles and Ga atoms by closed circles. The rectangles in a-c indicate a single unit cell, whose position is the same in all three pictures. Adapted from [27].

In addition to imaging bare metal or semiconductor substrate surfaces, STM can also be used to image surface adsorbed molecules. In a molecule, the energy levels of the electrons can be expressed as a set of orbitals relative to the highest occupied molecular orbital (HOMO) and the lowest unoccupied empty molecular orbital (LUMO) i.e. the LUMO + 1,2,3... or the HOMO - 1,2,3... levels. When adsorbed on the surface the molecule will be strongly coupled to the surface states and the energy levels of the molecular orbitals will be pinned relative to the Fermi level of the surface. This is shown in Figure 2.7 in which the tunnel junction between tip and sample is modified by the presence of a surface adsorbed molecule for the case of zero applied tip/sample bias.

In the case of a finite bias between the tip and sample electrons will

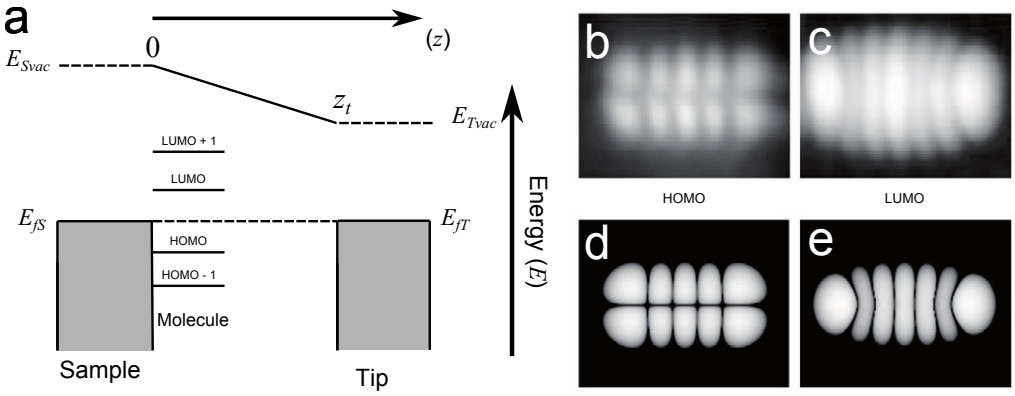

Figure 2.7: a) Energy diagram of an STM tunnel junction with adsorbed molecule on the sample surface. b-e) STM images of a pentacene molecule deposited on a NaCl monolayer on a Cu(111) substrate showing the electronic structure of the molecular orbitals at different sample bias. b) HOMO image taken at a sample bias of -2.5 V. c) LUMO image taken at a sample bias of +1.7 V. d-e) Density functional theory (DFT) calculations of the d) HOMO and e) LUMO. Adapted from [28] via [29].

tunnel to/from these molecular orbitals. For negative sample bias, electrons will tunnel from the HOMO of the molecule to the tip and from the tip to the LUMO for a positively biased sample. Therefore, imaging a molecule with a positive/negative sample bias will result in an image of the LUMO/HOMO states respectively. This is shown for a pentacene molecule in Fig 2.7b-e.

Modification of a surface by the adsorption of molecules onto a substrate may also result in the molecule being imaged in constant current mode as a depression rather than a topographically high region as the molecule acts as an energy barrier. As a result, care must be taken when interpreting 'height' values in constant current imaging. All measurements of height for the STM data presented in this thesis refer to the apparent height for constant tunnelling current.

A schematic for STM operation is shown in Fig 2.8. It shows an STM operating in constant current mode scanning in one dimension, in this case

the x direction. The tip follows a contour of constant tunnelling current and therefore (approximately) constant height from the surface. The tip position is controlled by feedback (see section 2.7) electronics.

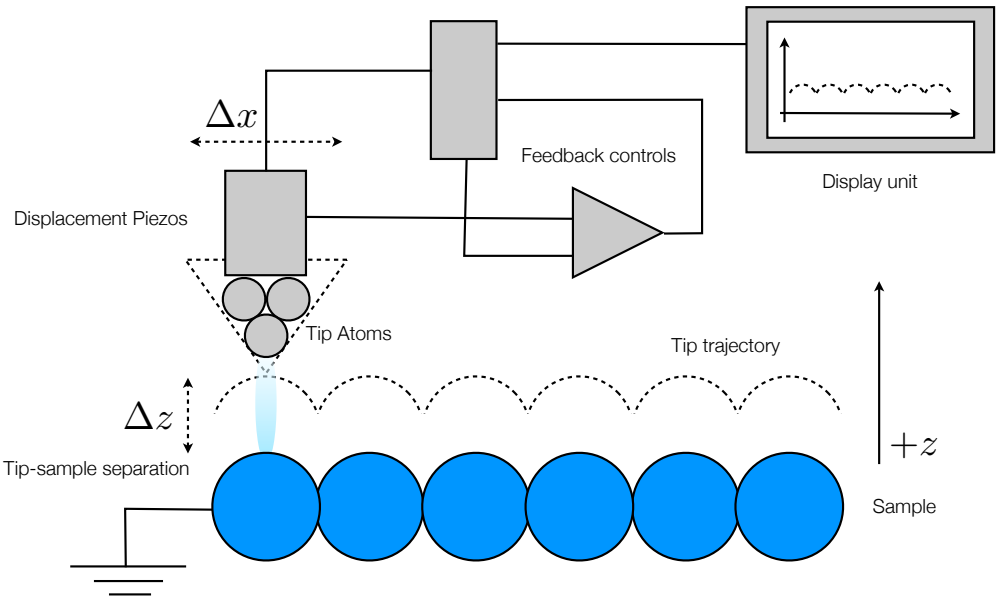

Figure 2.8: Schematic of STM showing operation in constant current imaging mode.

Further analysis of STM theory is not covered since it adds little extra insight into the origin of image formation of images for the STM data presented in this thesis. However, detailed consideration of surface states would be required in theoretical investigations and the simulation of STM images which are not considered in this work [30].

2.4 Atomic Force Microscopy

Soon after the invention of the STM, the atomic force microscope (AFM) was invented [31]. The mode of imaging in AFM is due to the short range attractive and repulsive interactions between a tip on the end of a deformable cantilever and the surface. The forces experienced by an AFM

tip may be a mixture of van der Waals forces (vdW), Pauli repulasion, capillary, chemical bonding and electrostatic forces. However, for simplicity the net interaction between the tip and sample can assumed to obey a Lennard-Jones potential which approximates the interaction between a pair of neutral atoms or molecules and is given by [32];

$$V(r) = E_0 \left[\left(\frac{r_0}{r} \right)^{12} - 2 \left(\frac{r_0}{r} \right)^{6} \right] \tag{2.16}$$

Where, E_0 is the depth of the potential well, r is the inter-particle distance and r_0 is the point at which the potential reaches it's minimum. The r^{-12} short-range repulsive term describes Pauli repulsion and the attractive r^{-6} term describes long-range attractive forces such as vdW. The distance dependence of the Lennard-Jones potential is shown in Fig 2.9 and shows how the forces at large distances ($r > r_0$) are attractive, balance at the equilibrium point (r_0) and then rapidly become strongly repulsive for small distances ($r < r_0$).

Since the force experienced by the tip is not dependent on conduction of electrons, AFM can be performed on almost any surface provided the sample roughness is low enough. The standard tip used in AFM consists of a microscopic cantilever (typically made from Si/SiN) with a MEMS[1] fabricated tip with a radius of curvature of the order of nanometers as shown in Fig 2.10.

The cantilever is brought close to the surface and moved using a three-axis array of piezo elements, typically in a raster scan motion. As the tip is scanned over the surface, the force between the tip and the sample results in a deflection in the cantilever. This deflection is typically measured by

[1]Microelectromechanical systems

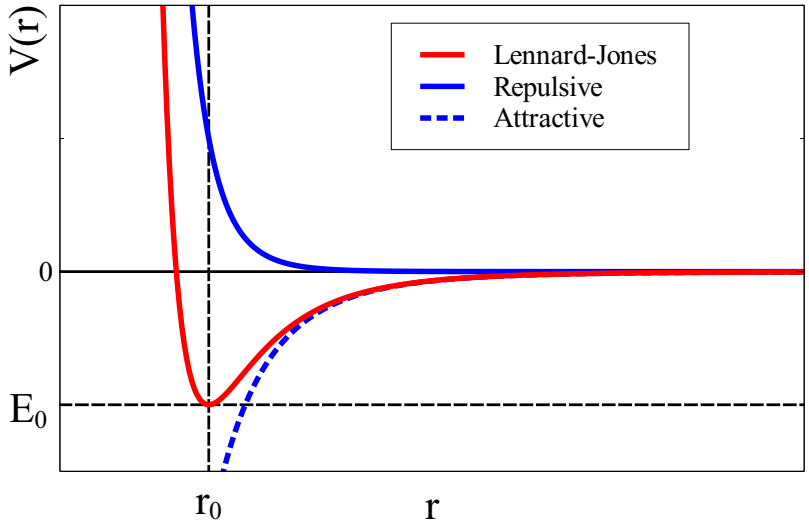

Figure 2.9: Lennard-Jones potential (solid red line) also showing repulsive (blue solid line) and attractive (blue dashed line) interactions.

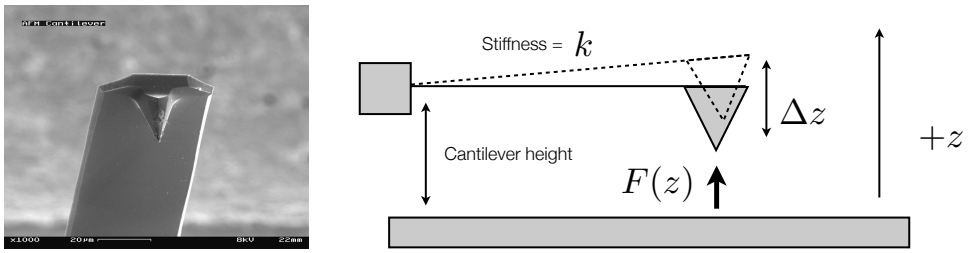

(a) (b)

Figure 2.10: a) SEM image of an AFM tip and cantilever. b) 1D cantilever displacement model.

reflecting a laser beam off of the tip (the backside of which is often coated in a reflective metal coating such as thermally evaporated Al) and detected by an array of photodiodes. Other methods such as detecting the voltage generated by the deformation of a piezoelectric cantilever also exist however they are not used in this work.

As shown in Fig 2.10, for small 1-D displacements, Δz, the force on a tip due to the cantilever-sample force, $F(z)$, for a cantilever of spring

constant, k can be expressed simply using Hooke's law;

$$F(z) = k\Delta z \tag{2.17}$$

By maintaining a constant deflection (therefore force exerted between the tip and the sample) as the tip is scanned, a map of the sample topography may be collected.

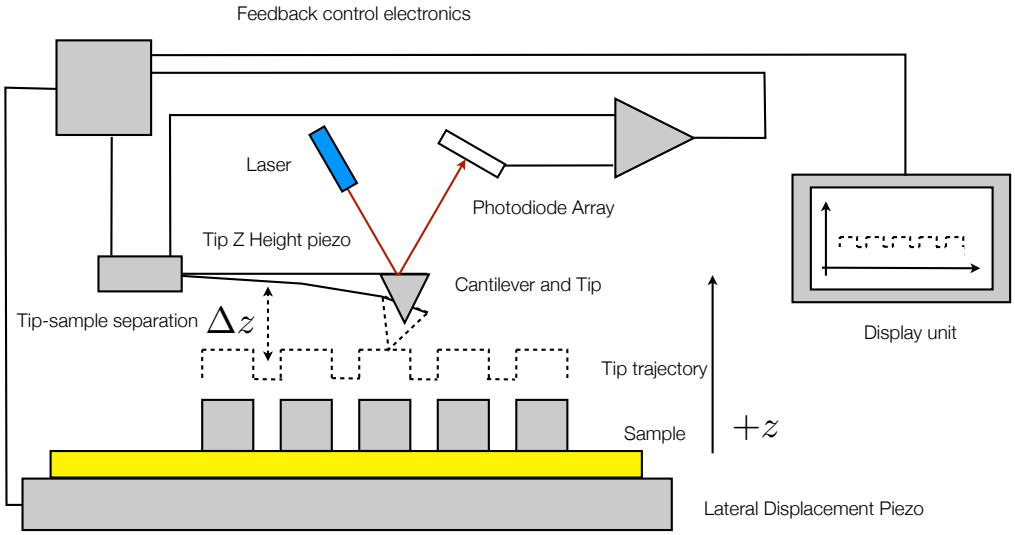

Figure 2.11: Schematic of AFM operation.

A general schematic for AFM operation can be seen in Fig 2.11. Since AFM shares many of the general SPM principles applied to STM and most commercial STM systems can be used as AFMs with a simple exchange of the tip holder.

2.5 Contact Mode

The simplest mode of operation for an AFM is contact mode in which a low stiffness cantilever (i.e. low k) is brought in contact with the surface and

the tip scanned at a constant deflection set-point to build up a topographic map of the surface. Contact mode can lead to tip or sample damage as the tip moves over the surface, particularly when imaging molecular monolayers which are easily disturbed by the tip. The tip deflection is kept constant to maintain a constant force between the tip and sample. Despite this, operating the AFM in a contact mode with an extremely small deflection (and therefore low force) set point in some instances enables molecular or even atomic resolution of a sample, examples of which are shown in Fig 5.25 and [6].

With a knowledge of the cantilever force-deflection relation, force spectroscopy can be performed in which the tip is gradually pressed into the sample and the deflection measured as a function of the tip displacement. Since the surface will also be deformed as a result of the tip pressing into the sample, knowledge of the mechanical properties of the surface such as the Young's modulus can be acquired on a specific region of a surface.

(a) (b) (c)

Figure 2.12: Examples of nanoindentation lithography. a) Chemical formula of polystyrene written in a thin spin coated polystyrene film. b) An input image which is used to generate a path for the AFM tip to trace c.) Result of etching Fig 2.12b into a polystyrene film. Images a and c are the work of the author and image b is from [33].

A variation of this mode of operation is known as nano indentation lithography. The tip is driven to a higher set point than would typically be used for contact mode imaging and the tip moved across the surface in a predetermined pattern. This causes etching of the surface and the resulting pattern can then be imaged at a lower set-point. Examples of this are shown in Fig 2.12 for a polystyrene surface. Apart from simply modifying the surface topography, contact mode lithography can also be used to change the chemical functionality of a surface in a specific region. By removing a passivating monolayer in the presence of a another molecule (typically in solution) the second molecule can be adsorbed on to the surface in the regions where the first molecule has been removed [34].

2.6 AC Mode

The second AFM operation mode is known as non-contact or tapping mode AFM (referred to as AC mode in this thesis for consistency with the literature). In AC mode the cantilever is oscillated at or close to its resonant frequency, ω_0. As the tip is brought towards the surface, the short range interactions of the tip with the surface cause a shift in the resonant frequency. This shift can be measured directly using frequency locking (FM-AFM) or by monitoring a reduction in oscillation amplitude from the free-air amplitude (AM-AFM). The tip is adjusted in height to compensate for this shift and a constant oscillation amplitude (or frequency) is maintained as a set point as the tip is scanned over the surface.

The oscillation of a cantilever (for small displacements from equilib-

rium) can be modelled as a simple driven harmonic oscillator;

$$\underbrace{m\frac{d^2z}{dt^2}}_{\text{Inertial force}} + \underbrace{\gamma\frac{dz}{dt}}_{\text{Damping term}} + \underbrace{kz}_{\text{Restoring force}} = \underbrace{F(t) \quad (\text{e.g.} \quad F(t) = F_0\cos(\omega t))}_{\text{Time-dependant driving force.}} \tag{2.18}$$

The magnitude of the cantilever response, z_ω, for a given drive frequency, ω, is given by;

$$|z_\omega| = \frac{F_0}{k}\frac{\omega_0^2}{[(\omega^2-\omega_0^2)^2 + (\frac{\omega\omega_0}{Q})^2]^{\frac{1}{2}}} \tag{2.19}$$

where, ω_0 is the resonant frequency of the cantilever, k is the spring constant of the cantilever, F_0 is the amplitude of the driving force and Q is the quality factor of the cantilever. In a force gradient, i.e. the tip being influenced due to substrate-tip interactions, oscillations ($z_{ac}(t)$) about this static position z_0 are considered:

$$z_t = z_0 + z_{ac}(t) \quad \Rightarrow \frac{dz}{dt} = \frac{dz_{ac}}{dt} \tag{2.20}$$

It can be shown (for small amplitude oscillations) that by expanding around the position z_0:

$$m\frac{d^2z_{ac}}{dt^2} + \gamma\frac{dz_{ac}}{dt} + \underbrace{kz_{ac} - \frac{dF}{dz}|_{z_0}z_{ac}(t)}_{=(k-\frac{dF}{dz})z_{ac}(t)} = F_0\cos(\omega t) \tag{2.21}$$

This implies that the tip motion can be modelled as a driven S.H.O with

a modified effective spring constant:

$$k_{eff} = k - \frac{dF}{dz} \tag{2.22}$$

leading to a shift in resonant frequency to:

$$\omega_{eff} = \left[\frac{k_{eff}}{m}\right]^{\frac{1}{2}} = \omega_0 + \Delta\omega_0 \tag{2.23}$$

As the amplitude response of an oscillator slightly off resonance is highly sensitive to frequency changes, by adjusting the tip height until the amplitude of oscillation matches a set value the tip will follow a contour of constant $\frac{dF}{dz}$ over the sample. This is analogous to constant current operation in STM but with the crucial difference that the topography is not dependent upon the electronic LDOS. Since the forces required to affect the amplitude of an oscillating cantilever near resonance are smaller than that required to induce static deflection in contact mode, AC mode is typically used for imaging delicate samples such as molecular monolayers.

AFM has undergone many considerable advances and there are a variety of difference operating modes not covered in this text. Many of these are dependent upon the use of specialised cantilevers for the detection of different interaction types, such as the use of magnetic cantilevers for imaging of magnetic domains [35].

2.7 Feedback

The most common feedback loop implemented in SPM equipment is a proportional-integral-derivative (PID) controller in which the error in the measured interaction signal relative to the set point is calculated along with the time derivative and integral of this error. These values are then used to calculate an output signal for the next time-step in order to minimise the error and maintain the desired set-point. The PID algorithm for the case of an SPM instrument is as follows;

$$O_z(t) = G_p e_z(t) + G_i \int_0^t e_z(\tau)d\tau + G_d \frac{d}{dt} e_z(t) \tag{2.24}$$

where, $O_z(t)$ is the output signal (in this case the z position) at a given time (t), G_p is the *proportional* gain, G_i is the *integral* gain, G_d is the *derivative* gain, e_z is the error signal (i.e. e_z = set point - measured position) and τ is the integrated time from $t = 0 \rightarrow$ present time.

The key values in this algorithm are the $G_{p,i,d}$ gain coefficients, these tune the response of the output signal to the error. The derivative gain is not usually used and therefore $G_d = 0$. Adjusting these values allows the tip to accurately follow the contours of constant set point. The precise values for the gain coefficients are system specific and require tuning depending on the surface/imaging method. Examples of feedback instability are shown in Fig 2.13.

If the gain values are set too low the system will not respond quickly enough and detail is lost, or in the worst case scenario the movement of the tip may not be quick enough to avoid a feature and the tip may crash or 'fly' off of an edge as shown in Fig 2.13a. If the values are set too

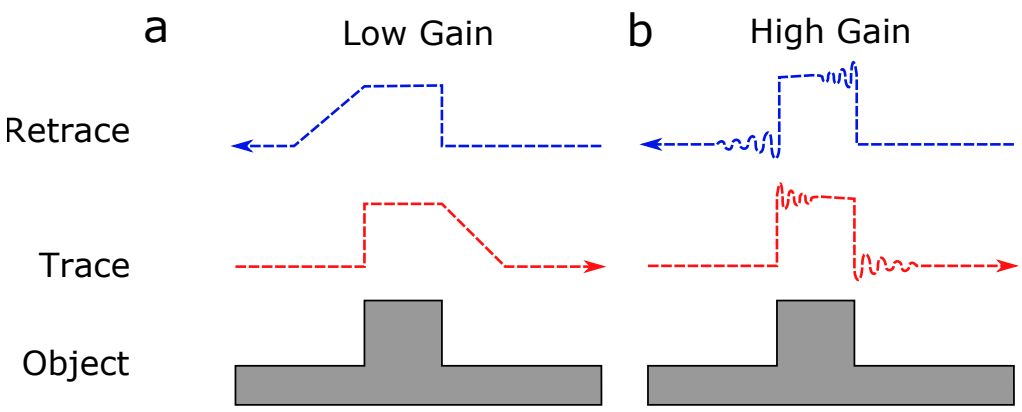

Figure 2.13: An example of how feedback instability affects the path the tip takes when the gain settings are a) too low and b) too high.

high, however, the system may over-correct and overshoot. This leads to feedback oscillations where the tip position oscillates around the set point value and often manifests as oscillatory noise on the image along the path of the tip as shown in Fig 2.13b.

2.8 Vibration and Temperature Isolation

The first SPM instruments were housed within UHV chambers to eliminate/minimise the effects of ambient environment and atmospheric contaminants. It was quickly realised that these instruments were capable of operation in ambient conditions (including liquids), allowing SPM to be performed on a wide variety of samples not compatible with UHV conditions. The main penalty for operating at ambient conditions is increased sensitivity to thermally induced drift. This means that under room temperature (RT) conditions, SPM images can experience significant distortion in both the x, y and z directions.

Due to the extremely small distances between tip and sample, any coupling of externally produced low-frequency mechanical vibrations to the

instrument may result in imaging artifacts or even tip crashes in extreme cases.

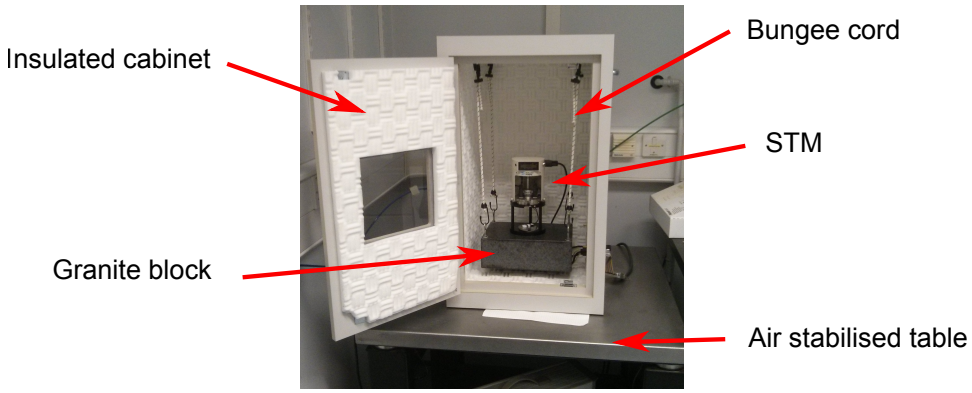

Figure 2.14: Ambient STM inside an isolation enclosure showing the various methods used to isolate the scanner.

As shown in Fig 2.14, several techniques are often used to mitigate against the effects of these vibrations. Most SPM instruments are mounted on air-stabilised tables and the scan heads themselves are typically suspended by springs or bungee cords on a heavy base such as a granite block. UHV SPM chambers are often coupled with cryostats to cool the sample to cryogenic temperatures, typically using liquid N_2 (77K) or liquid He (4K). This drastically reduces the thermal drift, allowing imaging of the same area for up to weeks at a time although this is not typically used when working in ambient conditions. A typical ambient STM isolation chamber is shown in Fig 2.14.

2.9 Image Processing and Presentation

Since all SPM instruments are subject to the effects of some thermal drift and mechanical vibration, SPM data must be processed and presented in an appropriate format. This may involve removing artifacts such as electronic

oscillations induced by AC mains voltage and correcting for the effects of thermal drift, particularly in experiments performed in ambient conditions. Care must however be taken in image processing to ensure that data is not manipulated in a way that may incorrectly introduce features, this is particularly relevant in the case of Fourier filtering in section 2.13. Most SPM imaging software packages can perform the processing methods detailed below and export either exported images or raw x, y, z data for further processing and numerical analysis.

2.10 Rendering

Multiple ways of rendering SPM data for presentation exist, the most common is to render the z-positions as an intensity value on a colour scale. This may be a simple gray scale where higher features correspond to a higher intensity value, a colour-height scale may be displayed next to the image to give an indication of the range of heights present in an image. The choice of either colour or intensity is arbitrary and non-linear maps may be used depending on the height scales of the feature(s) being studied.

3D rendering may also be used, however, the vertical size of features may typically be several orders of magnitude smaller than the lateral size of the image, particularly in the case of molecular monolayers on a flat substrate. Therefore a 1:1:1 representation of the x, y and z values may not show the features of the surface. In this case the z scale may be scaled to show the topography of the surface as is shown in Fig 2.16.

3D rendering of a surface can also be combined with other surface measurement techniques in order to display multiple properties of a surface in

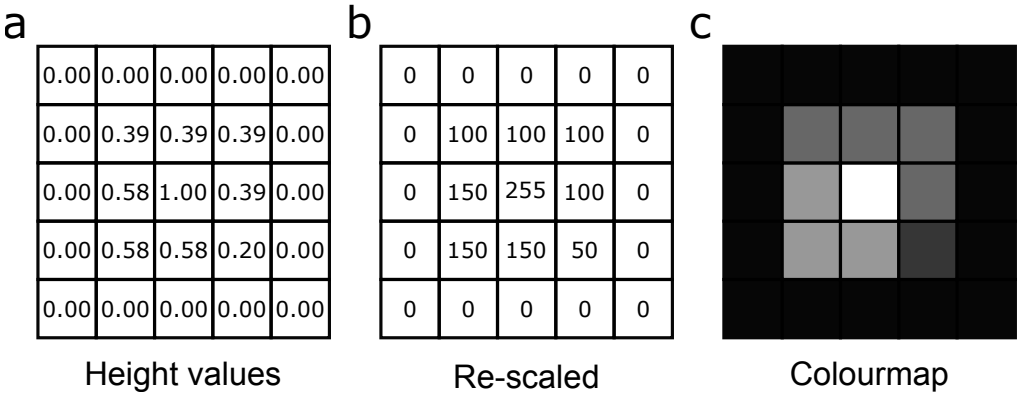

Figure 2.15: 2D rendering of SPM data. a) Height values are recorded at x and y positions. b) the values are then re-scaled and c) mapped to a colour intensity.

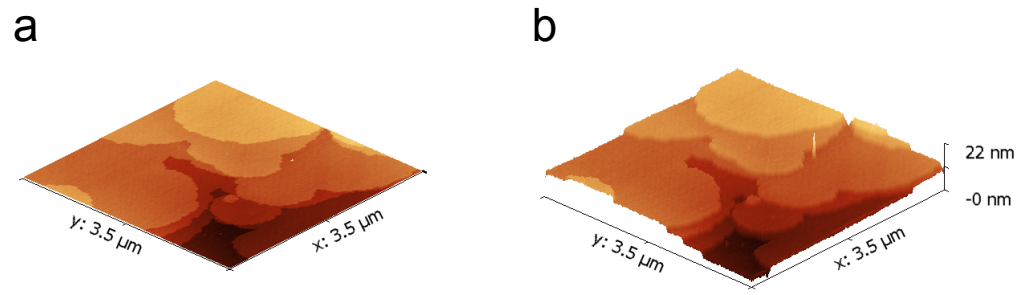

Figure 2.16: 3D rendering of SPM data showing a crystal surface at a) 1:1:1 $x : y : z$ scale and b) with the z axis multiplied by a factor of 30.

one image. For example, the topography of a sample may be rendered in 3D and then the surface coloured using the values from spectroscopic measurements of the same region. Alternatively a different channel of data from the SPM instrument may be used to overlaid onto the surface topography. For example, techniques such as magnetic force microscopy (MFM) allow a surface to be imaged in contact/AC mode and then re-scanned using a magnetic cantilever in order to overlay the magnetic domain information on the topographic structure of the sample.

2.11 Drift Correction

Thermal drift is a particular problem encountered when performing SPM experiments. The slow scan speed combined with thermal expansions of several nm over tens of minutes in some cases means that a feature drifts relative to the scan area, leading to a highly distorted image. Over long time scales this may even mean that the feature drifts out of range of the scanner. One way to mitigate this is to increase the tip rastering speed. However, this has the side effect of increasing the effect of noise as the acquisition time per point on the surface may not be sufficient to see the contrast variations on the surface.

In UHV conditions, the environment may be sufficiently isolated so that the drift levels are minimised through the use of cryogenic cooling. Ambient SPM experiments however, are highly susceptible to thermal drift, particularly at the beginning of experiments since the instrument may have been opened and components handled, heating them up above the ambient temperature. The effects of drift at the beginning of scanning can be seen in Fig 2.17.

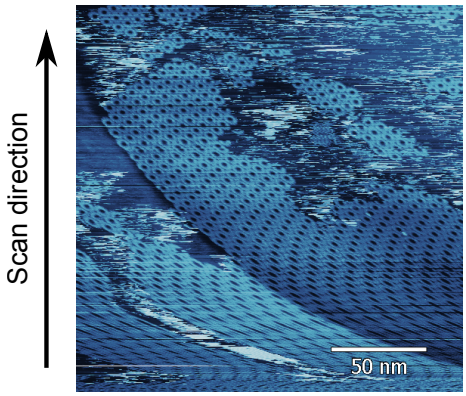

Figure 2.17: First scan of an ambient STM experiment showing significant thermal drift.

In order to minimise the effects of thermal drift, SPM instruments are typically situated in a temperature controlled room and the instrument located in an acoustically and thermally insulated cabinet. Despite this, the system may then still take several hours to equilibrate with the surroundings meaning that the images may show the effects of drift for some time. If a time sensitive sample such as one that degrades in the ambient environment then the effects of drift on the images must be taken into account.

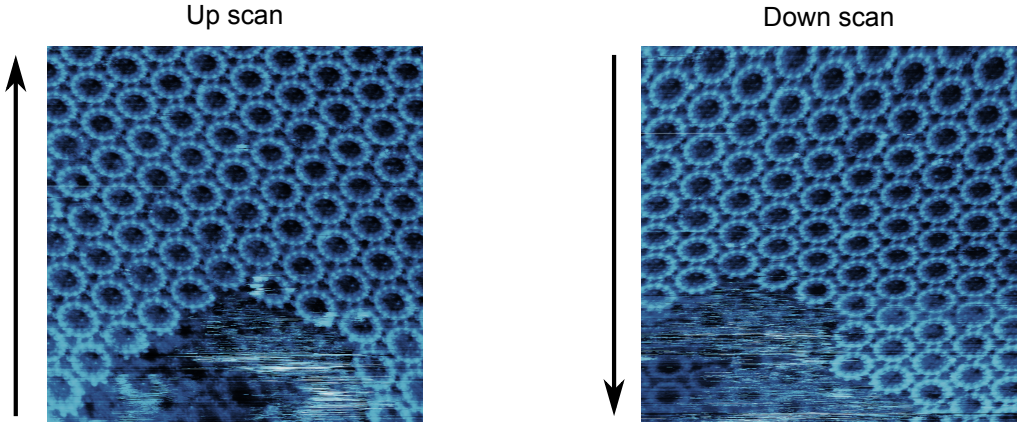

Figure 2.18: Sequential STM images showing the effects of thermal drift.

For example, a sequence of STM images showing the effects of drift are shown below in Fig 2.18. If the thermal expansion is linear then a velocity for the drift in x and y, $v(x, y)$ can be calculated in units of time per pixel. As the SPM tip movement is much faster in x than y. The drift in x may be considered negligible over the time scale in a single line scan. The next line scan will then be displaced by an amount $v(x, y)t$ from its expected position where t is the time taken to complete one line scan in units of time per pixel moved in the y direction. This means that if a point, $P_i(x, y)$ is measured in an image, the same position on the next image, $P_{i+1}(x, y)$ is given by;

$$P_{i+1} = P_i + v(v_x, v_y)Nt \tag{2.25}$$

Where N is the number of lines scanned in the y direction until the same feature is imaged again. If the velocity is then known it can be subtracted from this measured position and the original position found. The effect will appear in the final image as a combination of a stretch/compression in the y direction and a skew in x as shown in Fig 2.19.

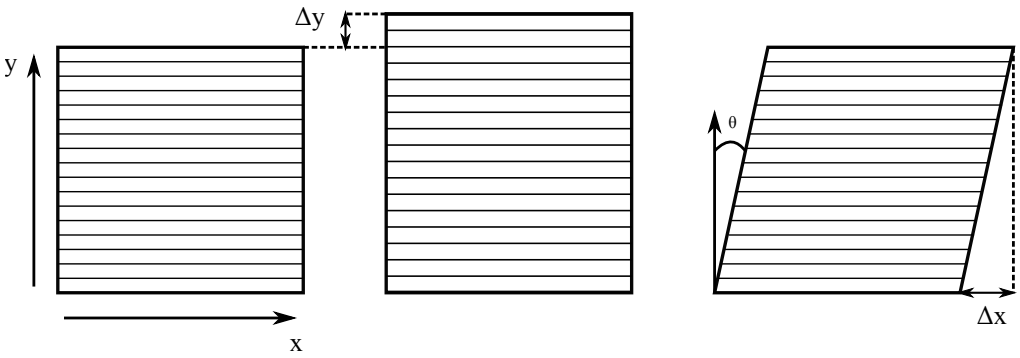

Figure 2.19: Illustration of stretching and skewing in SPM images.

A simple method for drift correction can be implemented by identifying a consistently present feature (or multiple features) and measuring the rate at which it moves over time during imaging. By taking a minimum of two sequential images with the same scanning parameters, one scanning up and one down (or vice versa) and marking the specific features, the drift velocity can be calculated.

Figure 2.20 shows a consistent feature on two hypothetical STM images that have been acquired sequentially. The position of this feature in the initial and final images is recorded, i.e. (x_i, y_i) and (x_{i+1}, y_{i+1}) respectively. In order to calculate the velocity, the relevant time interval, Δt, is calculated by adding the number of scan lines remaining in the first up scan,

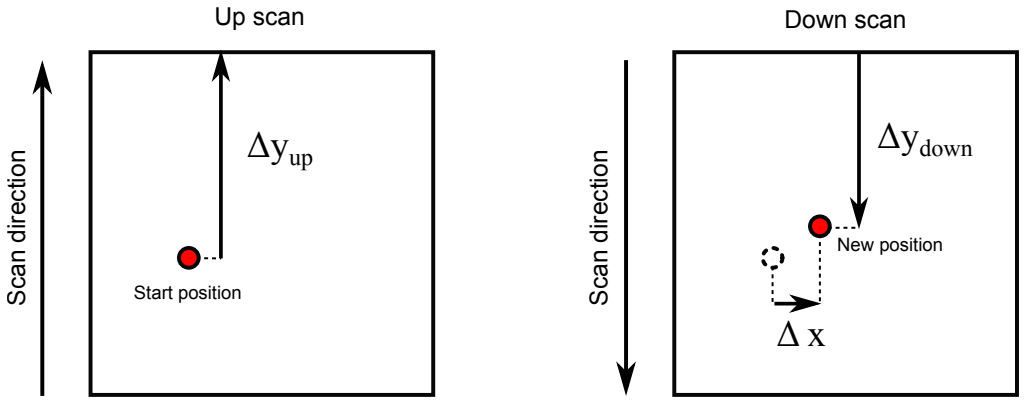

Figure 2.20: Marking positions to calculate drift velocity.

Δy_{up}, and the number of lines in the next scan until which are acquired before the feature appears again, Δy_{down};

$$\Delta t = \Delta y_{up} + \Delta y_{down} \tag{2.26}$$

Therefore the final velocity is given by;

$$v(x_i, y_i) = \frac{\Delta x}{\Delta t}\mathbf{i} + (\frac{\Delta y_{\text{up}} + \Delta y_{\text{down}}}{\Delta t})\mathbf{j} \tag{2.27}$$

In a real SPM image, this can be repeated for as many known points as possible and an average taken to give a net drift velocity and the correction required. This process of feature marking in sequential images is shown in Fig 2.21 for the STM images in Fig 2.18. Fig 2.21a and b show some consistent features in the two images. These positions are then used to calculate the average drift velocity and the image then skewed in x and stretched/compressed in y to correct the effect of drift as shown in Fig 2.21c. Since the drift corrected image will be a parallelogram, it is typically cropped to a square for the final image as shown in Fig 2.21d.

Hardware drift correction techniques also exist such as repeatedly mov-

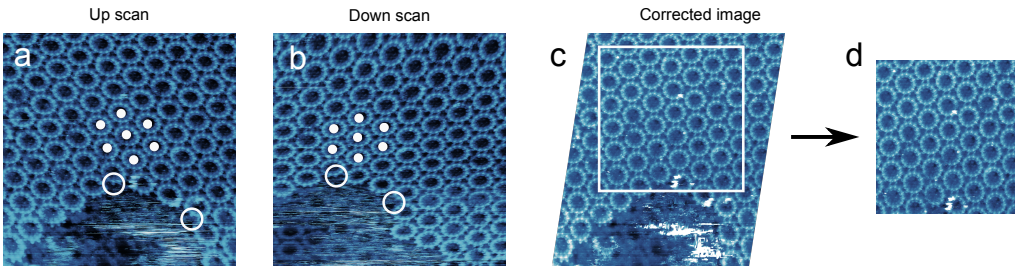

Figure 2.21: Final drift corrected image.

ing the tip back to a known atom repeatedly during a scan and measuring the displacement of the atom over time. This provides in-situ feedback to the system that can correct for drift by adjusting the tip scanning dynamically [36, 37]. However, this technique is typically limited to low temperature, low drift UHV environments.

2.12 Image Flattening

The x, y, z position of an SPM tip is in all cases is defined relative to some known position, e.g. the zero displacement position of the piezo actuator. This also means that if the sample position relative to the tip displacement is not known, any effects such as sample tilt will be recorded in the raw data and must be corrected for. Conversely, if the surface has a large height change (for example, closely spaced crystal planes) then simply representing the surface as a colour map as a function of recorded height may make small surface features on each terrace difficult to distinguish visually. In this case, flattening the data to a first order polynomial plane as is shown in Fig 2.22 may aid in distinguishing variations in the surface structure.

Figure 2.23 shows the effect that a first-order plane fit has on an image of a crystal surface. In Fig 2.23a an AFM image is shown where the colour scale is directly mapped to the change in height of the surface, i.e. the

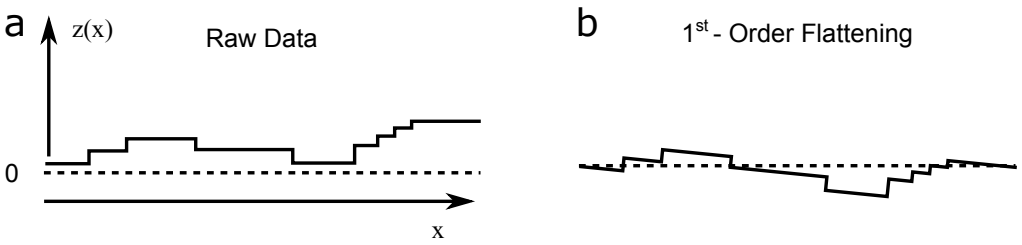

Figure 2.22: Illustration of flattening on SPM images showing a) an ideal raw 1D topographic profile and b) fitting the profile to a first order polynomial.

brighter the colour the greater the height. However, for an image where the height change is even greater this may cause a loss of detail on the highest and lowest crystal planes. By flattening the image to a first order polynomial (Fig 2.23b) the detail on the terrace surfaces is more pronounced. Fig 2.23c-d also shows the effect this has on the distribution of height values for the images in Figs 2.23a and b respectively with Fig 2.23c showing the height peaks associated with each crystal plane.

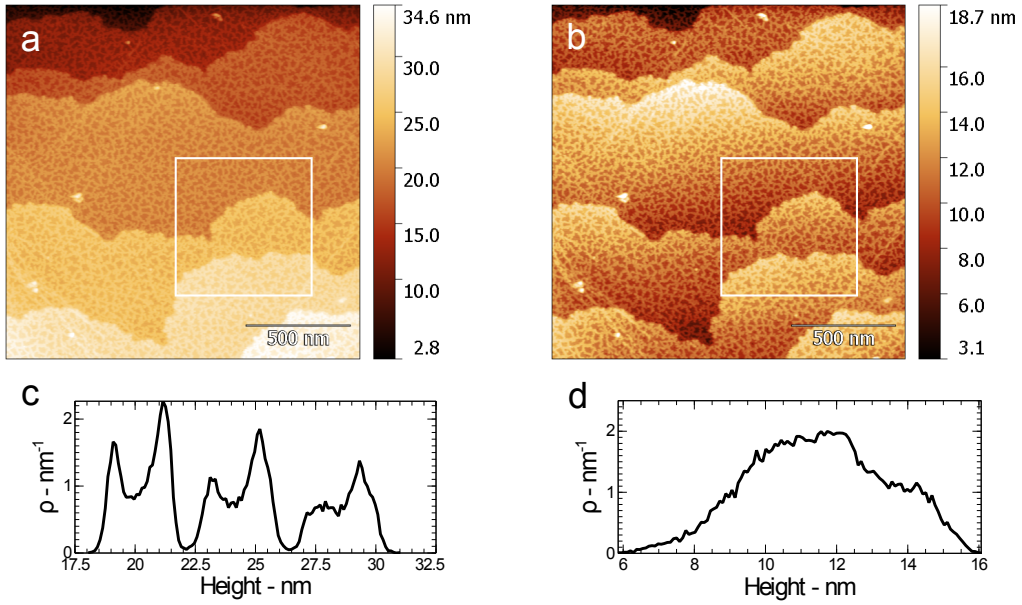

Figure 2.23: a-b) AC mode AFM images of a crystal surface showing the effect that 1^{st} order fitting has on 2D image presentation and c-d) the height distributions for a-b respectively.

Images may also be flattened using higher order polynomials. For example, if a substrate with an adsorbed monolayer of molecules has even a slight curvature, the contrast due to the monolayer may be lost if the deviation in z height due to the curvature of the substrate is significantly higher than the height of the monolayer relative to the surface. This is shown in Fig 2.24.

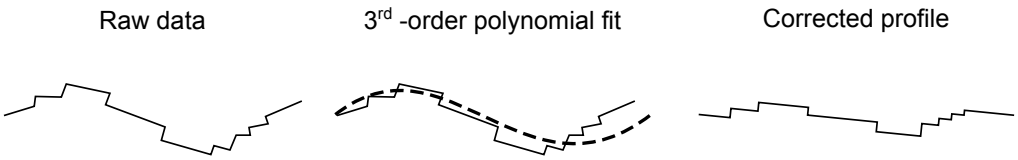

Figure 2.24: Fitting to a third order polynomial

2.13 Fourier Filtering

Manipulation of the 2D discrete Fourier transform (2DDFT) of an SPM image can be used to suppress particular spatial frequencies. When imaging periodic features or when artificially induced noise at a fixed frequency is present in SPM in images, such as electronic interference from mains AC signals at 50 Hz or periodic mechanical noise introduced by external source. It can be helpful to remove these unwanted frequencies.

In practice this is typically performed using a 2D fast Fourier transform algorithm (2DFFT) [38] and most SPM software packages have inbuilt routines to calculate the 2DFFT and interfaces to perform filtering of the spectra at selected frequencies. However, care must be taken when filtering using Fourier techniques as it is possible to introduce artefacts through improper removal of noise. For example, It is possible to filter white noise to the extent that non-physical periodic features are introduced [26].

2.14 SPM Substrates

Whilst the techniques of STM and AFM are applicable to surfaces with 'large' height differences such as biological samples, the study of molecular monolayers of sub-nm vertical feature size such as atomic step-edges typically requires highly-ordered substrates in order to achieve contrast of sub-nm nanostructures. The following sections discuss the structure and preparation of several substrates used in this thesis.

2.15 HOPG

Graphite is a crystalline form of carbon in the hexagonally close packed (hcp) crystal structure. The atomic arrangement consists of an sp^2 hybridised honeycomb array of covalently bonded planar carbon atoms with a bond length of 1.42 Å. The crystal structure of a graphite sheet is shown in Fig 2.25. The (0001) unit cell of graphite consists of two carbon atoms, labeled A and B as shown by Fig 2.25a which form a rhombic unit cell which makes up the structure of the bulk hexagonal lattice with a lattice constant of 2.46 Å shown in Fig 2.25b.

Each stacked plane of carbon atoms is held together by van der Waals forces and are separated by 3.40 Å. In the bulk structure of graphite, each plane is offset by one atomic spacing and the planes are stacked **AB**, known as *Bernal* stacking. The A atoms in the unit cell of the top layer sit above the displayed B atoms in the layer below and this pattern is repeated in the bulk crystal structure as shown in Fig 2.26.

Highly-ordered pyrolitic graphite (HOPG) is a grade of graphite in which the average angular separation between the sheets in the crystal

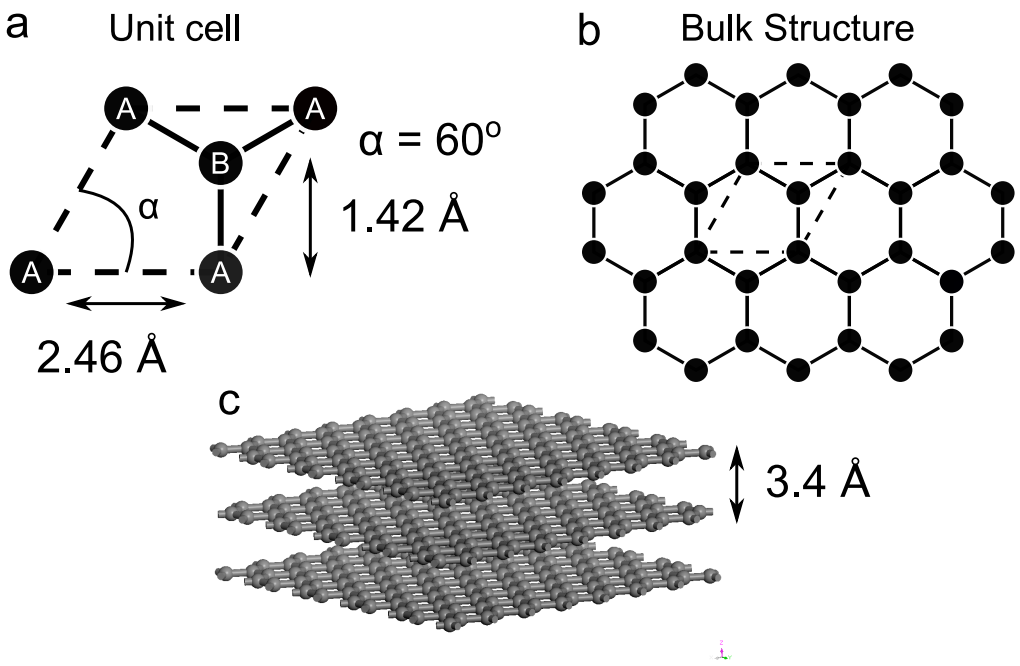

Figure 2.25: Graphite (0001) unit cell showing a) atomic positions in a single unit cell. b) Extended honeycomb crystal structure. c) The layered structure of graphite sheets.

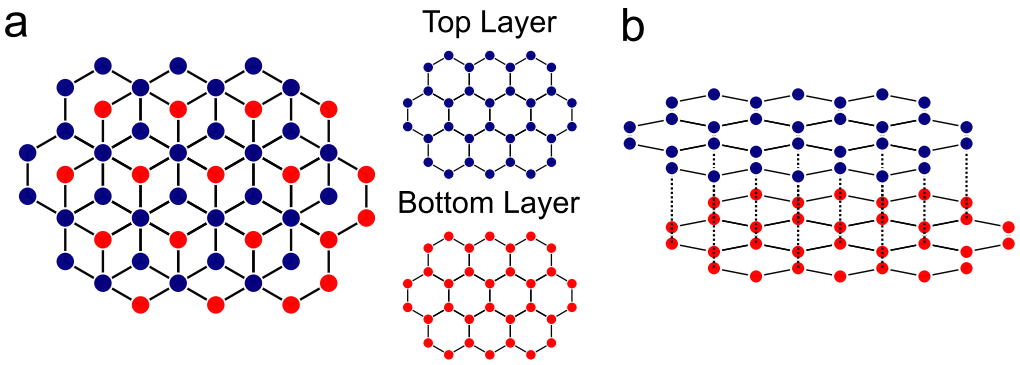

Figure 2.26: a) **AB** stacking in graphite showing the top (blue) layer of carbon atoms displaced relative to the layer below (red). b) Side view of **AB** stacking showing how the A atoms are positioned over the B atoms in the layer below.

is extremely low. It is commonly used as an SPM substrate as it is stable in ambient conditions and easy to prepare. Exposing a clean atomic plane of HOPG is as simple as removing the top layers with adhesive tape, known as mechanical exfoliation. This provides an extremely flat ordered

substrate in which the hexagonal lattice can be resolved in ambient conditions using STM as shown in Fig 2.27a. The step height between the planes of HOPG can also be used as a reference to calibrate the z axis of an STM or AFM instrument.

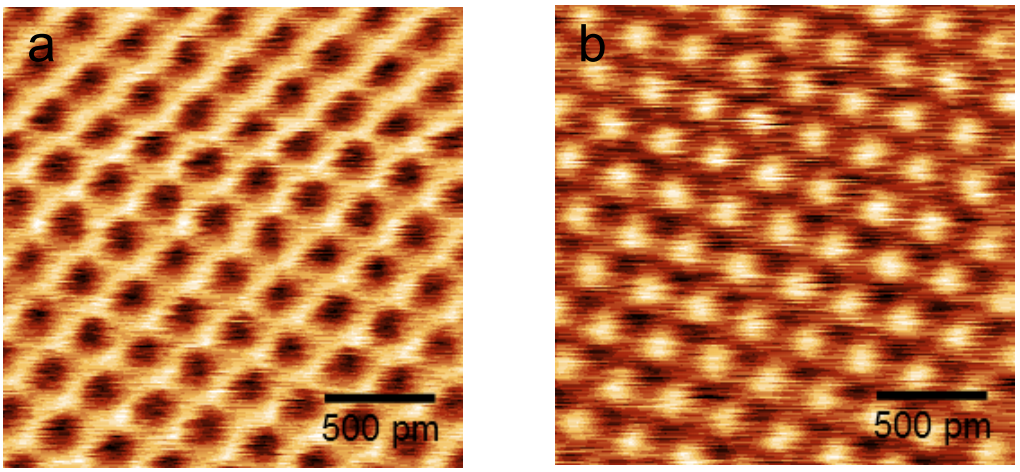

Figure 2.27: Ambient STM images of the HOPG surface showing different contrasts. a) The expected hexagonal lattice and b) trigonal lattice commonly observed in STM experiments with lattice constant of 2.46 Å. Tip Bias, 0.1 V, Tunnel Current, 1 nA.

The contrast that is observed in STM images of HOPG does not typically show the expected hexagonal lattice (Fig 2.27a) and instead a trigonal lattice with a lattice constant of 2.46 Å is commonly observed as shown in Fig 2.27b. This contrast is attributed to the **AB** stacking behavior on account of the asymmetry in the A and B lattice positions [39]. The relative alignment of the graphite sheets relative to each other can also vary leading to the existence of moiré patterns in STM images, these are discussed in section 5.6.

A single atomic layer of graphite, known as graphene, is discussed in more detail in Chapter 5 due to its unique properties. All HOPG substrates used in this work were purchased commercially from Agar Scientific as 1

cm square blocks.

2.16 Hexagonal Boron Nitride

Boron nitride (BN) is a highly insulating compound formed from a 1:1 ratio of B and N atoms and is commonly used as a high temperature ceramic in the cubic structure (cBN). The hexagonal-form of BN (hBN) consists of a hexagonal covalently bonded BN lattice $\pi - \pi$ stacked in an hcp structure analogous to HOPG with B and N atoms in the A and B positions respectively. The structure of hBN is shown in Fig 2.28.

The B and N atoms in hBN are covalently bonded with a separation of 1.45 Å and a lattice constant of 2.52 Å. The atomic layers stack in an **AA'** stacking arrangement with alternating B and N atoms above and below each other and each layer is separated by 3.3 Å.

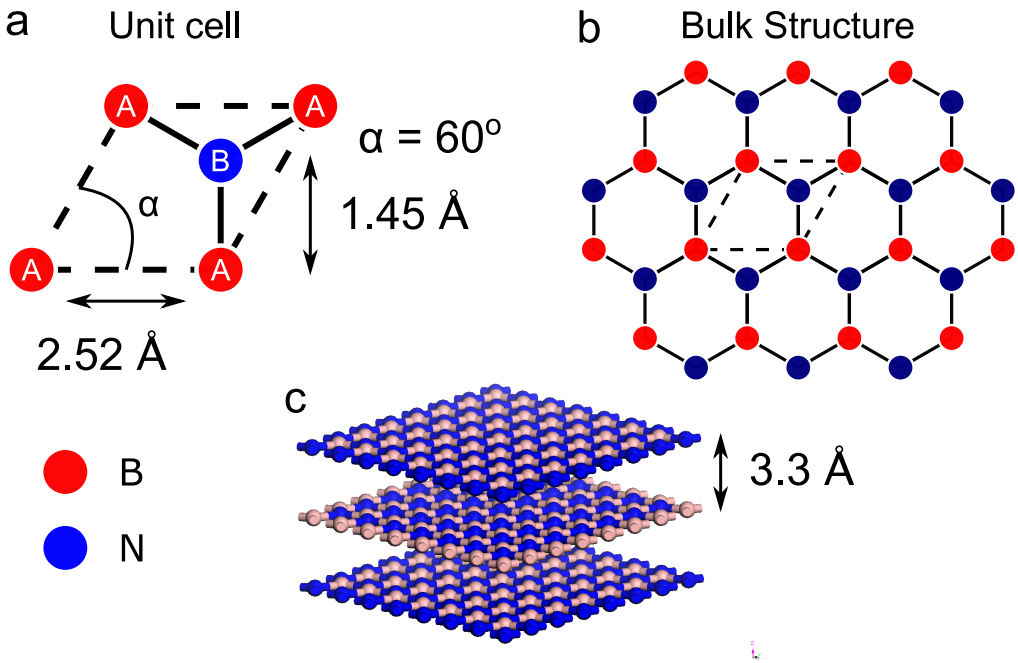

Figure 2.28: Structure of h-BN showing a) unit cell with bond lengths, b) bulk structure and c) separation between hBN sheets.

The hBN used in this work was grown via a high-temperature, high-pressure process in order to form small bulk hBN crystals [40]. Due to the weak in plane coupling between the (0001) planes hBN can be exfoliated to produce thin flat crystallites, exposing clean atomic planes for SPM study. The surface also supports molecular self-assembly on an insulating substrate in place of HOPG and for the creation of molecular electronic devices where an insulating substrate is necessary.

hBN has been frequently used in the growth and fabrication of graphene/hBN heterostructures due the low lattice mismatch with graphene ($< 2\%$) making it ideal as an insulating dielectric [19] or tunnelling layer in graphene-based electronics [41]. hBN/graphene heterostructures are discussed in chapter 5.

2.17 hBN Substrate Preparation

As the hBN used in this work is in the form of small (typically 10-100 μm) crystallites, they must be transferred onto an appropriate supporting surface [40]. Typically SiO_2 on Si is used, although sapphire is also used as a substrate as it has a much higher melting point which is required for the high temperature molecular beam epitaxy technique used in chapter 5. The preparation techniques outlined below are the same for both substrates. The process of exfoliating hBN onto substrates is shown in Fig 2.29a.

Firstly the crystallites are exfoliated by depositing one or two small hBN crystallites on to adhesive tape. The tape is then folded over and repeatedly peeled apart in order to cleave the layers of the hBN into thinner and thinner flakes covering the surface of the tape. The tape is then pressed

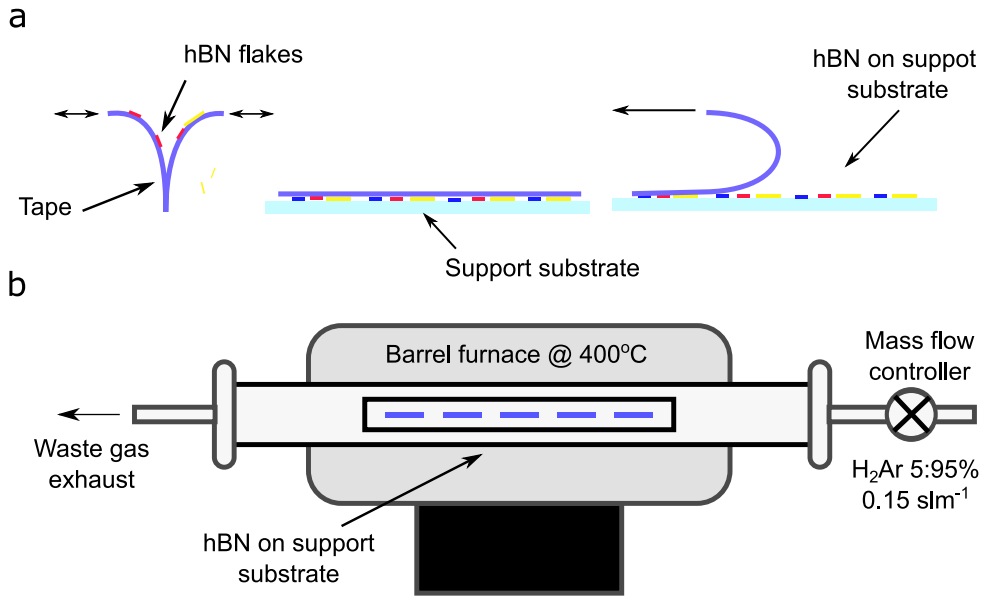

Figure 2.29: Steps in preparing hBN substrates. a) Flakes are first exfoliated using adhesive tape. This is then placed in contact with the substrate and then pealed off slowly. The substrate coated in hBN flakes is then immersed in toluene to remove the adhesive residue. b) The substrates are finally loaded in to a barrel furnace and annealed in H_2:Ar gas.

on to the surface of the desired substrate and then removed slowly, allowing some of the hBN flakes to stick to the substrate surface via vdW attraction as shown in Fig 2.29. Whilst some of the flakes will be cleaved as the tape is removed, leaving a clean hBN surface, some will still be covered in polymer adhesive from the tape. In order to remove this a two part cleaning process is used.

Following exfoliation the samples were immersed in toluene overnight (typically ∼18h) to dissolve the majority of the adhesive. During the course of this work, several different solvents, such as acetone, were used to find which removed the most tape reside. This means that the use of different adhesive tapes to exfoliate the hBN flakes may require a different solvent. After removal from toluene the substrates were dried rapidly using an N_2 gun. An optical image of hBN flakes deposited on to an SiO_2 surface are

shown in Fig 2.30.

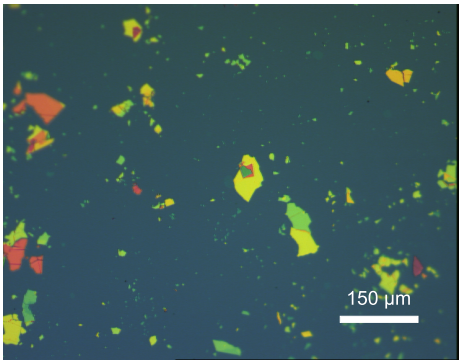

Figure 2.30: Optical image of hBN flakes deposited on 300 nm thick SiO_2 on Si wafer. The bight colouring of the flakes is due to interference effects on account of the thin oxide layer.

The substrates were then loaded in to a barrel furnace and annealed at 400°C for 8 hrs in a 0.15 standard litres per minute (slpm) flow of 5:95% H_2:Ar gas mixture as shown in Fig 2.29b. The flow rate was controlled using a mass flow controller and allowed to cool over approximately 6 hours in the gas flow following the annealing. The substrates were then used for either molecular deposition (see chapter 4) or MBE graphene growth (see chapter 5). AFM images of the hBN surface following cleaning using different solvents and methods are shown in Fig 2.31.

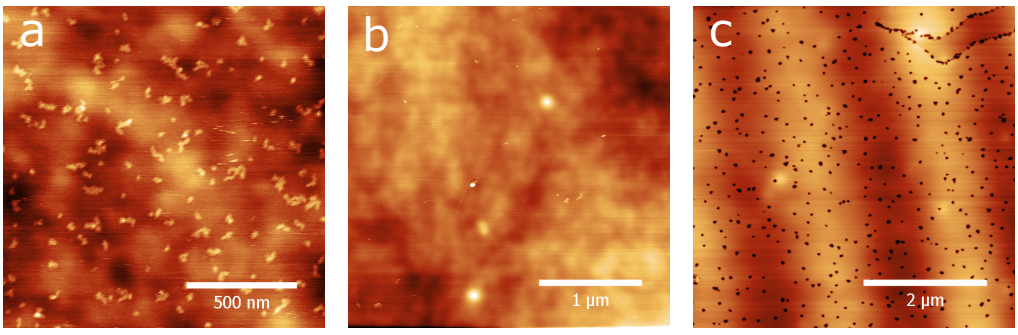

Figure 2.31: AC mode AFM images of hBN on SiO_2 surface after cleaning using a) acetone showing surface contaminants, b) toluene which has successfully removed the polymer residue and c) pitting on the h-BN surface caused by flame annealing.

Annealing the samples using a butane blowtorch until red hot for approximately one minute was also found to clean the hBN surface sufficiently. However, the presence of pits in the hBN surface seen in Fig 2.31c meant that for all the work presented in this thesis, the toluene solvent followed by barrel furnace method was used.

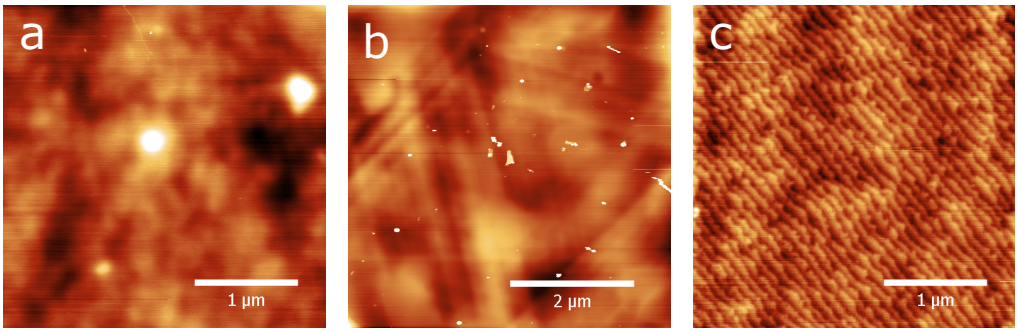

Figure 2.32: AC mode AFM images of hBN on a) SiO_2, b) Au(111) and c) sapphire showing the surface structure of the underlying support substrate.

.

The clean hBN is found to exhibit surface features of the underlying support when imaged with AFM. Figures 2.32a-c show hBN flakes on SiO_2, Au(111) and sapphire substrates respectively. In all cases, the hBN surface is found to adopt the underlying terrace structure of the support material. This is particularly obvious in the case of hBN on Au(111) (Fig 2.32b) as the triangular terraces of the Au surface underneath the hBN flake are visible in contrast to the non-crystalline SiO_2 surface (Fig 2.32a).

2.18 Au(111)

Au, as with most noble metals, crystallises into the face-centred cubic (FCC) crystal structure with a unit cell size of 4.08 Å. Surface studies of metals are typically performed on single crystal planes. These can be prepared by cutting, polishing and annealing a single metal crystal although

these crystals are expensive and require cleaning and re-preparing between each experiment. In practice, a thin-film of preferentially-oriented but laterally polycrystalline Au grown on an ultra-flat support substrate such as mica is used. Preparation of these surfaces requires highly specific conditions, and heating the substrate in UHV conditions is required to produce the Au (111) or (110) crystal surfaces. The Au(111) surface structure is shown in Fig 2.33b and c.

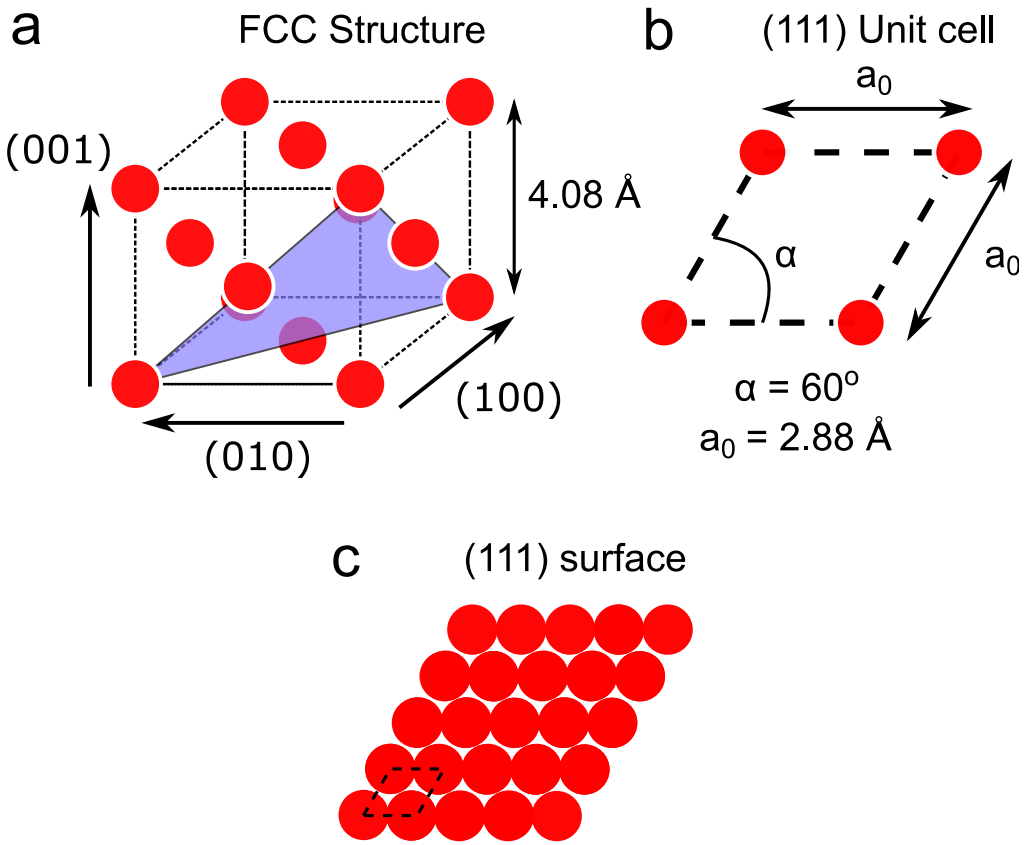

Figure 2.33: a) Au FCC unit cell showing a) the atomic positions (red) and the (111) plane (blue). b) (111) surface unit cell showing the lattice constants and c) extended crystal structure of the (111) surface.

Use of butane or hydrogen flame annealing is used to prepare Au(111) for STM imaging. Heating until the substrate is at a deep orange colour for ∼1 minute is typically enough to achieve an atomically clean substrate for

the study of the bare Au surface or depositing a monolayer of molecules. STM images of Au(111) surfaces are shown in Fig 2.34 and the expected trigonal symmetry of the Au(111) terraces can be seen in Fig 2.34a.

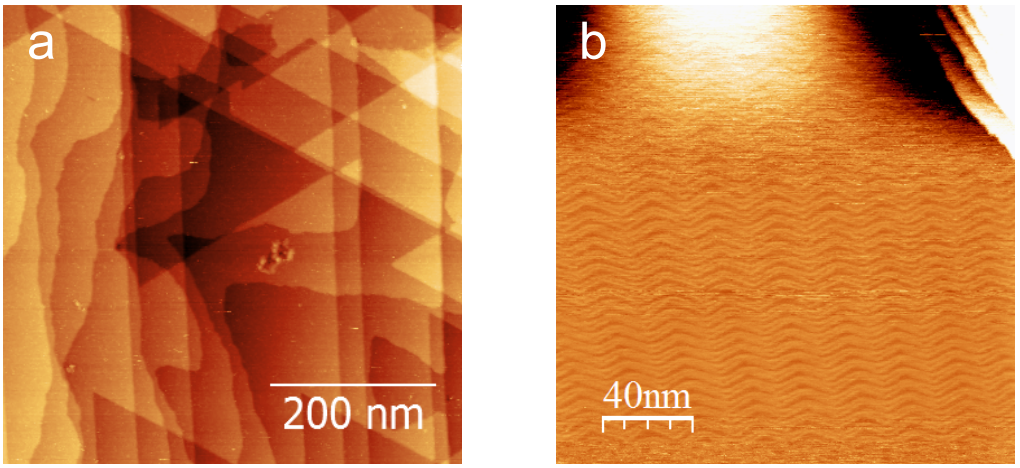

Figure 2.34: Ambient STM images showing a) the triangular symmetry of the Au(11) terrace structure following annealing. b) Characteristic 'zig-zag' lines indicative of the Herringbone reconstruction. Tip bias, 1 V, tunnel current, 50 pA.

By annealing the Au(111) surface it is possible to induce a surface reconstruction known as the herringbone reconstruction (also known as the 23 x $\sqrt{3}$ reconstruction). This feature manifests as a series of parallel zig-zag lines in STM imaging of the Au surface with a periodicity of ~6.3 nm as shown in Fig 2.34b. This is due to the surface atoms adopting a slightly different structure to that of the bulk crystal. This is the result of 23 surface atoms occupying the space of 22 lattice sites in the layer below [23].

Au surfaces are well-suited to SPM studies of molecular arrays since they are highly inert. Nevertheless, Au can be reacted with thiol compounds to form chemically functionalised surfaces [42, 43, 44]. The surface Au atoms form a covalent bond with an S atom in order to produce a

surface with an Au-S-R (where R is an arbitrary hydrocarbon fragment) surface termination. The -R group can also be terminated with different functional groups such as -CH_3, -OH or -COOH to modify the surface energy and control molecular adsorption on to the Au(111) surface [45]. The density of these functional groups may also be modified by using bulky aromatic structures in place of simple alkane chains [46]. The effect that surface functionalisation has on molecular adsorption on to the Au(111) surface is discussed in chapter 3.

2.19 SiO_2

SiO_2 grown on Si wafer provides an insulating substrate ideal for the preparation of nano-scale devices and is commonly used in semiconductor fabrication processes. The thickness of the oxide layer is sometimes of critical importance in optoelectronic devices due to interference effects caused by the thin-oxide and enables the identification of monolayers of materials such as graphene [17].

All SiO_2 used in this work was commercially purchased 300 nm thick SiO_2 formed by thermal decomposition of Boron-doped (p-type) Si(100) wafer.

2.20 Preparation of SPM Experiments

Fig 2.35 shows some of the steps taken in preparing an ambient STM experiment in this case imaging of a HOPG surface. Pt/Ir wire is first sheared by holding a short length of wire in between a pair of pliers and then cutting at an angle whilst pulling away, this often results in a tip

sharp enough for accurate STM imaging (Fig 2.35a). After placing the tip into the STM scanner head, the surface is then prepared. For example, Fig 2.35b shows a HOPG block being exfoliated using adhesive tape to produce a clean graphite surface.

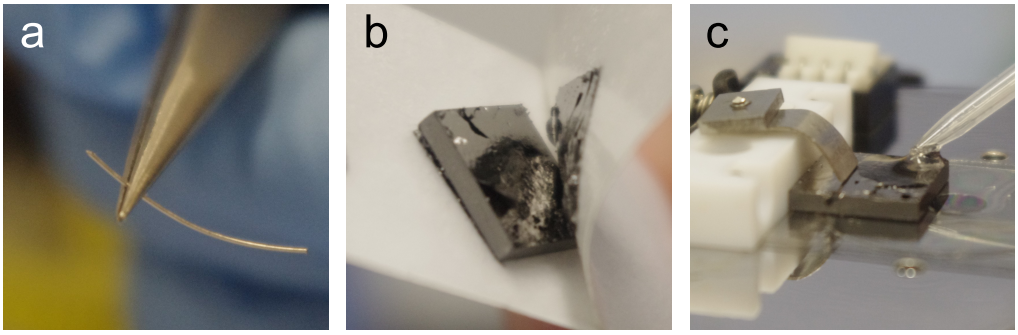

Figure 2.35: a) Pt-Ir STM tip ready for use. b) HOPG substrate being cleaved with adhesive tape. c) Imaging solvent being applied by pipette to the surface for liquid STM imaging.

The substrate is attached to a sample stage via a conducting clip and isolated from the rest of the apparatus using glass slides. This is shown for an HOPG sample in Fig 2.35c which also shows the deposition of a solvent on to the HOPG surface using a pipette for liquid imaging (see section 2.21).

The sample stage is then loaded into the STM, firstly a coarse approach is performed by eye to get the tip as close to the surface as possible without crashing and damaging the tip. Once the approach by hand is complete, a final approach is performed by the control computer in which the z-axis piezo is extended to test for a tunnelling current. If no current is detected then the sample is coarsely approached by a small amount using a stepper motor, the piezo is then re-extended to check for a tunnelling current. This process is then repeated until a tunnelling current is detected and the tip is then raster-scanned and images are acquired.

Preparation of an ambient AFM experiment involves many of the same steps as for STM sample preparation. Commercially available AFM cantilever tips are placed in a holder in mechanical contact with a drive piezo to oscillate the tip. The cantilever is then brought in close proximity by eye to the sample. The laser spot is aligned with the tip and the deflection measurement zeroed. If an AC mode experiment is to be performed then the resonant frequency of the cantilever is found by sweeping a frequency range close to the predicted resonance. The cantilever is then driven at a frequency slightly away from this to force the cantilever into the attractive/repulsive modes of imaging.

The cantilever is then coarsely approached stepwise identically to the STM and the z-axis piezo extended to check if the desired set-point is reached (In then case of contact imaging this is the desired deflection and in AC mode, a reduction to the desired oscillation amplitude or change of frequency from resonance for FM-AFM). Once the set-point is reached, the tip is then rastered over the surface and images are acquired.

2.21 Liquid Imaging

Depositing solutions onto substrates before or during SPM imaging allows the investigation of dynamic processes at the liquid-solid interface such as the growth of self-assembled monolayers (SAMs) when molecules are deposited onto a surface from solution. Liquid conditions also allow the response of SAMs to an environmental stimulus to be investigated. For example, SAMs may change their structure when exposed to liquids of varying pH or the introduction of another molecule. In addition, an imaging

solvent may allow investigation of a compound that is sensitive to ambient conditions by acting as a barrier to prevent decomposition. For further discussion of this subject, the reader is directed to the review by De Feyter [47] and the thesis of Stannard [48].

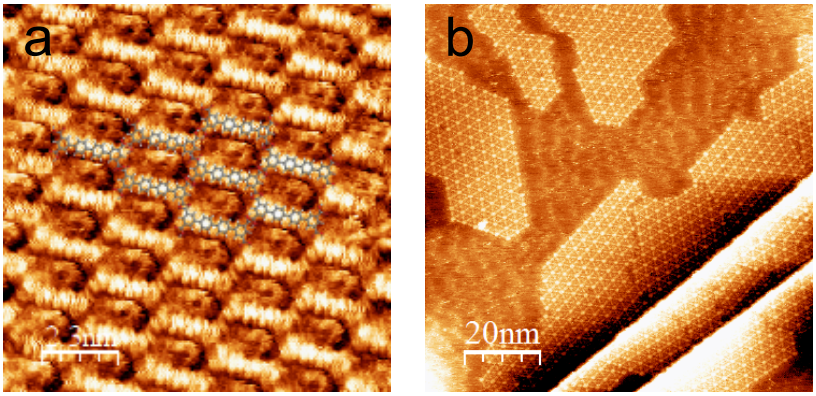

Figure 2.36: Example ambient STM images in liquid conditions showing quarterphenyl-3,3",5,5"-tetracarboxylic acid (QPTC) molecules on HOPG imaged in nonanoic acid exhibiting; a) parallel structure with the chemical structure overlaid for several molecules in the central region of the images and; b) Kagomé structure formed through coadsorption of coronene molecules with QPTC on multiple HOPG terrace steps. Tip bias, 1 V, tunnel current 50 pA. Images from [49].

If a liquid STM experiment is to be performed, a solvent (sometimes containing molecules) is drop-deposited on the surface, typically via a pipette although some STM liquid cells allow injection of a liquid during imaging. The STM tip is then brought in contact with the liquid until a meniscus is formed along the tip. The same standard approach steps are then taken to incrementally move the tip closer to the substrate until a tunnelling current is detected. Examples of the images that can be acquired by an STM in liquid conditions are shown in Fig 2.36.

AFM can also be performed in liquid conditions. However, the oscillation of the cantilever will be heavily damped by the liquid, changing the resonant frequency of the cantilever significantly. Also, changes in refrac-

tive index due to the liquid will affect the optical path of the detection laser meaning the set-up of the equipment must be adjusted to take this into account.

2.22 Optical Spectroscopy

Measuring the relative intensities of adsorbed/scattered light at different wavelengths gives information about the transitions and energy levels in molecules. In the case of photons the energy of the photon is simply related to the wavelength by the Planck formula;

$$E = h\nu = \frac{hc}{\lambda} \tag{2.28}$$

where E is the photon energy, ν is the photon frequency, h the Planck constant, c is the speed of light and λ is the photon wavelength.

For particles, such as neutrons, electrons and protons etc. The energy is given by the DeBroglie equation;

$$\lambda = \frac{h}{p} \tag{2.29}$$

$$E = \frac{hc}{\lambda} \tag{2.30}$$

By recording the emitted intensities as a function of wavelength, the energies of the energy level transitions in a particular material may be investigated. The transitions between energy levels are often illustrated using a Jablonski diagram as shown in Fig 2.37.

The diagram shows a simple process in which an electron is excited to a higher energy state by an incoming photon and falls back to the ground

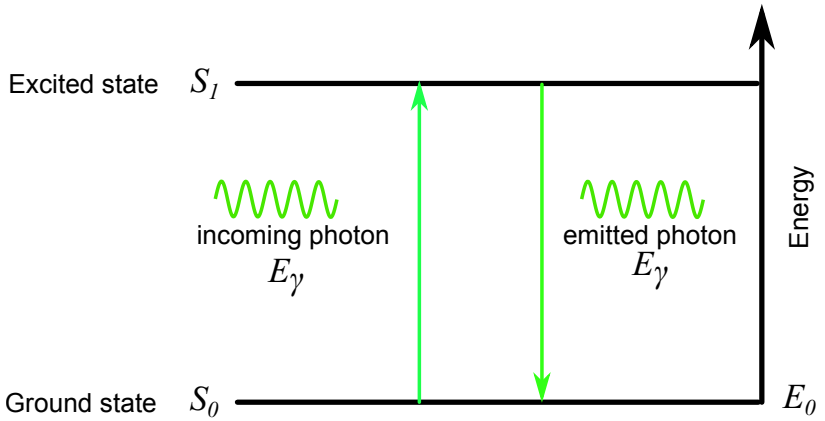

Figure 2.37: A Jablonski diagram.

state, emitting a photon of the same wavelength. In reality there may be many different pathways for the electron to lose energy causing photons of a range of energies to be emitted and the energy difference accounted for by a non-radiative transition.

2.23 Fluorescence

Fluorescence spectroscopy measures the light that is emitted after an electron in a molecule in the ground state, S_0 has been excited in to a higher singlet energy state by an incoming photon of energy $h\nu_{ex}$. For example, a transition from S_0 to S_1,

$$S_0 + h\nu_{ex} \rightarrow S_1 \tag{2.31}$$

which is shown in Fig 2.38 along with transitions from S_0 to the S_2 state. Following excitation, the electron will then relax to the S_1 state, typically via non-radiative conversions through loss of heat. The fluorescence process occurs after the electron undergoes a transition back into the ground state,

(from the lowest energy excited state, S_1) emitting a photon of energy $h\nu_{em}$.

$$S_1 \rightarrow S_0 + h\nu_{em} + \text{heat} \tag{2.32}$$

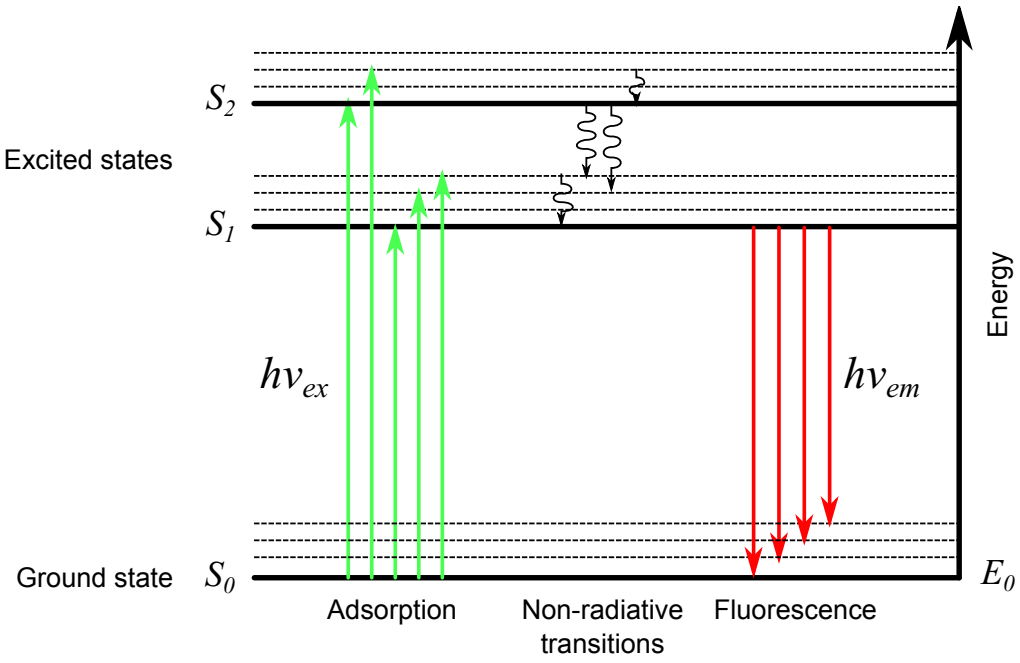

Figure 2.38: Jablonski diagram for a fluorescence

These processes are shown in Fig 2.38, the green and red arrows show the adsorbed and emitted photons respectively and the wavy arrows indicate non-radiative transitions.

In general, the emitted photon will be red-shifted relative to the excitation photon, this is known as a Stokes shift and is due to non-radiative decay such as heat or the photon transitioning to a higher vibrational level of the ground state. As a result, the spectrum of emitted photons will show peaks of various intensities corresponding to the energies of the transitions occurring. In practice there are often so many transitions that a broad continuum of intensities is observed.

The molecule to be studied is placed in the path of a monochromatic

light source (typically a laser) to give a single excitation energy. The molecule can also be suspended in a solution inside a clear cuvette or deposited on a surface as a mono/multi-layer. In the case of a liquid, the detection is usually performed at 90° to the incident excitation beam to minimise the amount of the light of the excitation reaching the detector, leaving only the fluorescent light. This light is finally fed in to a spectrometer and CCD and the data analysed using a computer.

Other experimental techniques involve varying the excitation wavelength in order to probe how the fluorescent emission varies due with different excitation energies. This can be achieved by using a broad emission light source and variable monochromator using a diffraction grating. Fluorescence spectrometers are often be mounted on microscopes allowing the fluorescent properties of surfaces to be mapped spatially in combination with x, y scanning stages.

In addition, ultra-fast optical measurement techniques allow time resolved fluorescence meaurements in order to measure the lifetime of excited states. One version of this, time correlated single photon counting (TCSPC) is performed by using a synchronisation pulse and measuring the time relative to the excitation pulse. A decay profile for the re-radiation of light can then be collected. Time-resolved fluorescence measurements of porphyrin nanorings are discussed in chapter 4.

2.24 Raman Spectroscopy

The Raman scattering effect, first reported by C. V. Raman in 1928 [50] is an extremely weak scattering effect due to scattering from vibrational

states occupied by electrons in molecules. In comparison with fluorescence, the process is non-resonant meaning that the specific wavelength used to excite the sample is not as critical as in fluorescent spectroscopy. Also the process is almost instantaneous as there is no excited state and associated lifetime.

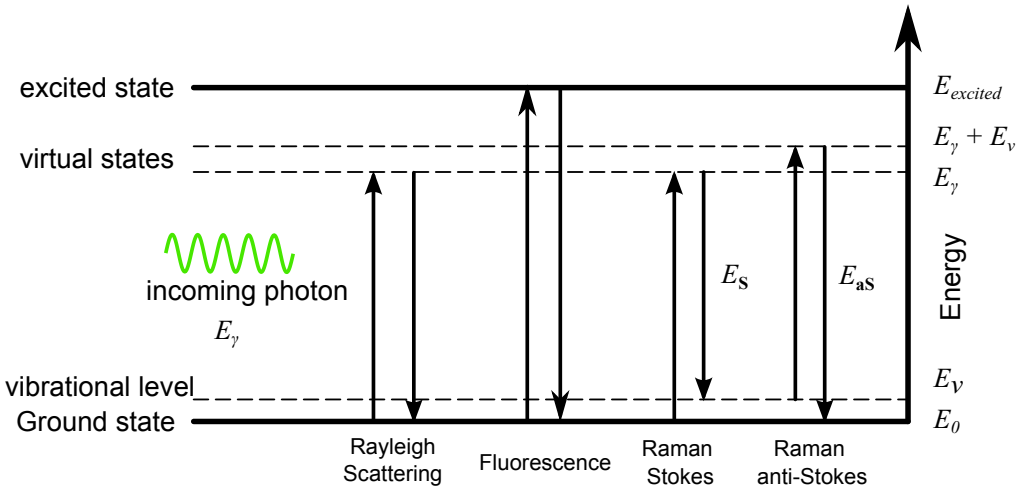

Figure 2.39: The Raman scattering effect shown with Rayleigh and Fluorescence transition processes. The diagram shows the Stokes/anti-Stokes scattering processes responsible for the Raman effect.

Figure 2.39 shows different scattering processes on a Jablonski diagram. Two different processes are present in a Raman spectrum (in addition to Rayleigh scattering) that produce the Raman spectra of a material. These are known as;

- **Stokes scattering:** The electron initially in a ground state, E_0, is excited into a virtual state by a photon of energy E_γ. The electron then falls back in to a vibrational level of energy E_v emitting a photon of energy $E_\mathbf{S}$, where;

$$E_\mathbf{S} = E_\gamma - E_v \tag{2.33}$$

Therefore, analogous to Stokes shifts in fluorescence, the emitted photon will be red-shifted relative to the excitation photon.

- **Anti-Stokes scattering:** The electron initially in a vibrational state, E_v, is excited into a virtual state by a photon of energy E_γ. The electron then falls back in to the ground state E_0 emitting a photon of energy $E_{\mathbf{aS}}$, where;

$$E_{\mathbf{aS}} = E_\gamma + E_v \tag{2.34}$$

As shown in Fig 2.40, the shifted beams are symmetric about the wavelength of the excitation wavelength since the Stokes and anti-Stokes shifts are equal in wavelength shift. However, the relative intensities between the two are typically not equal due to the relative number of electrons being in the ground state versus a higher energy vibrational level. Typically the Stokes shift is significantly more intense since a high fraction of molecules are in the ground state. Analysis of the Raman scattered light it therefore typically done using the Stokes side of the spectrum.

A schematic of a reflection Raman spectrometer is shown in Fig 2.41 (transmission versions also exist). The apparatus is typically attached to a conventional optical microscope system and the laser spot/sample can be moved in the x and y directions allowing mapping of the Raman spectrum over a sample. This may be combined with other equipment such as AFM in order to extract both topographic and spectral information from a sample.

An excitation laser is fed in to the system and is focused onto the sample at a specified point. The reflected beam containing both the excitation wavelengths and the Raman shifted photons from the sample is then fed

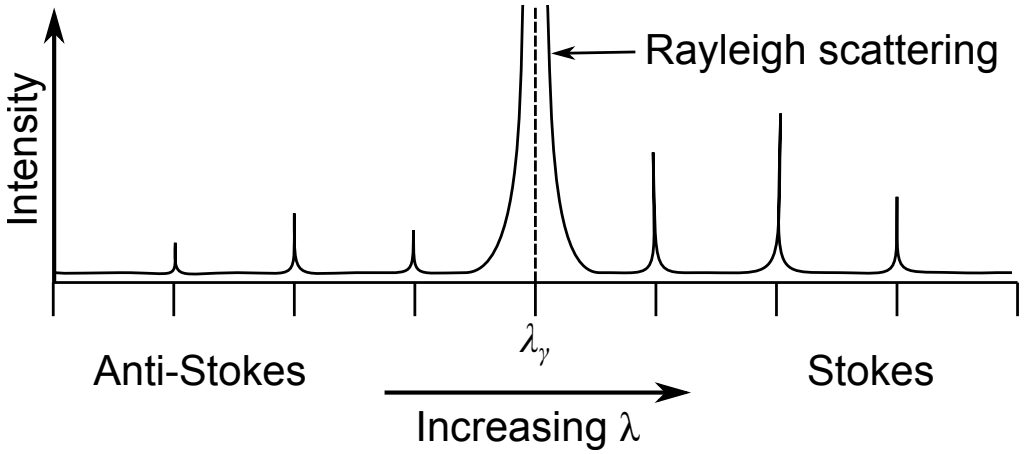

Figure 2.40: Diagram illustrating the positions of Stokes and Anti-Stokes Raman scattering on a model spectra. Note that the strong Rayleigh scattering peak at the centre would typically be removed using notch filters before being acquired and would not be present on the acquired Raman spectrum.

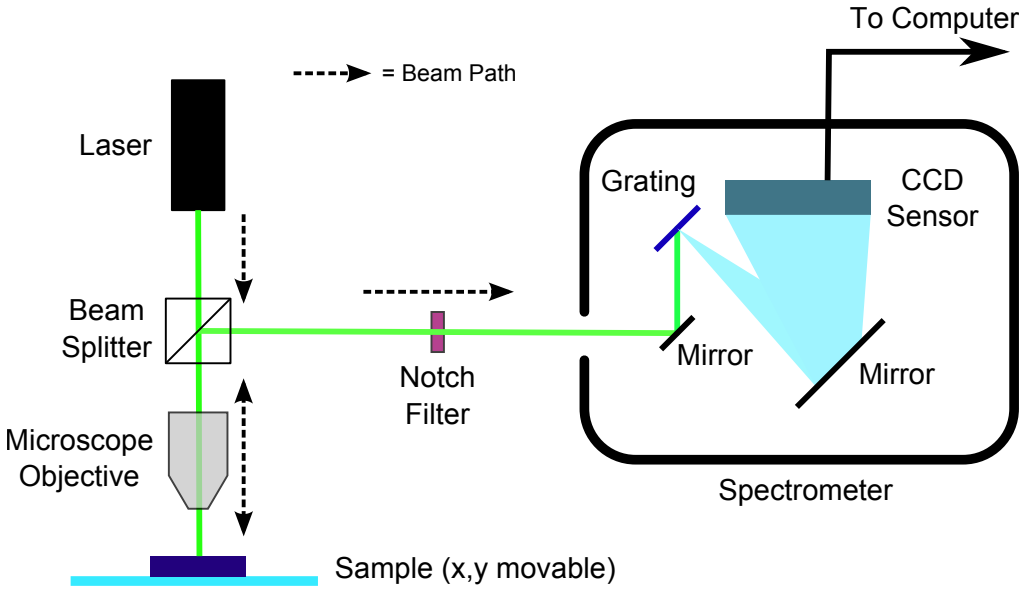

Figure 2.41: Schematic of a typical Raman spectrometer system.

through a beam splitter to divert the path into the optical processing equipment. The critical part in extracting the Raman shifted photons is the use of a notch filter on the reflected beam in order to remove the high intensity excitation wavelengths from the Rayleigh scattered light. The filtered

beam is then fed into a spectrometer, consisting of a grating followed by focusing on to a CCD (typically cooled using a Peltier element or liquid cooling to reduce instrument noise) where data is collected and processed using a computer.

Raman shifts are typically specified in a wavenumber shift from the excitation wavelength, λ_0;

$$\Delta w = \left(\frac{1}{\lambda_0} - \frac{1}{\lambda_1} \right) \tag{2.35}$$

Δw is the raman shift expressed in wavenumber given in inverse centimeters (cm^{-1}). λ_0 is the excitation wavelength and λ_1 is the Raman wavelength. Typically wavelengths are expressed in nm therefore the formula for conversion to inverse centimeters is given by;

$$\Delta w(\mathrm{cm}^{-1}) = \left(\frac{1}{\lambda_0(\mathrm{nm})} - \frac{1}{\lambda_1(\mathrm{nm})} \right) \times 10^7 \tag{2.36}$$

Raman scattering has been used in this thesis to analyse graphene samples and the specifics of the graphene Raman spectrum are discussed in chapter 5.

Chapter 3

MOFs on Surfaces

"If you are entering a new field, pick an experiment that has already been done but you wished that you'd been the one that did it and try it...."

Professor Alf Adams FRS recounting advice from Walter Spear
The Life Scientific, 25th March 2014

This is a study of a class of materials known as metal-organic frameworks (MOFs) grown on functionalised Au surfaces. MOFs are composed of metal clusters and organic ligands to form highly porous crystals with highly tailorable structures and chemical functionality. The growth of a well known MOF, HKUST-1, is investigated with AFM when grown on a thiol-functionalised Au surface using a layer-by-layer technique.

HKUST-1 is found to grow as a film composed of nanocrystallites when deposited in ambient conditions. A strong dependence of crystallographic orientation on the surface functionality is observed in agreement with the literature [12, 51, 45, 52, 53]. The size and structure of individual nanocrys-

tallites are repeatedly measured by returning to the same region between growth steps with sub-μm accuracy.

The growth rates of individual crystallites are found to exceed those reported elsewhere in the literature. This is in contrast to other studies which use the layer-by-layer technique and typically assume a homogeneous single-crystal growth interface and the addition of a single molecular monolayer during each growth step. These results have strong implications for the creation of devices from MOFs where the performance may by limited by the defects and domain boundaries present in a nanocrystalline film.

In addition, preliminary AFM studies of the NOTT-801 MOF that forms large, sheet-like crystals are presented. The size, stability and quality of the crystal surface makes it an interesting candidate material to study the pore structure of MOF crystals using AFM and potential integration with novel device structures.

3.1 MOFs

Metal organic frameworks (MOFs), also known as porous coordination polymers (PCPs) are a class of crystalline compounds formed from metal ions or cation clusters coordinated to organic ligands sometimes referred to as 'linkers'. The organic ligands studied here are carboxylic acids whose negatively charged carboxylate functionalised ends coordinate to the positively charged metal cations in repeating units to form the MOF framework structure. In these frameworks, the metal cations and organic ligands form multi-nuclear nodes with a well defined geometry [54] and may exist in 1,2 or 3D geometries. An example structure of MOF-5 [55] and the component

terephthalic acid linker and zinc coordination cluster is shown in Fig 3.1.

Examples of the metal nodes used include the copper and zinc paddle-wheel units (See Fig 3.6a). The organic ligands that form the 'backbone' of the MOF structure are highly variable in structure allowing a high level of 'designability' to the structure and chemical functionality of the MOF. This means that there are an almost limitless choice of potential MOF structures. In addition this also allows particular characteristics to be designed into the molecular framework with much greater flexibility than other crystalline compounds such as porous zeolites, which often rely on another structure-directing compound during synthesis.

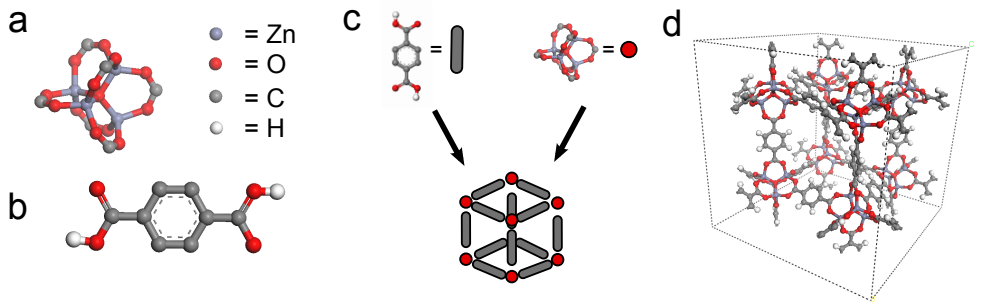

Figure 3.1: Molecular structures of a) Zn cluster and b) terephthalic acid c) these building blocks arrange into the MOF-5 [55] cubic structure as shown in d).

The most common method of MOF synthesis is via a solvothermal process in which solvents are heated to high temperatures and vapour pressures to crystallise the MOF material. Typical metal sources are soluble metal salts such as nitrates, sulfates or acetates [56]. The organic ligands are usually added in the presence of a polar solvent such as triethylamine (TEA) or dimethylformamide (DMF) as these encourage the reaction process without affecting the product and reaction times range from hours to days. The reaction yield is sensitive to factors such as solvent ratios and concentra-

tions that must be optimized to avoid forming the base metal salt instead of the desired MOF product [56]. Quite often the MOF product will still contain solvent molecules that need to be removed through an activation process such as high temperatures in UHV environments or through solvent exchange with a more volatile solvent such as acetone. Other methods have been investigated such as the use of super critical CO_2 to remove excess solvent [57].

For the formation of MOF compounds on surfaces, the reactions are carried out in the presence of a desired substrate, these may also be chemically functionalised through the addition of self-assembled monolayers (SAMs) in order to encourage MOF grown in a particular crystallographic orientation. There are also quasi-epitaxial methods that claim to be able to grow the material layer-by-layer, relying on monolayer by monolayer growth processes to direct the MOF structure formation [58, 52, 59]. These synthesic methods are discussed in more detail in section 3.2. These processes produce a product that may then be characterised by techniques such as XRD, SEM, AFM and also gas adsorption measurements in order to measure the pore size of the MOF structure.

The high porosity and potential for chemical functionalisation of MOFs has led to this class of materials having a wide range of possible uses, such as gas separation [60], gas storage [61], catalysis [56] along with sensors and other electronic devices [62, 63, 64].

Gas separation and storage has been one of the dominant avenues of research into these compounds, with particular emphasis on hydrogen and carbon dioxide storage. Hydrogen has many attractive properties as an alternative energy source. However, storing H_2 in a safe and compact form

represents a significant challenge, especially the ability to do this with fast kinetics and high reversibility over multiple loading cycles [54]. MOFs offer a potential route to solving this problem and it may be possible to develop a material capable of storing H_2 at near ambient conditions with high density [65].

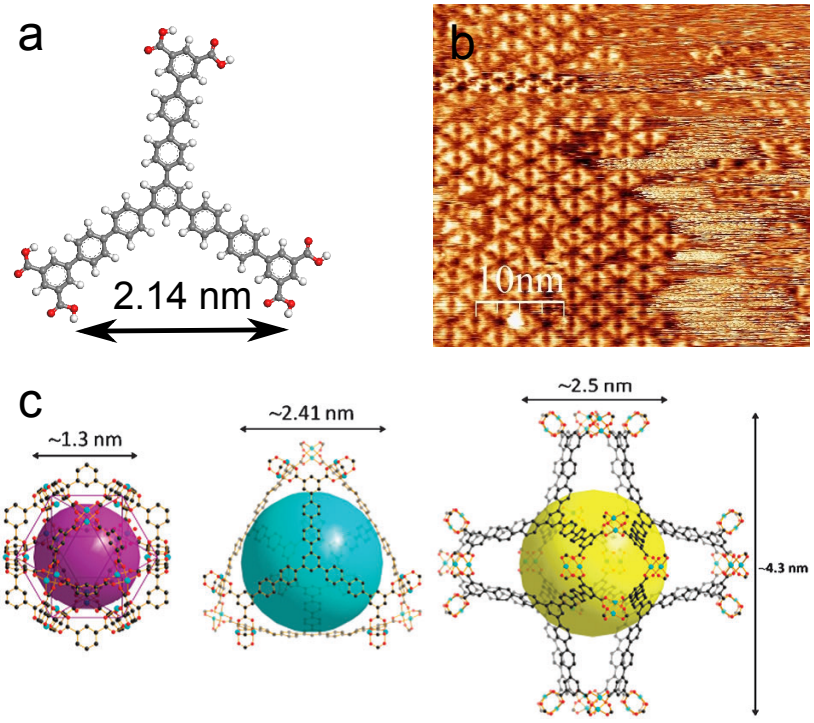

Figure 3.2: a) Structure of H_6L molecule; b) Ambient STM image of H_6L molecules self-assembled into a 2D hydrogen bonded network on the HOPG surface. Tip bias, 1V, tunnel current 50 pA; c) porous NOTT-119 MOF structures formed by H_6L. From [66]

The tailorable chemistry of the organic linkers has allowed the creation of MOFs with particular chemical functionality implanted in the framework. This is of particular interest for catalytic chemistry since a porous membrane with a well-ordered and defined chemical functionality integrated within the framework may act as a tailorable catalyst, i.e. the catalytic function may be varied by varying the functional group present

inside the pores.

Research within the Nottingham MOF group has so far focused on the formation of MOF compounds through the synthesis of new linker molecules. In addition the uptake of gases such as H_2, CO_2 and CH_4 is also measured. This has involved the synthesis of several new organic linkers such as the H_NL series of triangular carboxylate-terminated ligands as shown in Fig 3.2 where the subscript N indicates number of carboxylic acid groups present on each ligand [66]. The formation of MOFs using these ligands has led to the discovery of several compounds with high H_2 gas uptake [54, 67]. The formation of MOFs from tetracarboxylic acid molecules that self-assemble into ordered structures on HOPG substrates [9, 68, 69], have also been used to synthesise high H_2 uptake materials [54].

3.2 MOFs on Surfaces

Growing MOFs on substrates to form surface-mounted MOFs (so-called SURMOFs) is particularly interesting since they provide a route to the integration of functional porous materials with thin-film devices [70, 71, 72]. For example, SURMOF materials are promising candidates for fabricating highly responsive gas sensors since they strongly, and in some cases selectively, adsorb various gases [63]. There have also been recent advances in the fabrication of SURMOF prototype semiconductor devices and optical sensors based on interferometry [73, 74, 75, 76, 62].

There have been several reported approaches to the growth of SURMOF thin films [63]. The simplest method involves the immersion of a substrate in the solvothermal reaction solution. Under the right conditions, this leads

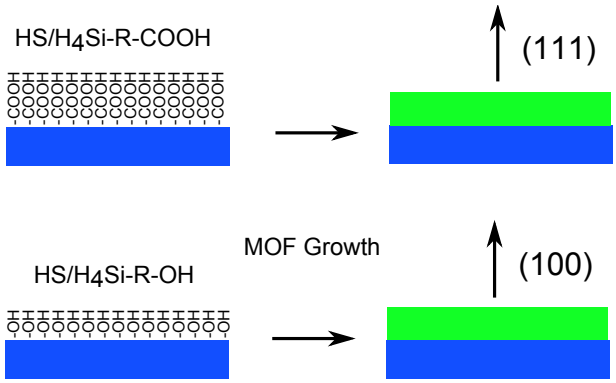

Figure 3.3: Oriented MOF growth due to SAM functionalisation of a substrate prior to growth

to the growth of a thin film of MOF crystallites [77]. It has been further demonstrated that modification of both noble metal and oxide surfaces via termination or functionalisation with, respectively, thiol and silane self-assembled monolayers (SAMs) can promote the growth of SURMOF films [78, 79]. In addition, the crystallographic orientation of the film may be controlled through the use of SAMs with specific terminating end-groups such as -COOH or -OH [80, 51] as shown in Fig 3.3. Combining surface functionalisation with lithographic techniques such as microcontact printing (μCP) enables the selective local inhibition or promotion of oriented SURMOF films [78, 80, 45, 34, 81] shown in Fig 3.8.

3.3 Layer by Layer Growth

Whilst these approaches represent significant progress, the direct synthesis of SURMOFs through solvothermal growth on a substrate often results in rough, polycrystalline films or, alternatively, an inhomogeneous coverage of isolated crystallites [78, 80, 82, 83]. An alternative approach has been proposed to solve this problem; the so-called 'Layer-by-Layer' (LBL)

technique [58] has been investigated as a possible route to providing finer control of the growth of SURMOF films including the fabrication of MOF heterostructures.

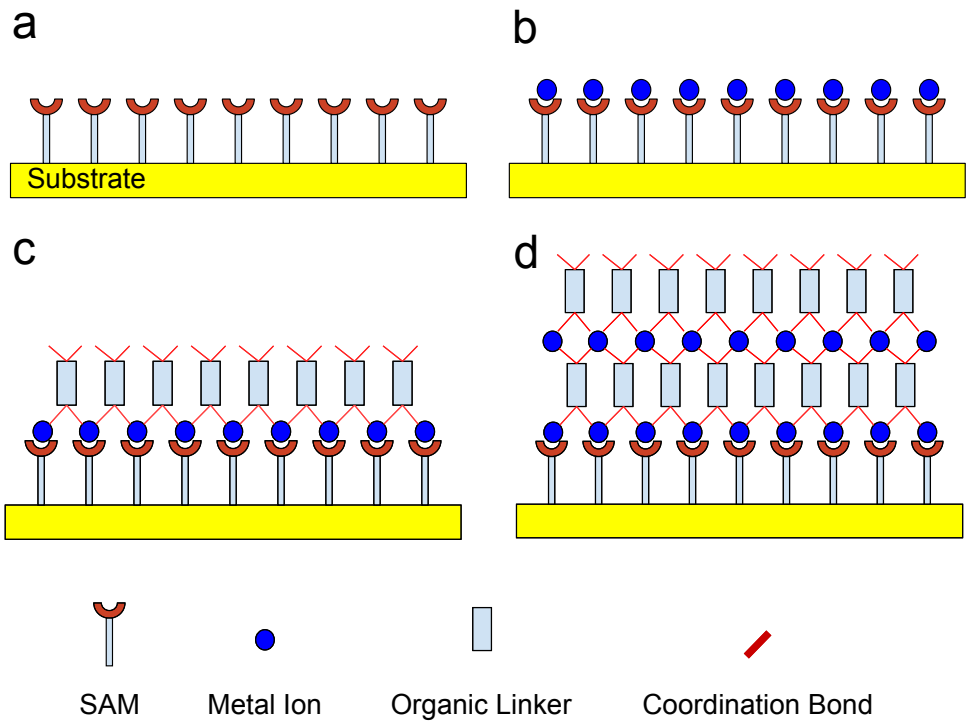

Figure 3.4: Layer-by-layer growth showing a) a SAM coated surface b-c) one LBL growth step showing; b) exposure to a metal ion and c) exposure to a ligand. d) This process is repeated N times to produce a final SURMOF structure, in this case N=2 layers.

In the LBL method a substrate undergoes cyclic sequences of immersion in a solution of the metal ion followed by immersion into a solution of the organic linker (or *vice versa*) with potential rinsing steps in between immersion [12] as shown in Fig 3.4 and 3.5. Variations on this implementation include exposure to metal/ligand solutions in flow reactors [53] and spray deposition [34, 52].

Importantly, the substrate is only exposed to a single component (metal or ligand) of the framework at each step in contrast to the solvothermal

approach which exposes the surface to both simultaneously. It has been proposed that this limits the rate of SURMOF growth to one monolayer per cycle of immersion and thus the SURMOF is grown in a controllable 'layer-by-layer' manner [84] with the relationship between the thickness, T, of the final film and the number of growth cycles, N being given by,

$$T = N\alpha d \tag{3.1}$$

where, d, is the amount added per cycle and is dependent on the crystallographic direction normal to the substrate and α is a constant indicating the number of layers added per immersion cycle and for ideal LBL growth $\alpha = 1$. For the addition of a multiple layers in a single growth step, $\alpha > 1$. Importantly, α does not have to be a whole number, such as the case where there is the addition of less than a whole monolayer in a single growth step and $\alpha < 1$. The LBL method can be combined with lithographic techniques and surface chemical functionalisation using SAMs to enhance further the degree of control of the lateral, vertical and crystallographic geometry of MOF material [45]. Extensions to this idea include the growth of MOF on MOF structures by changing the metal or ligands used during the growth process to create a layered material [85, 59, 86, 87, 88] and post-synthetic modification of linkers to change the chemical functionality of the linker molecules whilst preserving the MOF crystalline structure [89, 90].

The LBL method has been widely described as an epitaxial mode of growth and many of the more exotic approaches to SURMOF growth such as three-component pillared structure MOFs [88, 59] or heteroepitaxial structures [85, 87, 86] implicitly assume that the growth interface is, at least approximately, parallel to the substrate, analogous to the Frank-Van

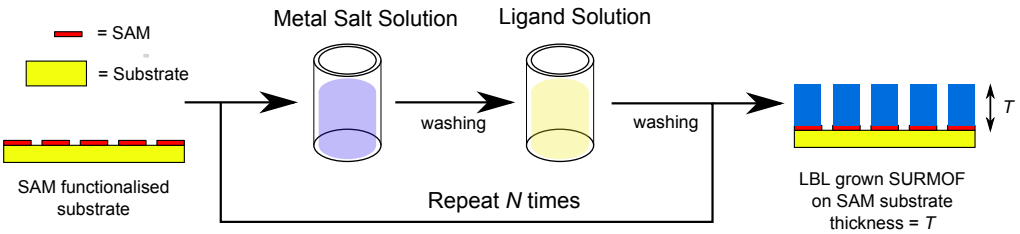

Figure 3.5: Overview of the layer by layer growth of SURMOF films. In this case, the SAM layer has been patterned to give control over the lateral growth of the SURMOF film (see section 3.6).

der Merwe mode of thin-film growth, and advances by a monolayer in each growth cycle. Quartz crystal microbalance (QCM) measurements of the mass uptake during each step of growth offer some support for this idealised model of growth [53, 87, 91], while images acquired using AFM have confirmed that the SURMOF thickness increases with the number of cycles, as expected [34, 52, 45, 59]. However, the growth rate in some cases vastly exceeds that predicted by the ideal LBL model [79, 52, 91, 92], and there is no direct evidence for the addition of precisely one monolayer in each growth cycle. Indeed a recent STM study has shown no clear evidence for epitaxial features during the growth of the first few monolayers of MOF growth [93].

The overall picture from the literature is that the growth of SURMOFs using the LBL method appears to be more complicated than that suggested by the idealised model. This has motivated this study of the very early stages of the growth of SURMOFs by sequential dipping described in section 3.9. In particular this study focuses on the nucleation and subsequent growth which occurs in the first ten growth cycles. AC mode AFM is used to acquire images of the surface after each of the first five cycles of growth, and then again after the tenth cycle. In order to compare with previous

work, both oriented and polycrystalline Au surfaces are used. These are also terminated by differing thiol layers to provide direct comparison with previous studies. The use of oriented substrates allows repeated imaging of individual nanocrystals and subsequent characterisation of their dimensions and orientation relative to the substrate at each stage of the growth process.

3.4 HKUST-1

HKUST-1 [94] was chosen for this study since it has been studied extensively as both a bulk material and as a SURMOF thin film [51] grown on thiol or silane functionalised surfaces [51, 12, 52]. The structure of HKUST-1 consists of a Cu(II) coordination clusters coordinated to benzene-1,3,5-tricarboxylic acid[1] (TMA or BTC) molecules, these are both shown in Fig 3.6a and b. Fig 3.6c shows how four TMA molecules coordinate to the Cu(II) cluster to form the repeating unit of the HKUST-1 structure, giving the full formula $[Cu_3(TMA)_2(H_2O)_3]_N$.

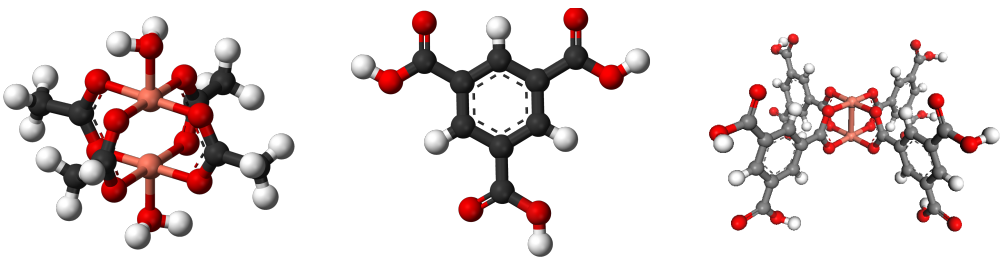

(a) (b) (c)

Figure 3.6: a) Cu(II) acetate cluster b) trimesic acid structure c) HKUST-1 repeating unit showing four TMA molecules coordinated around a Cu(II) cluster.

[1] Also known as trimesic acid

As shown in Fig 3.7 HKUST-1 forms an face centered cubic (FCC) crystal of unit cell side length $a = 2.63$ nm and 1.43 nm spacing between successive [111] planes. Due to the relative lability of Cu(II) centres, HKUST-1 can be deposited under ambient conditions at room temperature (RT) from dilute ethanolic solutions of both metal and salt ligand using a sequential exposure technique [53, 52, 45]. This makes systematic analysis of the growing SURMOF material possible as a result of the simple and easily repeatable deposition of each SURMOF layer.

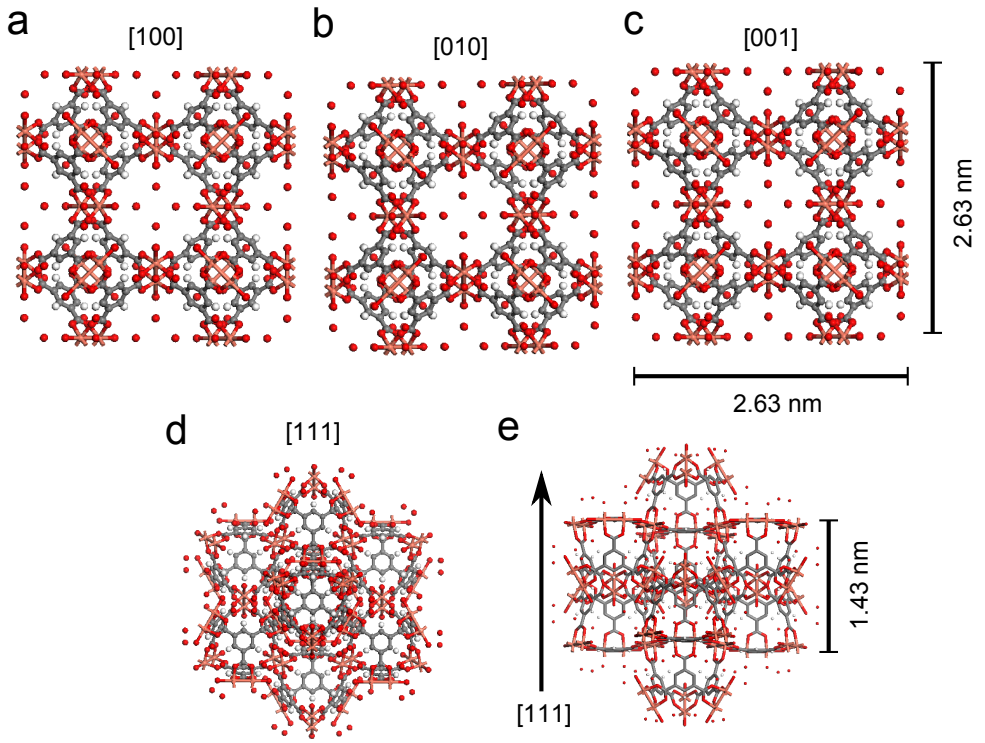

Figure 3.7: Crystal structure of HKUST-1 showing a unit cell of HKUST-1 along different crystallographic axes a) [100], b) [010], c) [001], d) [111] and e) perpendicular to the [111] direction. Structures generated from CCDC data in [94], CCDC number: 112954 [95].

3.5 AFM Studies of SURMOF Growth

In order to establish appropriate conditions for the growth of HKUST-1, several approaches were performed in an attempt to control and monitor the growth of HKUST-1. A number of experiments were performed, primarily to establish the procedures necessary to replicate films of a quality comparable with those in the literature. The Au(111) surface was chosen as a substrate since the highly ordered crystalline surface provides a uniform surface with a known crystallographic direction and has been used in other studies of the earliest stages of HKUST-1 growth [93].

3.6 Patterned Growth

Passivating the Au(111)/mica surface and inhibiting MOF growth on selective regions allows the thickness of the SURMOF film to be accurately measured relative to the substrate. In order to selectively deposit a SAM, micro contact printing was used (μCP) [96]. μCP is a form of soft lithography that uses patterns formed in polydimethoxysilane (PDMS) polymer stamps to pattern SAMs as an 'ink' on to a substrate. A master with the desired relief pattern is typically prepared (or any suitably patterned surface [97]) by photolithographic techniques and acts a mould for the PDMS stamp. PDMS elastomer and a curing agent are mixed and poured around the master and placed in an oven to harden. After curing the stamp can be removed by peeling the stamp from the master and the master re-used to form more stamps. The stamp can then be immersed in a solution of a SAM, dried and then transfered by contact with the target substrate to selectively deposit the SAM in the desired pattern. This process is shown

in Fig 3.8a.

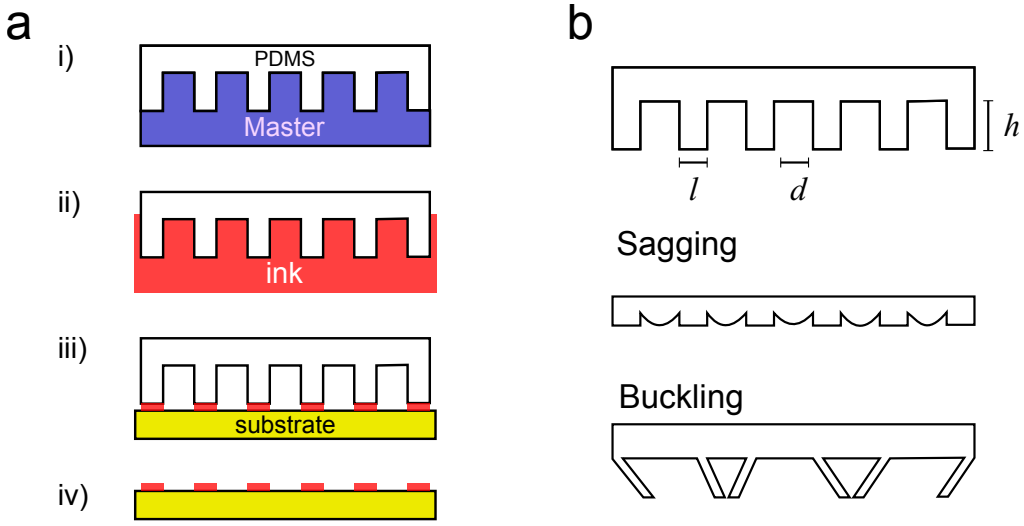

Figure 3.8: a) Overview of μCP process to deposit a SAM on a target substrate. i) First a PDMS stamp is formed around a master, ii) the stamp is then immersed in an 'ink' of the SAM to be deposited, iii) the stamp is brought in to contact with the target substrate and iv) finally the stamp is removed, leaving the patterned SAM. b) Dimensions of μCP structure shown with sagging/buckling at the extremes of dimension.

The dimensions of the features in the PDMS stamp are subject to geometric limitations to prevent undesired contact with the substrate surface. This is typically through two processes; sagging or buckling of the structure due to extremes in the aspect ratios of the structure as shown in Fig 3.8b. This limits the aspect ratio, l/h, of the features to be ≥ 0.2 and the feature separation, d, to be $\leq 20h$ to prevent buckling or sagging of the stamp respectively [98].

SURMOFs of HKUST-1 were grown on Au(111) (300 nm epitaxial Au(111) layer on mica, Georg Albert PVD, Heidelberg, Germany). Substrates were stored in a pressurised N_2 container before use. 1-octadecanethiol (ODT) was used to passivate the surface as it has been widely used in the literature to selectively pattern SURMOF growth on

Au(111) [99, 100, 101, 34, 81]. This technique may also be used to generate areas of selective MOF orientation by appropriate choice of the thiol 'ink' [102]. 1 mM ODT in ethanol (Fisher 99.95%) was transferred onto a PDMS stamp with a 25 x 25 μm pattern of squares prepared from a GaAs master as detailed above by immersion in the thiol solution for 30 minutes followed by drying in an N_2 stream. The stamp was then placed on a freshly annealed Au(111)/mica surface for 1 minute to transfer the ODT SAM. The HKUST-1 SURMOF was grown by immersion in separate 1mM solutions of $Cu(O_2CCH_3)_2$ and benzene-1,3,5-tricarboxylic acid (TMA) in ethanol as per Fig 3.5. Substrates were immersed for one minute in the metal solution after which the substrates were rinsed in ethanol, dried using N_2 and subsequently immersed in the ligand solution for a further one minute. The sample was again rinsed in ethanol to remove unreacted ligands and dried with N_2. This process was then repeated for the desired number of cycles.

AFM measurements were performed in amplitude-modulated tapping (AC) mode with an Asylum Research MFP-3D AFM using AC240TS AFM probes (Olympus) at set points betweem 400-700 mv (free-air amplitude normalised to 1V) in ambient conditions (k = 2 (0.5-4.4) Nm^{-1}, ω_0 = 70 (50-90) kHz).

Figure 3.9 shows the results of ten cycles of HKUST-1 growth on an ODT patterned Au(111)/mica surface. After ten cycles, the transferred pattern is easily observed optically as shown in Fig 3.9a, this enables easy alignment of the AFM cantilever with the region of interest.

Interestingly, it is possible to reproducibly observe HKUST-1 growth on the bare Au(111) metal surface. There have been several reports that MOF

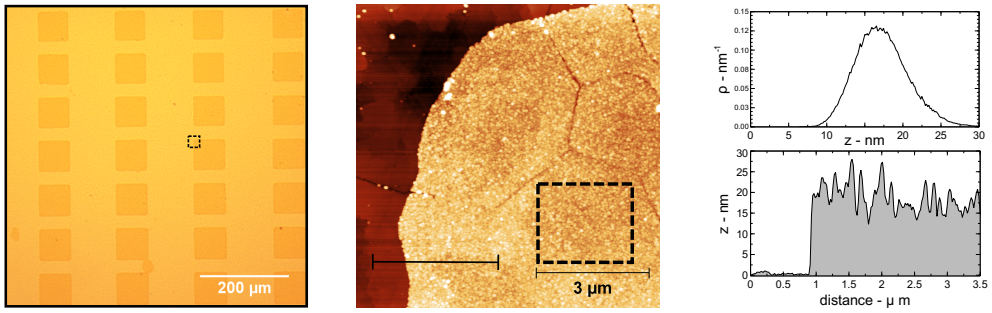

(a) (b) (c)

Figure 3.9: a) Optical image of HKUST-1 SURMOF on an μCP patterned ODT-Au(111)/mica after ten cycles of LBL growth, the lighter regions corresponding to the ODT passivated surface where MOF growth is inhibited. b) Ambient AC mode AFM image of the edge of the SURMOF highlighted in a) showing the nanocrystallite structure of the HKUST-1 MOF surface. c) (top) Histogram of the region marked in b where, ρ is the density of a given height value in the image per square nm (units nm^{-1}) and (bottom) line profile of the edge of the HKUST-1 SURMOF in b.

growth on bare (i.e. in the absence of functionalisation by thiol SAMs) gold does not occur, for example in attempts to grow MOF-5 [55] under solvothermal conditions [78], or HKUST-1 using the LBL technique on a polycrystalline Au surface [51], but these results confirm that the growth of HKUST-1 is possible on the Au(111) surface without the addition of thiols.

High resolution ambient AFM was performed on these samples to inspect the domain structure of the SURMOF layers as shown in Fig 3.10[2]. Figures 3.10a-b clearly show the nanocrystalline structure of the HKUST-1 surface although it is not possible to tell whether the nanocrystallites have coalesced. By viewing the phase channel information of Fig 3.10b in Fig 3.10c, the boundaries in between individual nanocrystallites are clearly visible. Varying the immersion time from 1-30 minutes was explored to try

[2]These AFM measurements were taken using a Bruker MultiMode AFM by Vladimir Korolkov.

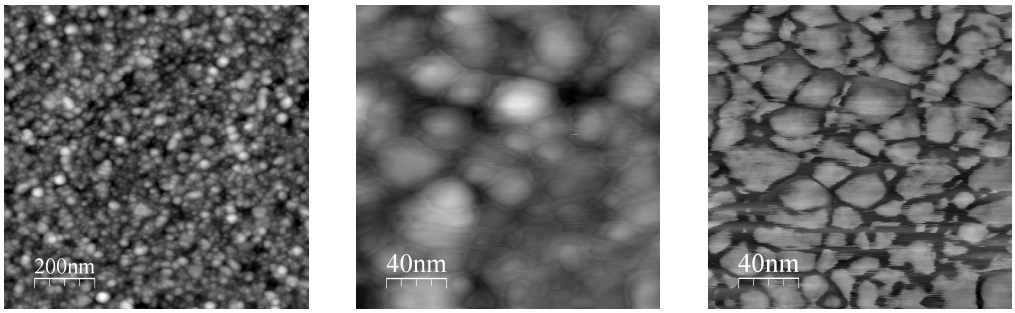

(a) (b) (c)

Figure 3.10: High resolution ambient AC mode AFM images of HKUST-1 SURMOF on Au(111)/mica showing; a-b) nanocrystalline structure of the surface. c) Phase channel image of the region in b highlighting the boundaries (dark regions) between individual HKUST-1 crystallites (light regions).

to increase the quality of the grown films, however, in all cases the same nanocrystalline structure was observed when inspected with AFM.

3.7 Oriented Growth of HKUST-1

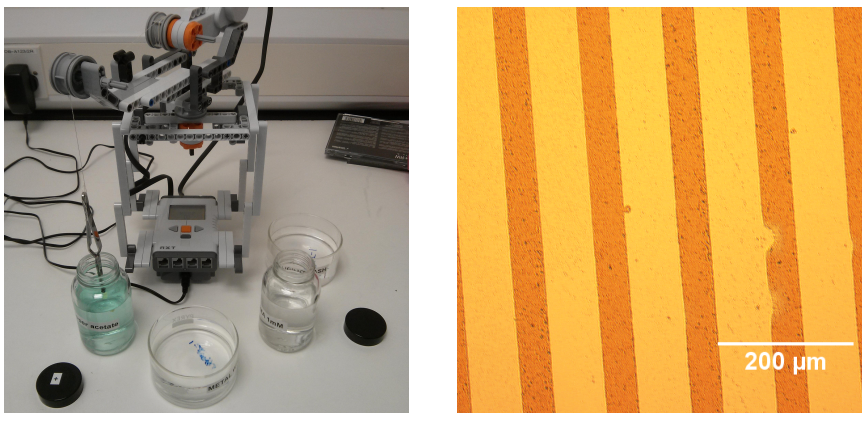

(a) (b)

Figure 3.11: a) Robot used to grow thick films of HKUST-1, the metal/ligand solutions are contained in the jars and the dishes contain the ethanol for washing the substrates. b) Optical image of μCP patterned HKUST-1 film grown with a robot after 10 cycles of LBL growth.

In order to generate thicker HKUST-1 films for XRD analysis to confirm that the films are crystalline MOFs, a technique inspired by that used to grow artificial bone composites in a similar manner to the LBL process was used [103]. A LEGO Mindstorms robot was constructed to automatically place the substrate in the required solution and grow the SURMOF film for longer periods of exposure/a higher number of growth cycles, this is shown in Fig 3.11a. The robot alternately places the substrate (held by tweezers) in each growth solution followed by rinsing in ethanol for the desired number of cycles.

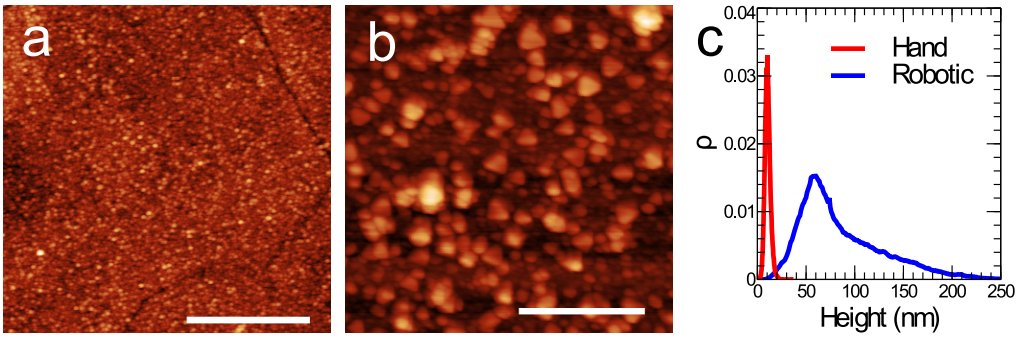

Figure 3.12: Comparisson of hand grown vs robotic grown HKUST-1 SURMOF on Au(111)/mica films showing ambient AC mode AFM images of a) hand grown, b) robotic grown samples and c) normalised histograms of images a and b showing the large differences in roughness between the two surfaces. Scale bars in a and b are both 2 μm.

Figure 3.11b illustrates the effect that growing with the robot has on the surface, the considerably darker surface corresponding to significantly thicker SURMOF material. This increased roughness was confirmed by the AFM measurements of hand and robot grown HKUST-1 samples as shown in Fig 3.12a and b respectively.

3.8 XRD

In order to confirm the crystallinity of the SURMOF layers grown using the robot system, θ-2θ XRD measurements were taken of HKUST-1 SURMOF samples. This technique has been used extensively in the literature as a way of confirming the selective orientation effect induced by the use of functionalised SAMs [63, 104]. Following growth, SURMOF samples were placed in a PANalytical XPert XRD system using Cu-Kα^1 X-rays of wavelength 1.54056 Å.

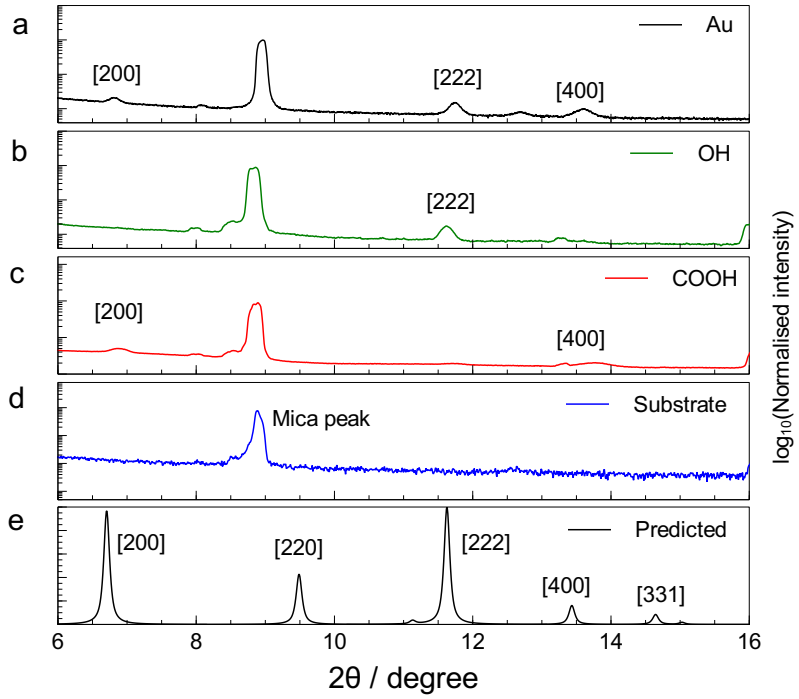

Figure 3.13: XRD data for 30 cycle HKUST-1 SURMOFs grown using a robotic dipping system on a) bare Au(111)/mica, b) MUDA SAM on Au(111), c) MHDA SAM on Au(111), d) Au(111)/mica substrate and e) HKUST-1 predicted powder pattern generated from data in [94] via [95].

The XRD data shown in Fig 3.13 confirms the influence of the SAM on the orientation of HKUST-1 crystallites normal to the substrate. This is in agreement with results in the literature for HKUST-1 grown on MHDA

and MUDA functionalised polycrystalline Au, i.e. the MHDA and MUDA terminated surfaces produce a [100] and [111] orientation of the HKUST-1 SURMOF respectively on polycrystalline Au [51, 12, 92, 102, 46].

Figure 3.13 also illustrates one of the problems with collecting the data using the Au(111)/mica as a substrate since the HKUST-1 peaks are much lower in intensity than the strong background produced by the mica support. This necessitates plotting the intensity logarithmically to identify the diffraction peaks associated with HKUST-1. The presence of the [200],[222] and [400] peaks also provide confirmation of the presence of crystalline HKUST-1 on the bare Au(111)/mica surface in agreement with the AFM results in section 3.6.

3.9 Studies of Nanocrystallite Growth

From the results discussed in sections 3.6 and 3.7 it was clear that consideration of the nanocrystallite nucelation at the earliest stags of SURMOF growth would be necessary to understand the subsequent evolution of LBL grown SURMOFs. The acquisition of a high resolution AFM system with fine control of coarse tip positioning on a substrate enabled the investigation of these early growth steps. By returning to the same region on the substrate, repeated measurement of individual nanocrystallites at various stages during the LBL process are possible.

3.9.1 Methods

Thiol SAMs were deposited by immersion of Au(111)/mica substrates for 30 min in 0.2 mM ethanolic solutions of either 16-mercaptanhexadecanoic

acid (MHDA) or 11-mercaptanundecanol (MUDA) to terminate the surface with, -COOH and -OH functional groups respectively. This was followed by rinsing in ethanol (99.9%, Fischer) and drying in an N_2 stream. Originally an electron beam lithography (EBL) method of marking the substrate was investigated in which the substrate was coated in a poly(methyl methacrylate) (PMMA) resist (PMMA A5, molecular weight 495K, 5% in anisole, Microchem) spin coated at 3000 RPM for 30s at RT and them patterned with an EBL system at 30 KeV at an exposure level of 74 μCcm^{-2}. The substrate was developed in a 3:7 H_2O:IPA mixture for 30 seconds and etched in a potassium iodide gold enchant (8g KOH: 2g I_2: 80 ml H_2O) diluted 1:5 by volume with H_2O for 1 min and stopped by immersion in ultra-pure water and drying in an N_2 stream.

Following etching, residual undeveloped resist was removed by immersing the substrates in acetone at 60°C for 30 min followed by cleaning at 400°C for 4 h in a H_2:Ar (95:5%) gas mixture in a barrel furnace. This technique was not used for the data presented in this work since residual resist inhibited the growth of the MOF layers. Instead, once the substrates had been prepared, a registration mark was formed on the Au layer using a pair of tweezers (cleaned by flame-annealing until red-hot in a butane flame for 30 s and allowed to cool). This has the effect of removing a small area of gold without introducing any organic contaminants to the clean Au(111) surface in addition to providing a unique mark that is easily identified using the optics in an AFM system. After loading the substrate into the AFM the cantilever was optically aligned with the registration mark using the coarse x, y movement of the AFM sample stage. This is shown in Fig 3.14 for a cantilever in close proximity to the surface.

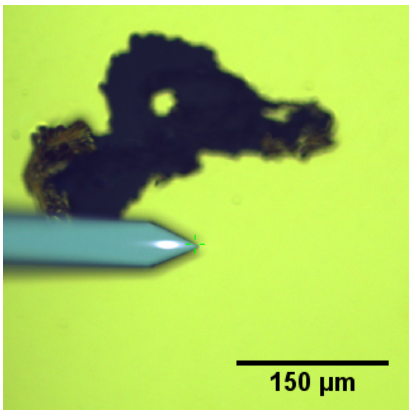

Figure 3.14: Registration mark on Au(111) formed by a pair of tweezers provides a registration mark to align the cantilever.

All AFM measurements were performed in amplitude-modulated tapping (AC) mode with an Asylum Research Cypher-S AFM using AC240TS AFM probes (Olympus) at set points betweem 400-700 mv (free-air amplitude normalised to 1V) in ambient conditions (k = 2 (0.5-4.4) Nm^{-1}, ω_0 = 70 (50-90) kHz).

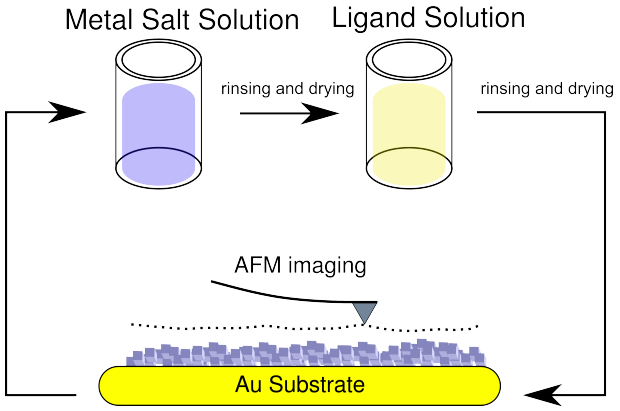

Figure 3.15: Schematic showing the process used to grow and analyse HKUST-1 SURMOF on Au(111) in between the growth steps, AFM images of the substrate are taken.

After each cycle of immersion in metal and ligand solutions the substrates were returned to the AFM for further imaging. The optics of the AFM were used to align the cantilever with the registration mark to an ac-

curacy of ∼10-20 μm. A large scale image (∼30×30 μm) was taken and the region of interest found through further alignment using the grain structure and terrace morphology on the Au(111) surface acquired in previous scans to provide registration. This process was then repeated for the desired number of cycles as shown in Fig 3.16.

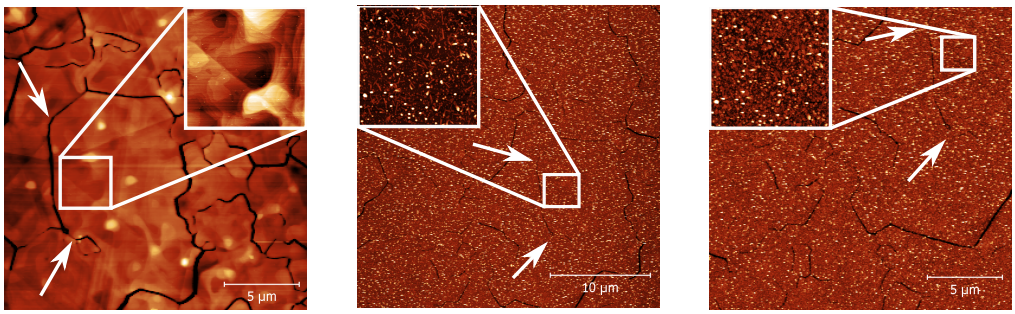

(a) (b) (c)

Figure 3.16: Ambient AC mode AFM images showing the identification of the region of interest on the Au(111) substrate at different stages during the growth process a) 0, b) 5, c) 10 cycles. The two arrows indicate features used for alignment and are the same in images a-c.

Films of HKUST-1 on polycrystalline Au were prepared using the same preparative and sequential dipping process on wafers of 300 nm polycrystalline Au on Si(100) with a 50 nm Ti bonding later (Georg Albert PVD). In the case of the polycrystalline Au, the lack of an easily identifiable grain structure and the isotropy of the Au surface structure prevented the repeated imaging of the same sub-micron area. An AFM image of this surface is shown in Fig 3.17.

3.9.2 Results and Discussion

Fig 3.18 shows AFM images at different stages of the growth process on various thiol-terminated Au(111)/mica substrates. Each column shows a

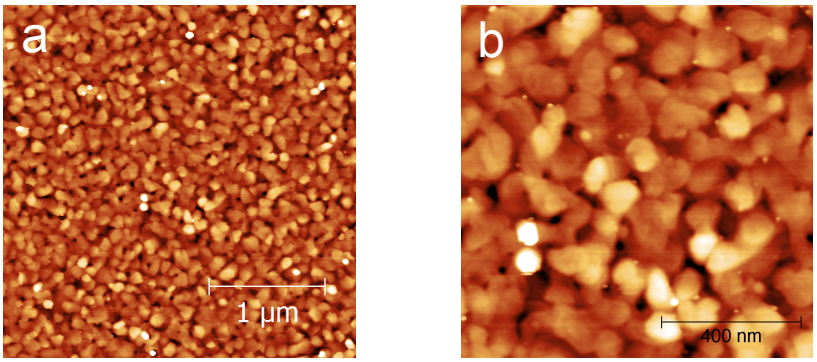

Figure 3.17: a-b) Ambient AC mode AFM images showing the surface structure of a clean polycrystalline Au surface on a Si wafer. Note the lack of an identifiable terrace structure compared to the Au(111) surface shown in Fig 3.16.

sequence of images acquired for Au(111) substrates prepared in a different way: the first column (Fig 3.18a) is a clean Au(111) surface; in the second column (Fig 3.18b) the Au(111) surface is pre-treated with MHDA to give a -COOH termination; in the third column (Fig 3.18c) the Au(111) surface has an -OH termination through pre-treatment with MUDA. Within each column AFM images are presented of the surface prior to deposition of the MOF in the top row, followed by images acquired after, running from top to bottom, 1,2,3,4,5 and 10 cycles of sequential dipping. Thus images within a column provide a comparison of surfaces at different stages of growth, while the rows provide a comparison of images acquired after the same cycle of growth but with different surface functionalisation.

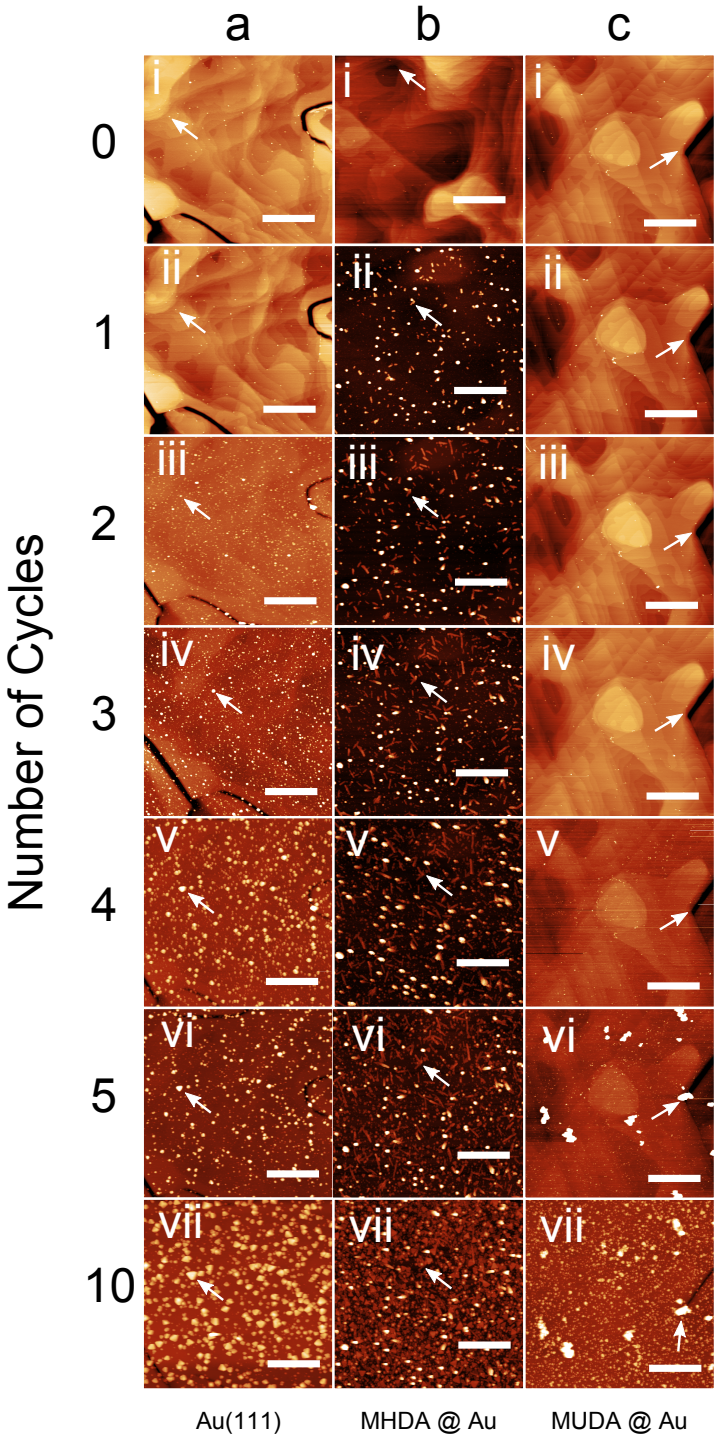

Figure 3.18: 1 μm square ambient AC mode AFM images of HKUST-1 growth on a) Au(111) b) MHDA on Au(111) and c) MUDA on Au(111) at different stages during LBL growth; the number of cycles of growth is shown along the vertical axis and varies from 0 in i to 10 in vii. The arrows in a-c) i-vii indicate specific surface features to provide registry between successive images. Scale bars in all images are 1 μm. Adapted from [105].

The use of registration marks to obtain images of the same region of the surface is highlighted in, for example Fig 3.18a i-ii and Fig 3.18c i-iv. In these images the terrace structure of the gold surface may be readily resolved and, further, the detail of this structure is immediately recognisable in successive images (down the columns). As the MOF layers grow in the subsequent dipping cycles, the contrast in the images becomes dominated by the MOF crystallites when their height is greater than the variation in height of the underlying gold surface (typically less than 2 nm over a 1 μm^2 area from AFM data of clean Au(111) surfaces). The terrace structure is not immediately visible in such images (see for example Fig 3.18a iii-vii, although it may be readily discerned in processed images in which the contrast of the terrace structure may be enhanced. To aid the identification of the registry in Fig 3.18, particularly for surfaces where there has been significant growth, an arrow is included on each image identifying a specific feature as a reference.

Note that the loss of contrast of the gold terraces provides an approximate indication of the point where there has been significant SURMOF growth. The images therefore highlight the differing growth rates due to surface functionality with the MUDA surface having little growth until at least five cycles, whereas in the case of the MHDA terminated surface the loss of contrast occurs after a single cycle indicating significant growth has already occurred.

Fig 3.19 shows some simple statistics characterising the growth on these surfaces. Fig 3.19a shows the fraction of the surface covered by the growing MOF film with increasing cycles of growth. For the -COOH terminated surface, there is already $> 5\%$ coverage after one cycle and this value in-

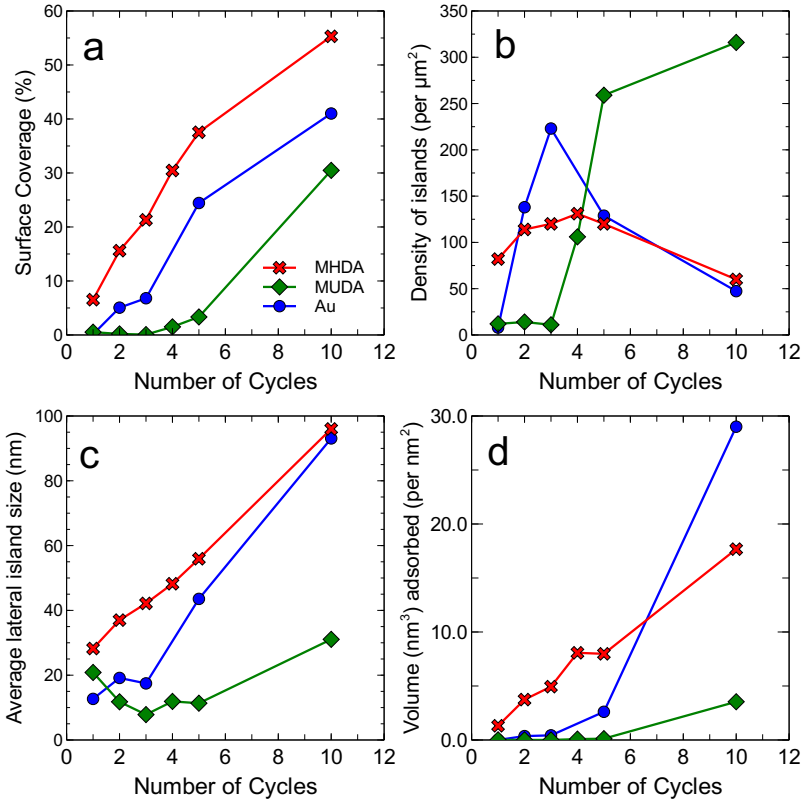

Figure 3.19: a) Surface coverage, b) island density, c) average lateral island size and d) volume of material per unit area (or equivalently average thickness) deposited during the growth process plotted as a function of the number of growth cycles for Au(111), MHDA and MUDA surfaces.

creases monotonically over subsequent cycles, although the rate of increase drops between five and ten cycles when the overall surface coverage is > 50%. On the unfunctionalised Au(111) surface there is very little growth after one cycle and the subsequent rate of increase of surface coverage is also lower than for the -COOH surface. For the -OH terminated Au(111) surface there is still a very low fraction of the surface covered even after four growth cycles; after which the coverage increases very rapidly. These data confirm that growth occurs immediately for the -COOH terminated surface, much more slowly for the -OH terminated surface, while the clean Au(111) is an intermediate case.

There are further differences in the morphology of the growing surface, for example related to the number of nucleated islands of MOF crystallites. In Fig 3.19b, the number of MOF islands per unit area is shown. For the -COOH terminated surface there are ∼80 islands per square micron after one cycle corresponding to an average centre-centre island separation of ∼ 110 nm. This increases to ∼130 islands μm^{-2} after four cycles, which then decreases after further cycles indicating that islands have started to merge at this point. The island density on the clean Au(111) follows a similar dependence with a value which falls after five cycles. The growth on the -OH terminated surface differs markedly with very few islands after three cycles followed by a sharp increase in areal density.

From the data in Fig 3.19a and b it is possible to derive the average lateral island size (Fig 3.19c). From the AFM data it is also possible to estimate the total volume of material deposited and this is shown in Fig 3.19d as a volume measured in nm^3 adsorbed per area (in nm^2) of substrate (equivalent to the average height of the film in nanometres). For the -COOH terminated surface a near-linear increase in both the island size and the total volume of material deposited is observed. This implies that for this surface a near constant amount of material is added in each growth cycle, consistent with previous studies of polycrystalline gold terminated by -COOH [58, 45, 91]. From the gradient of the data in Fig 3.19d)an estimated growth rate (averaged across the sample) of ∼ 1.7 nm per cycle is calculated, which is much greater than the thickness of a single Cu/TMA layer, ∼0.6 nm (the lattice constant of the unit cell of cubic HKUST-1, which contains four layers of Cu/TMA is 2.6nm [45]; note that in Ref [45] a 'cycle' is defined as two immersions in the metal and ligand, rather than

a single immersion in each solution as adopted here, so that in Ref [45] the expected growth rate within the layer-by-layer model is 1.3 nm/cycle for a 'halflayer' comprising two layers of metal ions and two layers of molecules). In previous work a constant growth rate has been interpreted as supporting evidence for layer-by-layer growth in the direction perpendicular to the substrate [58, 91, 106], but it is clear that in this case a constant growth rate occurs in combination with the locally accelerated growth of nanocrystallites, rather than an extended even growth of homogeneous layers.

The growth rate on the -OH terminated surface is much lower compared with the case of the -COOH terminated substrate and, in agreement with previous studies [63, 91, 92], more non-linear. This results in a more inhomogeneous distribution of island sizes leading to, after 10 growth cycles, a combination of a small number of large crystallites and a large number of very small crystallites. Growth on the clean Au(111) surface is also rather non-linear. Overall these results indicate that nucleation of MOF on these surfaces does not occur immediately but is likely preceded by an accumulation of physisorbed material, possibly mediated by inhomogeneities on the surface. It was therefore decided to focus discussion on the -COOH surface on which, as show below, it is possible to monitor the progressive growth of individual crystallites. This is also the most common choice of termination for growth of HKUST-1 on surfaces reported in the literature [78, 80, 58, 12, 53, 45, 82, 46].

Figure 3.20a-d shows images of a single 1 μm^2 region on MHDA terminated Au(111) acquired over four stages of the growth process, together with selected height profiles (Fig 3.20e-h) which are extracted from the same positions in successive AFM images (shown as the coloured lines in

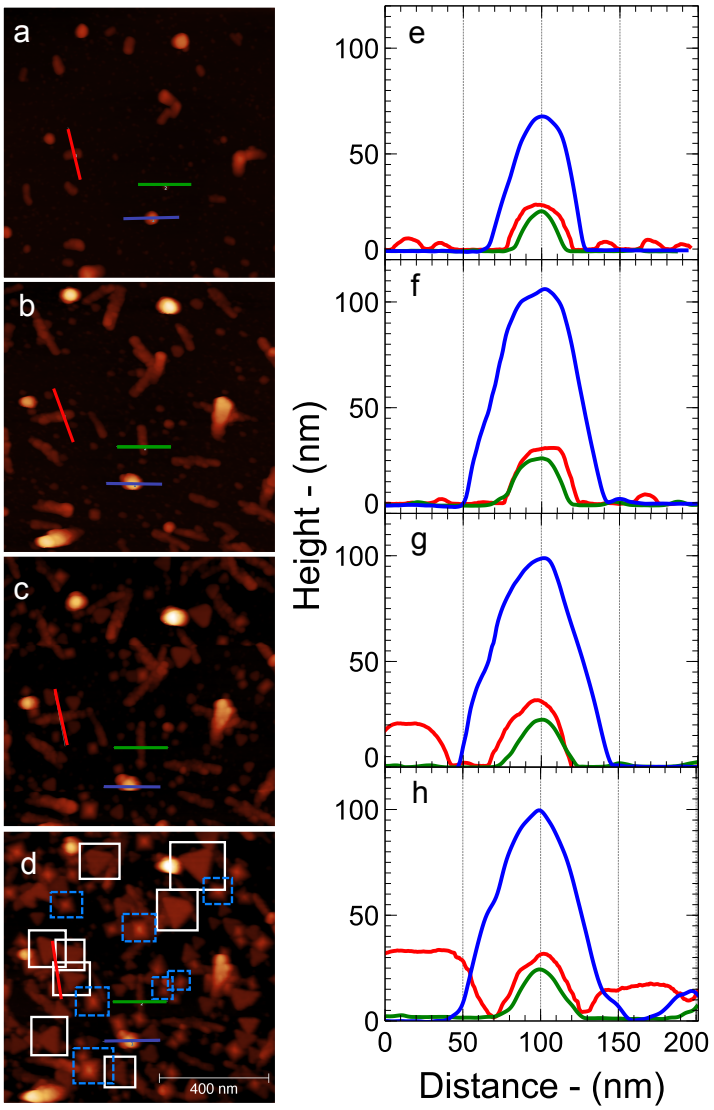

Figure 3.20: Ambient AC mode AFM images showing the evolution of the same 1 μm^2 region on an MHDA terminated Au(111)/mica substrate at 1,3,5 and 10 LBL cycles (a-d respectively) showing the growth of HKUST-1 crystallites. e-h) height profiles across the features in a-d. The z-colour scale is limited between 0 and 150 nm in images a-d.

Fig 3.20a-d). These images confirm unequivocally that it is possible to image the same area on the substrate due to the presence of identical, growing features, for example the two bright (topographically high) features close to the top of each image.

In Fig 3.20 it is possible identify four distinct types of surface feature;

the first of these are high features with a near circular shape and no obvious faceting. Examples include the islands mentioned above and also the feature through which a blue line passes; the blue height profiles are acquired along this trajectory and show the height of these islands. Surprisingly even after one growth cycle the profile indicates a height, and apparent width, of ∼65 nm. This feature grows so that after three cycles (Fig 3.20b, f) the height is ∼110 nm; the vertical size of this island is approximately constant after this cycle. It is possible that this feature corresponds to a non-crystalline material, or a three dimensional aggregate, since there are no obvious facets as expected for a crystallite. Control samples which were exposed to only the metal, or only the ligand showed no growth after repeated immersion in one of these growth components. From these controls it is clear that all the feature observed are formed only after immersion in both the metal and the ligand, ruling out the possibility that any features are due to one of these single components.

Linear islands are also observed; see for example Fig 3.20b where many linear features are present. A comparison with the surface earlier (Fig 3.20a) and later (Fig 3.20c) in the growth process shows that these features grow rapidly in one lateral direction in the first few growth cycles (they are clearly present, but shorter in Fig 3.20a). However, after an initial stage of growth the sizes of these features saturate at a typical length of ∼150 nm and, from the profiles, a width of ∼50 nm and a height of ∼30 nm (see green and red profiles).

The other two types of surface features are highly facetted with either a triangular or square base. These features are seen most clearly in Fig 3.20d where they are identified with white (triangular) or blue (square)

outlines. Unlike the linear and globular features, these crystallites become progressively larger through the cycles of growth; their size increases and does not saturate. For example, the red profiles in Fig 3.20 extends over two triangular islands on either side of the linear island on which the profile is centred; these triangular islands become higher and wider as the growth progresses.

The pyramidal features correspond to [100] oriented islands terminated by {111} planes, while the triangles correspond to [111] oriented crystallites, also terminated by {111} surfaces. It is possible to identify all of these features at earlier stages of growth (for example the triangular features in Fig 3.20c, and, more difficult to resolve on the scale of these images, Fig 3.20b).

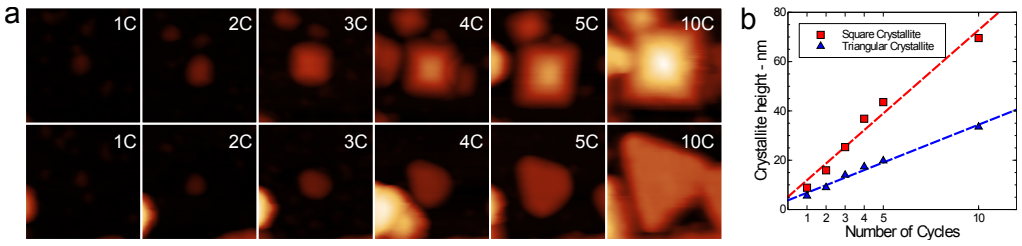

Figure 3.21: a) Ambient AC mode AFM images of two crystallites highlighted in Fig 3.20d after successive growth steps. AFM images are 120 nm square; b) plot of the height for each crystallite in a vs the number of growth cycles with a linear fit to the data measured from line profiles across the crystallites relative to the surrounding substrate.

To highlight the 'history' of a particular crystallite Fig 3.21a shows the progressive growth of a pyramidal (upper row) and triangular (lower row) crystallite. The square and triangular bases of these structures are very clearly resolved after ten growth cycles and it is possible to track these features back to earlier stages in their growth; the faceted shape is apparent after three cycles, but is poorly resolved after two cycles. After one cycle

it is possible to resolve the presence of a nucleated island but the shape cannot be identified with confidence at this stage.

These images allow the determination of the growth rate of individual crystallites which complements the average growth rates discussed above. Figure 3.22 shows the variation of height with growth cycle for the square and triangular islands highlighted in Fig 3.20d. Although there is some variation between individual crystallites the rate of increase in height is 4.9 nm per cycle and 3.2 nm per cycle for the square and triangular islands, respectively. Again, it is emphasised that this is not consistent with a model in which the growing interface advances uniformly by one layer per cycle.

The exposed facets for both island shapes are attributed to {111} planes given their triangular symmetry; in addition this is consistent with the formation of free surfaces of bulk HKUST-1 crystals by {111} planes [82, 102, 107, 108]. The geometry of the square features is consistent with a crystallite growing with the [100] direction oriented normal to the surface, leading to a pyramidal structure (a square base formed by a {100} plane and four faces formed by {111} planes; see for example ref [108]). The ratio of height to the half-diagonal width of the base is expected to be 1:1 for a face centred cubic crystallite with this geometry. This is consistent with observations shown in Fig 3.22c, where this ratio is plotted for the square islands highlighted in Fig 3.20d at different stages of their growth. The presence of a [100] orientation is consistent with previous data for HKUST-1 grown on polycrystalline Au substrates functionalised with -COOH end groups [51, 92].

The triangular features are assigned to [111] oriented crystallites ter-

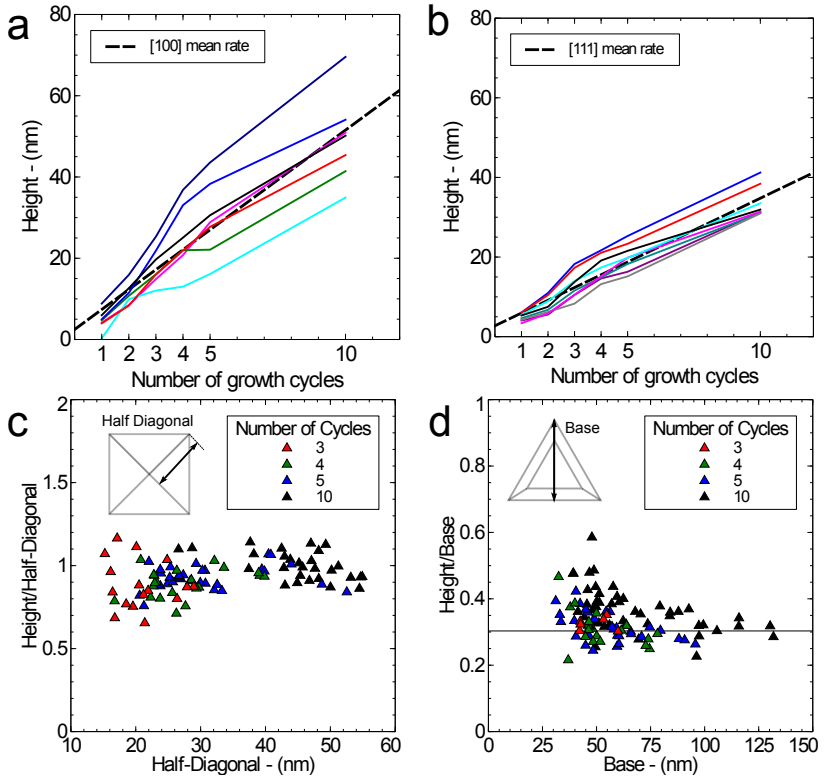

Figure 3.22: Height as a function of growth cycles for individual; a) [100] oriented HKUST-1 crystallites measured by AFM for, b) [111] type crystallites, c) height vs width (see inset for location of measurement) for [100] type crystallites and, d) height vs width for [111] type crystallites.

minated by a {111} surface. For these crystallites the growing surface is near parallel to the substrate, but a preferred in-plane orientation is not observed implying that there is no epitaxial relationship with Au(111) surface. The presence of these [111] crystallites is not expected from previous studies of HKUST-1 on MHDA terminated Au. However, in these previous studies [12, 52, 91, 46] polycrystalline gold films were used as substrates, rather than the oriented gold films used here.

To check whether this difference is significant, HKUST-1 SURMOF was grown using the protocols described in section 3.9.1 on MHDA-terminated polycrystalline gold. The results, shown in Fig 3.23, indicate the presence of

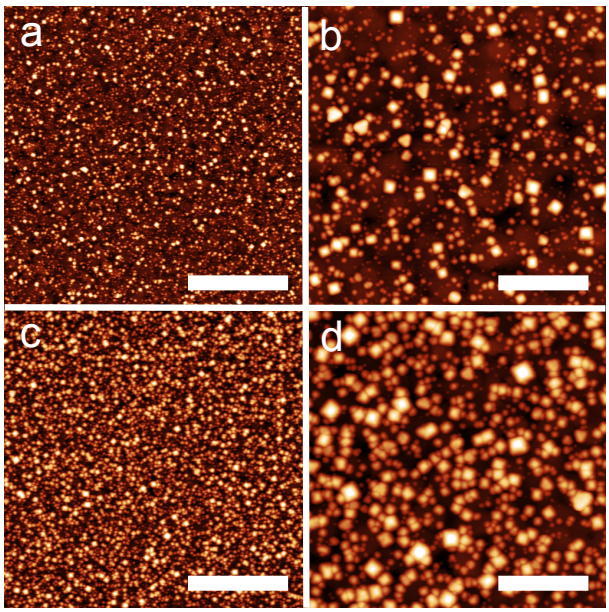

Figure 3.23: AFM images of HKUST-1 LBL growth on MHDA-terminated polycrystalline Au at; a-b) 5 cycles and c-d) 10 cycles of LBL growth. Scale bars in a/c are 1 μm and b/d are 150 nm.

many islands with typical dimensions 5-40 nm which have a faceted shape similar to that of the pyramidal [100] oriented islands discussed above, but the triangular islands are not observed; this observation is consistent with previous work [51] showing the selective growth of [100] crystallites on similar surfaces and other recent AFM studies [109]. The pyramidal shape implies that these crystallites are terminated by {111} planes.

3.9.3 Evaluation of LBL methodology

The growth of HKUST-1 on Au(111)/mica islands shows significant differences to previous work on polycrystalline gold substrates. Firstly, contrary to previous work, growth on clean Au(111)/mica is observed, however, more interesting effects relate to growth on MHDA-terminated surface, which introduces a -COOH functionality. Here, four distinct types of is-

land are observed, two of which may be readily identified as [100] and [111] oriented crystallites. Using AFM it is possible to measure not only the average growth rate across the surface, but also the local growth rate both horizontally and vertically to the surface for individual crystallites. Both these rates are greater than one layer/per cycle as expected in simple models of layer-by-layer growth, while the local increase in height per cycle, measured to be 4.9 nm and 3.2 nm for, respectively, [100] and [111] type crystallites, is significantly greater than the thickness of a single Cu/TMA layer, ∼0.6 nm. This observation demonstrates that in local regions of the surface, multiple (5-10) layers of MOF are grown in each cycle, which is not consistent with the fundamental mechanism assumed in LBL growth models.

Interestingly the largest crystallite features which are identified in Fig 3.20d may be traced all the way back to the first deposition step in Fig 3.20a. This implies that the nucleation of all these islands has already occurred after the first cycle of growth. Furthermore, it is possible to address the question of whether the growing crystallites are re-dissolved or significantly re-distributed when the substrates are re-immersed in the relevant solutions. The reproducible appearance of growing islands and traceability of the location of structures on this highly inhomogeneous surface implies that very little re-organisation or solvent assisted re-crystallisation of material occurs under the conditions used in this work.

For HKUST-1 grown on polycrystalline gold significant differences are observed; the lateral size of individual crystallites is considerably smaller, and triangular islands are not observed. The larger crystallite size on Au(111)/mica may be due to the presence of larger, flatter terraces, as

compared to the rougher evaporated polycrystalline gold surfaces on which a higher density of nucleated islands is observed. This enhancement in nucleation density may be due to inhomogeneities in the gold film, or in the MHDA termination. However, the observation of oriented [100] growth is consistent with previous studies of thicker film grown on this surface.

The termination of the faceted crystallites by {111} planes of HKUST-1 is observed for both [100] and [111] crystallites, and in addition, for the pyramidal shapes resolved on polycrystalline gold. As stated above, the free and therefore lowest energy, surfaces of bulk HKUST-1 crystals are formed by {111} planes, and the termination of the SURMOFs by these planes is therefore expected. This implies that for growth under near-equilibrium conditions, for which the lowest energy surface will dominate, the growing interface is only parallel to the substrate if the crystallographic orientation is normal to the lowest energy surface plane. This is observed for triangular [111] oriented islands, but not for the pyramidal [100] crystallites. These results do not therefore appear to be consistent with one of the central assumptions of simple models of layer-by-layer growth, since the growing interface, for example of [100] crystallites on both Au(111) and polycrystalline gold, cannot be parallel to the substrate. A further discrepancy with the model of layer-by-layer growth is that the rate of propagation of the growing interface is not homogeneous across a surface, and that the local rates vary significantly. Accordingly the incorporation of single layers of MOF cannot be inferred from the rates averages across a surface measured, for example, using a QCM to measure mass uptake [91, 53]. These results imply that such films are actually nanocrystalline and should not be considered as epitaxial, although, in agreement with previous work with a strong

dependence of orientation on the surface termination and morphology.

It is interesting to consider the implications of these observations for device architectures grown using the layer-by-layer growth approach. For some applications, for example optical thin-films, the noncrystalline morphology of a SURMOF may not be critical since, when averaged over a length comparable with the wavelength of visible light, the films may be considered homogeneous with a uniform refractive index. However, if the response of the film to, for example, gas exposure is of interest, it is likely that the presence of defects and boundaries inherent in a noncrystalline film will play a major role in controlling diffusion. In addition, in some cases the motivation for the growth of SURMOFs by the layer-by-layer approach has been to provide access to epitaxial single crystals allowing investigation of intrinsic properties of a MOF, for example mechanical properties [110]. It is difficult to reconcile this approach with the observations presented in this thesis.

In light of these observations it is suggested that the layer-by-layer method for SURMOF growth would be best suited to materials for which it is possible to select, for example using self-assembled monolayers, a crystallographic orientation that is normal to the lowest energy surface of the MOF. Under these circumstances the growing interface might be selected to be parallel to the substrate, consistent with one of the major underlying assumptions for layer-by-layer growth of SURMOFs, although even under these conditions it is possible that nanocrystalline growth could dominate.

3.10 Single Crystal MOFs

From the results in section 3.9.2 it is clear that there are significant areas for improvement in the understanding of the LBL process for growing SURMOFs. Whilst the properties observed for SURMOF films both in this work and in the literature (nanocrystalline, highly defected, non-uniform thickness) may be sufficient for some applications. The significantly increased size of solvothermally synthesised crystals may allow investigation of intrinsic properties of MOFs without the high defect densities observed in LBL grown SURMOF films. Additionally, recent advances in the positioning and manipulation of two-dimensional materials may allow integration of single MOF crystals into novel device architectures by positioning crystals over pre-fabricated contacts. This approach to device fabrication has been reported for photocurrent generating crystalline materials such as InSe/graphene heterostructures [111] and may be applicable to MOFs with desirable optoelectronic or gas adsorption properties.

One of the most widely researched applications for MOFs is gas storage and delivery and typically there is a correlation between the uptake of various gases and the pore size of a MOF [112]. A simplistic approach is to assume that by elongating the linker, the pore size of the MOF will increase along with gas uptake. However, there are a number of undesirable effects that this may cause. For example, elongation of the linkers may lead to interpenetration of the frameworks or a reduction in the gas-framework interaction as a result of the higher pore volume to surface area ratio [113, 114]. This has motivated the study of so-called *isoreticular* MOFs (IRMOFs). This term defines a group of MOFs that have the same network topology whilst having different pore sizes through the use of dif-

ferently sized linkers in an attempt to optimise the balance between the porosity, gas-uptake and stability [115, 70, 112].

3.11 NOTT-18X Series of MOFs

A newly synthesised family of IRMOF structures with pore volumes which can be systematically varied have recently became available through collaboration with chemists in Nottingham, the so-called NOTT-18X (X = 0,1,3,5) family of MOFs [112]. The NOTT-18X series of MOFs are composed of Cu(II) paddlewheel cores and 8-connected carboxylic acid ligands. Figure 3.24 shows the structures of NOTT-180-185. The general formula of the NOTT-18X MOFs is $Cu_4L^{1-4}(H_2O)_4$ where L^{1-4} is one of the octacarboxylate linkers shown in Fig 3.25. It is important to note that the superscript number between 1 and 4 indicates the size of the linker[3].

These MOFs form large (50-100 μm) flat crystals when synthesised solvothermally and make ideal systems to investigate the surface structure of MOFs without the nanocrystalline domain boundaries present in LBL grown SURMOF films. Pore-level resolution using AFM in both UHV and ambient conditions has been reported in recent studies [82]. However, beyond this there are no other reports in the literature of pore-level resolution of MOFs using AFM. Recent SEM [70] and TEM studies [116] have enabled imaging of the MOF pores, however these techniques must be used with care as the MOF structure is easily damaged by an intense electron beam [117, 118]. This provides strong motivation to study the surface structure of MOFs using high resolution AFM as these techniques are typically

[3]Higher numbers refer to a longer ligand backbone, however, this does not strictly correspond to the number of benzene rings and is therefore used as an internal numbering system in the research group to refer to each ligand.

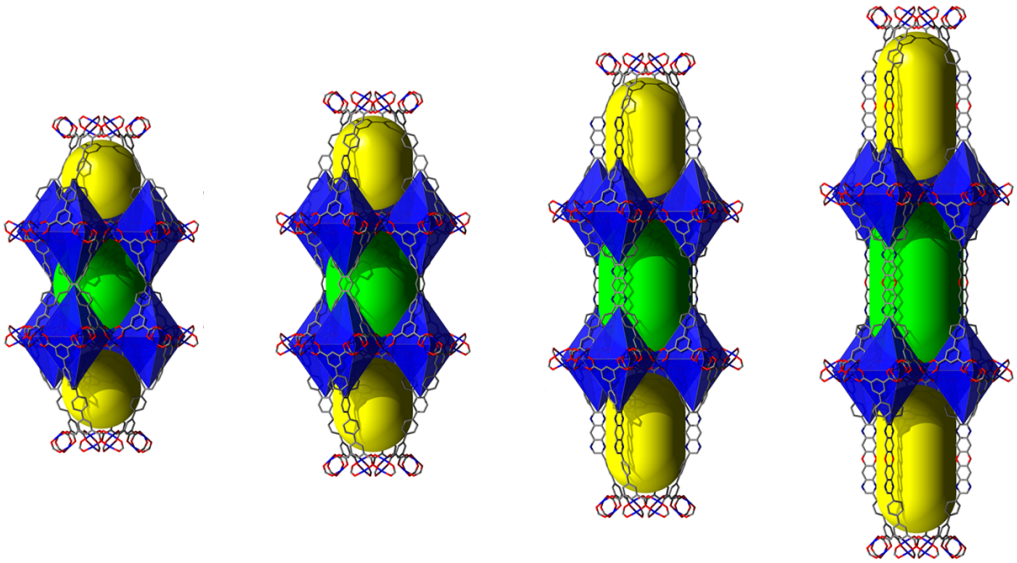

Figure 3.24: NOTT-18X MOF structures from [112] showing the two available pores, highlighted in green/yellow. The pores can be seen to elongate through extension of the linker backbone from NOTT-180 to NOTT-185.

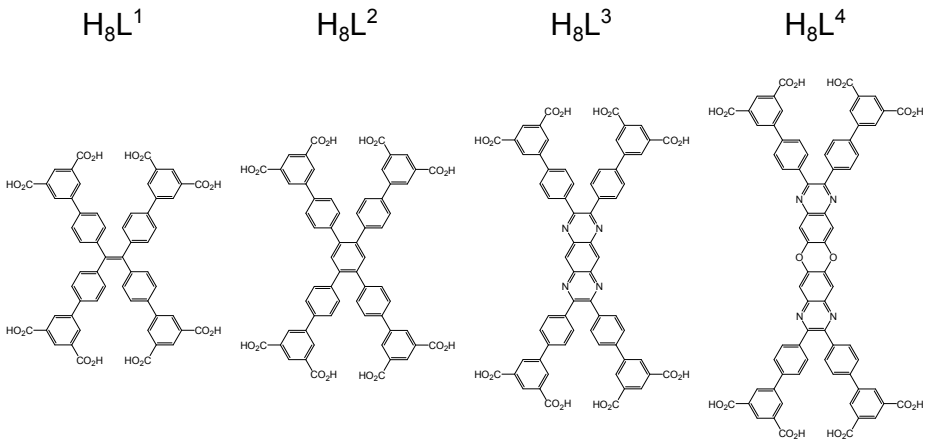

Figure 3.25: Octacarboxylate H_8L^N Linkers used in the synthesis of MOFs NOTT-180-185. From [112].

non-destructive to the bulk structure and can be used to image molecular monolayers without damage to network structures formed by, for example, weak intermolecular hydrogen bonding [6].

3.12 Synthesis and Sample Preparation

The synthesis of NOTT-180 has been previously reported, however, this was via an indirect synthesis route in which the Zn version of the MOF was synthesised followed by exchange of the Zn^{II} ions with Cu^{II} [119]. NOTT-180/181/183/185 crystals were directly synthesised solvothermally, the H_8L^N linkers were reacted with $CuCl_2$ in a diethylformamide (DEF), ethanol and aqueous 0.1 M HCl (2:2:1 by volume) solution in a sealed vial at 60-80°C in an oven for 16 hours to yield the MOF. The crystals were then washed in dimethylformamide (DMF) and methanol [112].

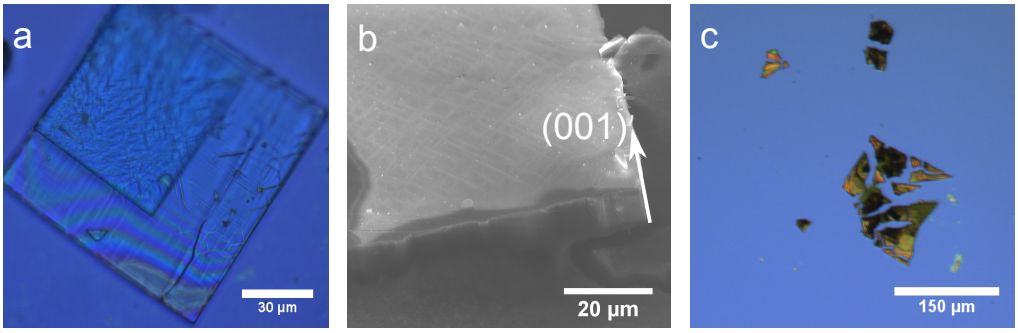

Figure 3.26: a) Optical image of NOTT-181 crystals on SiO_2 surface. b) SEM image of NOTT-181 crystals highlighting the [001] crystal direction, note the crystal does not lie flat in this image as it was deposited on to a conductive adhesive pad and was immobilised unlike on the SiO_2 surface where it typically lies flat after deposition on the surface. c) Optical image of NOTT-183 crystals on SiO_2 wafer showing rapid decomposition after several minutes following removal from acetone solvent.

Both NOTT-180 and NOTT-181 are stable in ambient conditions when removed from the synthesis solution and dried. However, the NOTT-183 and NOTT-185 MOFs are not air stable and quickly decompose when exposed to ambient conditions. This is shown in Fig 3.26c for a NOTT-183 crystal on the SiO_2 surface. The MOF crystals were stored in acetone until required for AFM imaging. Current experiments have been limited to the

NOTT-181 MOF since this was more readily available than NOTT-180 in a sufficient quantity. Optical and SEM images of NOTT-181 crystals are shown in Fig 3.26a-b. The NOTT-181 MOFs form flat square crystallites of approximately 100 x 100 μm lateral size and typically $\sim$10 μm thick as shown for NOTT-181 in Fig 3.26a-b. Prolonged SEM imaging of NOTT-181 at 15 keV caused fracturing of the crystallites due to the electron beam.

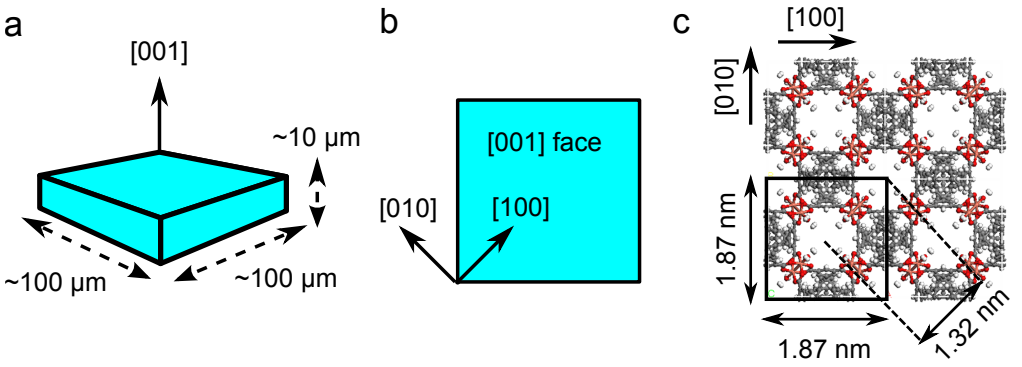

Figure 3.27: a-b) Typical dimensions of NOTT-181 crystals and indexed faces from [112]. c) [001] face of NOTT-181 crystal structure showing pore-pore spacing.

XRD data indicates that the large flat surface of the crystallites is parallel with the [001] plane of the crystal structure allowing investigation of a known crystal face [112]. The high aspect ratio typically means that crystals deposited on to a substrate will lie flat with this [001] plane normal to the substrate surface. For AFM imaging the crystals were drop deposited from the acetone solution on to a wafer of 300 nm SiO_2 on Si wafer using a glass pipette and allowed to dry in ambient conditions since use of an N_2 gun would blow the crystals off of the substrate. The crystals were then imaged in ambient conditions at RT using AC mode AFM in an Asylum Cypher-S AFM with Multi75Al-G cantilevers (Budget Sensors).

3.13 AFM Imaging

NOTT-181 crystals on SiO_2 surfaces were imaged using AC mode AFM in ambient conditions. Figures 3.28 and 3.29 show the terrace structure of the crystal surface. Measurements of the terrace step height for NOTT-181 give a value of 2.3 ± 0.2 nm in agreement with the XRD results for $\frac{1}{2}$ the unit cell length in the *c* direction (4.1 nm) [112].

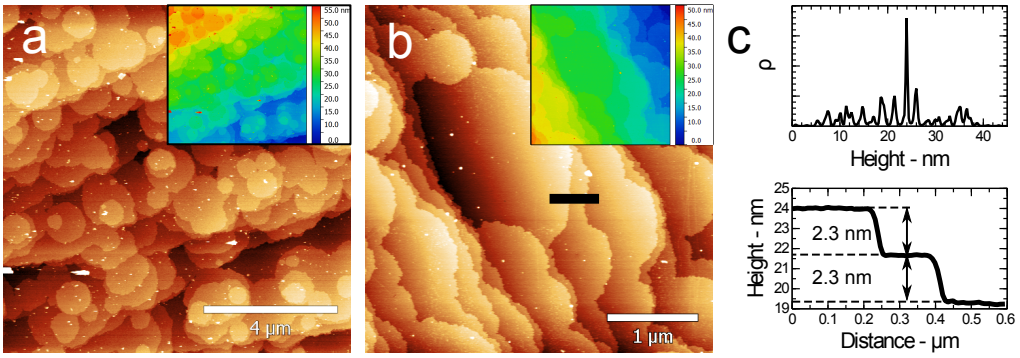

Figure 3.28: a-b) First-order flattened AFM images of NOTT-181 crystals showing the terrace structure and (inset) colour-height mapping for each image. c) (top) Height distribution of image b and (bottom) profile across the terrace steps indicated by the black line in b). Images a and b were taken using AC mode AFM in ambient conditions at RT.

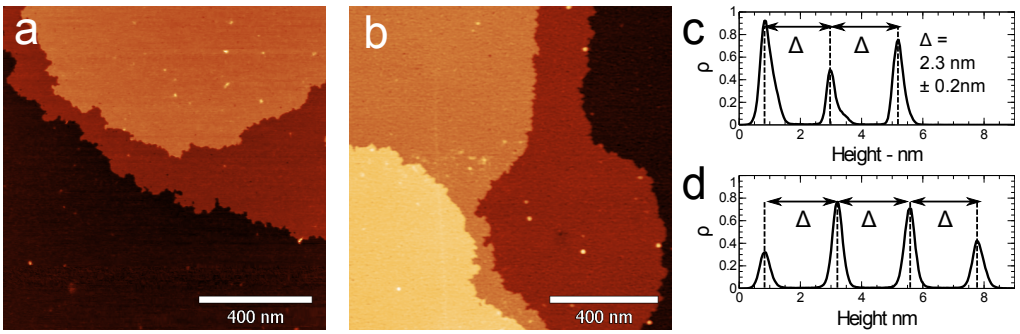

Figure 3.29: a-b) AFM images of the NOTT-181 surface. c-d) Height distributions of the AFM images in a and b respectively showing the consistent step height of 2.3 nm between planes. Images a and b were taken using AC mode AFM in ambient conditions at RT.

AFM images of the [001] surface and 2DFFT's of the images are shown

in Fig 3.30. Periodic structures with a square symmetry were found through Fourier filtering of images with weakly visible periodic features (see Fig 3.30d-i) with a periodicity of ∼1.8-2.0 nm. The repeated observation of periodic features with this spacing at different scan sizes, locations and at different rotations suggests that these are real features and not imaging artifacts. However, this distance does not agree well with the expected pore-pore spacing of 1.32 nm across the [001] face from the NOTT-181 crystal structure shown in Fig 3.27c. In addition, the observation of lattice defects in the Fourier filtered AFM images in Fig 3.30g-i may indicate that the surface has undergone some reconstruction. High-speed contact mode AFM imaging was also performed on the NOTT-181 terraces. Use of this technique has so far been unable to resolve any periodic structures on the (001) face of NOTT-181 and typically results in damage to the surface.

The difficulty in resolving the pore structure of the NOTT-181 [001] surface may be attributed to a combination of surface structure decomposition, surface reconstruction or adsorption of contaminants from the synthesis solution although the cause in this case is unclear and further imaging of the NOTT-181 surface will be required.

Some NOTT-181 crystals were observed to have a mottled surface with a deposit with a thickness of 2.0 ± 0.2 nm on top of multiple crystal planes. This is shown in Fig 3.31a-c (Another image of this surface feature is also shown in Fig 2.23 in section 2.12). The origin of this surface feature is unknown and may be a deposit from the growth solution. However, given that crystals with isotropic flat crystal planes such as those in Fig 3.28 were also part of the same batch of MOF crystals this is unlikely since any contaminant would likely affect all the MOF crystals in the same solution.

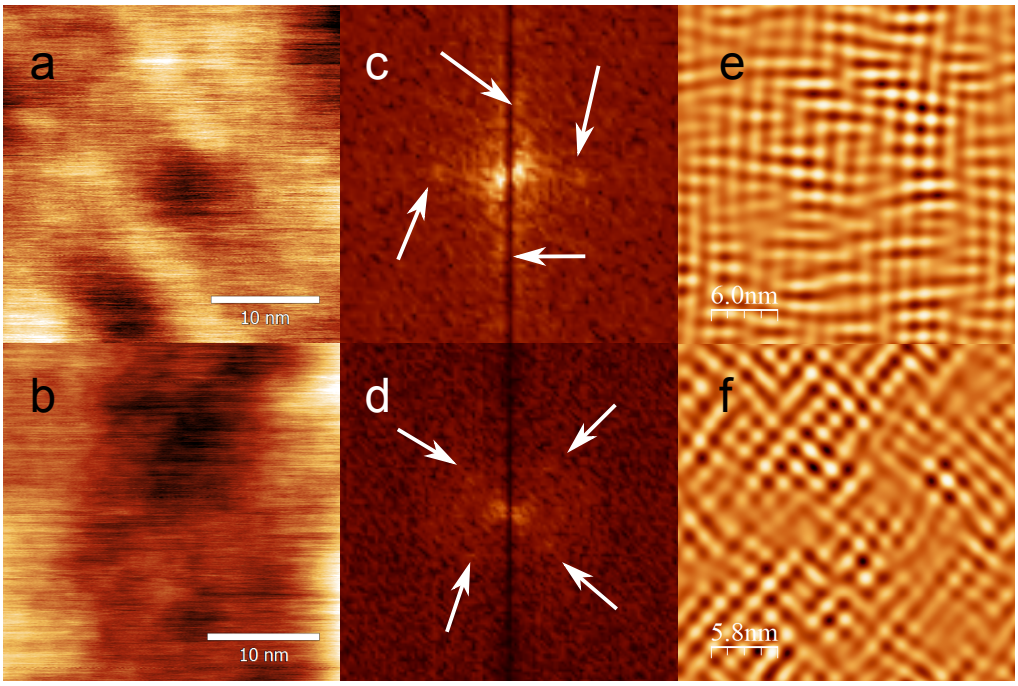

Figure 3.30: a-b) AFM topographies of NOTT-181 surface showing weakly periodic features. c-d) 2DFFT of images a and b showing Fourier peaks. e-f) Images a-b following Fourier filtering of the peaks indicated by the arrows in c and d. Images a-b were taken using AC mode AFM in ambient conditions at RT.

An alternative explanation might be the incomplete formation of a surface layer given the height of this surface feature is similar in thickness to the [001] plane spacing.

In an attempt to remove this material, the sample of NOTT-180 on SiO_2 shown in Fig 3.31a was annealed in a vacuum chamber at 100°C for six hours and imaged using AFM. Taking large area scans of the crystal surface allowed identification of the previously imaged region as shown in Fig 3.31b, this indicates that the surface has not been affected by the annealing since the same terrace structure is clearly visible. Further annealing to 200°C resulted in destruction of the MOF crystals. The origin of this surface feature has yet to be determined although in general, the NOTT-181 surface

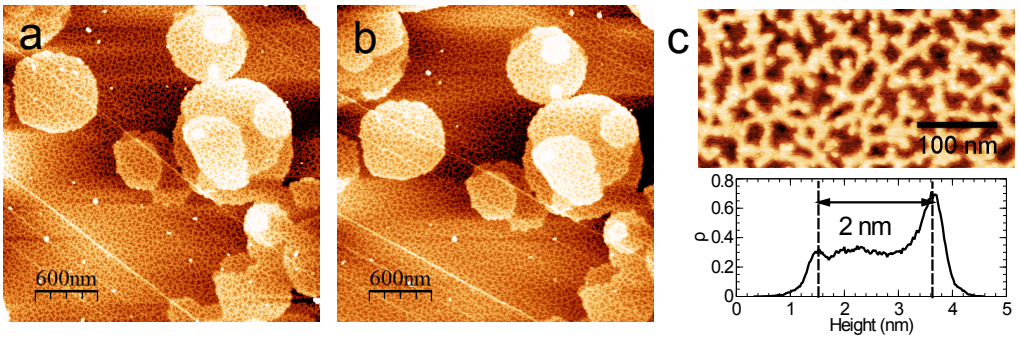

Figure 3.31: AFM image of the mottled surface of a NOTT-181 crystal a) before and b) after annealing at 100°C for six hours. c) (top) Detail of the mottled surface and (bottom) height distribution of the image above showing the 2 nm height variation of the surface. Images a-c were taken using AC mode in ambient conditions at RT.

was found to be clean with well defined terraces as shown by the images in Figs 3.29 and 3.28 and the mottled surface was rarely observed.

3.14 Surface Functionalisation

Successful growth of crystals directly on a substrate as a SURMOF allows for liquid-AFM measurements to be performed as the crystals remain in place upon addition of a suitable imaging solvent. This removes the need to use an adhesive which may contaminate the imaging solution and the MOF surface. This may allow pore-level resolution of the MOF as liquid AC-mode AFM techniques have been able to achieve resolution of atomic point defects on the calcite surface [120]. Transferring the substrate straight in to the AFM after synthesis of the MOF whilst still submerged in the solvothermal growth solution (or transfer to a suitable solvent that is compatible with the AFM liquid imaging cell and protects the MOF) may protect the surface from the effects of solvent removal and exposure to the ambient environment. This prevents decomposition of the MOF as

observed in the case of NOTT-183/185.

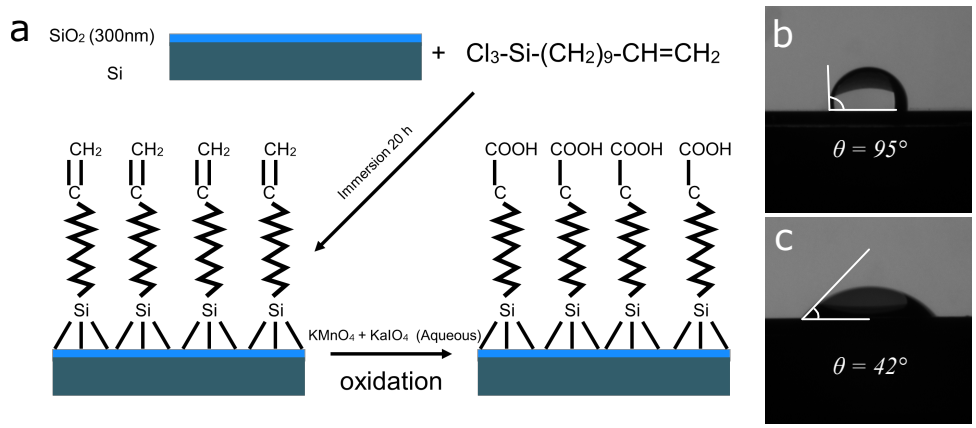

Figure 3.32: a) Steps in silanating the SiO_2 wafer and converting the vinyl terminated surface to -COOH. b-c) Contact angle measurements of water droplets on silanated SiO_2 surfaces, b before and, c after oxidation showing the reduced contact angle indicating the vinyl terminated surface has been converted to -COOH.

In an attempt to synthesise a continuous layer of NOTT-181 as a SURMOF, surface functionalisation with silanes was used to grow NOTT-181 crystals directly on the substrate. Silanation has been used extensively as a SAM in studies of solvothermal SURMOF growth as silanes are known to be more thermally robust than thiols and can survive the synthesis temperatures [83]. 300 nm SiO_2 on Si wafers were silanated with -COOH functional groups according to procedures previously reported for growth of HKUST-1 SURMOFs [80]. Contact angle measurements were taken to confirm the successful conversion of the vinyl (-$CHCH_2$) group to -COOH. The vinyl surface was found to have a contact angle of 95° and 42° after conversion to -COOH in good agreement with those reported in the literature [80]. The silanation steps and contact angle measurements are shown in Fig 3.32.

Current attempts to grow a continuous layer of NOTT-181 on silane

passivated SiO_2 under the same solvothermal conditions used in section 3.12 have so far been unsuccessful. Following solvothermal growth of NOTT-181 in the presence of the -COOH passivated SiO_2 substrate, the wafer surface was found to be covered in a dense film of crystals which initially suggested that the MOF crystals were chemically attached to the -COOH surface as desired. However, this material fell off when gently rinsed with acetone after removal from the growth solution meaning that that they were not well-attached to the surface in a continuous layer.

3.15 Summary and Future Work

Early investigations of the NOTT-181 MOF show promise that investigating single crystal samples can give a high quality surface with a known crystal orientation. This is something that has so far not been possible with LBL grown SURMOFs in the literature due to their nanocrystalline surface structure. The AFM results in Fig 3.30 show that high resolution imaging of the crystal surface may be able to facilitate pore-level resolution of the MOF surface. Currently the effect that removal from the growth solution has on the crystals surface structure is unclear, making in-situ liquid AFM measurements desirable to minimise the effects of desolvation and exposure to the ambient environment.

Further work is needed to produce a continuous SURMOF layer of NOTT-181 and it is hoped that the optimum conditions for growing NOTT-181 on the silane-passivated SiO_2 surface will be identified in future experiments. In addition, the use of micrometer-scale positioning techniques will provide a route towards the fabrication of novel optoelectronic devices from

single-crystal MOFs, potentially in the form of heterostructures consisting of materials such as hexagonal boron nitride and graphene as dielectric/-conductive layers respectively. These devices may be able to overcome the theoretical performance limitations caused by defects and grain boundaries in nanocrystalline SURMOF devices.

Chapter 4

Surface Studies of Porphyrin Nanorings

This chapter is a study of a family of synthetic nanorings formed from a class of light-harvesting compounds known as porphyrins. The assemblies formed by these porphyrin nanorings on surfaces is studied using ambient SPM on both conducting and insulating substrates. Small differences in the number of porphyrin macrocycles in each ring are found to have a strong effect on the stability and size of ordered networks formed when the nanorings are deposited in ambient conditions.

In addition, simulations of the distortion observed for nanorings on surfaces using a simple bending and stretching model are presented. The results of these are used to discuss the effects that nanoring size and thermally-induced distortion have on the lifetime of delocalised states that occur in these rings in solution.

4.1 Porphyrins

Observing and mimicking nature may greatly enhance the development of novel materials for optoelectronic devices. For example, photosynthetic organisms have evolved to use chlorophylls to serve the purpose of harvesting sunlight through the use of delocalised electronic states to adsorb and transfer energy [16]. It has been suggested that delocalised excited states may aid charge separation following the adsorption of light in organic semiconductors. These materials are incorporated in artificial photovoltaic devices providing strong motivation to synthesise materials that can mimic this behaviour [15].

Large networks of light-harvesting molecular films have obvious potential for optoelectronic devices. However, the fabrication of these devices will likely require the use of bottom-up self-assembly techniques on surfaces in order to produce ordered thin-films of these light-harvesting compounds [121]. One important consideration is that many organic compounds cannot be sublimed and as a result need to be deposited onto surfaces using 'gentle' techniques such as solution deposition or electrospray techniques. As a result, studying the structures formed by these compounds when deposited using these techniques is critical if the light-harvesting potential of these materials is to be fully exploited.

Porphyrins are a class of organic dyes consisting of four pyrrole rings linked by methine groups. The simplest porphyrin complex, porphine, is shown in Fig 4.1a. The central site in the free base porphyrin may be occupied by a metal atom such as Fe or Zn to form a metal complex. They are extremely common in nature, being found in the light-harvesting compound chlorophyll in plants and part of the haem group in human red

blood cells.

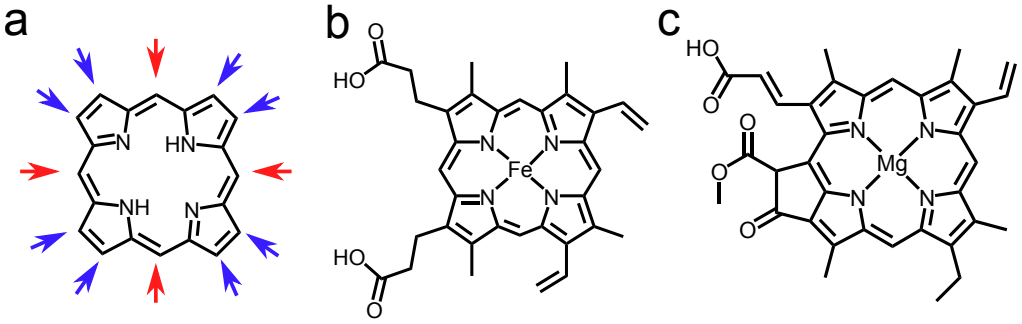

Figure 4.1: Structures of a) porphine (The *meso* and β-pyrrole positions are labeled by the red and blue arrows respectively), b) haem-b and c) chlorophyll c1.

Artificially produced porphyrin compounds typically have the *meso*-positions (indicated by the red arrows in Fig 4.1a) substituted by various groups and are not found in nature. The blue arrows in Fig 4.1 show the β-pyrrole positions and are widely substituted in natural porphyrin compounds such as in the structures of haem-b and chlorophyll c1 shown respectively in Fig 4.1b and c.

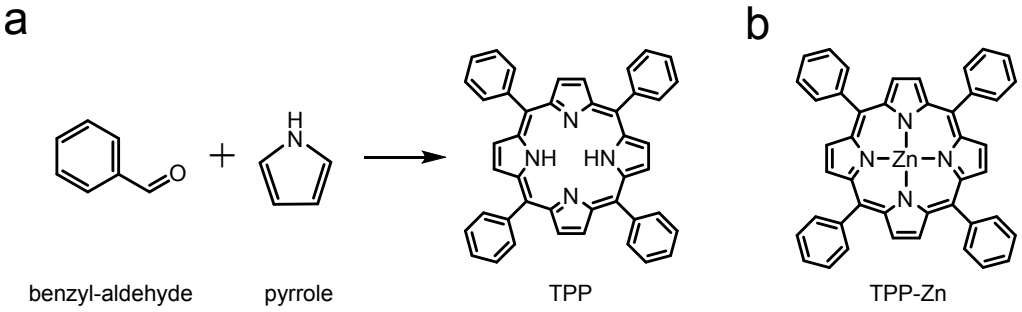

Figure 4.2: Synthesis of a) TPP and b) addition of Zn ion to the centre of the porphyrin macrocycle produces TPP-Zn.

Production of artificial porphyrin compounds was developed by Rothemund in the 1930s [122, 123]. Starting from pyrrole and benzylaldehyde the two compounds were reacted in a sealed vessel at 150° for 24hrs produce tetra-phenyl-porphyrin (TPP) as shown in Fig 4.2 a. The process was

refined by Adler and Longo [124] and further to a two-step room temperature reaction by Lindsey et al [125], enabling the benzylaldehyde to be substituted with a range of different aldehydes with the general structure R-CHO to change the *meso* substituted benzene group. The centre of the porphyrin macrocycle may also be occupied by a metal (II) ion by reaction with an acetate or acid. The TPP-Zn complex is shown in Fig 4.2b.

4.2 Optical Properties

Porphyrins are delocalised systems and obey Hückel's 4n + 2 rule for aromaticity with 22 delocalised π-electrons [126]. As a result they are typically dark in colour due to their intense adsorption bands involving $\pi - \pi^*$ transitions in the porphyrin ring orbitals unlike most transition metal complexes. The optical bands of porphyins are named the Soret (or B) band [127] and the Q band shown in Fig 4.3 which shows the adsorption (solid line) and fluorescence spectra (dotted line) of TPP in benzene. The porphyrin adsorption spectrum consists of an intense peak due to a transition from the $S_0 \rightarrow S_2$ state at around 400 nm constituting the Soret band. Several weaker peaks around 450-700 nm are observed which form the Q band and are due to $S_0 \rightarrow S_1$ transitions

Gouterman proposed a 'four-orbit' model to explain the adsorption spectrum of porphyrins in the 1960s [129]. In this theory, the adsorption bands in porphyrin systems arise from transitions between two π HOMO orbitals with roughly the same energy and a degenerate pair of π^* LUMOs.

Porphyrins also strongly fluoresce and the emission spectrum shows two strong emission peaks from the $S_1 \rightarrow S_0$ transition and are typically

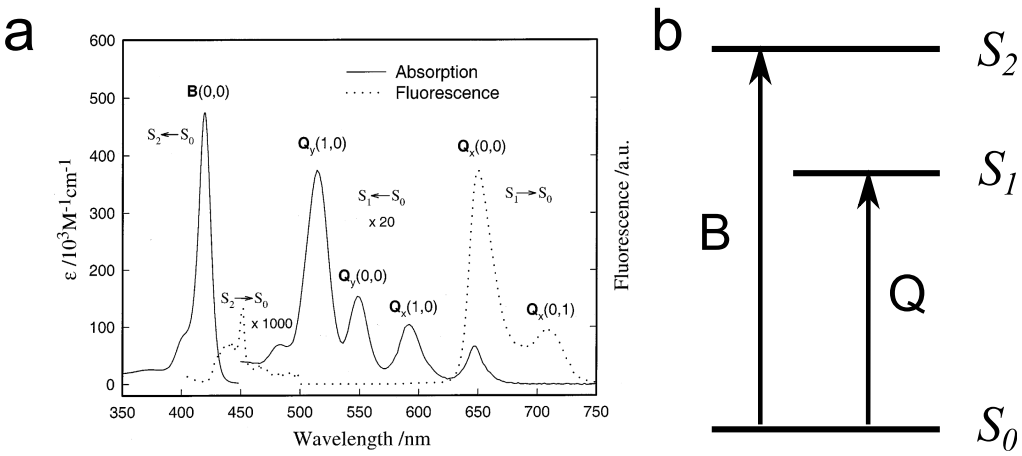

Figure 4.3: Adsorption and fluorescence spectra of free-base TPP showing Soret and Q bands. Spectra taken of 4 μM TPP in benzene using a 397 nm wavelength laser. From [128]. b) Excited state diagram showing B and Q band transitions.

located at wavelengths between 650 and 750 nm respectively. There is also an extremely weak B band attributed to the $S_2 \rightarrow S_0$ transition located at approximately 450 nm. However, as shown in Fig 4.3 the intensity is $\sim$1000 times lower than the Q band peaks.

The UV visible spectra of porphyrins have been studied extensively and the splitting and relative intensities of the B and Q bands are strongly affected by the type and position of substituents onto the porphyrin ring or the metal core in metalloporphyrin compounds. For further explanation of these effects, the reader is directed to [130] as detailed consideration of the origin of these peaks is outside of the scope of this thesis.

4.3 Porphyrin Nanorings

Studying delocalised electronic states in synthetic porphyin molecules is interesting due to their structural similarity with biological light-harvesting complexes [131]. In particular ring structures of porphyrins share many similarities with the naturally occurring light-harvesting complexes LH1 and LH2 [132]. AFM images showing the ring structure of both LH1 and LH2 are shown in Fig 4.4. As a result, structures formed by LH1 and LH2 in biological systems have been studied extensively with SPM [133, 134, 135, 136, 137]. As a result of their similarity with these natural compounds, synthetic conjugated porphyrin polymers have stimulated interest in non linear optics, light-harvesting and electron transport [121, 138, 131, 15].

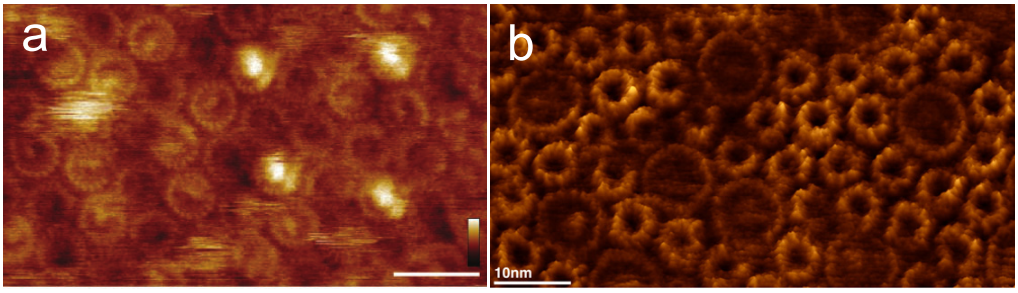

Figure 4.4: a) AFM image of LH1, scale bar 20nm. b) AFM image of LH2 rings (small rings) around larger LH1 reaction centres. a and b are from [134] and [135].

All porphyrin polymer molecules considered in this thesis have the general repeating structure shown in Fig 4.5a. These consist of a Zn-porphyrin macrocycle with two sets of two long octyloxy side chains coupled to aryl rings on opposite *meso* positions which promote solubility in organic solvents [139]. These side chains are typically labeled using the -Ar suffix on structural diagrams of porphyrin nanorings. The macrocycles form linear polymer chains, *oligomers*, of length N porphyrin groups connected by

butadiyne groups forming a conjugated oligomer. The structure of these chains is referred to using the notation l-PN where N is the number of porphyrin units in the chain.

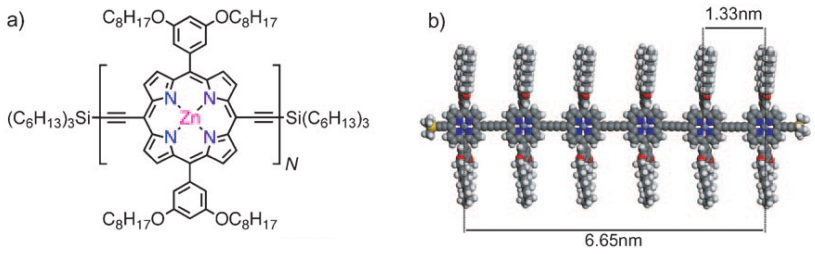

Figure 4.5: a) General structure of Zn porphyrin polymer (shown with $Si(C_6H_{13})_3$ protecting end groups). b) structure of l-P6 linear porphyrin oligomer (end groups truncated). Both figures from [139].

Oligomers consisting of butadyine coupled Zn-substituted porphyrins were first synthesised by Anderson et al [140, 141]. The synthesis of oligomer chains from porphyrins makes use of a template-directed approach to synthesis in which template molecules are used to encourage intermolecular coupling [141]. The porphyrins with protecting end groups (see Fig 4.5a) are coupled to a pyridine template by coordination to the Zn atom in each macrocycle following deprotection of the end groups by conversion of the -$Si(C_6H_{13})_3$ groups to -H groups. The ends are then oxidatively coupled using a palladium/copper catalyst and iodine as the oxidant (also known as Glaser-Hay coupling [142, 143]). This produces the l-PN chain and the template is then removed using pyridine or similar amines to liberate the oligomer molecule [141]. The l-P6 oligomer is shown in Fig 4.5b and the full synthesis methods for various length oligomers are detailed in [138] and [14].

This template-directed approach was further used to produce butadyine linked cyclic porphyrin dimers, trimers and tetramers (c-P2, c-P3 and

c-P4 nanorings) from Zn-porphyrin macrocycles around bi, tri and tetra pyridines [144, 141]. The production of larger nanorings was later reported by Hoffmann et al using this template based method to couple the ends of single l-P8 chains around a T-8 template [13]. This process was further refined to produce a smaller c-P6 ring by coordinating three l-P2 chains into a ring using a T-6 template which has the advantage of bypassing the synthesis of larger oligomers [14]. By synthesising the appropriate template it is possible to couple oligomers together to produce increasingly larger nanorings.

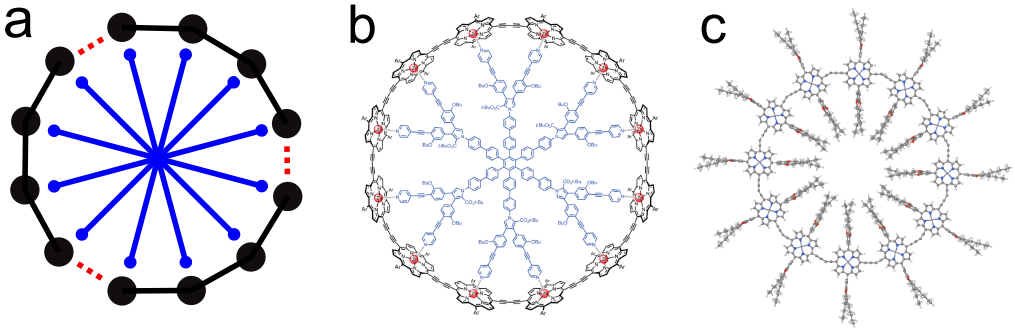

Figure 4.6: Synthesis of c-P12 showing template directed assembly of three l-P4 chains around a T-12 template. b) Structure of c-P12 showing porphyrin ring with coordinated template (blue) following coupling. c) Full structure of c-P12 nanoring following synthesis. b and c from [145]

The single template approach has previously been used for rings up to c-P12 as shown in Fig 4.6a from three l-P4 oligomers [145]. However, this technique is limited by the complexity and stability of the template molecule. The synthesis of rings with larger than 12 macrocycles using a single template would obviously require the complicated synthesis of a large and potentially unstable ligand complex.

An approach to making larger rings of an arbitrary and highly controllable size was realised by using Vernier scales [145]. In this approach,

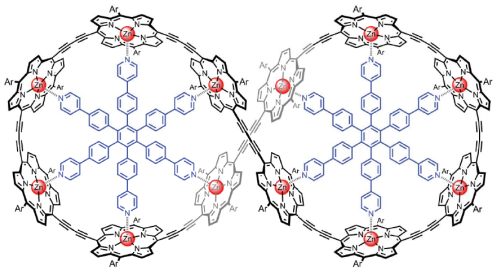

Figure 4.7: Vernier templating of c-P12 using two T-6 ligands. From [145].

a template and linear oligomer is chosen such that the lowest common multiple of the number of ligand sites on the template molecule, N_L, and porphyrin macrocycles in the linear oligomer, N_P gives the desired number of porphyrins in the final nanoring. This allows the use of multiple small templates to form the larger nanorings negating the synthesis of large and complicated template molecules. Use of Vernier templating has enabled the synthesis of nanorings consisting of up to 50 macrocycles at the time of writing [146].

Fig 4.8 shows a schematic overview for the synthesis of both c-P12 and c-P24 using the Vernier templating method. All porphyrin nanorings used in this work were synthesised externally by collaborators at Oxford using the processes reported in [13, 146, 145] for the c-P8, c-P10, c-P12 and c-P24 nanorings.

4.4 Nanorings on Surfaces

Nanorings have previously been deposited onto substrates in UHV using an electrospray deposition (ESD) technique also used to deposit linear porphyrin chains on Au(111) surfaces [139]. In ESD molecules are deposited from a solvent solution in ambient conditions through an aperture using

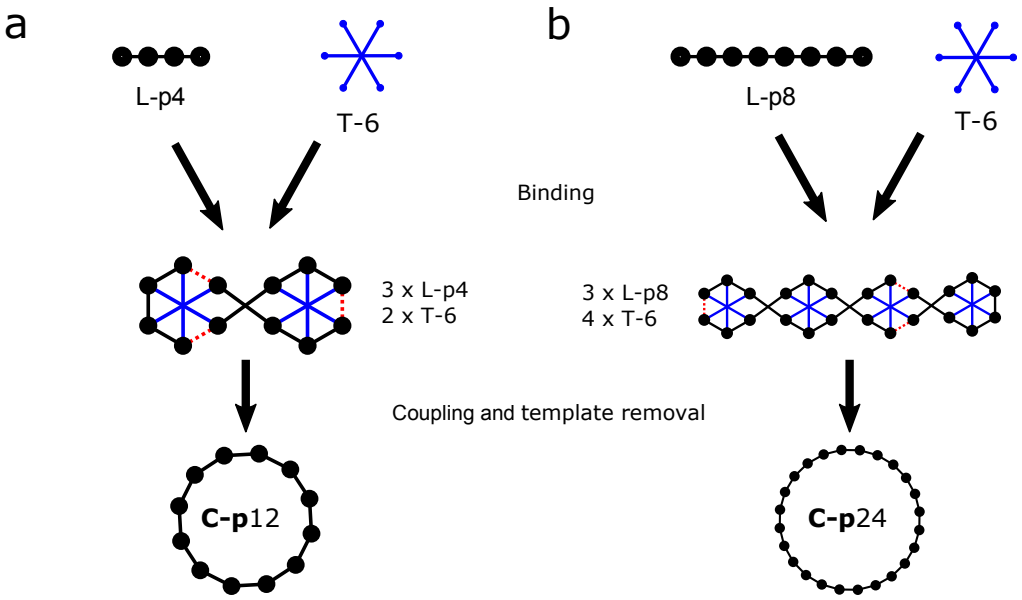

Figure 4.8: Schematic for Vernier synthesis of both c-P12 and c-P24 porphyrin nanorings from linear l-P4/8 porphyrin oligomers. In both cases a T-6 template ligand is used to form the immediate complex before the ends of the l-PN chains are coupled at the positions indicated by the dotted red lines. The template is finally removed leaving the final nanoring structure.

a high accelerating voltage into successively pumped chambers where the solvent evaporates, leaving a stream of molecules [147]. The molecules finally enter the UHV environment where they are deposited onto a clean Au(111) surface. A schematic of the ESD technique is shown in Fig 4.9.

ESD has been used to deposit various species onto surfaces and subsequently studied by SPM techniques such as nanotubes [148], dye complexes [149] and porphyrins [139, 150, 151, 152, 146]. STM images of the electrosprayed nanorings reveal that the rings adopt various configurations on the Au(111) surface and in some cases are highly distorted from a circular shape [145, 150, 151]. It is clear from Fig 4.10b that the larger c-P24 rings clearly show a higher ellipticity than the c-P12 rings.

The rings are also found to stack to form structures of two, three and four nanorings high. The relative frequency of the stacking height is control-

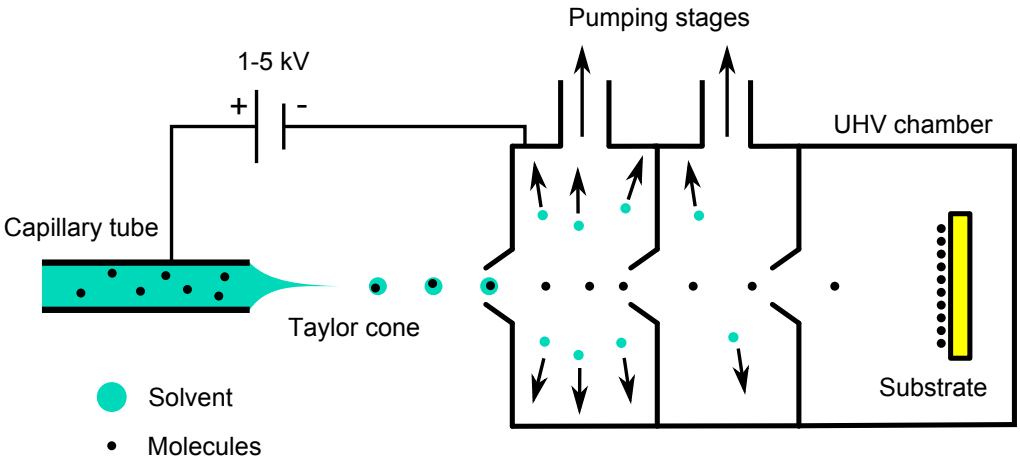

Figure 4.9: Schematic of ESD, the molecules are accelerated by an electrical field to produce a fine spray of droplets. These pass through small holes in the pumping stages where the solvent rapidly evaporates leaving a beam of molecules that deposit onto the target substrate.

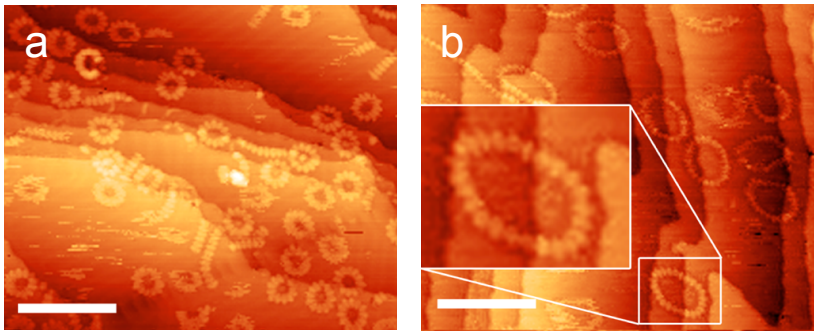

Figure 4.10: UHV STM images of ESD a) c-P12 and b) c-P24 porphyrin nanorings showing increased ellipticity for c-P24 Nanorings in b). Tunnel current, 30 pA, sample voltage, -1.8 – -2.0 V for both images. Also visible in both images are linear porphyin chains due to ether the breaking of nanorings or linear chains that have been unsuccessfully coupled during the Vernier templating synthesis. Scale bar is 20 nm in both images from [151].

lable by varying the solvent environment of the nanorings by limiting the aggregation of nanorings before deposition onto the surface [151]. Highly distorted nanorings have also been observed to occupy the centres of other rings [146]. Examples of these are shown in Fig 4.11.

This level of distortion in nanorings has obvious implications for the

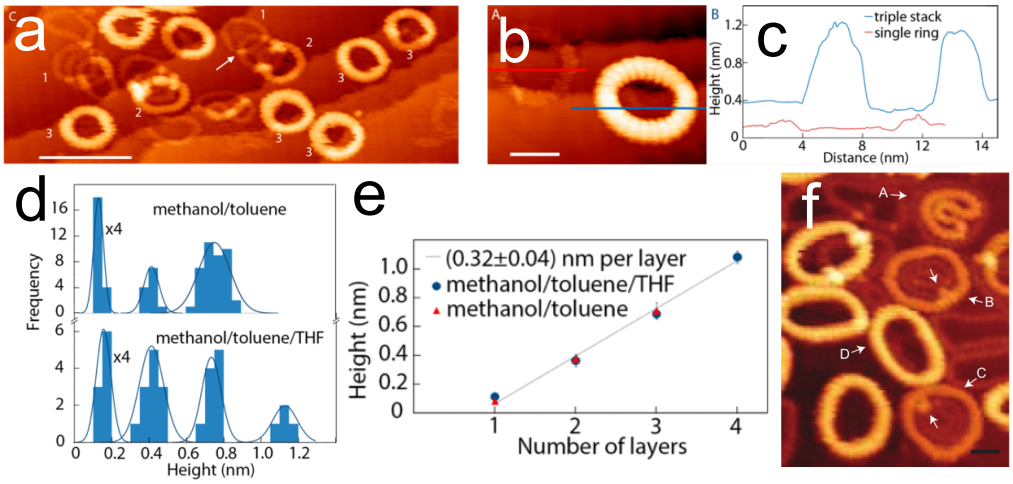

Figure 4.11: a-b) UHV STM images and, c) height profile across stacked ESD nanorings on Au(111) taken at RT. Tunnel current, 30 pA, sample voltage -1.8 V. d) Histogram of stacking height when rings are deposited from different solvent mixtures. e) Plot showing the linear relationship between the stacking height and the number of nanoring layers. f) UHV STM image of nested c-P30 nanorings deposited using ESD at RT. a-e are from [151] and f is from [146].

packing density and arrangement on surfaces and the distortion may also affect the performance of a light-harvesting device based on porphyrin nanorings. In order to quantise the distortion of nanorings as a function of ring size, the degree of distortion is measured as a distortion from circular, $\bar{\mathbf{g}}$ [151];

$$\bar{\mathbf{g}} = \frac{a}{b} - 1 \tag{4.1}$$

where a and b are the lengths of the long and short axes across an ellipse or in this case the nanoring. Since the ring is N membered rather than a continuous loop, an approximation is used. The value of $\frac{a}{b}$ used to calculate $\bar{\mathbf{g}}$ is the maximum value found around the ring i.e. the maximum measured distortion. Therefore, for a perfect circle $\bar{\mathbf{g}} = 0$ and $\bar{\mathbf{g}}$ will gradually increase with increasing distortion as shown in Fig 4.12

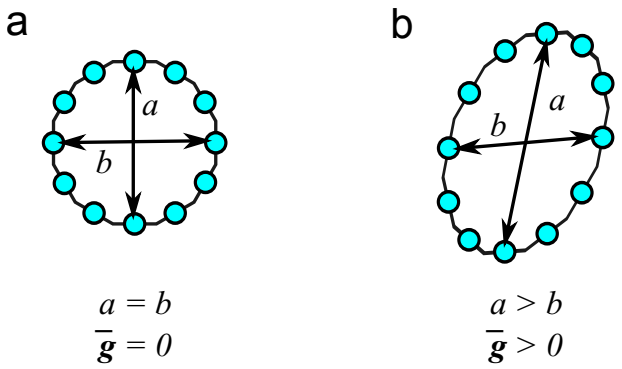

Figure 4.12: Diagram showing a model of a nanoring in, a) a circular configuration (i.e. $\bar{\mathbf{g}} = 0$) and, b) an elliptical nanoring (i.e. $\bar{\mathbf{g}} > 0$).

Stacked nanorings are observed to have a lower $\bar{\mathbf{g}}$ value than the equivalent single nanorings and implies an increase in mechanical stiffness as the stacking is increased from one to four nanorings [151]. Measurements of the rigidity as a function of the stack height show a positive linear relationship implying that the stacking 'stiffens' the structure leading to a lower ellipticity as shown in Fig 4.13b. Monte Carlo modelling of the nanoring distortion of c-P12/24 using a hard-disk and bending points model in [151] shows good agreement with the observed values of $\bar{\mathbf{g}}$ for the same stiffness value for both c-P12 and c-P24.

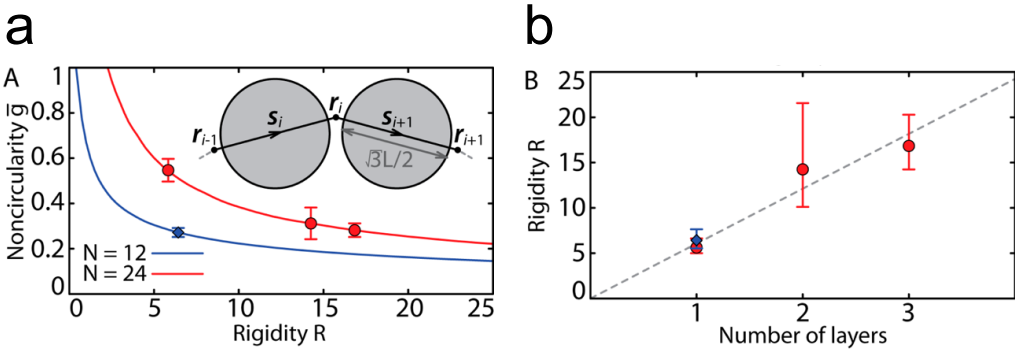

Figure 4.13: Measured distortion of porphyrin nanorings overlaid with simulation results showing how; a) distortion varies as a function of nanoring size and bending rigidity and, b) how the rigidity in measured nanoring stacks varies as a function of the number of layers. Both from [151].

Despite the volume of work on imaging isolated nanorings deposited using ESD, there have been no reported instances of large scale structure formation from porphyrin nanorings. This may be due to low mobility on the Au surface following deposition. Unpublished STM results of ESD c-P12 nanorings on HOPG in UHV conditions have shown evidence of packing behaviour. However, for reasons unknown, the c-P12 nanoring on HOPG system is extremely difficult to image repeatedly in UHV.

4.5 Self-Assembled Nanoring Networks

Studying the behaviour of nanorings deposited under ambient conditions is interesting as bottom-up self-assembly techniques such as liquid deposition will likely be required to fabricate devices from these compounds. As a result, it was decided to investigate the behaviour of nanorings deposited from solution using ambient SPM.

It was found that c-P10 and c-P12 nanorings could be easily deposited in ambient conditions from solution and reliably imaged in liquid with STM on HOPG. Discussion of results is limited to the c-P12 and c-P10 systems because these are the only nanoring sizes which have been successfully resolved repeatedly on both the sub-molecular scale with STM and AFM.

4.5.1 Experimental Techniques

Nanorings of various sizes were deposited on freshly cleaved HOPG substrates by immersion in a toluene solution (Concentration 2 μgml^{-1} in all cases) for various times at RT. After removal from the nanoring solution and rapidly drying in an N_2 stream to prevent aggregation on the surface,

the sample was mounted in an STM stage and a 10 μl drop of nonanoic acid deposited on the surface for imaging. The sample was then imaged in an ambient STM in constant current mode using tunnelling currents in the range 20-50 pA and a bias of +1-1.5 V applied to the tip. Attempts to image dried HOPG samples with the STM were unsuccessful and resulted in multiple false tip approaches and crashes. This may be due to the presence of either multi-layers or disordered deposits (such as broken chains other reaction byproducts) on top of the monolayer that are removed from the substrate surface in the liquid environment.

For AFM experiments, the same deposition steps were used as the STM experiments but with the omission of the nonanoic acid and the substrates were transferred into the AFM following nanoring deposition. hBN substrates were also used and prepared using the cleaning method outlined in section 2.17. All AFM measurements were performed in amplitude-modulated tapping (AC) mode with an Asylum Research Cypher-S AFM using Multi75Al-G AFM probes (Budget Sensors) at set points betweem 400-600 mv (free-air amplitude normalised to 1V) in ambient conditions (k = 3 (1-7) Nm^{-1}, ω_0 = 75 (60-90) kHz).

4.5.2 Results

Figure 4.14 shows STM images of the c-P12 network on HOPG. The nanorings adopt a highly-ordered hexagonally packed arrangement with ring centre-centre spacing of 6.2 $\pm$ 0.1 nm (shown in Fig 4.14b) from measurements of drift corrected STM images. Large unbroken domains of nanorings up to $\sim$1 μm are observed. Isolated nanorings are not observed in the regions between domains in contrast to the observation of isolated nanor-

ings of various sizes on Au(111) previously reported [150, 151, 152, 146]. This suggests that formation of the network stabilises the adsorption of the nanorings and the interaction with the HOPG surface in liquid conditions is significantly weaker than the gold surface.

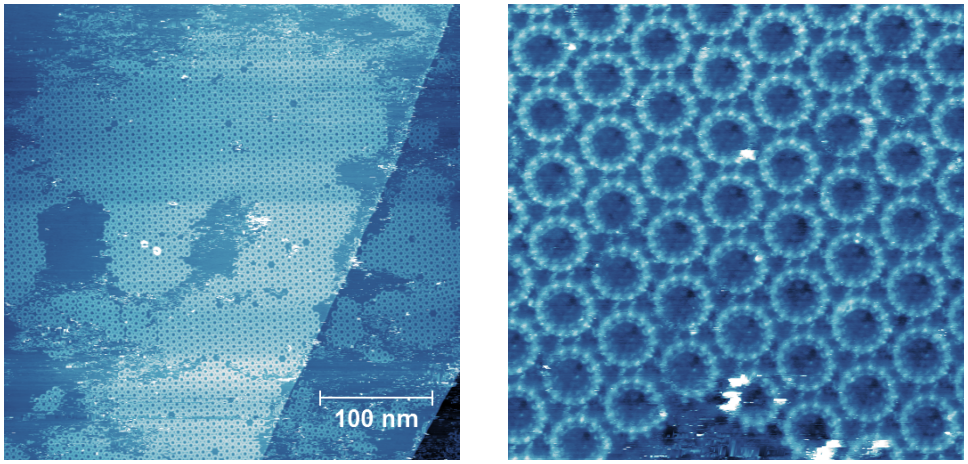

(a) (b)

Figure 4.14: Ambient STM images of c-P12 porphyrin nanorings on HOPG in liquid conditions showing; a) large-scale hexagonal packing of nanoring networks and b) drift corrected arrangement of porphyrin macrocycles in the network with a periodicity of 6.2 nm. Tunnel current, 50 pA, tip bias, 1 V.

Figure 4.15 shows the apparent height of both a monolayer, (a) and stacked nanorings, (b). The monolayer thickness was measured to be 0.4 nm and the stacked rings are an additional 1nm on top of the monolayer. The height of the stacked nanorings is indicative of a triple nanoring layer on top of the monolayer from measurements of the heights observed in UHV [151]. Stacking was rarely observed in these experiments unlike those reported on Au(111) in which double, triple and quadruple stacks of nanorings have also been observed [151].

Increasing the tunneling current and decreasing the tip bias reveals the HOPG lattice orientation relative to the nanoring network and shows that

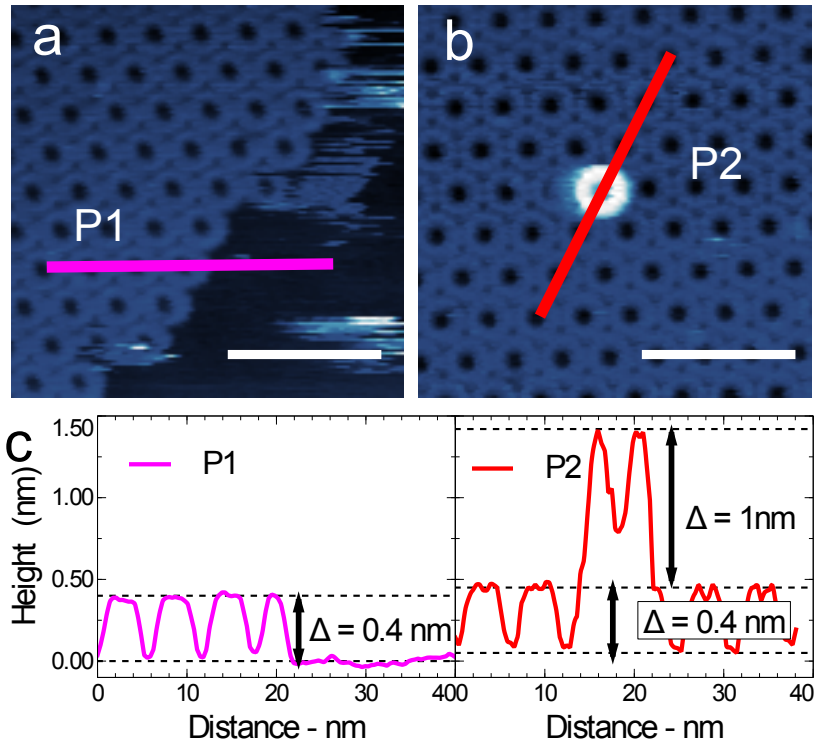

Figure 4.15: a-b) Ambient STM images with, b) apparent height measurements of c-P12 nanorings showing, a) single layer c-P12 and b) stacking behaviour. Tunnel current, 50 pA, tip bias, 1 V. Scale bars in both images are 50 nm.

the two are aligned as shown in Fig 4.16. This preferential alignment with the substrate is also supported by larger scale images such as Fig 4.14a that show several isolated c-P12 domains that are in the same orientation despite being on separate HOPG terrace steps indicating a favorable lateral orientation relative to the substrate.

At high magnification, the intramolecular structure of the nanorings is resolved. The 12 bright features around the circular perimeter of the nanorings correspond to the component porphyrin macrocycles. The rotational arrangement of the porphyrin rings is shown clearly in Figs 4.14b, 4.16a and 4.17a. A hexagonally closed-packed array would be expected to maximise the isotropic inter-ring van der Waals interactions and as the

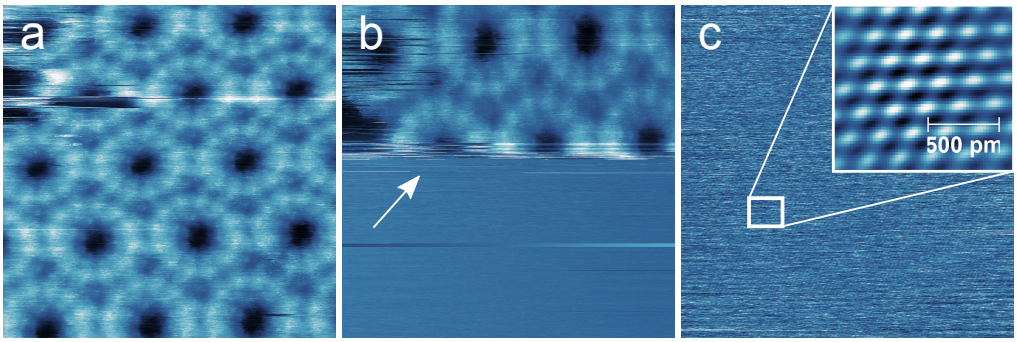

Figure 4.16: Sequential STM images of c-P12 nanorings on HOPG in ambient conditions in nonanoic acid showing; a) up scan at a tip bias of 1 V, tunnel current, 50 pA; b) down scan showing reduction of tip bias to 0.1 V and tunnel current increased to 1 nA at the scan line indicated by the arrow exposing the underlying HOPG lattice through the c-P12 monolayer. c) Up scan showing the orientation of the carbon atoms at the HOPG surface (inset) Fourier filtered image of the central region of c showing the hexagonal atomic arrangement on the HOPG surface.

STM imaging shows that the aryl chains align between the c-P12 rings and form a triangular (or equivalently, hexagonal) packing. This is shown in Fig 4.17.

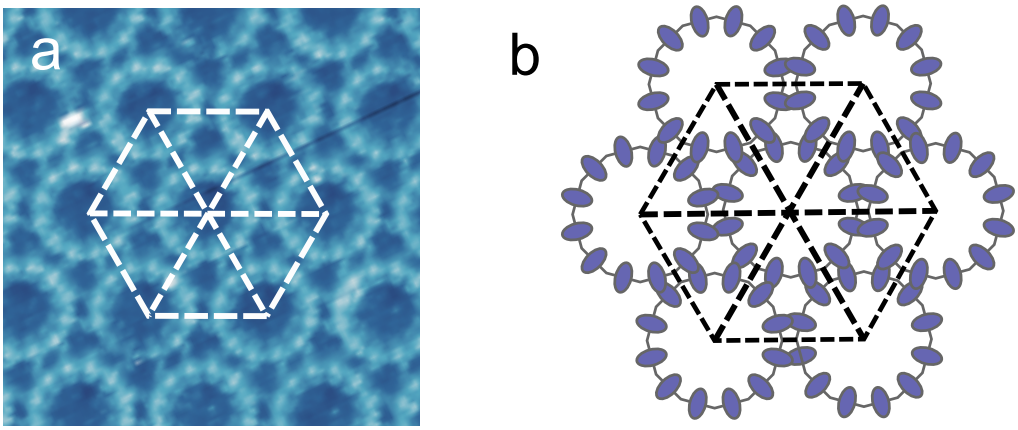

Figure 4.17: a) Ambient STM image of c-P12 nanorings on HOPG with the packing arrangement overlaid in white. Tunnel current, 50 pA, tip bias 1 V. b) Schematic showing the arrangement of the porphyrin groups in neighbouring nanorings.

AC mode AFM imaging was performed on nanorings in ambient conditions without the use of the nonanoic acid imaging solvent to remove the

dynamic effects observed in the liquid environment. This reveals that stable c-P12 domains are present on the HOPG surface with typical domain sizes of $\sim$1 μm as shown in Fig 4.18. During imaging it was found that high set points (i.e. gentle tapping of the cantilever) were necessary to image the networks as the network was easily damaged at low set points, causing voids in the network. The periodicity of the hexagonally packed network was found to be 6.2 $\pm$ 0.2 nm in good agreement with the STM data shown in Fig 4.14b.

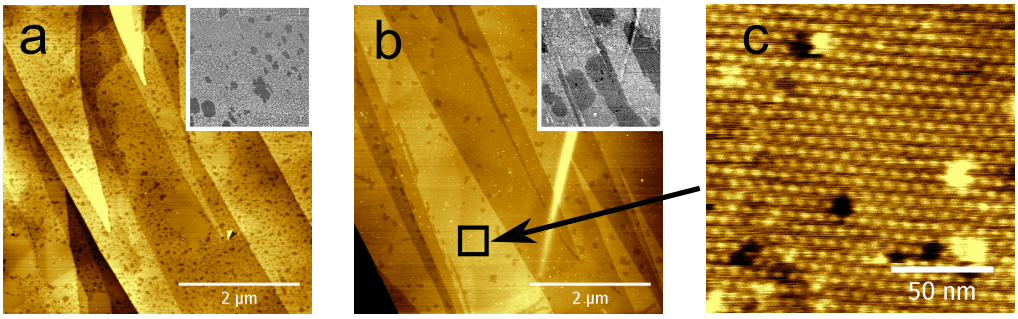

Figure 4.18: AFM image of c-P12 domains on HOPG after a) 10 minutes and b) 30 minutes of immersion in the nanoring solution. The insets to each image show the phase channel of images a and b, the dark areas correspond to highly-ordered domains when imaged in high resolution. c) High resolution image of the region indicated by the arrow in b with periodicity of 6.2 nm. All images taken in ambient conditions at RT using AC mode AFM.

In addition to HOPG, hBN is an interesting substrate to study the adsorption of light-harvesting complexes such as porphyrin nanorings since it has an identical crystal structure and low lattice mismatch ($\sim$1.8%) to HOPG. Adsorption onto hBN allows fluorescence measurements of highly-ordered porphyrin structures to be performed since hBN does not quench fluorescence like a conducting substrate such as HOPG. Recent results show that adsorption of porphyrins onto crystalline hBN surface induces a shift in the fluorescence spectrum of 5,10,15,20-tetrakis(4- car-

boxylphenyl)porphyrin (TCPP) networks relative to solution measurements or TCPP deposited on SiO_2 [6]. This is attributed to adsorbate-substrate van der Waals interactions distorting the porphyrin structure. The observation that supramolecular organisation on surfaces can change the optical properties of these molecules gives strong motivation to study the arrangement of larger porphyrin complexes such as nanorings on hBN. As a result, c-P12 rings were also deposited on a hBN surface. hBN surfaces were prepared using the methods discussed in chapter 2.17.

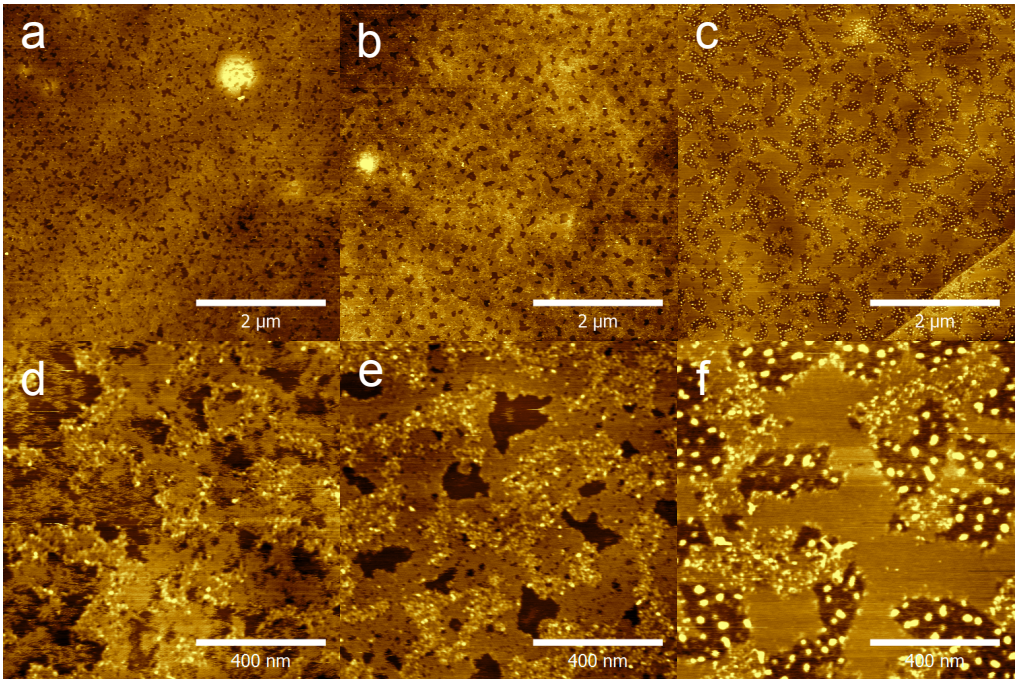

Figure 4.19: AFM images of c-P12 nanorings on hBN after different immersion times. a/d) 10 min, b/e) 30 min & c/f) 5h. All images taken in ambient conditions at RT using AC mode AFM.

Adsorption of c-P12 onto hBN was found to be slower than on HOPG. Fig 4.19 shows the c-P12 on hBN after various deposition times. The substrate needed to be immersed for a minimum of 30 minutes for high coverage of ordered domains on the hBN surface although the maximum

size of the domains appears to be limited by the co-adsorption of material in between the domains after long immersion times. This is shown in Fig 4.19c and f for c-P12 on hBN immersed in the nanoring solution for 5h.

4.5.3 Varying the Nanoring Size

The highly circular configuration of the c-P12 rings in a hexagonal network is not surprising due to the six-fold symmetry of the individual rings. This allows two macrocycles in each ring to align with each adjacent nanoring as shown by the schematic in Fig 4.17. The additional stabilisation provided by the alignment of the porphyrin pairs is only compatible with hexagonal order if the number of porphyins in each ring is a multiple of six. Using a ring with a non six-fold symmetric number of porphyrin groups would potentially be expected to result in different network configurations and even the inability to form long-range order.

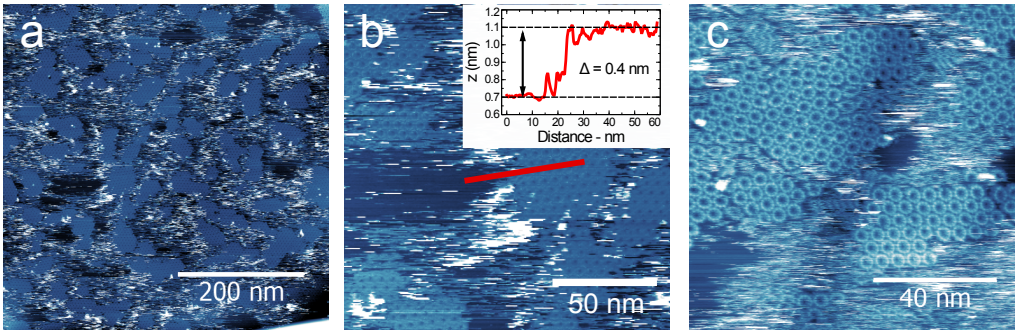

Figure 4.20: Ambient STM images of c-P10 on HOPG showing a) domain structure and b) the apparent height of a c-P10 monolayer from a line profile accross the domain edge (inset). c) Detail of a c-P10 domain. Tunnel current, 50 pA, tip bias, 1 V.

c-P10 nanorings were deposited onto HOPG followed by ambient STM imaging in nonanoic acid. Figure 4.20 shows the domain structure formed by the c-P10 nanorings. Despite the presence of what appears to be a

hexagonally packed array, the long-range order seen in the case of c-P12 is not observed and domains with maximum sizes between 50-100 nm are formed. Repeated observation of domains with these dimensions suggests that this may be an approximate upper limit on the size of the domains formed by c-P10 in this environment. Additionally, isolated nanorings are not observed in the regions in between the molecular domains consistent with the images of c-P12. This suggests that the formation of a network may stabilise adsorption of the nanorings. The c-P10 islands are also rather unstable during imaging, leading to the streaky appearance of the images in Fig 4.20. This is consistent with mobile material on the surface meaning that prolonged STM imaging is not possible as the c-P10 networks will gradually disperse. Molecular resolution was often lost after several scans making imaging of the c-P10 system difficult.

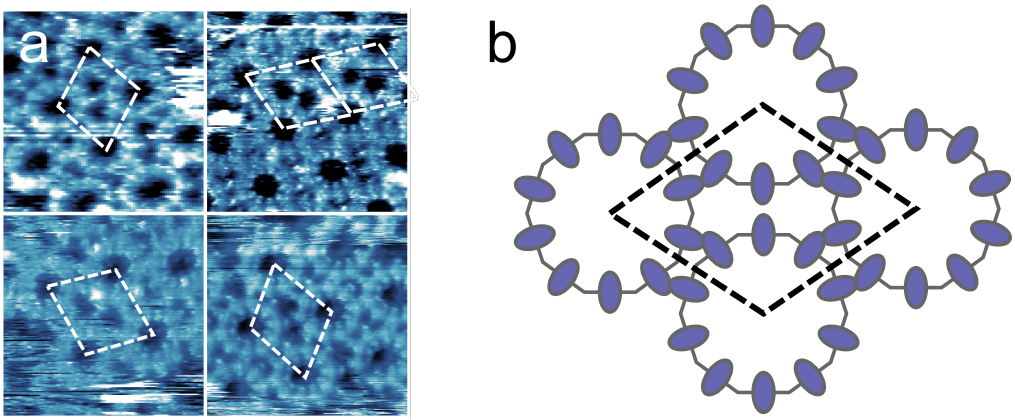

Figure 4.21: a) Ambient STM images of rhombic structure formed by c-P10 nanorings on HOPG. Tunnel current, 50 pA, tip bias, 1 V. b) Schematic of the rhombic structure showing the rotational position of the porphyrin macrocycles relative to each other from STM observations.

High resolution imaging of the individual nanorings in the c-P10 network rings reveal that in some regions, a rhombic structure is formed by the arrangement of the side group chains as shown in Fig 4.21. The measured

periodicity from multiple images is approximately 5.5 nm and the apparent STM height of the monolayer is 0.4 nm in agreement with c-P12 on HOPG indicating that the c-P10 network is also monolayer.

Within the individual c-P10 domains, elliptical nanorings were observed in high resolution images in contrast with c-P12 in which all rings were always observed to be highly circular. Figure 4.22 shows an example STM image of two neighbouring c-P10 sub-domains with ellipticities in different directions. The observation of two different orientations in the same image rules out the possibility of a drift induced distortion as linear thermal drift would be expected to induce a unidirectional distortion across all rings in the image.

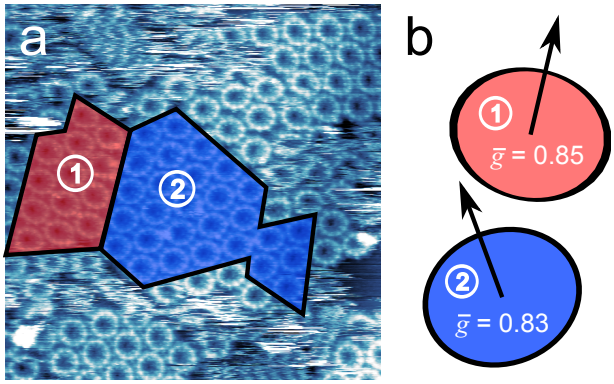

Figure 4.22: a) Ambient STM image of two neighbouring c-P10 domains with differing orientations. Tunnel current, 50 pA, tip bias, 1 V. b) Average $\bar{\mathbf{g}}$ values for the two regions highlighted in image a with a vector indicating the average direction of the 'flat' side of the nanorings in each domain.

However, due to the combination of drift and changes in the domain structure between sequential images, this also means that the precise value of $\bar{\mathbf{g}}$ for each sub-domain can only be measured with significant error.

The observation of a smaller nanoring with a greater ellipticity than the c-P12 ring is surprising due to the increased distortion for larger nanoring sizes predicted by the simulation results in section 4.6.3 and confirmed by

STM observations of isolated nanorings [151, 146]. It is suggested that the rotational alignment of the monomers in c-P12 domains may act to stabilise the c-P12 rings into a circular configuration which facilitates the formation of long-range order and as a result, large domain sizes are observed. However, this is not the case for the c-P10 rings and, as a result, smaller domains are formed by c-P10 nanorings.

AFM imaging of c-P10 on HOPG was also found to support the STM observations of an upper limit of ∼50-100 nm domain size when compared to c-P12 as shown in Fig 4.23. The periodicity of the molecules within the domains was measured to be approximately 5.5 nm in agreement with the STM results in liquid on HOPG.

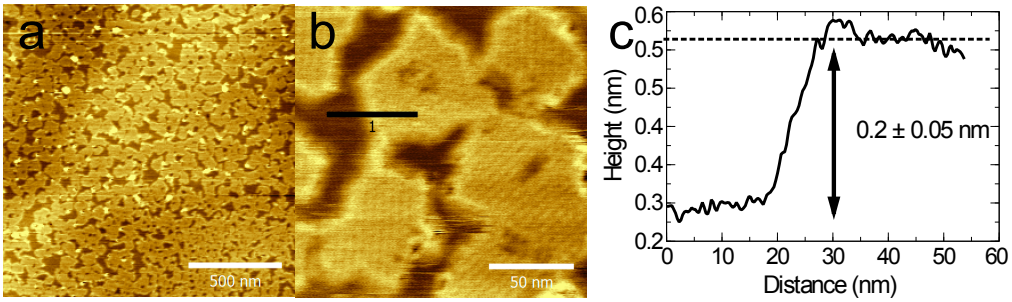

Figure 4.23: Ambient AC mode AFM images of c-P10 on HOPG after 30 mins of immersion in the nanoring solution showing; a-b) the domain structure at different scales and c) height profile across the black line in image b.

Attempts to deposit c-P10 onto the hBN surface and achieve molecular resolution to investigate the domain structure have, at the time of writing, been unsuccessful. Further investigation by varying the deposition time and the concentration of the c-P10 solution may allow formation of a similar structure to that observed on HOPG. However, the observation of similar structures on both hBN and HOPG surfaces implies that the non six-fold rotational symmetry of the c-P10 rings plays a significant part in the

domain structure formed by the nanorings.

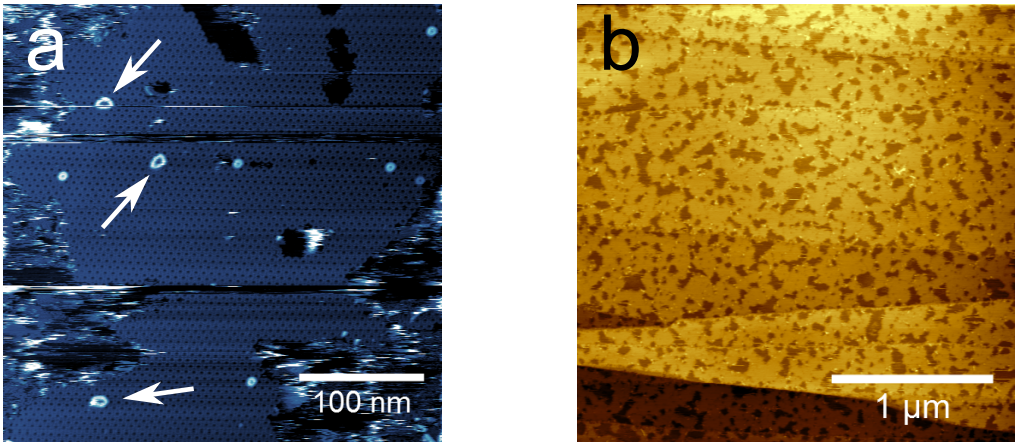

Figure 4.24: a) Ambient STM image of c-P24 co-deposited with c-P12 nanorings on HOPG showing several c-P24 nanorings (indicated by the arrows) on top of an underlying c-P12 monolayer. Tunnel current, 50 pA, tip bias, 1 V. b) Ambient AC mode AFM image of c-P8 nanorings on HOPG.

Other sizes of nanoring have been investigated. Images of c-P8 and c-P24 are shown in Fig 4.24. It was not possible to deposit and image c-P24 onto HOPG and image using STM. However, by depositing c-P12 and c-P24 using a 1:1 (by volume) mixture of of c-P12 and c-P24 in toluene solutions gave some success. Several c-P24 nanorings on top of the underlying c-P12 monolayer were resolved using liquid STM. This is shown by the arrows in Fig 4.24a.

Attempts to resolve the intramolecular structure of c-P8 using STM have not been successful as the c-P8 system is not stable to imaging in liquid conditions. Despite this, the large-scale network structure of the rings has been imaged using AFM as shown in Fig 4.24b. Sub-molecular resolution of c-P8 has not yet been achieved and will require further work.

4.6 Modelling Nanoring Distortion

Recent spectroscopic investigations over a wider range of nanoring sizes than previously studied in solution has shown that there are significant differences in the electron delocalisation and polarisation anisotropy due to temperature or size dependent distortions of the nanoring structure [15, 16]. These spectroscopic results provide strong motivation to investigate the nanoring model over a wide range of ring sizes. In this section, a simple model of the temperature and size-dependent distortion in the nanorings has been implemented and the results compared with optical experiments performed by collaborators in Oxford. This has been achieved by adopting the model used in [151] and optimising the simulation to consider a wider parameter space by using a low-level compiled programming language. The full findings of this work are presented in [15].

4.6.1 Nanoring Model

In the model proposed by Svatek et al. [151] a nanoring is modeled as a continuous ring of hard-discs (i.e. overlaps incur an infinite energy penalty) connected by elastic bonds, the mid-points of which may bend. A schematic of this model is shown in Fig 4.25.

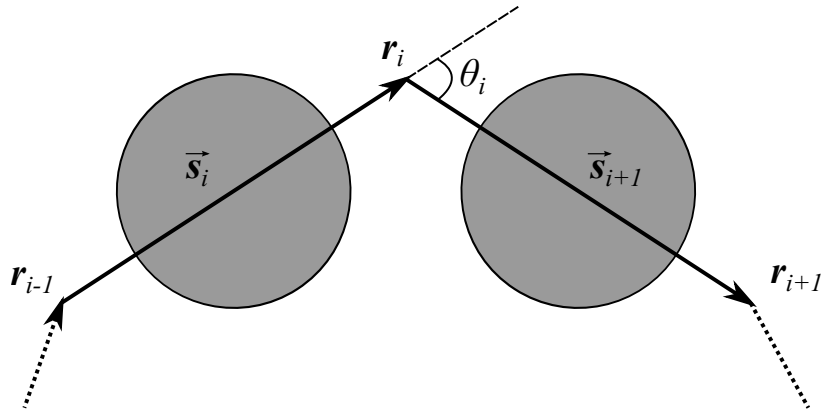

Figure 4.25: Model used in nanoring Monte Carlo simulations showing the bending ($\mathbf{r}_n$) and vector ($\vec{\mathbf{s}}_n$) positions. Macrocycle positions are calculated as being halfway between the $\mathbf{r}_n$ points.

Since the expression for the bending energy of a complete nanoring is a discretised analogue of the elastic bending energy of a continuous closed loop;

$$U_B = \frac{K_B}{2} \oint C^2(s) ds \tag{4.2}$$

where, $C(s)$ is the local curvature, s is the loop coordinate, and K_B is th bending rigidity. For the case of a discrete c-PN nanorings, the total bending energy equation can be rewritten as a series of N bending points, labelled by index i at positions $\mathbf{r_i}$. Vectors connecting these points, $\vec{s}_i = \mathbf{r_i} - \mathbf{r_{i-1}}$ are subject to periodic boundary conditions around the ring. These are shown in Fig 4.25. Therefore the contribution to the total bending energy around the ring in this discrete model can be re-written in the following form;

$$U_B = \frac{K_B}{2} \sum_{i=1}^{N} C_i^2 \Delta \vec{s}_i \tag{4.3}$$

Where C_i is the local curvature due to the bending of an angle θ_i at the i^{th} bending position as shown in Fig 4.25. The contribution from stretching of the bonds is;

$$U_S = \frac{K_S}{2}\sum_{i=1}^{N}(L - |\vec{s}_i|)^2 \tag{4.4}$$

Where L is the ground state length in between two adjacent bending positions.

Therefore the total energy due to both bending and stretching is;

$$U_{total} = \frac{K_B}{2}\sum_{i=1}^{N} C_i^2 \Delta\vec{s}_i + \frac{K_S}{2}\sum_{i=1}^{N}(L - |\vec{s}_i|)^2 \tag{4.5}$$

$$\Rightarrow U_{tot} = \frac{K_B}{2L}\sum_{i=1}^{N} LC_i^2 \Delta\vec{s}_i + \frac{K_S L^2}{2}\sum_{i=1}^{N}(1 - \frac{|\vec{s}_i|}{L})^2 \tag{4.6}$$

The prefactors can be expressed as characteristic bending and stretching energies, $\epsilon_B = \dfrac{K_B}{L}$ and $\epsilon_S = \dfrac{K_S L^2}{2}$. By defining length relative to the equilibrium bend separation (i.e. setting $L = 1$), the energy equation can be re-written;

$$\Rightarrow U_{tot} = \epsilon_B \sum_{i=1}^{N} C_i^2 \frac{\Delta\vec{s}_i}{2} + \epsilon_S \sum_{i=1}^{N}(1 - |\vec{s}_i|)^2 \tag{4.7}$$

In order to convert this into a computable model, the energy equations for the ring must be re-written in terms of the vectors and bend positions. The total energy of the system can be written entirely in terms of the $\vec{s}$ vectors

between each bending position (see appendix section 8.1) i.e.;

$$U_{tot} = \underbrace{\epsilon_B \sum_{i=1}^{N} \frac{\left(1 - \left(\frac{\vec{s}_i \cdot \vec{s}_{i+1}}{|\vec{s}_i||\vec{s}_{i+1}|}\right)^2\right)(|\vec{s}_i| + |\vec{s}_{i+1}|)}{|\vec{s}_i + \vec{s}_{i+1}|^2}}_{\text{Energy due to bond bending}} + \underbrace{\epsilon_S \sum_{i=1}^{N} (1 - |\vec{s}_i|)^2}_{\text{Energy due to bond stretching}} \tag{4.8}$$

In order to ensure that the nanoring conformations that are probed are dominated by bending rather than the stretching of bonds; a value of $K_S \gg 2K_B$ is used. To prevent the overlapping of neighbouring and distant porphyrin groups, bending limitations are introduced by placing hard discs of diameter $\frac{\sqrt{3}}{2}$ at the midpoints between bending positions. This has the effect of limiting bending to 60° by placing an infinite energy penalty for potential positions exceeding this limit in agreement with maximum bending values observed experimentally for single nanorings [151].

As a result of the distortion being dominated by bending rather than stretching. The bending, ϵ_B, and thermal, k_bT, energies are the only energy scales. This means that the ratio between the two defines a dimensionless bending rigidity, $R = \frac{\epsilon_B}{k_bT}$, the sole parameter controlling the energetics of the model.

4.6.2 Monte Carlo Algorithm

To find the equilibrium configurations of the nanorings, a Monte Carlo algorithm is used as described below.

1. Firstly a random position, i, on the ring between 0 and N is chosen.

2. The bond position is then moved in a randomly chosen direction (up,

down, left or right) by an amount P on a square grid.

3. The energy change of the potential move is then calculated and accepted according to a Metropolis algorithm [153]. If the move is not accepted then the bond position is moved back and a new position chosen.

4. The process is then repeated $N_{MCS} = 1 \times 10^6$ times.

5. The average distortion is extracted from the mean of the last 100 Monte Carlo steps.

6. The simulation is run 100 times to calculate the mean value of $\mathbf{g}$ and it's standard deviation at each value of ϵ_B and N.

The algorithm above was programmed in the C programming language, compiled using the GCC [154] compiler and run on a quad-core i7 processor running 64-bit Ubuntu linux. The use of a CPU clock random number generator requires that the code is re-compiled for each run of the code to ensure that the pseudo-random number generator is seeded with a different starting integer[1]. The results were processed and data plots produced using Python 2.7 and Matlab software packages.

4.6.3 Results

Figure 4.26 shows the values of $\bar{\mathbf{g}}$ for $N = 4 \rightarrow 32$ and $R = 0 \rightarrow 30$. For all simulations $\epsilon_s = 10\epsilon_B$.

Correlating the $\bar{\mathbf{g}}$ values measured in [151] with these simulation results shows that using a value of $R = 6$ reproduces the nanoring configurations

[1]The source code for this simulation can be found at the following github repository: www.github.com/Scummerfield/Nanoringsim.git

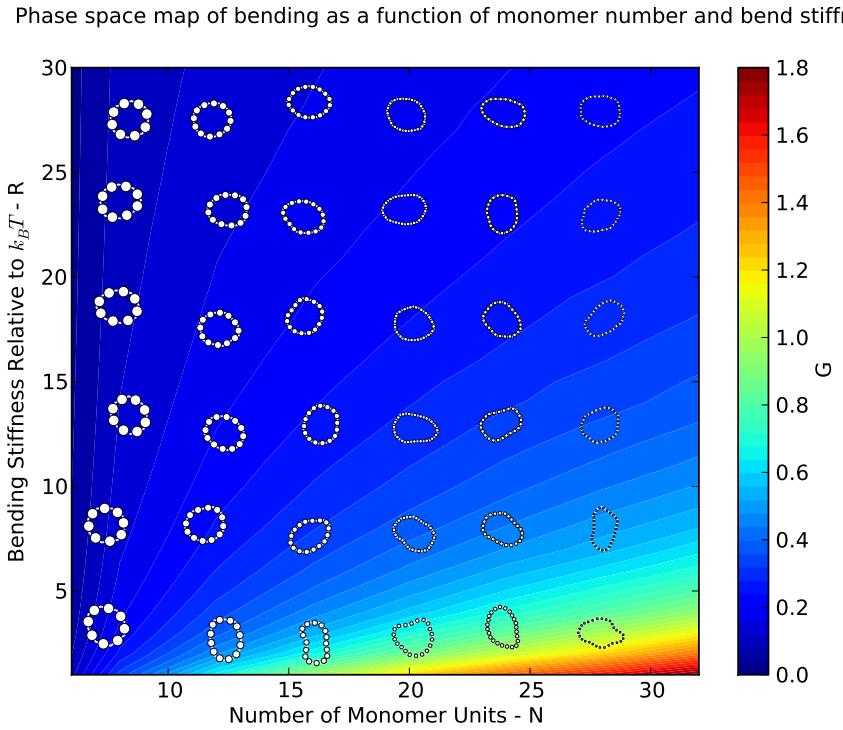

Figure 4.26: Interpolated phase map of average ring distortions as a function of dimensionless bending stiffnesses, R, and number of porphyrin units, N. Random snapshots of nanorings during the simulation are overlaid onto the phase map at their appropriate R and N Values.

for c-P12 and c-P24 on Au(111) in UHV at RT (290 K). Applying this to the data in Fig 4.26 gives the rigidity as a function of temperature from the relation $R = 6 \times (290/T)$ and is shown in Fig 4.27.

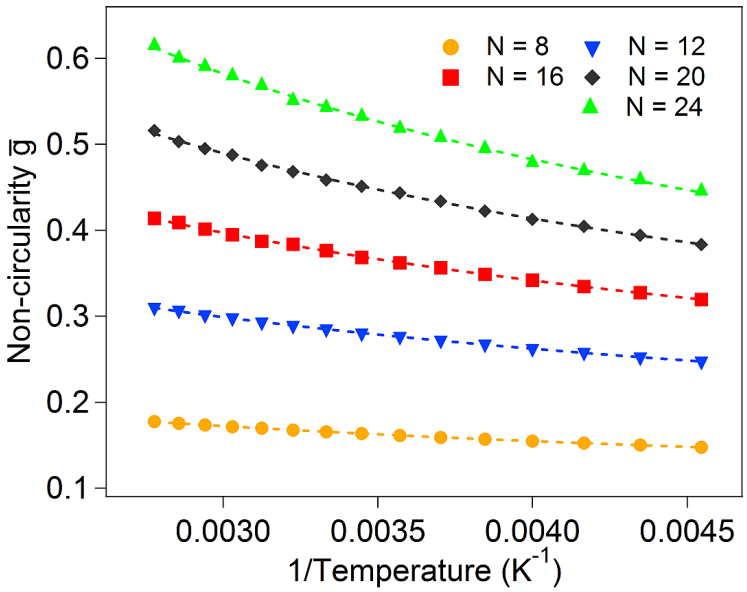

Figure 4.27: Nanoring simulation results as a function of inverse temperature.

From the data shown in Figs 4.26 and 4.27 it can be seen that for a given ring size, increasing the temperature increases the average distortion from circularity of a nanoring. Also for a given temperature, increasing the ring size also drastically increases the $\bar{\mathbf{g}}$ value at a fixed temperature.

4.7 Distortion and Delocalisation

The size-dependent distortion shown in section 4.6.3 has significant implications for the light-harvesting properties of nanorings. Optical measurements of nanorings in solution were performed by Yong et al as part of a collaboration between Nottingham and Oxford on a range of nanoring sizes consisting of 6-24 macrocycles [15]. Included were measurements of linear oligomer chains and small nanorings with the template molecule still at the centre of the ring (non-vernier templated c-P6 and c-P8) in order to limit

distortion of the nanorings (i.e. a T-N template is used to form a c-PN nanoring giving the c-PN.T-N complex such as the c-P12.T-12 structure in Fig 4.7b). For a full explanation of the spectroscopic techniques the reader is referred to the full text of [15] and more recent work on larger nanoring sizes and modelling of the excitation of both linear porphyrin oligomers and nanorings [16].

Excitation of a molecule such as a porphyrin nanoring may be understood using the Kasha model [155, 156]. Changing the geometry of a porphyin chain from linear to cyclic imposes symmetry-related constraints on the electronic transitions which may be understood qualitatively in terms of a simple exciton model shown in Fig 4.28 [14].

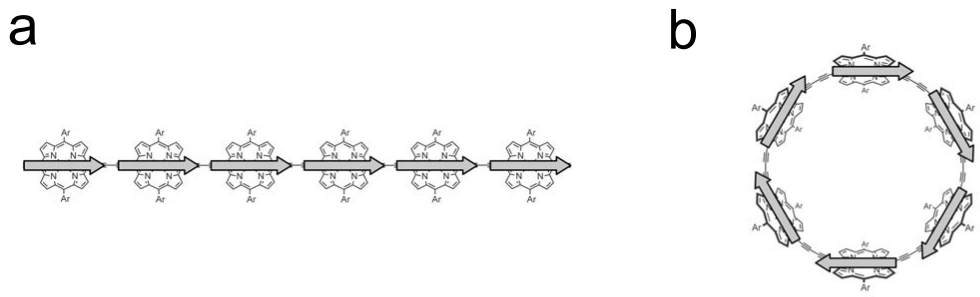

Figure 4.28: Diagram of polarisation in a) a linear porphyrin oligomer and b) a porphyrin nanoring. From [14].

In this model, the porphyrin compound can be thought of as a sequence of small dipoles attributed to each porphyrin sub-unit that may be excited, the net polarisaiton of the whole molecule being the sum of all the individual sub-unit polarisations. For the case of a linear chain, there is a net polarisation along the chain as shown in Fig 4.28a. However, for a perfectly symmetric nanoring the net polarisation is zero since all the dipoles aroung the ring cancel out. If the symmetry in the ring is broken due to

distortions of the ring structure as a result of thermally induced distortion or an increase in ring size then a net polarisation may be present in an excited nanoring.

Ultra-fast time-resolved PL anisotropy measurements were used to probe the dynamics of delocalisation following excitation of nanorings in solution when compared with the linear counterparts. By exciting the porphyrin compounds with a polarised pulsed laser and then detecting at a polarisation either a parallel or perpendicular to the excitation pulse the degree of anisotropy, γ, can be determined. γ is given by the following relation;

$$\gamma = \frac{I_{para} - I_{perp}}{I_{para} + 2I_{perp}} \tag{4.9}$$

Where I_{para} and I_{perp} are the intensity components of the parallel and perpendicular polarisation relative to the excitation pulse respectively. Typical values of γ for short linear chains are around $\gamma = 0.4$ which is indicative of a dipole that does not re-orient following excitation. For a molecule with a high 2D rotational symmetry such as a nanoring, the value is around $\gamma = 0.1$ [16]. As a result of molecular re-orientation in solution, the value of γ falls rapidly over time, meaning that time-dependant measurements are typically restricted to times less than several hundred ps after excitation [157, 15, 16]. Figure 4.29 shows how γ, the radiative rate and modeled values of $\bar{\mathbf{g}}$ vary for different sized nanorings and linear oligomers at 290 K.

Figure 4.29a shows the PL anisotropy for both linear and cyclic chains as a function of size for the first few hundred fs after excitation. The observation of a constantly low PL value for the nanorings suggests that there

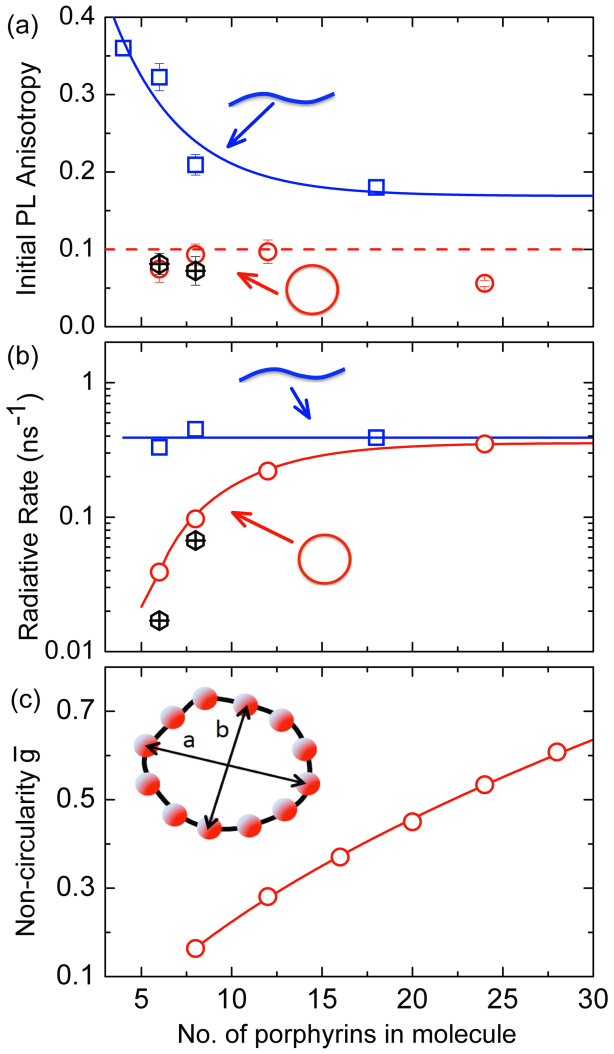

Figure 4.29: a) Initial anisotropy as a function of the number of porphyrins for free nanorings (red circles), template bound nanorings (black crossed hexagons) and linear oligomers (blue squares). b) Radiative rate as a function of the number of porphyrin units. c) Average distortion, $\bar{\mathbf{g}}$ as a function of ring size at a simulated temperature of 290 K from Monte Carlo modelling in section 4.6.3. Figure from [15].

is a polarisation memory loss which Yong attributes to either adsorption into a fully delocalised state around the ring or a more localised state that rapidly moves around the ring. However, it is not possible to distinguish between the two explanations using this technique [16]. The linear chains show significantly higher values of γ when compared with the nanorings,

and show a decrease in γ for longer chain lengths.

Figure 4.29b shows that the radiative rate from the nanorings increases substantially by almost two orders of magnitude from the c-P6 ring to the c-P24. The observation of a low radiative rate for smaller rings is interpreted to be similar to small, highly-symmetric, ring molecules such as benzene. However, for larger rings the increase in distortion, (shown by the Monte Carlo model results in Fig 4.29c) lifts the symmetry constraint and the radiative rate is increased. Measurements of the template bound nanorings c-P6.T-6 and c-P8.T-8 (see the black crossed circles in Fig 4.29b) show a reduced radiative rate relative to their free nanoring counterparts as would be expected for a system in which the distortion is limited by the rigidity the presence of the template causes.

These results suggest that for all nanorings the exciton wave packet is thought to be delocalised around the entire ring due to the rate at which the nanoring is observed to depolarise following excitation. For small nanorings, the high symmetry (increased by the presence of a template molecules in the c-PN.T-N complexes which reduce distortion in the molecules) means that the rate of re-radiation from the rings is suppressed. Increasing the ring size allows increased distortion which in turn increases the radiative rate. Whilst a direct quantitative link between the values of $\bar{\mathbf{g}}$ calculated in section 4.6.3 and the spectroscopic measurements is beyond the scope of the work presented in [15], the correlation between these results implies that the distortions of large nanorings have significant effects on their optical properties.

4.8 Optical Measurements on hBN

The results in section 4.5.2 show that the nanorings can be readily adsorbed onto the hBN surface. As a result it is possible to measure fluorescence of nanoring monolayers since the hBN surface will not quench fluorescence unlike Au or HOPG substrates [6]. This, in combination with the ring size dependant optical effects reported by Yong and Parkinson [15, 16] provide strong motivation to study the optical properties of nanorings on surfaces. The following are early results of surface adsorbed nanorings.

Steady state PL measurements were performed on c-P12 rings deposited onto hBN on SiO_2 substrates. Nanorings were deposited onto hBN by immersion in a c-P12 solution for one hour and a florescence spectrum taken using an excitation wavelength of 500 nm. In addition, time-correlated single photon counting (TCSPC) measurements were taken to measure the lifetime of the excited state using a 500 nm laser excitation followed by detection at 883 nm over a laser spot area of 640 μm^2. Steady state measurements were performed by V. Korolkov[2] and TCSPC measurements were performed by J. Gong[3] using samples prepared by the author.

Figure 4.30a shows PL results of the porphyrins on the hBN flake surface. The dashed black line shows PL for c-P12 in toluene as a reference with a dominant peak position at around 850 nm. All surface PL measurements (solid lines) were taken from the hBN flakes as measurements on the SiO_2 regions in between the flakes show no fluorescence. Shoulders are present on most of the spectra and in one case a double peak is visible. The origin of these is not currently clear and may be due to either different

[2]Beton Group, Nottingham
[3]Herz group, Oxford.

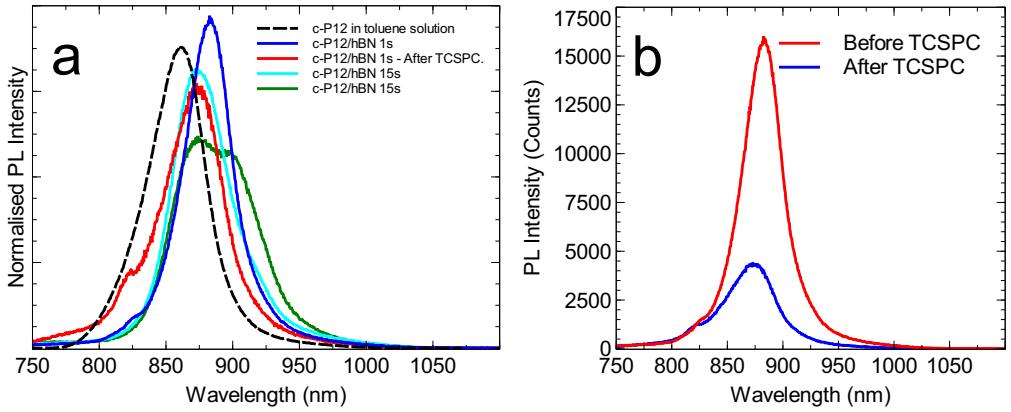

Figure 4.30: a) Normalised fluorescence measurements of c-P12 deposited on hBN shown with a reference spectra for c-P12 in a toluene solution. b) PL of a spot on the hBN flake before and after TCSPC showing strongly reduced intensity. All measurements in a are normalised to the integrated area under spectra. Data courtesy of V.Korolkov and J. Gong.

species or configurations present on the surface such as the aggregates in between or on top of the domains such as those shown in Fig 4.19e and f. Further study will be necessary to establish the cause of these shoulders.

For all measurements of c-P12 on hBN there was a red shift of ∼20-30 nm relative to the solution measurements of c-P12. This is interesting as other studies by the group at Nottingham have shown consistent red-shifting of fluorescence peaks when hydrogen bonded 2D porphyrin networks are adsorbed on hBN as discussed in section 4.5.2.

TCSPC measurements indicate that the PL lifetime on the hBN surface is significantly shorter than solution measurements (∼200 ps vs ∼792 ps in solution). A shorter PL lifetime has been previously correlated with ring size and typically the lifetime is increased for larger rings which show higher $\bar{\mathbf{g}}$ values. Stabilising nanorings by leaving the template molecule at the centre of the molecule was also found to decrease the PL lifetime in solution (see Fig 10 of the SI in [15]). SPM images in section 4.5.2 give a value of $\bar{\mathbf{g}} \approx 0$ on HOPG (it is assumed that due to the same lattice

periodicity and large network formation that the value of $\bar{\mathbf{g}}$ is the same on hBN) compared to a value of $\bar{\mathbf{g}} = 0.27 \pm 0.02$ for isolated c-P12 molecules on Au surfaces [151]. The intensity of the fluorescence peak was also found to decrease substantially after the TCSPC measurements suggesting that the laser radiation causes damage to the nanorings as shown in Fig 4.30b.

The stabilisation of nanorings due to network formation has may be responsible for this reduction in PL lifetime in the same way the effect that the template has on nanorings in solution [15]. Higher resolution AFM measurements of the intramolecular structure of the nanorings on hBN will be necessary to confirm that the $\bar{\mathbf{g}}$ value is comparable with that observed for c-P12 on HOPG. Calculation of the radiative rate for nanorings in solution also suggests that a shorter PL lifetime means the radiative rate is reduced. Given that the lifetime in the case of c-P12 on hBN is significantly shorter than in solution this may imply that the radiative rate is also significantly reduced through adsorption onto the hBN surface although further work will be needed to confirm these early results.

4.9 Summary

From the results presented in section 4.5.2, the self-assembly of c-P12 and c-P10 nanorings on HOPG and hBN surfaces shows that stable μm-scale monolayer supramolecular networks of these light-harvesting molecules are easily formed in ambient conditions. The nanoring size is found to induce significant differences in the subsequent domain size through changes in the rotational symmetry due to the number of porphyrin groups in each nanoring. Determining the structures that form when light-harvesting materials such as these are deposited on surfaces is important because mesoscopic order in large π-conjugated systems may be strongly linked to device performance [158]. This is the first reported instance of large network formation from these compounds.

The differences in long-range order observed in the domain structure of the two sizes of nanoring used in this work has yet to be fully understood beyond simple differences in rotational symmetry. The lack of strong localised intermolecular bonding in these assemblies when compared to carboxylic acid molecular networks such as those in [69] suggests that the weak van der Waals interactions play a significant role in stabilising the molecular networks. Further study of a wider range of nanoring sizes will help to clarify the relationship between nanoring size and network stability. Encouragingly, the repeatability of depositing and imaging in ambient conditions will allow for rapid investigation of the parameter space in future work when compared to the time consuming electrospray deposition and imaging steps used when working in UHV conditions.

Monte Carlo simulation results of single nanorings show that an increase in ellipticity is to be expected at higher ring sizes at room temperature.

Increasing the stiffness limits the distortion and the expected ellipticity of the nanorings. This is in agreement with STM results previously reported in the literature [151]. Comparing these simulated results with optical measurements shows that the distortion of nanorings has significant effects on their optical properties. In particular, the long lifetime of the delocalised state as a result of the high symmetry in smaller nanorings [15].

A Monte Carlo simulation of nanoring networks using the model outlined in section 4.6 and including the effects of van der Walls interations between the nanorings was considered in an attempt to understand the differences in network structure observed in this work. However, modelling the distortion, intermolecular interactions and spatial arrangement of a large number of nanorings would require considerable computational resources. This would also require a more detailed understanding of the nature of intermolecular interactions between the nanorings. The high circular symmetry observed in the c-P10/c-P12 ring networks using SPM may validate the use of a simpler model that does not consider the deformation of the individual nanorings. Results reported using the 'patchy-disk' model used by Whitelam et al. have suggested that using a ring system with a non six-fold rotational symmetry may give rise to the formation of rhombic tilings such as those formed by c-P10 in section 4.5.3 [159].

Chapter 5

Graphene Growth by High Temperature Molecular Beam Epitaxy

"Mission is Possible!"

Professor Sergei Novikov, repeatedly

2015

The characterisation of graphene grown using high temperature molecular beam epitaxy on hBN surfaces is the topic of this chapter. AFM measurements indicate that the graphene forms continuous domains of the order $\sim$10 μm making these results the first reported growth of graphene at high temperatures using molecular beam epitaxy (MBE). AFM imaging also reveals that the graphene surface has moiré patterns which have been attributed to commensurate-incommensurate transitions between the

graphene and hBN [160]. Furthermore, high resolution AFM imaging shows that the graphene and hBN lattices are aligned, providing evidence that the graphene has been epitaxially grown on the hBN surface. Extensive mapping of the moiré periodicity across the graphene domains shows significantly higher moiré period sizes than previously reported. Raman mapping and correlation with the moiré period shows that the characteristic graphene Raman peaks are split and shifted in the high periodicity regions which is indicative of strain. In addition, highly anisotropic and defective moiré patterns are also observed at breaks in the graphene domains suggestive of strain relaxation. These breaks can also be formed by modification of the surface using an AFM probe and represent a new approach to modifying strain in graphene.

5.1 Graphene

Graphene was the first isolated two-dimensional material and resulted in Andre Geim and Konstantin Novoselov being awarded the 2010 Nobel prize in physics for *"groundbreaking experiments regarding the two-dimensional material graphene"* [161]. Since the first reported isolation of graphene by Geim and Novoselov et al. [17] there has been huge interest in the study and production of graphene for a variety of uses and it has been touted repeatedly as a 'miracle' material on account of its many remarkable properties [162].

Structurally, graphene is a single layer of carbon atoms bonded in a hexagonal lattice with two atoms per unit cell. Each carbon atom is bonded to three other atoms covalently with a 1.42 Å separation. Graphene is an

sp^2 hybridised material and as a result has a delocalised plane of π electrons above and below the plane of the graphene sheet. In effect graphene can be thought of as an infinitely extending sheet of benzene molecules fused together at the positions the hydrogen atoms would occupy. A schematic representation of a graphene sheet is shown in Fig 5.1.

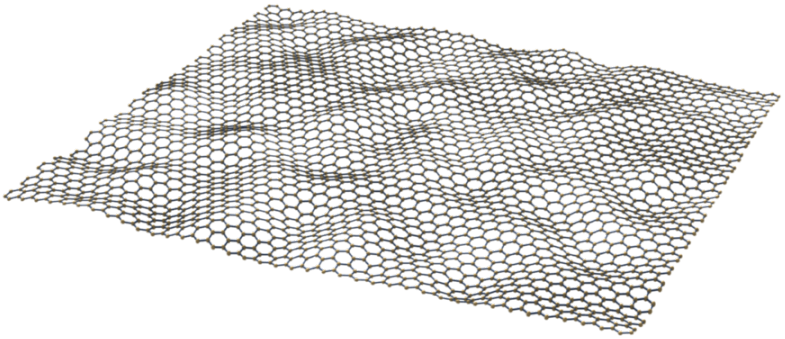

Figure 5.1: Schematic representation of an isolated graphene sheet [163].

Multiple layers of graphene can stack to form bulk graphite (see section 2.15) and it is the basic building block for several carbon nanomaterials as shown in Fig 5.2.

A single graphene sheet rolled-up forms single-walled carbon nanotubes (SWNT) (Fig 5.2a), multiple sheets of graphene rolled-up can form a multi-walled carbon nanotube (MWNT) (Fig 5.2b) and fullerenes which consist of carbon atoms arranged at the vertices of a truncated icosahedron (Fig 5.2c).

Weak van der Waals forces hold the layers in graphite together whereas the covalent in-plane σ bonds between each carbon atom holding each sheet of graphene together are extremely hard to break. This was exploited to enable the first isolation of graphene since the individual graphene sheets can be pulled apart easily using adhesive tape (see section 5.4) [17]. This

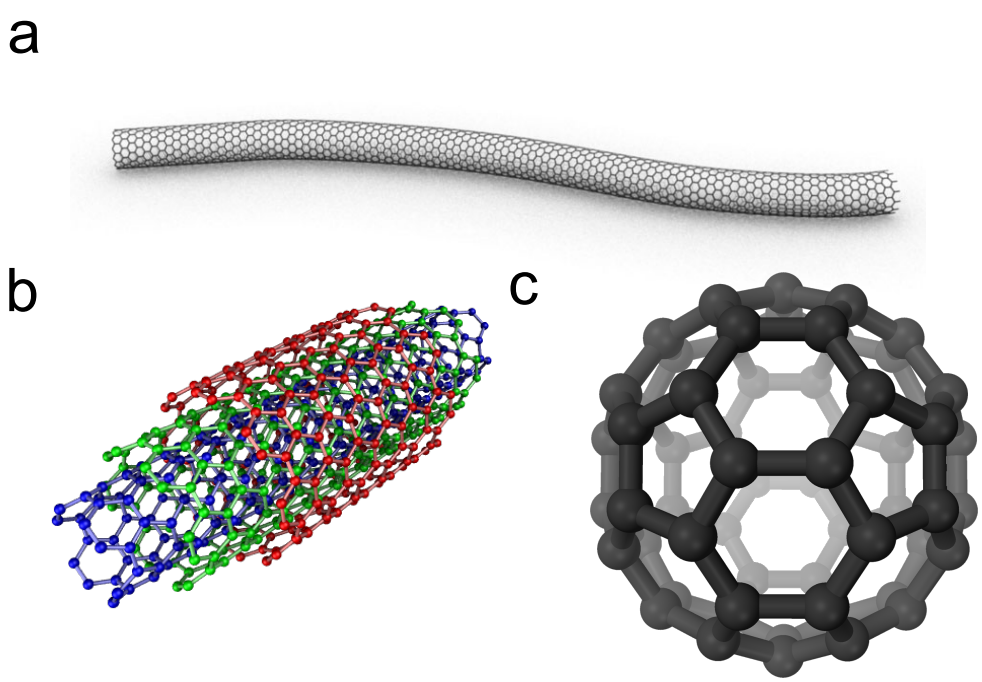

Figure 5.2: Structures of a) SWNT, b) MWNT (each colour corresponds to different SWNTs that make up the MWNT structure) and, c) a C_{60} fullerene. Images a and c are from [163] and b is from [164].

bonding structure is also responsible for many of graphene's remarkable physical properties.

5.2 Properties of Graphene

Graphene has a long list of interesting properties, both physical and electronic which have attracted intense interest from a diverse range of scientific fields. Some of these are discussed below and provide motivation for the growth of MBE graphene presented in this work, particularly with regard to electronic devices where the production of high-quality, epitaxially grown graphene is critical for the fabrication of high performance graphene devices.

The crystal lattice is hexagonal and composed of two atoms per unit

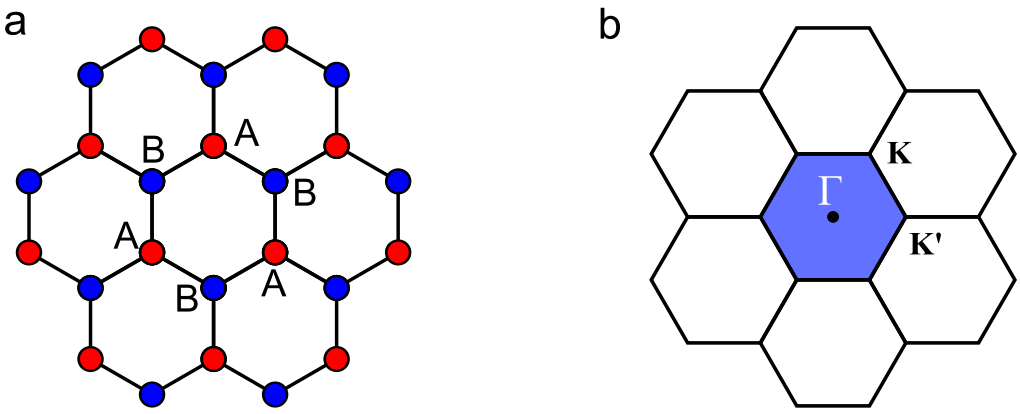

Figure 5.3: a) Real space and b) reciprocal space structures of the graphene lattice. The Brillouin zone is shown by the central blue hexagon in b.

cell, A and B as shown in Fig 5.3a. In reciprocal space the unit cell (the Brillouin zone) is also hexagonal and contains three important points as shown in Fig 5.3b; the centre, Γ, is the origin in reciprocal space (i.e. **k** = 0); The corners of the Brillouin zone (corners of blue hexagon in Fig 5.3b) correspond to two inequivalent points labeled **K** and **K**' which are associated with the A and B atoms of the unit cell.

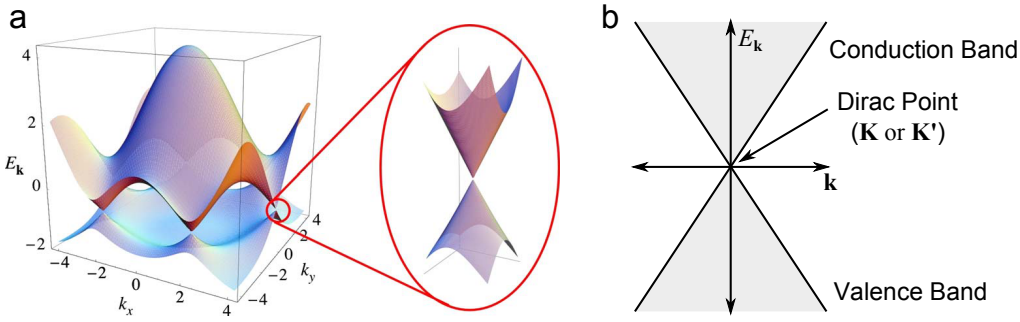

Figure 5.4: a) Band structure of graphene showing the Dirac points. From [165]. b) Position of the conduction and valence bands meeting at the Dirac point.

The electronic band structure of graphene (i.e. the allowed energies of electrons as a function of their wavevectors, **k**) was described by Wallace in the 1940s using a tight binding model [166]. The band structure of graphene is shown in Fig 5.4 and shows the valence and conduction bands.

A gap at all regions in the Brillouin zone separates the two bands except for the six **K** and **K'** points where they meet as shown in Fig 5.4a.

These positions, known as the Dirac points, correspond exactly to the Fermi energy for (undoped) graphene as shown in Fig 5.4b in one dimension and makes graphene a zero-gap semiconductor. For low values of **k** near the Dirac points, graphene has a linear dependance of $E_{\mathbf{k}}$ on **k** i.e.

$$E_{\mathbf{k}} = \pm v_F \sqrt{\mathbf{k}_x^2 + \mathbf{k}_y^2} \tag{5.1}$$

Where $v_F \simeq 10^6$ ms^{-1} is the Fermi velocity, k_x and k_y are the wavevector components in the x and y directions respectively.

Graphene is a potential successor to silicon-based electronics and as result a large amount of work has been dedicated to fabricating electronic devices from graphene. The first publication reporting an isolated monolayer graphene by Novoselov et al. demonstrated the observation of a field effect in graphene by showing that it can be gated by a doped silicon substrate [17]. A schematic of this device arrangement is shown in Fig 5.7a.

Graphene exhibits an ambipolar field effect which means that the charge carriers can be changed from electrons to holes by the application of an external electric field using a gate voltage [17]. The effect on the band structure can be seen in Fig 5.5. The conductivity would be expected to vanish at the Dirac point where the density of states (DOS) vanishes, but is not observed in practice possibly due to the presence of inhomogeneities in the graphene lattice which are either induced by the corrugation of the substrate or chemical dopants [167]. Depositing graphene onto hBN has been found to drastically improve the quality relative to early studies on SiO_2 due to the atomically smooth hBN surface [19].

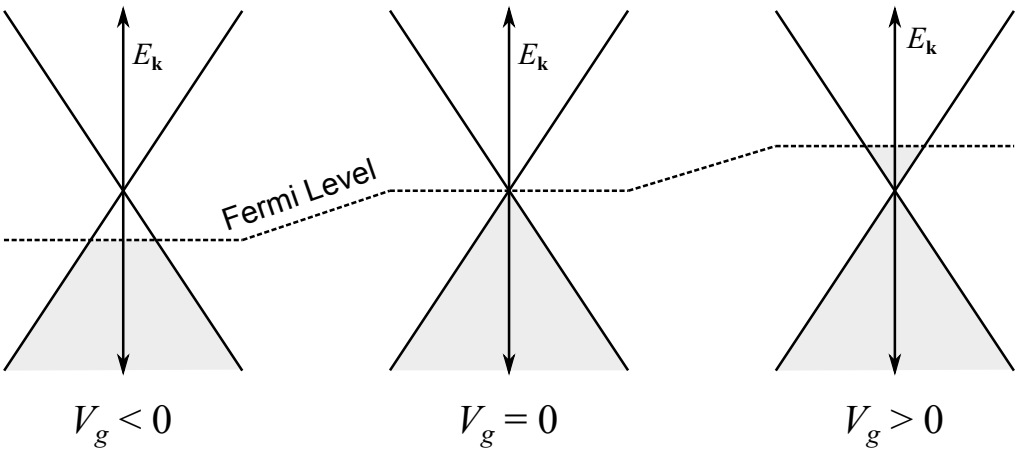

Figure 5.5: When subjected to an external electric field, the Fermi level is shifted and changes the charge carriers in graphene from holes to electrons.

These measurements have demonstrated that graphene has an exceptionally high electron mobility at room temperature with early reported values in excess of 15,000 $cm^2V^{-1}s^{-1}$ at RT on SiO_2 surfaces, and more recently up to 100,000 $cm^2V^{-1}s^{-1}$ at RT when encapsulated in hBN flakes [168]. These values are found to be weakly dependent on temperature which suggests that the values are limited by impurity scattering [167].

Another consequence of the linear band structure near the Dirac point is that electrons in graphene behave as massless Dirac fermions and propagate according to the Dirac equation instead of the Schrödinger equation [169]. In addition, graphene was found to exhibit the anomalous quantum Hall effect (the quantum mechanical version of the Hall effect in which a voltage is produced across an electrical conductor transverse to the current and a perpendicular magnetic field) at room temperature [170].

In terms of its mechanical properties, graphene is the strongest material ever measured with a Young's modulus of 1 TPa [171]. Graphene also exhibits an extremely high thermal conductivity of 3,000 WmK^{-1} [172]. Graphene absorbs $\pi\alpha \approx 2.3\%$ of visible light where α is the fine structure

constant meaning it is highly transparent [173]. Despite this, it is still possible to identify single layer graphene when deposited on a suitably prepared substrate (such as SiO_2 of a specific thickness) due to interference effects [17].

5.3 Raman Signature of Graphene

Raman microscopy is particularly useful in detecting graphene since it has characteristic spectral peaks that may be used to distinguish it from bulk graphite in a non destructive manner [174, 175]. There are three main Raman peaks typically used in the analysis of graphene and these are often used determine the presence of graphene and infer its quality and thickness. These peaks are labeled the G, D and 2D and are shown in Fig 5.6a, which shows Raman spectra from both pristine and defected graphene [176].

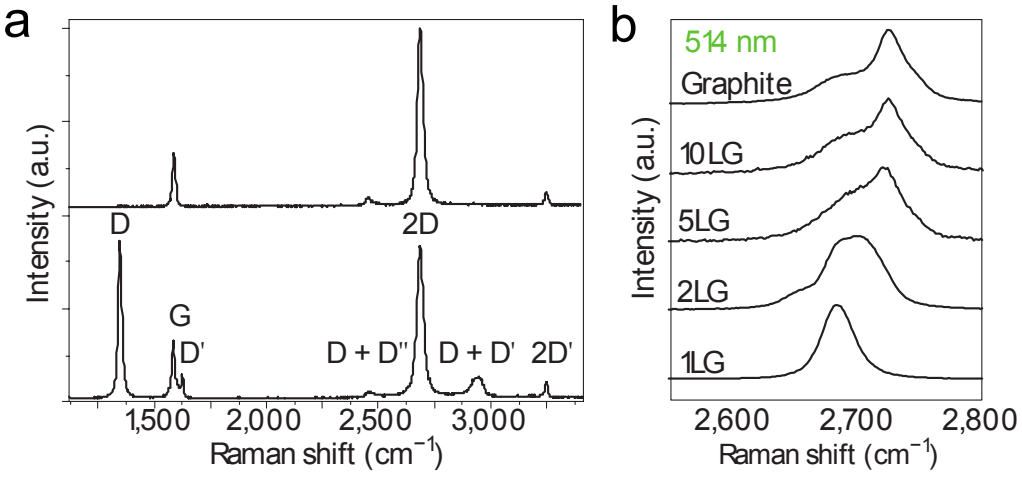

Figure 5.6: a) Raman spectrum for pristine (top) and defected (bottom) graphene b) 2D region as a function of the number of graphene layers. Both from [176].

The G peak at around 1600 cm^{-1} is present in all sp^2 carbon materials such as nanotubes and fullerenes. The D peak at 1350 cm^{-1}, however,

signifies that non-sp^2 binding is present. This can be interpreted by either the effects of the edges of graphene domains or defects in the graphene lattice and is commonly referred to as the 'defect peak'. The intensity ratio between these peaks, $\frac{I_D}{I_G}$, is commonly used as a measure of the quality of the graphene and is often reported [177]. Finally the 2D peak at 2700 cm^{-1} has been extensively used as an accurate measure of the graphene thickness on freely suspended samples [174] and various substrates such as SiO_2, Sapphire and SiC. The 2D peak broadens and and blueshifts with an increasing number of graphene layers and tends towards the shape expected for bulk graphite as shown in Fig 5.6b [176].

For the defected graphene spectra shown in Fig 5.6a several additional peaks are shown. The D' peak is attributed to double resonance of the D peak and its overtone, the 2D' peak. In addition the D + D" and the D + D' (sometimes labeled the D + G peak) are also defect associated peaks due to phonon assisted processes [176]. There also exists a low shift C peak at < 50 cm^{-1} as a result of interlayer coupling which is strongly related to the number of graphene layers. However, for single layer graphene (SLG) this peak would obviously be absent. Also the extremely low shift position requires the use of high-fidelity filters since notch filters which are commonly used would cut this peak out and are not widely available [178].

Shifts in the position of the 2D peak has also been attributed to uniaxial strain induced in graphene. By depositing graphene onto a polymer substrate and bending it uniaxially, the 2D band was found to red-shift by an amount directly proportional to the mechanical strain [179]. The strain dependant shifting of the 2D peak is particularly relevant for the results presented in section 5.6.

The Raman spectrum of graphene and few-layer graphene (FLG) have been the focus of much study since it is a rapid and non destructive way to investigate the quality and thickness of graphene layers. The nomenclature used in describing the peaks of graphene, in particular characterisation of the defect peaks often varies and has been subjected to differing identification (in some cases misidentification [176]) in the literature. Pollard et al. rightly suggest that there is a need for standardisation amongst groups, in particular for industrial applications of graphene [180]. The reader is directed to reviews by Ferrari [176], Malard [181] and Wang [175] for more comprehensive theoretical discussions of the Raman spectrum of graphene.

5.4 Graphene Production and Devices

Production of graphene in the literature has been predominantly reported using two methods. Exfoliation from bulk graphite using adhesive tape (also known as micromechanical cleaving) was used in the initial reported isolation of SLG and FLG [17]. It was discovered that growth of graphene was possible using chemical vapour deposition (CVD) of methane (and subsequently other hydrocarbon gases) on Cu/Ni films [18]. This is typically followed by a process to transfer the grown graphene film to a suitable insulating substrate such as SiO_2 for further processing into useful devices such as those shown in Fig 5.7 [182].

Fabrication of graphene devices typically requires the use of electron beam lithography (EBL) to process device structures and contacts to make electronic measurements [17, 41]. The EBL patterns used to contact the graphene structures often have highly specific geometries to account for

variation in the dimensions and irregularities in the size of the flakes used in each device rather than lithographic techniques using photomasks. The reader is directed to Figures S1 of [41] and S9 in [183] to illustrate the complexity of these EBL fabricated structures.

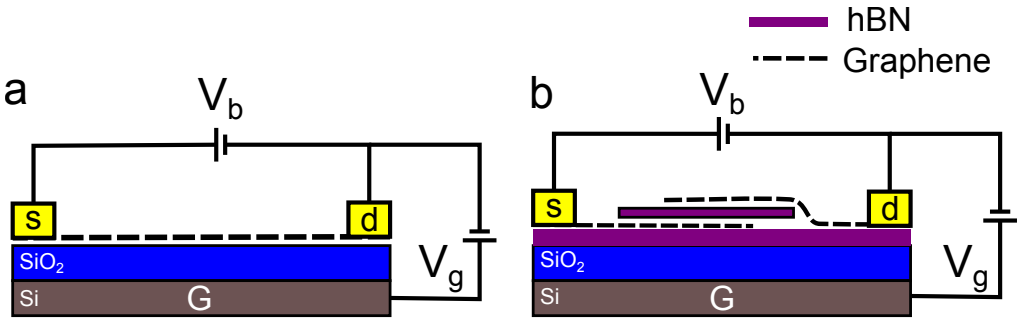

Figure 5.7: a) Graphene FET device structure used in [17]. b) Tunneling graphene FET device using a thin hBN layer as the tunnel barrier and substrate as used in [41].

Growing/transferring onto a hBN substrate is a potentially promising route to fabricating structures using graphene as the identical 2D crystal structure and the lattice mismatch between graphene and hBN is $< 2\%$ [19, 184]. Time consuming top-down methods have been used to fabricate heterostructures from hBN/graphene layers and other 2D materials [19, 168, 41, 185, 186, 187, 160, 111]. Using these techniques, devices such as tunneling field-effect transistors (FETs) using ultra-thin layers of hBN as the tunnel barrier have been reported, a schematic of this structure is shown in Fig 5.7b [41].

These techniques have also been used to fabricate highly aligned graphene/hBN heterostructures in which the rotational mis-match in the hBN/graphene crystal structure is less than 1°. SPM imaging of the surface of these samples shows that a range of moiré patterns are present due to the graphene/hBN lattice mismatch[160]. This requires careful alignment

of the crystal directions of the graphene and hBN through identification of appropriate flakes, followed by delicate micromanipulation to bring the samples in to contact to form the final structure. The origin of these moiré patterns are discussed in further detail in section 5.6. In addition, recently reported CVD methods have also been used to grow highly aligned graphene directly onto hBN [188, 189]. AFM images of these hexagonal moiré patterns are shown in Fig 5.8.

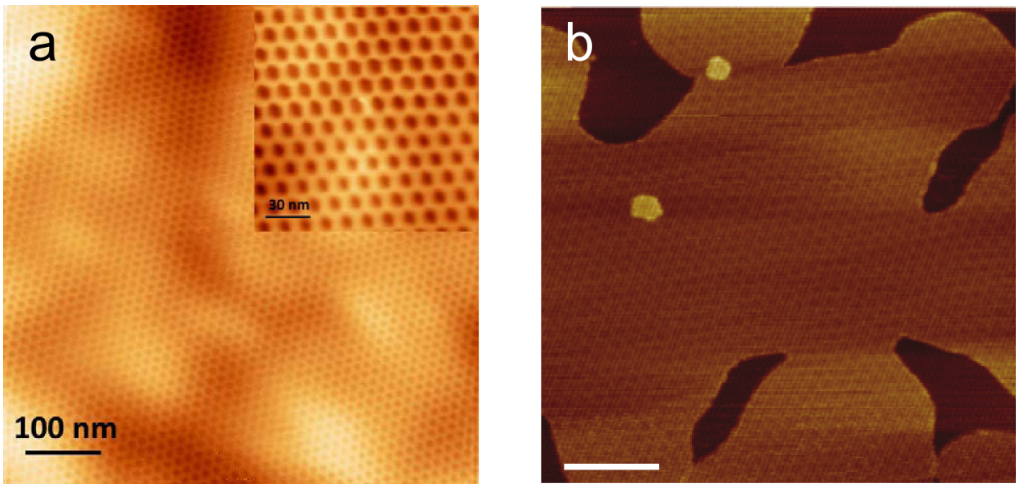

Figure 5.8: a) STM image of moiré patterns on aligned graphene/hBN heterostructure fabricated by micromanipulation of graphene flakes. Scale bar 30 nm. b) AFM image of moiré pattern formed by direct growth of graphene onto a hBN surface using plasma assisted CVD. Scale bar 100 nm. Images from [160] and [183] respectively.

The introduction of strain also provides a route to modify both the electronic properties and the phonon spectrum of graphene monolayers [179, 190, 191, 192]. Introducing strain into graphene can lead to the formation of an energy gap which is a crucial requirement for applications such as transistor action and has been observed when graphene is placed in an aligned configuration on hBN [193, 194, 195, 196, 197, 183]. As a result attempts to engineer strain in graphene have been investigated by

depositing onto deformable substrates [179, 198] or surfaces patterned using lithographic techniques [199, 200, 201].

The applications of graphene will very much depend on the quality (i.e. number of defects, grain size, substrate etc) which is strongly affected by the particular production method [162]. The combination of flexibility, conductivity and transparency will likely see use in flexible electronics along with a transparent protective coating on account of its impermeability. For example, graphene makes a desirable replacement for indium tin oxide (ITO) in transparent touch screens since ITO is brittle and In is rare [202]. For these relatively low performance applications the presence of areas of multi layered graphene rather than a monolayer may not be an issue. However, for high performance applications (e.g. high-frequency transistors), there is a clear need to grow high-quality epitaxial graphene over a large area.

5.5 Graphene Grown by MBE

Molecular Beam Epitaxy (MBE) is a process in which atomic or molecular layers are deposited onto a heated crystalline substrate to produce epitaxially grown layered crystal structures [203]. The beam of deposited species is typically generated by evaporation or sublimation of suitable materials from ultra-pure crucibles in UHV conditions to produce highly pure, epitaxial structures [204]. The high temperatures that substrates are heated to allow the migration of adsorbed species in order to form a highly-ordered lattice (for example 500-600°C for GaAs). Effusion, or Knudsen cells provide the atomic beam.

MBE is a potential route to the production of high quality, defect-free, graphene. MBE is typically used to grow semiconductor devices, particularly those which incorporate heterojunctions. However, use of MBE has had little impact on the growth of graphene and few works have been published on graphene growth using MBE. Previous studies of graphene growth by MBE have typically made use of two strategies, growth of carbon on surfaces using a carbon flux or thermal decomposition of SiC substrates.

Growing graphene using MBE is, in principle, simpler than for many materials since graphene is a monatomic compound and the stoichiometry of the beam flux species need not be considered as is the case for binary compounds such as III-V semiconductors. This means that the parameter space for optimising the growth may in theory be reduced down to the substrate temperature, carbon beam flux and exposure time. Despite this, literature exploring MBE as a technique for graphene growth is currently scarce. This is, in part, due to the relative complexity and expense of the technique when compared to CVD based approaches.

The evaporation of a carbon source directly onto a substrate using MBE has previously been investigated [205, 206, 207]. However, these studies have had mixed success, the presence of graphene on hBN and sapphire substrates have been detected with Raman spectroscopy although subsequent AFM imaging of growth on hBN flakes reveals that these deposits are typically confined to the edges of bulky deposits [207] or are pitted bi-layers when grown directly on a sapphire surface [208]. The substrate temperatures used in these studies (typically $< 1000°C$) may not be high enough to facilitate migration of carbon across the substrate, and therefore the growth is confined to bulk deposits rather than forming an epitaxially-

grown graphene monolayer. Unreported work using this approach at Nottingham has supported this hypothesis and has provided the motivation to study the high temperature regime used in this work.

The other reported method, whilst not technically MBE since no incoming molecular flux beam is used, is the thermal conversion of SiC to graphene [209]. Heating a SiC wafer to ∼1300°C in controlled conditions will cause evaporation of Si atoms at the surface, the exposed carbon atoms then bond to form a layer of graphene on the surface of a SiC substrate [210]. Despite the reproducibility and relative ease of growing wafer-scale graphene using this technique, the cost of SiC wafer is at present prohibitively high for large-scale production although techniques to grow monolayers of SiC on Si are being explored as a solution to this problem [177].

5.6 Moiré Patterns

Moiré patterns are formed by the superimposition of two (or more) patterns to create a secondary pattern by overlaying repeating patterns that have either a different spatial frequency or two identical patterns that have been rotated relative to each other. In the case of hexagonal lattices, the moiré pattern between two mismatch hexagonal lattices would also be hexagonal with a period determined by a combination of the rotational mismatch and any relative difference in the lattice constant between the two lattices.

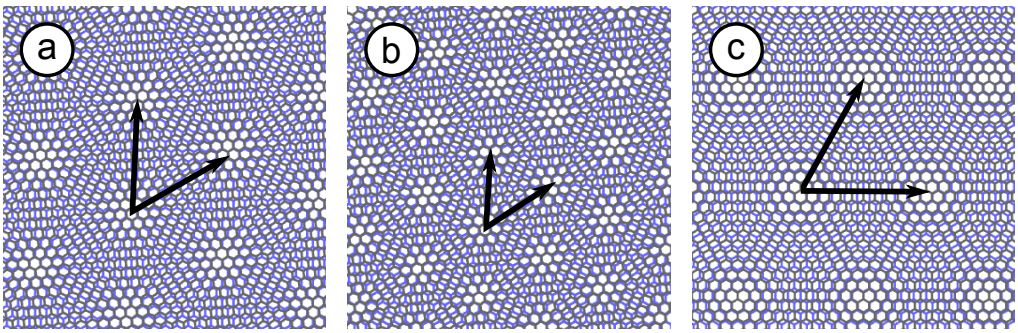

Figure 5.9: Moiré patterns formed by mismatched hexagonal lattices showing two lattices with a) 6° and b) 9° rotational mismatch. c) two aligned hexagonal lattices with a 10% lattice constant mismatch.

Examples of 2D moiré patterns formed by two hexagonal lattices are shown in Fig 5.9. In the context of SPM this can lead to moiré patterns appearing in STM imaging where the LDOS of a monolayer is modified by an underlying substrate. The creation of heterostructures from different thin crystalline materials such as graphene and hBN provides conditions in which the presence of moiré patterns formed by different atomic lattices are observable with SPM. The moiré wavelength, λ, is given by;

$$\lambda = \frac{(1+\delta)a}{\sqrt{2(1+\delta)(1-cos\phi)+\delta^2}} \tag{5.2}$$

where; δ is the fractional lattice mismatch ($\delta = \frac{b}{a} - 1$. a and b are the lattice constants for the larger and smaller lattices respectively), a is the graphene lattice constant and ϕ is the relative rotation angle between the two lattices [211]. For graphene and hBN the value of $\delta = 1.8\%$ and for an aligned graphene sheet on hBN (i.e. $\phi = 0°$), gives a maximum moiré period of $\lambda = 13.6$ nm. Yankowitz et al. reported that the weak potential variation in graphene/hBN structures causes the appearance of a range of moiré patterns for randomly aligned graphene flakes on hBN as shown in

Fig 5.10a-c [211].

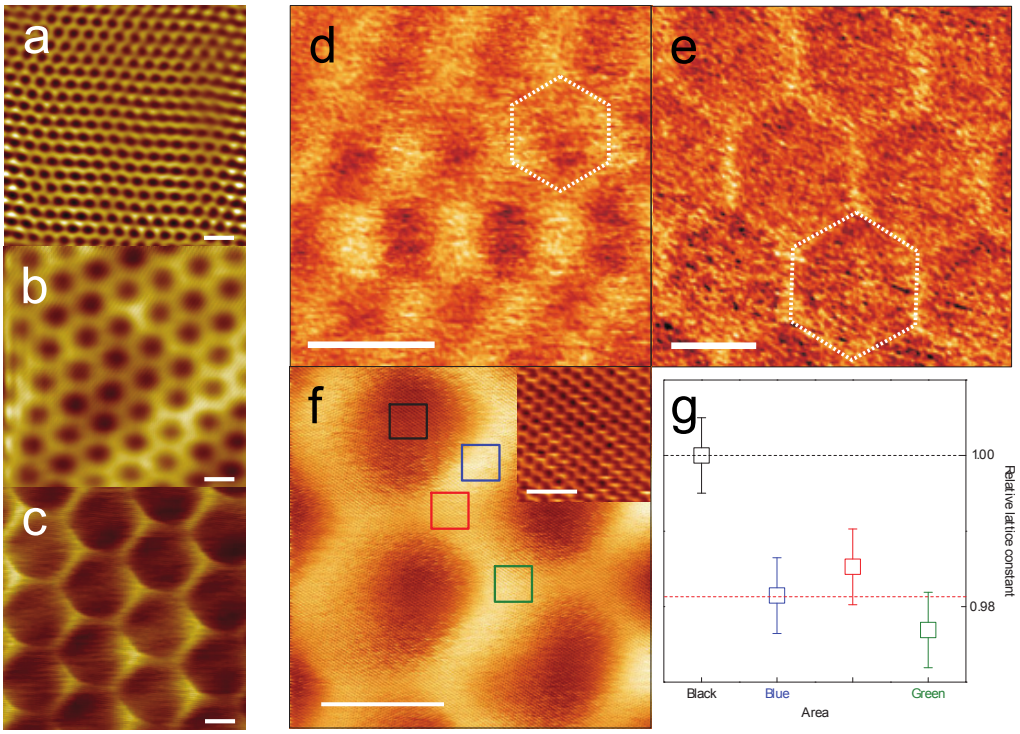

Figure 5.10: Literature examples of hexagonal moiré patterns formed by graphene/hBN heterostructures. a-c) STM images of moiré patterns of different sizes formed by graphene on hBN. Moiré periods for a, b and c are 2.4 nm, 6.0 nm and 11.5 nm respectively. Scale bars are all 5 nm. e) Young's modulus distribution (measured from tip/samples adhesion using an AFM in ambient conditions) for moiré patterns with a periodicity of 8 and 14 nm respectively. Scale bars are 10 nm. f) STM image of an aligned graphene sample showing both the moiré pattern and the atomic structure of the aligned graphene/hBN structure. The coloured boxes show the positions that were used to determine the lattice periodicity. Scale bar 10 nm. g) Relative graphene lattice periodicity at the positions indicated by the coloured boxes in f. Images a-c adapted from [211] and d-g are adapted from [160].

In Woods et al. the relative angular alignment between monolayer graphene flakes on hBN flakes was adjusted using micrometer positioning stages before the two are brought into contact (The lateral crystallographic orientation of the two flakes having been determined prior to the transfer) [160]. SPM imaging of the surface reveals the presence of various moiré pe-

riodicities dependent on the relative rotation angle between the graphene and hBN lattice as shown in Fig 5.10d and e.

At small ($< 8°$) angular rotation between the two lattices, a moiré pattern that is strongly dependent on the relative rotation of the two lattices is observed. Atomic resolution STM imaging of aligned structures (i.e. $\phi = 0°$), as shown in Fig 5.10f, reveals that at there is a spatial variation of the graphene lattice periodicity across the unit cell of the hexagonal moiré pattern as shown in Fig 5.10g. The atomic spacing is found to be at a maximum at the centre of the moiré pattern where it is suggested that the graphene lattice is stretched to match the hBN lattice and decreases at the edges of the hexagonal pattern. Initially these hexagonal patterns were only observed using AFM tip-sample adhesion measurements. However, more recent AFM studies have been able to resolve these patterns using height channel measurements and have shown that there is a topographic height variation at the edges of the hexagonal patterns of [183].

Woods proposes that this change in atomic periodicity occurs since mismatch between the two lattices causes a local competition between the van der Waals interaction between the C and BN atoms and the strain in the graphene lattice. It is argued that, for small angles of misalignment between the principal axes of exfoliated graphene and hBN substrate, a commensurate-incommensurate phase transition occurs which leads to a spatial variation of the lattice constant of the graphene. The central areas of the hexagonal repeating unit correspond to the low contrast regions in the STM image shown in Fig 5.10f, the graphene is stretched to lattice match the hBN in these regions. At the edge regions, which appear bright in the STM image, the graphene is compressed so that N periods of graphene

are overlaid onto N-1 periods of hBN. N is reported to be ∼10 in [160]. These patterns have also been observed in CVD grown graphene on hBN samples at 500°C as shown in Fig 5.8b [183].

For both exfoliated graphene and CVD grown samples, the period of the moiré pattern is reported to be in the range 14-15 nm which is consistent with the value expected for unstrained graphene, 13.6 nm. The similarity of the structures observed in the CVD grown graphene on hBN also shows that bottom-up growth of graphene is capable of producing these aligned structures, as opposed to time consuming top-down transfer and alignment techniques typically used to prepare aligned heterostructures.

5.7 Experimental Techniques

The growth system used in this work is based on a Veeco GenXplor MBE system that has been modified to reach a substrate temperature 1850°C, far in excess of the typical maximum temperatures used in MBE (around 1000°C), and is compatible with substrates up to three inches in diameter[1].

The substrates are mounted in a vertical configuration as shown by the schematic in Fig 5.11 with the sample heater mounted above the substrate. Carbon is deposited using a SUKO-63 sublimation source, a graphite filament which undergoes joule heating using a constant current of 100-110A (Dr. Eberl, MBE-Komponenten GmbH)[2]. The MBE system and a carbon filament is shown in Figs 5.12a and b.

[1]The system is a dual-chamber design, there is an identical MBE chamber connected to the graphene chamber by a UHV transfer tunnel with atomic boron and plasma N_2 sources with the aim of epitaxially growing hBN by MBE. Results on the growth of hBN by MBE are not reported here and it is hoped that in future the use of both chambers will allow the growth of epitaxial graphene/hBN heterostructures.

[2]Deposition of carbon using the MBE system was performed by Tin Cheng on substrates prepared by the author.

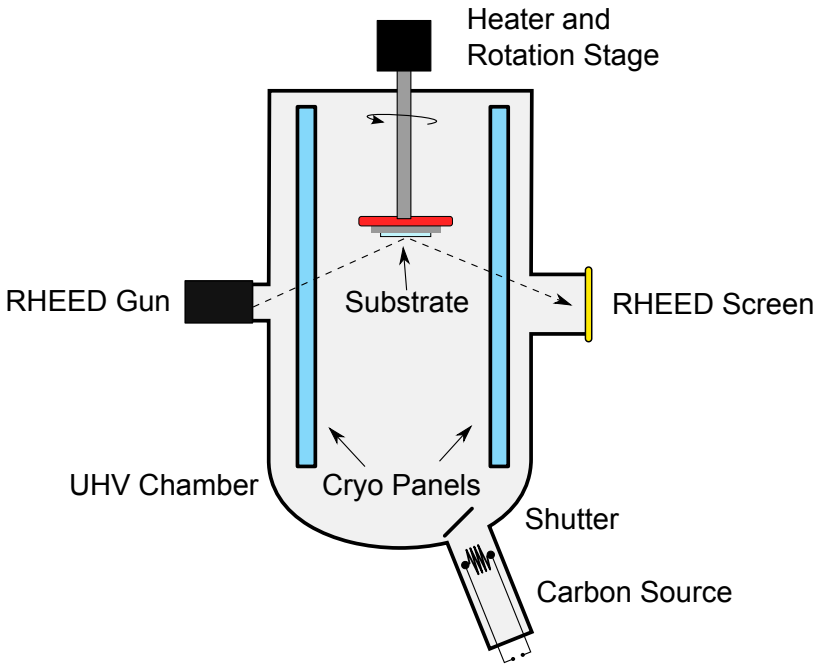

Figure 5.11: A schematic of the MBE system used in this work showing the arrangement of the substrate and heater relative to the carbon source.

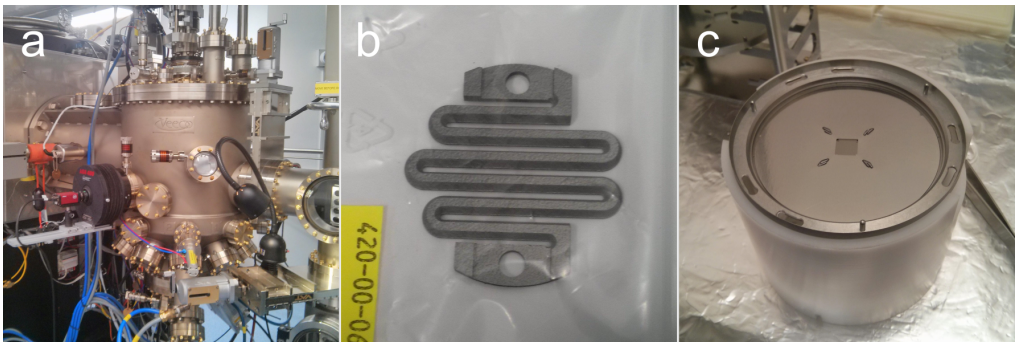

Figure 5.12: a) Growth chamber of the MBE system used in this work. b) Carbon sublimation source prior to loading in the MBE system. c) Sample holder, the square window at the centre is where the sapphire substrate is positioned during growth.

Exfoliated hBN flakes were used as a flat growth substrate for further studying the growth of graphene since hBN has been reported to be a desirable substrate for high quality graphene electronics [19, 168]. In addition, wafer-scale hBN substrates are not currently available. Exfoliated hBN flakes have been reported to seed the growth of highly aligned graphene

with CVD approaches [189] and early MBE studies have suggested that growth on these exfoliated flakes can produce deposits with graphene-like Raman signatures on the hBN surface [207, 212]. However, to date, there are no reports of graphene grown using MBE that have demonstrated the quality reported for exfoliated samples or over the large areas that are grown using CVD techniques.

Substrates used were hBN flakes exfoliated from high-temperature high-pressure grown bulk hBN crystals synthesised according to the procedures reported in [40]. These were exfoliated using low tack PVC with acrylic adhesive tape (Loadpoint Ltd) and deposited on 1 cm square double sided polished sapphire (0001) substrates (SurfaceNet GmbH) cleaned using the toluene immersion and hydrogen cleaning techniques discussed in section 2.16. The cleaned substrates were then transfered to a Ta sample holder (see Fig 5.12c) and transferred in to the MBE system. Following loading, the samples were annealed at 800°C for one hour prior to growth. Due to the use of transparent sapphire substrates, pyrometer measurements of the sample temperature only give the reading of the heater temperature. Instead the sample temperature is estimated using a thermocouple mounted behind the substrate heater.

All AFM measurements (with the exception of those in Fig 5.25) were performed in amplitude-modulated tapping (AC) mode with an Asylum Research Cypher-S AFM using Multi75Al-G AFM probes (Budget Sensors) at set points betweem 400-600 mv (free-air amplitude normalised to 1V) in ambient conditions (k = 3 (1-7) Nm^{-1}, ω_0 = 75 (60-90) kHz). The lattice images shown in Fig 5.25 were also acquired with a Cypher-S AFM in a low set-point (0.1 V) contact mode in ambient conditions using Arrow

UHF (Asylum Research) cantilevers (k = 6 (1.5-21.0) Nm^{-1}, ω_0 = 850 (500-1500) kHz).

Raman spectra were recorded on a Horiba-Jobin-Yvon LabRAM Raman microscope, with a laser wavelength of 532 nm operating at low power (4 mW) and a 600 lines/mm grating. Spectra were recorded using a Synapse CCD detector[3].

5.8 Growth Rate Calibration

Preliminary experiments using the MBE system concerned growth on the bare sapphire surface. For all substrate temperatures (T_{sample}) in the range 700-1630°C, bulky carbon deposits were found to grow readily on the sapphire surface. AFM images of material grown at different substrate temperatures for a fixed growth time (t_{growth}) of one hour are shown in Fig 5.13a and b respectively. For low temperatures ($T_{sample} < 1000$°C) the deposits were granular and for higher temperatures ($T_{sample} > 1300$°C), worm-like carbon growths were observed.

Raman spectra of this material were acquired following growth. For lower growth temperatures no 2D peak was observed, only the D and G were present which is indicative of amorphous carbon formation [213]. For $T_{sample} = 1380 - 1630$°C, the formation of graphene was observed as demonstrated by the presence of the G,D and 2D bands. The AFM images clearly demonstrate that the material is not an epitaxially grown graphene monolayer, however, the 2D bandshape is consistent with the formation of turbostratic graphene. At even higher temperatures of $T_{sample} > 1700$°C, no bands were observed which is likely due to re-evaporation of carbon from

[3]All Raman data presented in this chapter was acquired by Andrew Davies.

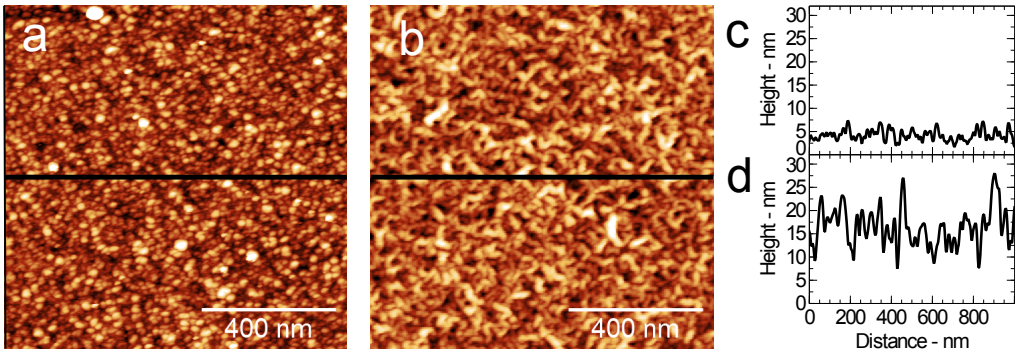

Figure 5.13: 1 μm square ambient AC mode AFM images of sapphire substrates for t_{growth} = 1h at different substrate temperatures. a) T_{sample} = 780°C and b) T_{sample} = 1500°C. In both cases the carbon filament current used during growth was 110 A. c) and d) show line profiles taken across the central black lines in images a and b respectively.

the hot substrate. Raman spectra of these samples are shown in Fig 5.14.

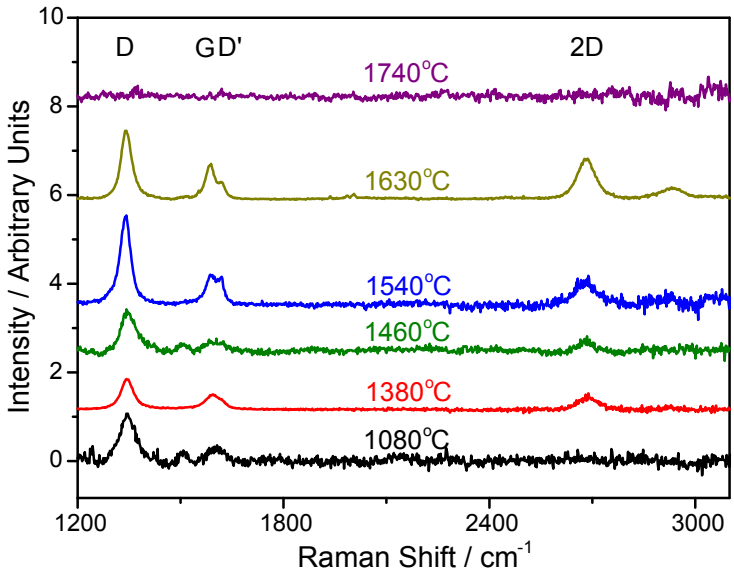

Figure 5.14: Raman spectra showing the effect of the substrate temperature on the growth of carbon films on sapphire. D and G bands were observed for all of the growth temperatures apart from the highest (1740°C). The 2D band is observed for values of T_{sample} in the range 1380-1630°C.

The structure and properties of this material is not discussed further since this work is concerned with the growth of graphene on hBN surfaces.

Nonetheless, in order to calibrate the arrival rate of carbon to the substrate, the amount of material deposited onto the supporting sapphire surface was measured. The material was found to be easily removable using a pair of plastic tweezers and were used to mechanically remove a small region of the carbon deposit from the sapphire surface. The thickness of the edge between the carbon and the exposed sapphire was then measured using AFM as shown in Fig 5.15a.

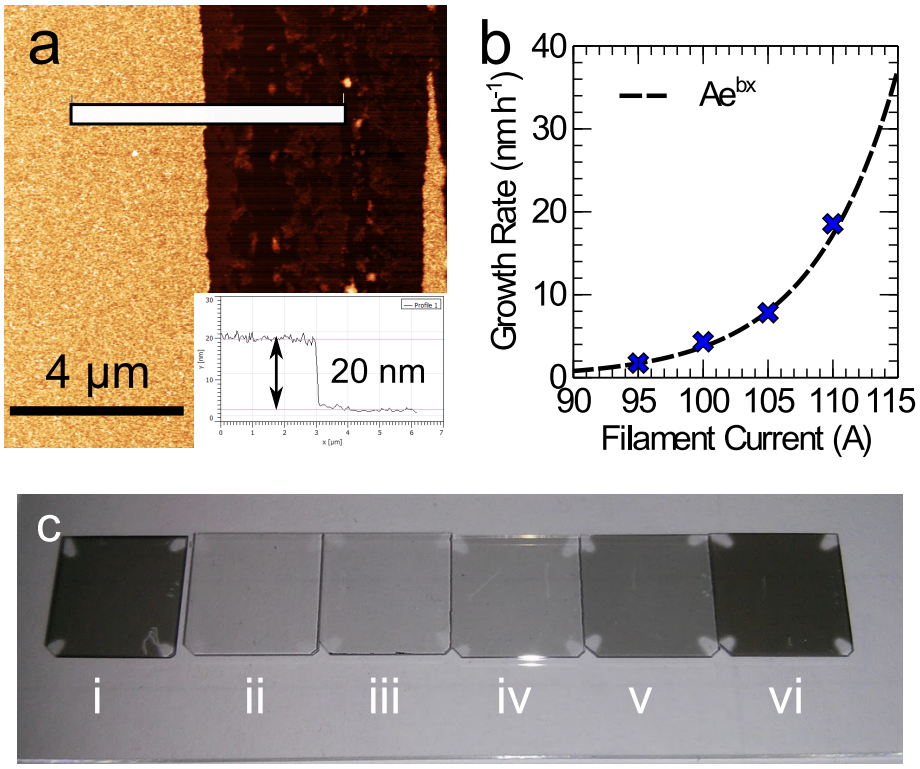

Figure 5.15: Calibration of the carbon flux rate using bulky deposits on sapphire showing; a) AFM image of the turbostratic graphene (bright) and sapphire surface (dark) following mechanical removal of deposits on the surface, T_{sample} = (inset) height profile across the region indicated by the white line in the main image. b) Carbon thickness as a function of carbon filament current for samples ii-v. c) Sapphire samples following growth of carbon; i) sample following filament failure after 2 hours of growth showing excessive carbon deposition ($T_{sample} = 1500°C$); ii-v) samples at increasing carbon filament currents of 95, 100, 105 and 110 A respectively ($T_{sample} = 1500°C$); vi) low substrate temperature sample ($T_{sample} = 780°C$). Full growth conditions for these samples are given in table 5.1.

Table 5.1 shows the conditions for the samples shown in Fig 5.15c. Holding the substrate at a fixed temperature and varying the carbon filament current (samples ii-v) allows the deposition rate to be well controlled as shown by the growth rate plot in Fig 5.15b. Samples darken progressively with increasing carbon thickness as expected. The significantly darker samples in Fig 5.15c, i and vi, are the result of a much thicker layer of carbon being deposited on to the sapphire surface. The increased thickness of sample i is the result of a carbon filament failure after ∼2 h of deposition (see section 5.10) which causes a significantly increased flux of carbon to be deposited. Sample vi is the result of lowering the sample temperature, this increases the sticking coefficient of carbon on the sapphire surface and as a result the carbon thickness is increased.

Sample	Filament Current (A)	t_{growth} (h)	T_{sample} (°C)	Thickness (nm)
i	110	2	1500	109.8
ii	95	4	1500	7
iii	100	4	1500	17.3
iv	105	4	1500	31.3
v	110	4	1500	74.2
vi	105	4	780	133

Table 5.1: Table showing the growth conditions for the samples shown in Fig 5.15c. t_{growth} for sample i corresponds to the time at which the carbon filament failed.

Using a carbon filament current of 110 A at T_{sample} = 1500°C, the carbon deposition rate onto the sapphire surface is estimated to be in the range 18-22 nm/h from the growth rate data in Fig 5.15b. These figures are significant since they correspond to the sample temperature and flux rate used for samples that exhibit total coverage of graphene discussed later in this chapter.

5.9 Island Growth

Initial experiments growing on the hBN surface were primarily aimed at identifying the temperature window for MBE growth of graphene. After annealing with no carbon deposition, the hBN surface is found to wrinkle and produce 'walls' in the surface with a height of ∼50-100 nm (see Fig 5.16), this is likely due to the mismatch between the thermal expansion coefficient of hBN and sapphire at these high temperatures, causing the hBN to wrinkle on cooling. The surface also reveals evidence of the underlying sapphire terraces showing through the hBN as is the case for Au(111) and SiO_2 shown in Fig 2.32, these features were present before annealing as shown in Fig 5.16b and are typically more pronounced for thinner hBN flakes.

For $t_{growth} = 1$h and $T_{sample} = 1350 - 1630°$C, samples showed evidence of carbon deposits on the hBN surface consistent with those reported in the literature, in particular the reader is referred to Fig 3d in [207] to note the similarity with Fig 5.17a and b. For longer t_{growth}, deposits of carbon were found to grow along the hBN step edges with a height of approximately 10-30 nm relative to the hBN surface measured by AFM (see Fig 5.17). For lower sample temperatures, the hBN flakes were often completely covered in carbon.

Further inspection of these deposits with AFM (Fig 5.18) shows that the edges of this bulky material have faceted edges and a measured height of 0.4 nm, suggesting that these features are graphene monolayers growing at the edges of the carbon deposits. This is shown in Fig 5.18b and c. Fig 5.18c shows that some of these regions exhibit hexagonal patterns adjacent to regions without. This suggests that graphene that is both aligned and

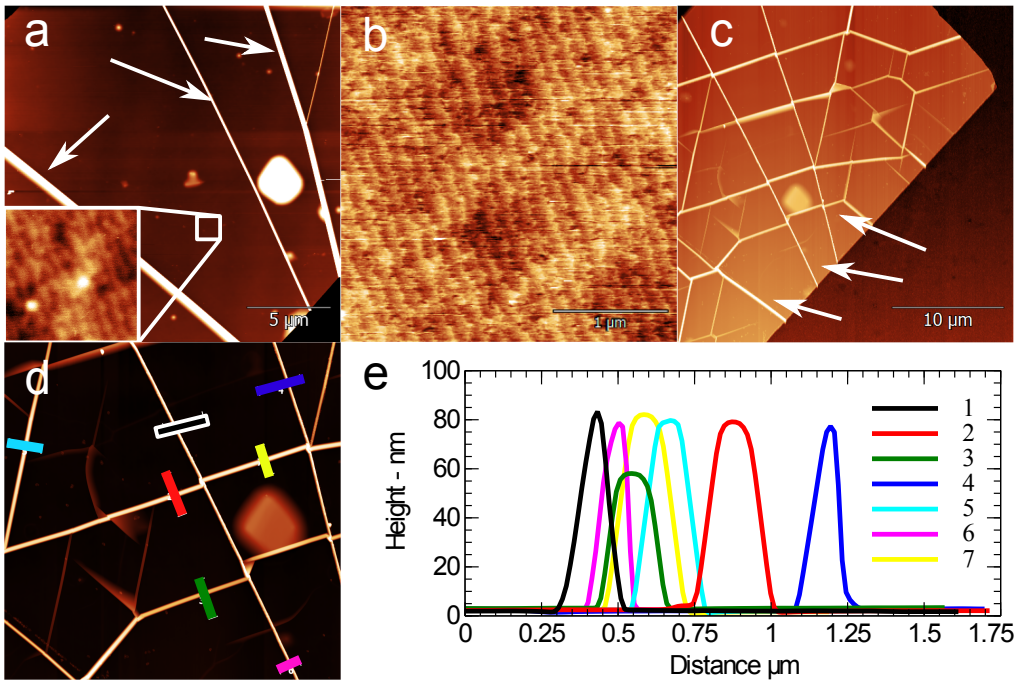

Figure 5.16: a) AFM image of hBN flake on sapphire substrate after cleaning in H_2:Ar gas and (inset) the presence of terrace-like structures is observed on the hBN surface. b) AFM image of the bare sapphire surface near to the flake in image a showing the periodic terrace steps in the same orientation as the lines on the hBN surface. c) AFM image of the flake in a) after heating to $T_{sample} = 1630°C$ and $t_{growth} = 1h$ showing the clear presence of wrinkles induced by the heating process, the arrows indicate the positions of the wrinkles labeled in a. d) Centre of region indicated in c. e) height profiles across the wrinkles indicated by the coloured lines in d. All AFM images were taken in AC mode in ambient conditions.

misaligned with the hBN surface is present.

Further imaging of graphene islands at the edges of the bulk carbon deposits reveals that these hexagonal patterns are present at the edges of most of the graphene islands. Figure 5.19a shows multiple examples of these islands after 1 h of growth. Figure 5.19b shows a higher resolution image of the box marked in Fig 5.19a showing that the highly regular hexagonal pattern is present across the entirety of the island's surface. In Fig 5.19c two domains are observed to coalesce. Interestingly the moiré patterns

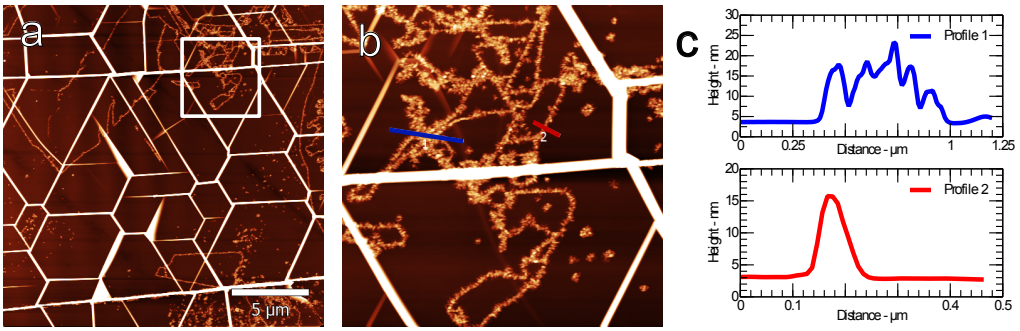

Figure 5.17: a) AFM image of hBN surface for $t_{growth} = 1$ h and $T_{sample} = 1500°C$ showing carbon deposits. b) AFM images of the area highlighted by the box in a. c) Height profiles across the features highlighted in b. AFM images were taken in AC mode in ambient conditions.

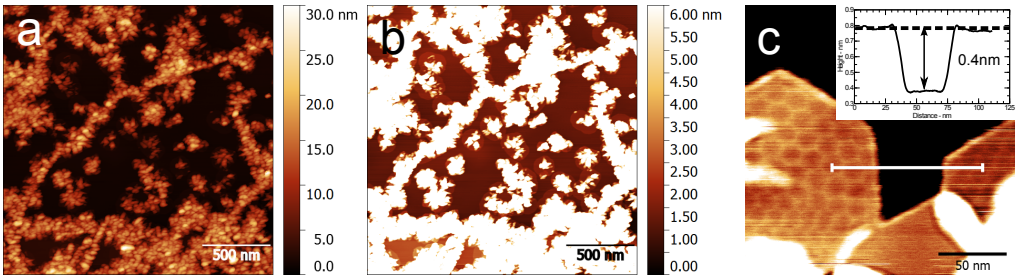

Figure 5.18: a) AFM image of carbon deposits on the surface of hBN following growth. b) Reducing the z-range of the colour map in image a reveals the graphene islands growing from the edges of the bulk carbon deposits (white blobs). c) Higher resolution AFM image of the edge of a carbon deposit from a different sample showing the hexagonal faceted material growing from the edge of the carbon deposit and also showing the presence of moiré patterns on the graphene surface. (inset) Height profile across the white line in c showing the 0.4 nm height expected for a graphene monolayer on hBN. All AFM images taken in ambient conditions using AC mode AFM.

are not aligned and the pattern is discontinuous through the region that connects them. The periodicity of the moiré patterns are typically ∼14 nm as shown in Fig 5.19d and all regions show the same 0.4 nm thickness relative to the underlying substrate as shown by the height profiles in Fig 5.19e.

From these images it is assumed that the aggregates act as nucleation

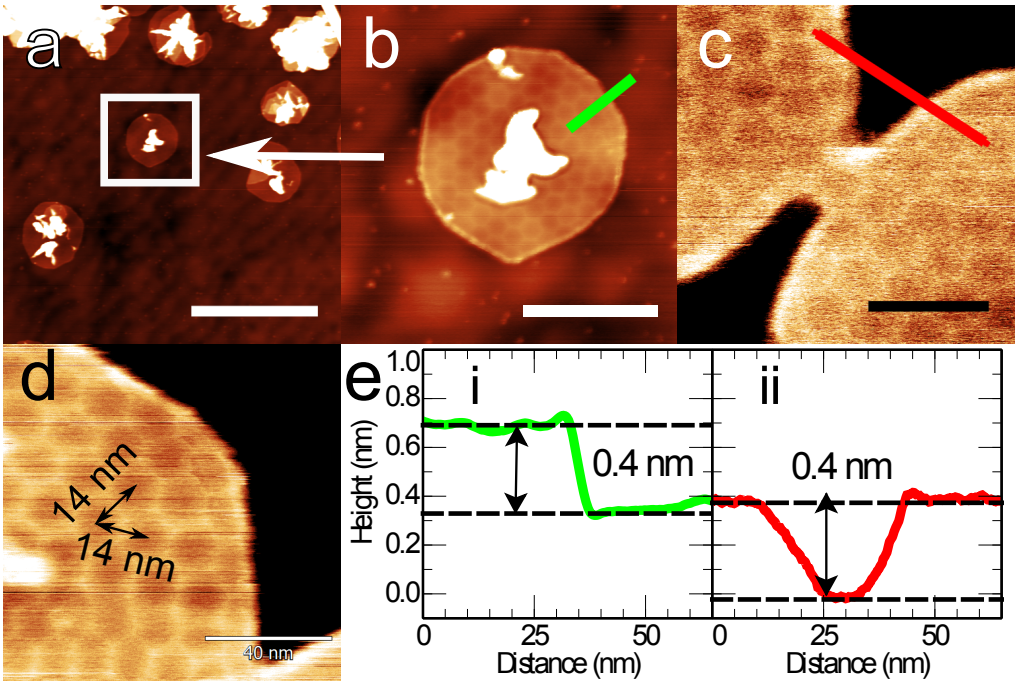

Figure 5.19: a) AFM images of graphene islands forming around carbon deposits on the hBN surface after 1 h of growth. Scale bar 400 nm; b) island indicated by the box in a. Scale bar 100 nm; c) two graphene domains coalescing, each island has hexagonal patterns that are not orientationally aligned. Scale bar 40 nm; d) the periodicity of the hexagonal patterns is approximately 14 nm; e) AFM height profile across the regions indicated in b and c. AFM images taken using AC mode AFM in ambient conditions.

sites for graphene growth and these islands will ultimately coalesce to form a continuous layer.

5.10 Complete Coverage

Further increasing t_{growth} to 4 h at T_{sample} = 1500°C led to total coverage of the surface in graphene. Lowering the substrate temperature was found to cause complete coverage of the hBN in bulk carbon deposits. For $T_{sample} > 1600$°C, no growth on the regions between the bulky carbon deposits on the hBN surface were observed suggesting the carbon evaporates

from the hBN surface and the growth temperature is too high. As a result T_{sample} was fixed at 1500°C. However, exploration of the parameter space for graphene growth is ongoing and it is likely that the optimum parameters for monolayer growth have yet to be found.

Prolonged growth for $t_{growth} \approx 4$ h has, on several occasions, caused failure of the carbon filament as shown in Fig 5.20a leading to a large amount of carbon being deposited onto the surface from measurements of the turbostratic carbon thickness on the sapphire surface. The sapphire substrates were also noticeably darker indicating that more carbon has been deposited on the surface as shown by sample vi in Fig 5.15c.

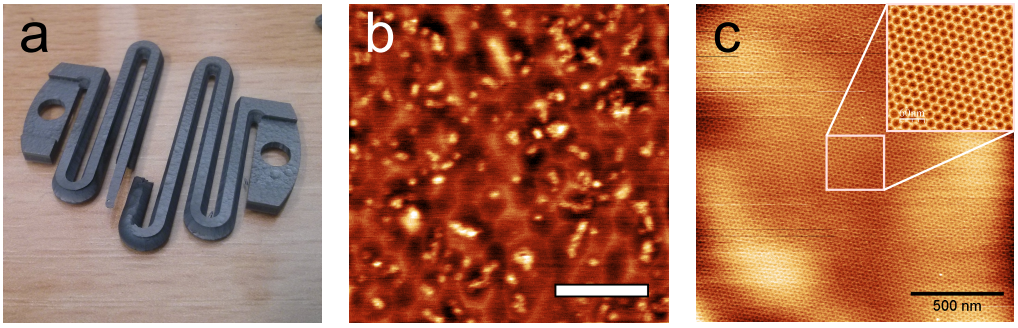

Figure 5.20: a) Blown carbon filament. b) Distorted moiré patterns on a sample after filament failure. Scale bar 100 nm. c) 1.6 μm square region in between carbon deposits showing total coverage of graphene. (inset) 300 nm square region showing the uniformity of the moiré pattern. AFM images taken in ambient conditions using AC mode AFM.

Upon inspection with AFM the areas in between the bulk carbon deposits were found to be exhibit highly distorted moiré patterns as shown Fig 5.20b. These coexist with small, topographically bright dot-like features (typical width and height 10 nm and 0.2 nm respectively). The presence of a continuous moiré patterns suggest that the regions in between the bulk carbon deposits are completely covered with graphene.

In subsequent experiments it was possible to grow the graphene on hBN

without filament failure indicating that the high instantaneous carbon flux caused by the failure of the filament is not necessary to grow a continuous monolayer of graphene. In these samples, high quality and uniform moiré patterns over continuous regions of up to 2 μm square (the typical separation of bulk carbon deposits on the hBN surface) are observed. An image of a region showing a highly uniform moiré pattern is shown in Fig 5.20c.

Imaging at random positions across hBN flakes show that the graphene completely covers the regions in between the carbon aggregates as shown in Fig 5.21a and b i-xv. However, upon inspection of the moiré patterns, the periodicity is found to grossly exceed the previously reported value of ~14 nm [160]. The average moiré period for the images in Fig 5.21i-xiv is measured to be ~22.5 nm. In addition, distorted moiré patterns are also observed as shown by Fig 5.21b xv.

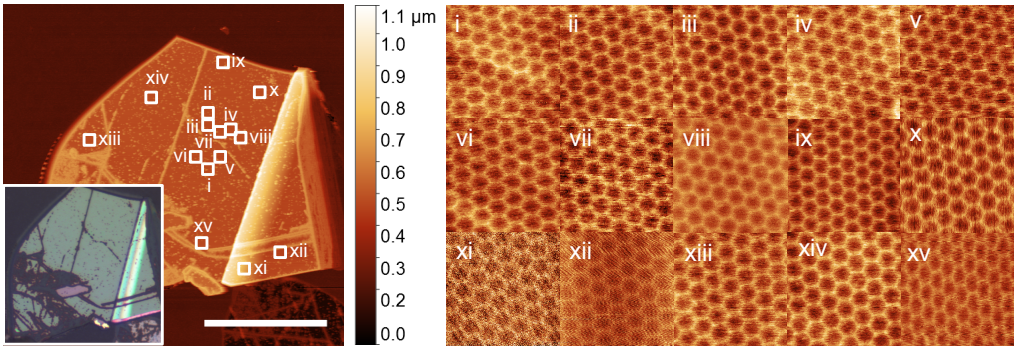

Figure 5.21: AFM images of graphene on hBN showing a large area image of the hBN flake indicating the position that the smaller images, i-xv were taken. (inset) Optical image of the flake. The scale bar in the larger image is 30 μm and images i-xv are all 150 nm square. AFM images taken using AC mode AFM in ambient conditions.

These observations were confirmed by the observation of high moiré periods on different samples and large variation in the moiré period over areas on the same hBN flake are commonly observed. Figures 5.22b-d and their measured periodicties in Fig 5.22e show the large variation in moiré

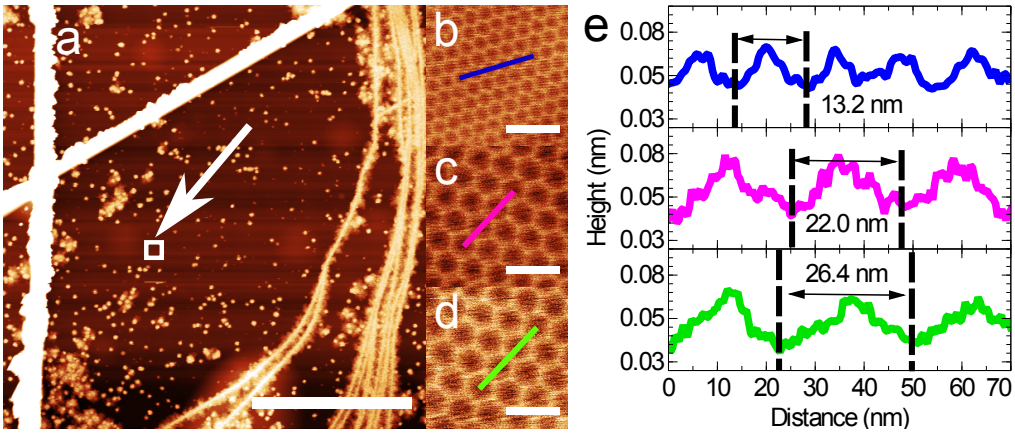

Figure 5.22: a) 30 μm square image of a hBN flake showing the distribution of carbon deposits across the surface, the arrows indicate the positions where images b and d were taken respectively. Scale bar 10 μm. b-d) 150 nm square images of different size moiré patterns observed across the substrate. Scale bars all 50 nm. e) line profiles across the images indicated in images b-d showing the periodicity of the moiré pattern in each image. AFM images taken using AC mode AFM in ambient conditions.

period. The period of the hexagonal array in Fig 5.22b, 13.2 nm, is close to that reported previously [160], however, the larger periods such as those shown in Fig 5.22c and d which are 22.0 nm and 26.4 nm respectively have not been reported. The observation of a larger period, λ_s, implies that the mismatch between the graphene and the hBN has been reduced and, consequently, that the graphene is under tensile stress.

For the high moiré periods observed in MBE graphene, the increase in lattice constant, a, averaged over a moiré unit cell is denoted Δa, and the strain, $\frac{\Delta a}{a}$, may be deduced from the increase in moiré period, $\Delta\lambda = \lambda_s - \lambda_0$ through the approximation;

$$\frac{\Delta a}{a} \approx \left(\frac{\delta a}{a}\right)\left(\frac{\Delta\lambda}{\lambda_s}\right) \tag{5.3}$$

where the graphen/hBN lattice mismatch, $\frac{\delta a}{a} = 1.8\%$. Using the moiré

period in Fig 5.22d, equation 5.3 gives the strain, $\frac{\Delta a}{a}$, as 0.9%.

As previously mentioned, in other areas of the flake shown in Fig 5.23 the hexagonal network undergoes significant distortion. The zoomed region in Fig 5.23a shows strong asymmetry in the moiré pattern. In addition, topological defects in the moiré pattern are observed combined with a local distortion of the orientation and period of the network. Figure 5.23b shows the presence of a dislocation where a row of the hexagonal pattern terminates and the local coordination of the cells in the moiré pattern is 5 and 7 rather than 6. The presence of these defects causes long-range curvature of the network as shown by the larger scale image in Fig 5.23d.

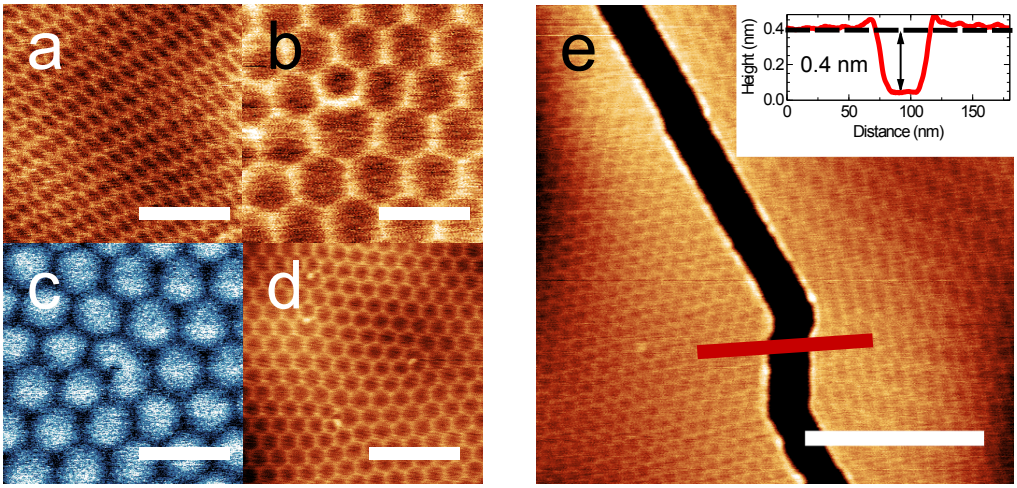

Figure 5.23: a) anisotropic moiré pattern on the graphene surface. Scale bar 100 nm. b) point defect in the moiré pattern. Scale bar 50 nm. c) Similar point defect observed in the phase channel. Scale bar 50 nm. d) Several point defects inducing long-range curvature in the moiré pattern. Scale bar 170 nm. e) Cracked region in between two graphene domains and (inset) the line profile across this crack as shown by the red line. Scale bar 150 nm. AFM images taken using AC mode AFM in ambient conditions.

Breaks in the graphene layer are also observed as shown in Fig 5.23e, across which there is an abrupt change in the moiré periodicity from ∼13 nm to a highly distorted hexagonal pattern. The presence of these features

demonstrates that the distortion is not due to an imaging artefact such as thermal drift or tip asymmetry. The height change across this boundary, 0.4 nm, also confirms that the material is a single layer of graphene. All other breaks in the graphene sheet were measured to have this 0.4 nm height change. The presence of multi-layer graphene would be implied by multiples of this value, however, this has not been observed on any of the breaks in the graphene domains observed in this work.

Some small multi-layered graphene islands have been observed and some regions of bi-layer and tri-layer graphene are observed in regions close to the carbon deposits. AFM images of these multi-layered regions are shown in Fig 5.24. However, the isolated multi-layered islands shown in Fig 5.24b and c are rarely observed (typically there are less than five of these islands over a 30 μm area) and the surface in between the bulk carbon deposits is covered by monolayer graphene[4].

There are two possible sources of these breaks in the graphene sheet as shown in Figs 5.23e and 5.25a. The gap between the separate domains may be caused by two domains which have not coalesced, or the breaks may have been formed post-growth by tearing of the sheet. Inspection of the edges as shown in these two examples and many other examples shows that the edges are highly parallel along the entire length of the crack. This suggests that these breaks form after the growth and result in a relaxation of strain towards the moiré period for unstrained graphene.

For a simple moiré pattern caused by overlaying of the graphene and hBN lattices, the defects and distortion in Fig 5.23 would not be expected.

[4]The area surrounding the hexagonal multi-layered island exhibits moiré patterns, however, the contrast is extremely weak due to the small height change relative to the thickness of the island.

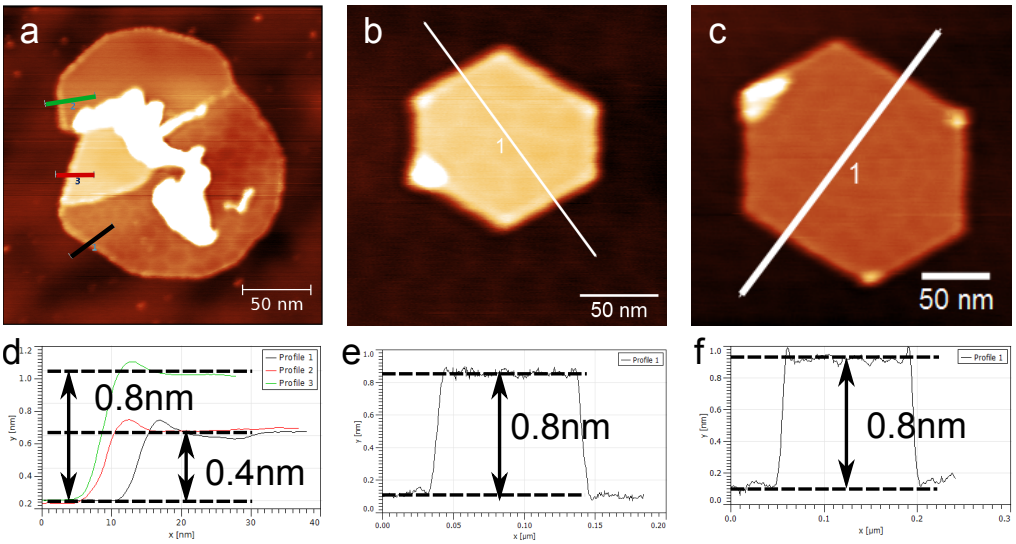

Figure 5.24: a-c) AFM images of regions with multi-layered graphene and d-f) height profiles across the regions indicated in the images. AFM images taken using AC mode AFM in ambient conditions.

However, the origin of the bright boundary features in the hexagonal patterns here are attributed to the regions where there is a mismatch in the lattice constants of the hBN and graphene (using the model proposed by Woods [160]). It is intuitive to assume that these regions run along the principal axes of the hBN and graphene, and indeed, may correspond to the lowest energy configuration. Despite this, there is no reason why the boundaries could not run in other directions, and variation in the orientation of moiré patterns has been reported for CVD grown graphene on hBN by others [188].

Contact mode AFM was performed on the graphene surface in order to resolve the atomic lattice of graphene and hBN and check the alignment of the graphene relative to the underlying hBN[5]. Operating in contact mode has been used in the literature to resolve the atomic lattices of both

[5]These measurements were performed by Vladimir Korolkov.

graphite, graphene and hBN in ambient conditions [214, 188, 6][6].

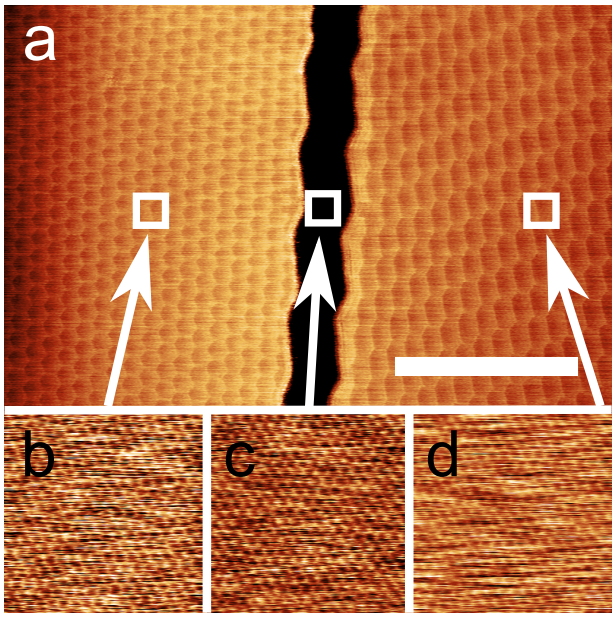

Figure 5.25: Contact mode AFM images of; a) graphene domains either side of a tear (dark central region); b-d) contact mode images of, b) graphene, c) hBN and, d) graphene lattices at the positions indicated by the boxes in a. Scale bar in a is 200 nm and images b-d are all 5 nm square. Images taken in ambient conditions with Arrow UHF cantilevers (Asylum Research).

Figure 5.25a shows two neighbouring graphene domains (bright regions with hexagonal moiré patterns) and an exposed region of the hBN surface (dark central stripe). The matching wavy edges of the graphene domains indicate that the graphene edges were once joined as a single continuous graphene domain which has torn following growth. Figures 5.25b-d show lattice images acquired at the positions indicated in Fig 5.25a across two distinct graphene domains (Fig 5.25b and d) and the hBN between the graphene domains (Fig 5.25c). These lattice images show that the graphene is aligned in both domains with the underlying hBN (within experimental error) lattice. The 120° angles of the wavy edges also suggest that the

[6]The detection mode in [214] and [188] used friction force microscopy whereas the results presented here and in [6] use the AFM cantilever deflection as the detection channel.

graphene has torn along the principal axes of the graphene lattice which is further supported by the fact that the edges are aligned with the graphene lattice in Fig **??**b and d. This is despite the clear difference in symmetry and period of the moiré pattern both sides of the crack in Fig 5.25a. These images also show that the moiré pattern does not necessarily need to be aligned with the graphene lattice and also confirms that the graphene is epitaxially grown on the surface.

5.11 Strain in Graphene

The highly anisotropic moiré pattern on the right side of Figs 5.23a and 5.25e imply that the graphene is anisotropically strained. The most distorted region in 5.23e has dimensions of approximately 60 nm which correspond to a strain of $\sim$1.4%. Following the observation of breaks in the graphene lattice and the highly anisotropic moiré patterns it was decided to investigate the spatial variation of strain and the size of the graphene domains.

A 30 μm square region was mapped in order to determine the size of the graphene domains (see Fig 5.26). These are phase channel images since it is easier to resolve the domain boundaries over larger areas in this mode. The maximum size of the domains in this region is found to be approximately 20 μm (the largest domain being marked by the number 2 in Fig 5.26).

To map the variation in moiré period across the boundary between domains 1 and 2, the area indicated by the white box in Fig 5.26a was mapped by the acquisition of 425 successive 0.5 μm square AFM images (resolution $\sim$0.5 nm pixel^{-1}) over this area taking approximately 100 hours

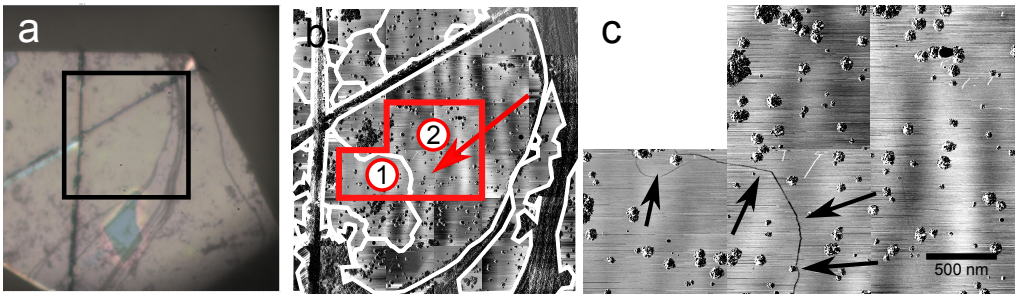

Figure 5.26: a) Optical image showing the hBN flake used for mapping the moiré periodicity. The intersecting straight lines correspond to folds in the hBN flake and the dark spots and curved lines are the bulky carbon deposits. b) 30 μm square ambient AC mode AFM phase image of the region indicated by the box in a, the thick white lines indicate the edges of domains due to cracks in the lattice, the numbers indicate two separate domains referred to as 1 and 2. c) High resolution phase image of the area in b marked by the red box clearly showing the boundary between domains 1 and 2 which is further indicated by the arrows.

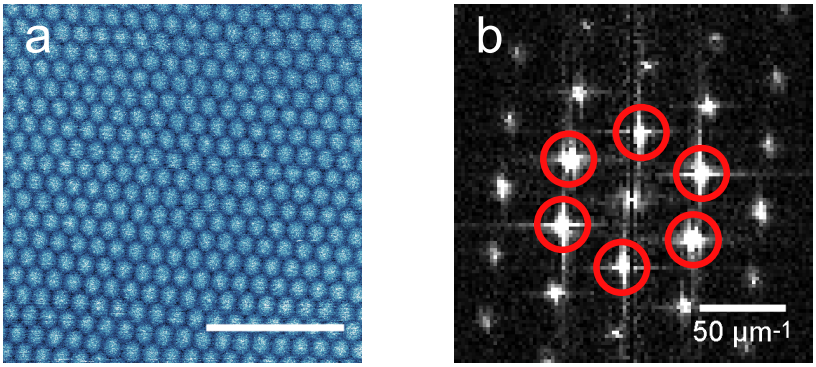

Figure 5.27: a) Phase channel of AC mode AFM image of the graphene surface showing a moiré pattern. Scale bar in a is 200 nm. b) Central region of a 2DFFT of image a, the first-order peaks that correspond to the moiré periodicity are shown by the red circles and are used to extract both the moiré period and the distortion value, $\bar{\mathbf{g}}$.

of continuous scanning time.

The moiré period of the graphene was extracted by sub-dividing each AFM images in to 250 nm square regions and performing a 2DFFT on each. The phase image was used for image processing as this typically more reliable at achieving good contrast as shown by Fig 5.27a. The moiré

period corresponds to the first order Fourier peaks of the transformed image and these are extracted at each position. In addition the degree of anisotropy, $\bar{\mathbf{g}}$, is calculated using the same method as discussed section 4.4 by extracting the maximum and minimum moiré periodicities (λ_{max} and λ_{min} respectively), i.e. $\bar{\mathbf{g}} = (\frac{\lambda_{max}}{\lambda_{min}} - 1)$.

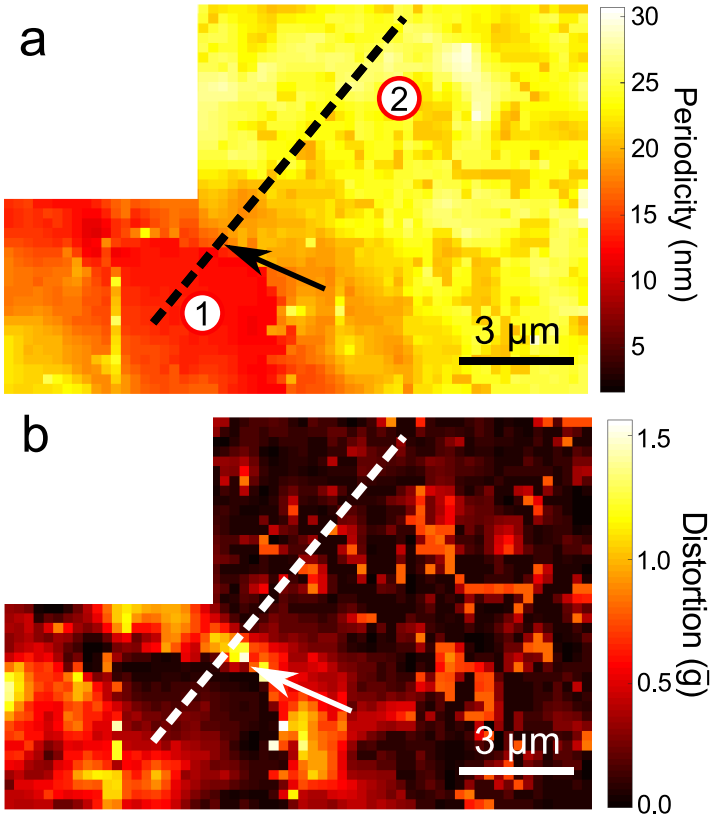

Figure 5.28: a) Map of the moiré periodicity and b) distortion across the region indicated in Fig 5.26. The profile indicated in a shows where a succession of high resolution Raman spectra were taken. The arrow in a and b show the psition of the discontinuity where the break in the graphene domains is observed in Fig 5.26.

Figure 5.28 shows the moiré periodicity and distortion across the region indicated by the red box in Fig 5.26b. Both maps in Fig 5.28 show a sharp discontinuity in moiré period (and therefore strain) across domains 1 and 2 along with a sharp increase in the distortion across the boundary from

left to right in agreement with the high resolution images of this region shown in Fig 5.25a. The period across domains 1 and 2 is approximately constant over each domain (apart from the region close to the crack) and have values of ∼13 nm and ∼25 nm respectively.

5.12 Raman Mapping

Since the strain is expected to affect the Raman spectrum of graphene [179], 2D Raman mapping was performed by taking grid spectra[7] on the hBN flake shown in Fig 5.26 and subsequently mapped by AFM in Fig 5.28. In addition, higher acquisition time spectra were taken along the trajectory indicated by the dotted line in Fig 5.28a which intersects the boundary between region 1 and 2 that have been previously mapped by AFM in section 5.11.

Upon inspection of the raw spectra, the graphene 2D region was found to vary strongly with position on the hBN flake and can be broadly classified into three types as shown in Fig 5.29a. The first type, represented by the blue spectra in Fig 5.29a is a strong unshifted high-energy 2D peak and is found to be strongest in regions with high concentrations of bulky carbon deposits. The green spectrum corresponds to a red-shifted single peak and the red spectra are highly red-shifted peaks that exhibit splitting, these are found to correlate strongly with the moiré periodicity (and therefore strain) as discussed below.

To generate the Raman map, the 2D peaks of the Raman spectra at each point were fitted to the model red, green and blue spectra in Fig 5.29a. The colour at each point in Fig 5.29b is determined by the relative

[7]Raman mapping and CLS fitting was performed by Andrew Davies.

weights of the model spectra in Fig 5.29a from a classical least squares (CLS) analysis.

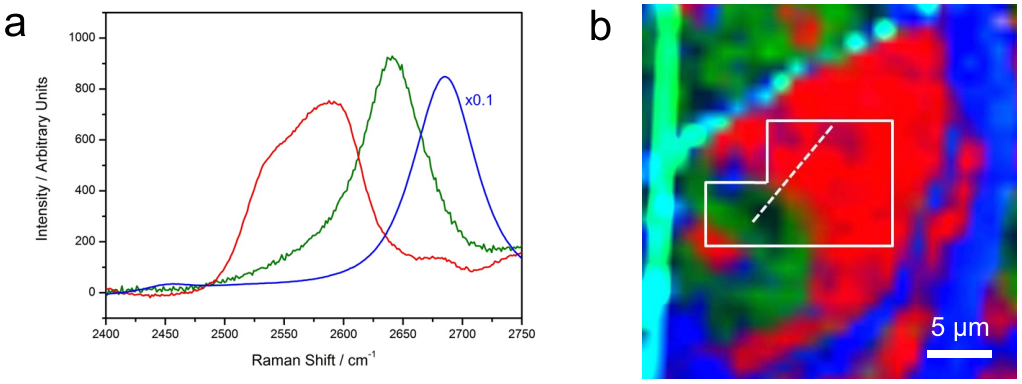

Figure 5.29: a) Multiple spectra from 2D regions of Raman mapping data used for CLS fitting of the data, the red, green and blue spectra are model spectra used to generate the map in b. b) Raman CLS map of graphene on hBN showing the variation in 2D spectral type by weighting using the model spectra in a.

Figure 5.29b shows the Raman map produced by the CLS fitting. The map shows that the different peak types (i.e. areas that are strongly coloured red, green or blue) are typically localised to specific regions on the hBN flake. Interestingly there is a strong and abrupt change from green to red type spectra in the region indicated by the white box in Fig 5.29b. This box corresponds to the region where the moiré period map (section 5.11) shows that there is also an abrupt change in moiré period across the boundary between two different graphene domains.

In order to deconvolve the overlapping peaks in the red-shifted 2D regions, the Raman spectra were fitted to multiple Gaussian functions. For high moiré periods, (such as the top spectra in Fig 5.30b showing a region with a 22.6 nm moiré period) the 2D region may be decomposed into three peaks. These consist of a high energy peak at 2682 cm^{-1} and two red-shifted peaks. The high energy peak is close to the value expected for

monolayer (and turbostratic graphene) [176] and is attributed to the presence of the large carbon aggregates as mentioned above. This is reflected in the CLS mapping which shows a strong signal from this peak as shown by the blue-type regions in Fig 5.29b which correspond to regions where the carbon aggregates are observed in the AFM images in Fig 5.22a (the surrounding regions on the bare sapphire substrate also are of this 'blue' type). Despite this, the peak is present in nearly all spectra with a constant energy, but large variations in amplitude due to the irregular distribution of aggregates. The presence of this peak in the spectra is unavoidable since the size of the laser spot size used for these measurements is of the same order as the separation between aggregates ($\sim$1 μm).

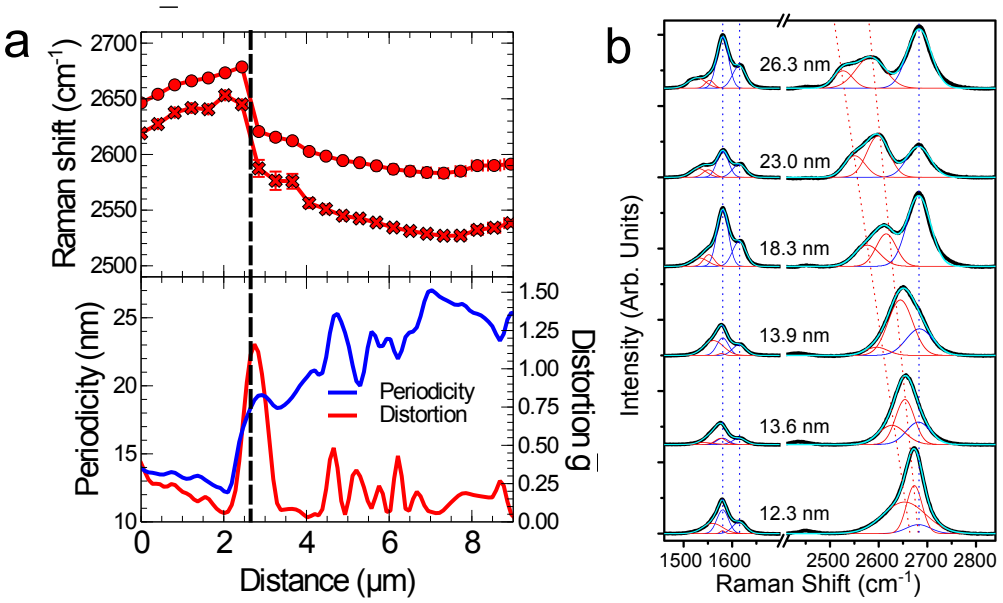

Figure 5.30: a) (top) Raman shift of the two most red-shifted 2D peaks as a function along the profile marked in Fig 5.29b, (bottom) periodicity and distortion along the same profile, interpolated from the moiré periodicity map in Fig 5.28a and b. b) Selected Raman spectra from the same profile with their associated moiré periodicities determined by correlation with the profiles in a.

Figure 5.30a shows the fitted 2D peak positions along the profile in

Fig 5.28a and Fig 5.29b shown along with the periodicity and distortion[8]. Figure 5.30a shows the sharp rise in periodicity and distortion across the boundary between graphene domains 1 and 2. The increase in periodicity is accompanied by an abrupt red-shift in the positions of the two most red-shifted 2D peaks consistent with the CLS and confirms the spatial correlation of the Raman features with the moiré period. The profile of $\bar{\mathbf{g}}$ also shows that the distorted region is localised to a region in domain 2 which is within $\sim$2 μm of the crack at the boundary with domain 1. The abrupt red-shift in the 2D peaks coincides with the point where the periodicity and distortion experience a sudden change as indicated by the dotted line. This indicates that there is a clear correlation between the Raman peak positions and moiré period.

Figure 5.30b also shows the dependence of the G peak on the moiré period. The G and the D' peaks are observed at respectively 1581 cm^{-1} and 1615 cm^{-1} close to the expected values for graphene. However, a shoulder is also observed on the low energy side of the G peak which evolves into a more distinct feature which can be decomposed into two broad peaks centered at 1553 and 1527 cm^{-1} for $\lambda_s = 26.3$ nm shown by the top spectra in Fig 5.30b. Other peaks present in the spectrum but not shown in Fig 5.30b are the D peak at half of the unshifted 2D peak, and the peak due to the hBN substrate.

Determining the strain from the moiré period allows the 2D peak positions as a function of strain to be calculated. This is shown for the red-shifted 2D and G peaks in Fig 5.31 along with 1st order polynomial fits

[8]The periodicity and distortion along these were determined by interpolation of the moiré period map in Fig 5.28

to the data[9]. Errors in the Raman peak positions are given as the standard error of the fitting. The errors in the strain are due to the resolution limit of the 2DFFT which accounts for the higher error at larger moiré periods and therefore lower spatial frequency. For the 2D positions as shown in Fig 5.31a, a shift of -119 ± 9 $cm^{-1}\%^{-1}$ and -86 ± 6 $cm^{-1}\%^{-1}$ is observed. It has previously been shown experimentally that the 2D peak shifts under uniaxial stress at a rate of -64 $cm^{-1}\%^{-1}$ and it is predicted that under biaxial stress the rate is -190 $cm^{-1}\%^{-1}$ [179].

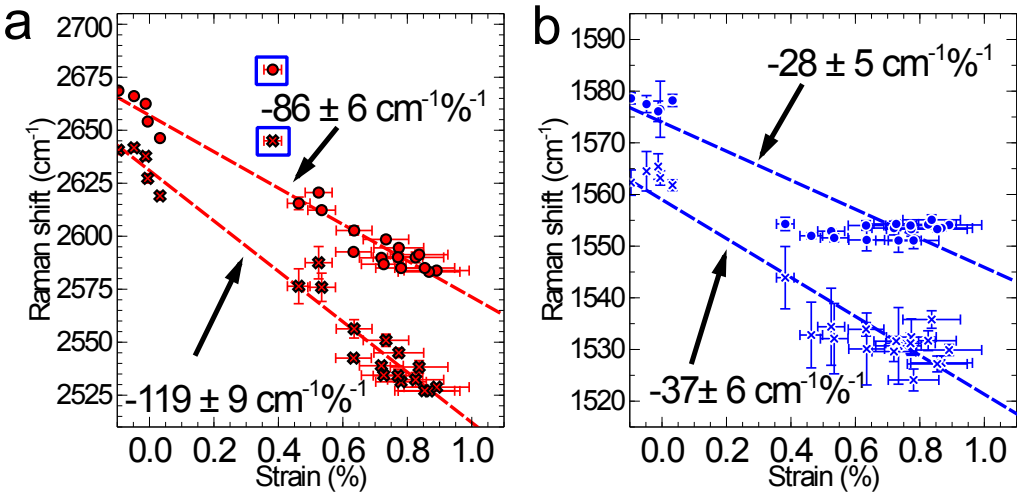

Figure 5.31: Red-shifted a) 2D and b) G peaks as a function of strain for the Raman spectra along the profile in Fig 5.30a. Both are shown with a 1^{st} order polynomial fit to the data with an uncertainty using 95% confidence bounds. The blue boxes in a indicate outliers values close to the boundary region and were not used to calculate the gradient.

The dependence of the red-shifted G peaks is more difficult to determine from this data since the peaks are rather broad as shown in Fig 5.30b. The peak positions give a red-shift dependence of -28 ± 5$cm^{-1}\%^{-1}$ and -37 ± 5$cm^{-1}\%^{-1}$ assuming a linear relationship (which is not completely clear from the data as shown by the uncertainties in the 1^{st} order polynomial

[9]Fitted using the 'cftool' function in Matlab

fit).

From symmetry considerations, the splitting of the G and the 2D peaks of graphene would not be expected for isotropic strain as seen in these measurements. However, the splitting may be due to interactions with the hBN substrate, for example a difference in the local environment of carbon atoms [176].

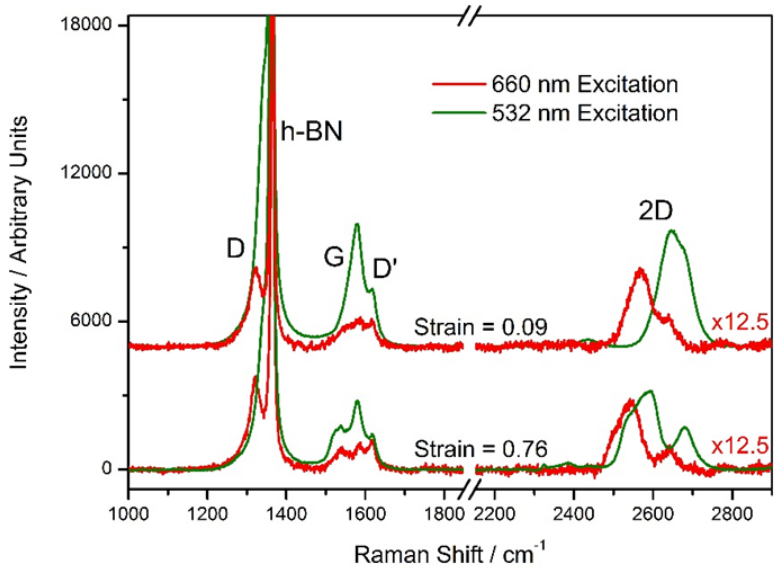

Figure 5.32: Dispersion of graphene on hBN at 660 nm and 532 nm laser excitation for different strain values. The quoted strain values were determined using the gradients in Fig 5.31a.

Figure 5.32 shows the Raman spectra of graphene on hBN for two postitions corresponding to two different strain values at wavelengths of 660 nm (red laser) and 532 nm (green laser). The strain values were inferred from the red-shift of the split 2D peaks using the gradients determined in Fig 5.31a for the linear red-shift/strain relationship. This confirms that, as expected, the 2D peaks are dispersive with excitation wavelength, while the G peaks are not [176]. This also shows that unlike the turbostratic regions, a partner D peak at half the wavenumber of the red-shifted 2D

peak position is not observed which indicates that the strained graphene monolayer has a low defect density and is therefore of high quality.

It is proposed that the strain in the graphene layer is introduced during the high temperature growth process and is maintained by a quasi-random distribution of nucleation sites which act to pin the material. The simplest explanation for the origin of the strain is a difference between the thermal coefficients of expansion of graphene, $\propto_g$, and hBN, $\propto_{hBN}$. A tensile strain of $\sim$1%, as observed here (for the high 26.3 nm moiré period), implies that ($\propto_g$ - $\propto_{hBN}$), averaged over the relevant temperature range (300-1770 K) is positive with a value 8 x 10^{-6} K^{-1}. The coefficient for hBN (the bulk value is relevant for the flakes used here) is -2.9 x 10^{-6} K^{-1} at 300K and remains negative, but with reduced magnitude, up to 800 K. There is considerable divergence in the published values for $\propto_g$; Bao et.al. [215] argue that $\propto_g$ is negative at 300 K, but then increases to a positive value for a temperature, T > 350 K, while Yoon et.al. find a negative value up to 400 K [216]. Most recently, Linas et.al. argued that $\propto_g$ is positive over all measured temperatures in agreement with theoretical predictions [217]. For the maximum temperature (800 K) for which data are available [217], ($\propto_g$ - $\propto_{hBN}$) $\sim$ 3 x 10^{-6} K^{-1}. This is lower than the average quoted above, but it is emphasised that data are not available between 800K and the growth temperature, 1770 K, and, given the uncertainty related to these quantities, thermally-induced strain is a plausible origin for the observed effects.

Graphene grown by CVD on hBN does not exhibit the large moiré pattern reported here and one possible reason for this difference is the pinning role of the nucleation sites in MBE growth; these are not observed

in CVD growth [188, 183, 189]. There are other differences, for example the growing edge of graphene is likely terminated by hydrogen in CVD growth, while hydrogen should be absent during MBE growth (due to the use of a pure carbon source) leading to a more reactive edge and potentially stronger local interaction with the hBN substrate [212].

The overall significance of the Raman data is that the graphene on hBN is highly strained and the spatial strain dependence is well-correlated with the observation of significantly higher moiré periods than reported elsewhere in the literature for epitaxially grown graphene on hBN [183, 188, 189] and graphene/hBN heterostructures formed from exfoliated graphene [160].

5.13 Strain Modification

During contact mode imaging of the graphene lattice, damage to the graphene surface was induced by the cantilever being inadvertently engaged at a high set point for a single line scan. Imaging of this region shows that the graphene has been removed along the trajectory of the cantilever, this is shown in Fig 5.33a. Raman mapping of this hBN flake after the damage shows a distinct difference in CLS fitted Raman maps indicated by the boxed region in Fig 5.33b and c. The green region in Fig 5.33c is indicative of a change in the spectral response (and strain) of the graphene in this region.

Inspection of the moiré patterns in the graphene that remained intact either side of the damaged region suggested that the moiré period had been reduced following the damage which would be indicative of strain

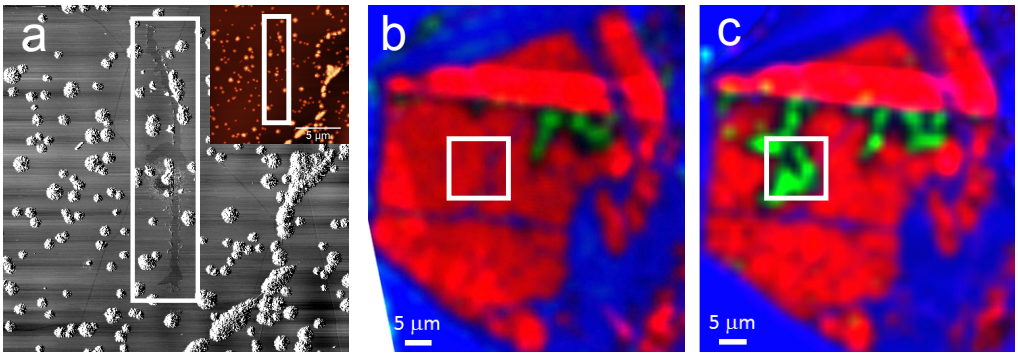

Figure 5.33: a) 15 μm square AC mode AFM phase image of damage to a graphene domain following high set point contact by the AFM cantilever indicated by the box. (inset) Height channel image of the same region. b) Raman mapping of the flake in a before and, c) after damage was induced by an AFM tip showing the change in the Raman signature. The white box in b and c shows the region imaged in a.

relaxation (no moiré patterns were observed in the region at the centre of the damage suggesting that the graphene had been removed and the bare hBN substrate is exposed). Direct registry between the areas before and after the damage had been induced was not possible since the area had not been extensively mapped before the damage had occurred.

To test this hypothesis, damage was intentionally induced on a region of the graphene surface using an AFM tip at a high set point. Several attempts were made to damage the graphene using lines 'drawn' on the graphene with the AFM in lithography mode at high set points but were unsuccessful. Eventually a small damaged area with dimensions ~500 x 150 nm was eventually formed by scanning in contact mode at a high deflection set point of 10 V at a rate of 10 Hz for several seconds[10].

Figures 5.34a and b show amplitude (error signal) channel images (this channel was used as the contrast is clearer than the height channel) of this area before and after the damage had been induced by the AFM tip. This

[10]For comparison, typical set points are < 0.5 V for contact mode imaging such as those shown in Fig 5.25

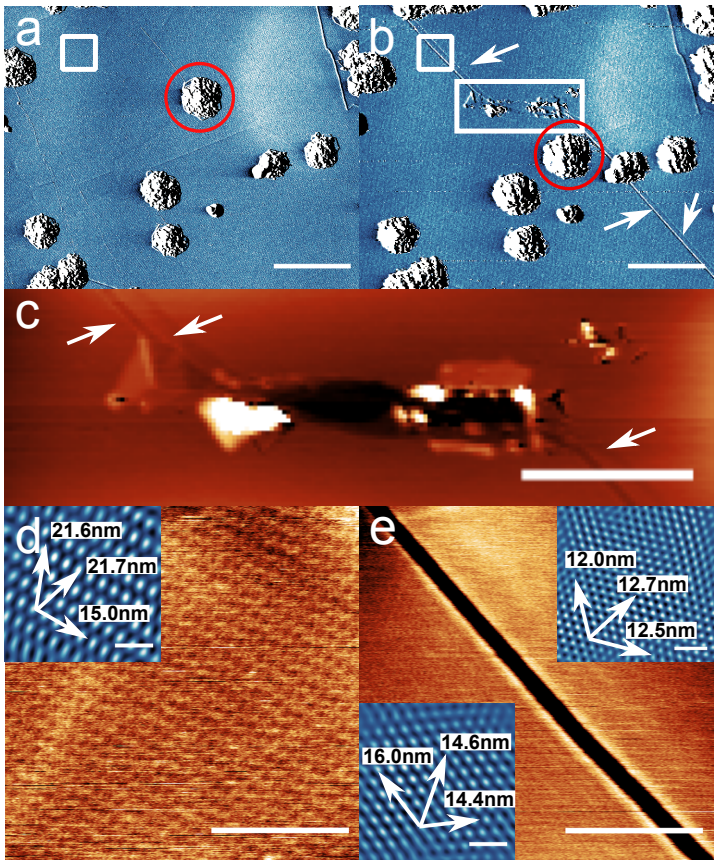

Figure 5.34: a) Amplitude channel AC mode AFM image of a region on the graphene surface before, and b) after the introduction of damage by the AFM tip. The rectangular box in b shows the position of the damaged region and the arrows show the propagation of cracks away from the damaged area. In addition the red circle shows the position of a carbon deposit before and after the damage. Scale bars in a and b are both 880 nm. c) Height images of the damaged region. Scale bar 440 nm. d) Height image of the region indicated by the box shown in a and (inset) phase image showing the moiré period in different directions. e) Height image of the region indicated in the top left of b after the formation of a crack and, (insets) phase images of each side of the crack showing the reduction in moiré period in all directions indicating the strain has been relaxed. Scale bars for d and e are 175 nm in the main images and 45 nm for the inset figures. All images taken in AC mode in ambient conditions.

damaged region is shown in 5.34b and c. Interestingly, two parallel cracks in the graphene are seen to propagate from the centre of the damaged region, these are indicated by the arrows in Figs 5.34b and c and have a

depth of 0.4 nm which is again consistent with what would be expected for a graphene monolayer.

The bulky carbon deposits shown in Fig 5.34 a and b provide registry with the surface and allow inspection of the moiré pattern in a specific region before and after the damage. Figure 5.34d and e show the same area, indicated by the white boxes in the top left corners of Fig 5.34a and b before and after the damage. Viewing the height channel information clearly shows that a crack has propagated through the region and the continuous graphene has been split into two separate domains. The lattice constants of these domains were measured using Fourier filtered images of the phase channel as in section 5.11 and are shown in the insets of Fig 5.34d and e. The lattice constant (averaged over the three principal directions since the graphene is anisotropically strained) of the moiré pattern was reduced from 22 nm to 17 nm and 14 nm for the regions in Fig 5.34e on the left and right side of the tear respectively.

Interestingly, as a result of the modification process, one of the carbon aggregates has been displaced as shown by the red circles in Fig 5.34 a and b. The narrow cracks that propagate from the centre of the damage also run continuously underneath a neighbouring aggregate which implies that the graphene is continuous inderneath these large 3D islands. Raman mapping of this area did not show a noticeable change although this could be due to the small area of damage when compared to the first example shown in Fig 5.33 (500 nm vs 10 μm) and the size of the Raman laser spot ($\sim$1 μm diameter).

5.14 Molecular Adsorption on Graphene/hBN

The incorporation of molecular monolayers with graphene structures make interesting candidates for novel optoelectronic devices, particularly in the case of MBE grown graphene since the high quality of the graphene is comparable with clean exfoliated HOPG surfaces used for the study of adsorbed molecular networks discussed in chapter 4. c-P12 porphyrin nanorings were deposited using the procedures previously detailed onto a graphene/hBN sample with partial graphene coverage. This sample was chosen since c-P12 adsorption onto both HOPG and hBN surfaces has been previously demonstrated in this thesis.

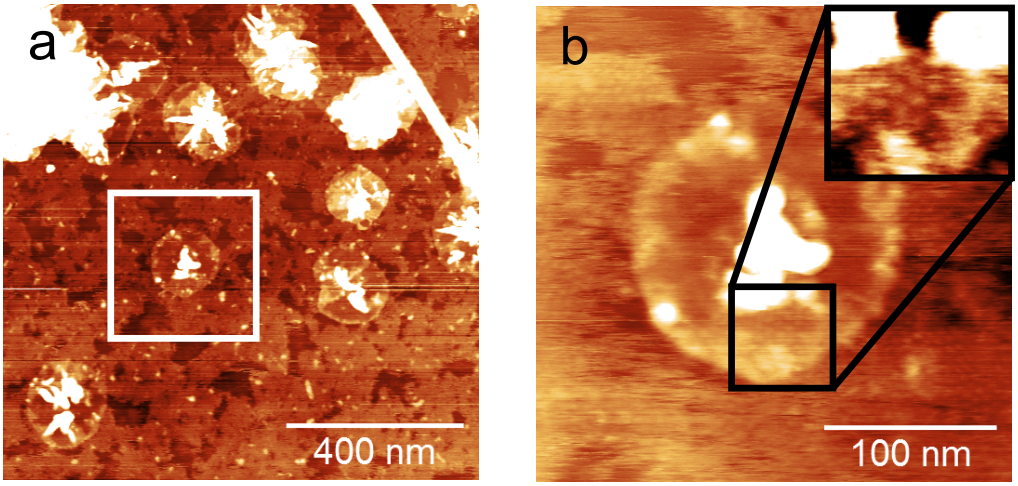

Figure 5.35: a) AC mode AFM image of c-P12 nanorings on the graphene/hBN surface. b) higher resolution images of the region marked in a. The island indicated by the arrow is the same as the one shown in Fig 5.19a and b.

Figure 5.35 shows the structure of small nanoring domains formed on the graphene/hBN surface. The domains are observed to form on both the hBN and graphene areas of the sample. Detailed inspection of the arrangement of c-P12 on the graphene islands is, however, limited by the small size

of the graphene domains and further investigation of c-P12 deposited onto these surfaces is required. The results, however, demonstrate that molecular adsorption on MBE graphene is possible and there are many potential studies that can be performed on the behaviour of these supramolecular assemblies at the graphene/hBN interface. This is of particular interest for the creation of devices that require an electrical contact between the molecular domain and a graphene electrode for example.

5.15 Summary

The results presented in this chapter represent the first reported examples of $\sim$10 μm scale single-crystal graphene grown epitaxially using MBE. They also demonstrate that the graphene is highly strained when graphene is grown on hBN at high temperatures, and that, following growth, the strain in the graphene may be modified by an AFM tip. This indicates the possibility of better controlled routes towards the engineering of more complex strain fields in graphene. This may take the form of lithographic formations of etched holes in the graphene following growth or through fabrication of structures on the hBN surface prior to growth. The work presented here provides strong motivation to study MBE as a route to produce high-quality graphene and to introduce strain in a controlled manner.

The electronic properties of this material also need to be measured to determine the quality of the graphene for comparison with samples reported in the literature. This will likely involve developing a process for the transfer of graphene/hBN onto an insulating substrate such as SiO_2, or removal of the turbostratic graphene from the surrounding sapphire substrate to

electrically isolate the graphene on hBN, critical to the fabrication of electronic devices. Preliminary experiments have shown that hBN flakes can be removed from the sapphire surface and transferred to an SiO_2 surface using adhesive tape, but the associated contamination and the quality of the transfered material has yet to be investigated. There is also the possibility that the strain will be released during transfer, altering the properties following growth in a potentially uncontrolled manner.

The ultimate objective of growing graphene by MBE to make useful devices will make use of a wafer-scale hBN substrate rather than the exfoliated flakes used in this work. This will enable the growth of multiple layer graphene/hBN heterostructures to fabricate many interesting device architectures. As mentioned previously in section 5.7 work is underway to grow hBN on sapphire by MBE and the growth of hBN onto the graphene surface will also need to be investigated.

Chapter 6

Conclusions

The growth of HKUST-1 as a SURMOF presented in chapter 3 raises important questions regarding existing interpretations of the LBL method for SURMOF growth. The results clearly demonstrate that the films deposited using the LBL are not a uniform crystalline film. These results are supported by other reports of a similar nanocrystalline surface structure over a range of growth temperatures on functionalised surfaces [109]. This is in contrast to the uniform growth interface consistently reported in most LBL studies of SURMOF growth. The effects that this nanocrystalline structure has (in particular applications that rely on diffusive processes such as gas absorption into the MOF framework) will need to be studied as it may limit the performance of thin-film MOF devices.

Due to the fact that almost all MOFs, including HKUST-1, are insulating there are few publications on the electronic properties of MOFs. However, Dragässer et al. reported that molecules such as ferrocene can be included in the MOF pores following LBL synthesis to act as a redox mediator and allow the study of charge transport between the MOF pores

[218]. In addition, recent work by Talin et al. has reported that HKUST-1 can be made electrically conductive by the inclusion of a guest molecule absorbed in to the MOF pores following growth [74]. This may allow exploration of the effects of domain boundaries and defects on the conductivity. This would ideally be in a vertical device configuration since control of the crystallographic orientation normal to the substrate, which has been demonstrated in this thesis and repeatedly in the literature, is possible. This would allow measurements of electron transport along known crystallographic directions.

Supramolecular networks of porphyrin nanorings show promising results for the study of large assemblies of light-harvesting molecules on surfaces. The data presented in chapter 4 represents the first example of large-scale structure formation from these nanorings in ambient conditions. Previous studies having been confined to UHV environments and the study of immobilised and isolated rings. These results show how the weak interactions that affect the network formation are sensitive to changes in the rotational symmetry of the nanorings. Further SPM imaging of a wider range of nanoring sizes, in particular rings with six-fold symmetry such as the c-P6 and c-P18 complexes will potentially provide insight into domain size due to the number of porphyrin macrocyles in each ring.

The observation of nanorings forming ordered networks on the hBN surface and the spectroscopic results in section 4.7 also demonstrate that there is potential for integrating these molecules in optoelectronic devices. This may be achieved using techniques for assembly of heterostructures from two dimensional materials. In particular the deposition of nanorings on hBN may allow a layer of nanorings to be integrated as an optically active

layer in a tunelling device or as part of a resonant optical structure such as an etalon. It is planned to fabricate sandwich structures using techniques for the assembly of thin-film devices employed in making graphene/hBN heterostructures that have been reported in the literature.

The growth of graphene on hBN surfaces discussed in chapter 5 demonstrates that high temperature MBE is a viable approach to the growth of high-quality epitaxially-grown graphene. The AFM and Raman results presented in this work clearly demonstrate that graphene can be grown on hBN. The observation of moiré patterns on the surface also supports the theory that the graphene is strained due to the lattice mismatch with the hBN substrate. The observation of highly anisotropic and large moiré patterns on the graphene surface provides motivation to study new approaches to the introduction and modification of strain. However, the parameter space for MBE graphene growth is still relatively unexplored; further work will hopefully address the issue of bulky carbon deposits also present on the hBN surface and lead to higher quality samples. Systematic study of the temperature range where graphene growth is possible may also provide the ability to introduce strain controllably during growth and open up a band gap which is critical if graphene is to be used as part of a transistor device. The epitaxial growth of multi-layered graphene/hBN heterostructures also necessitates the study of hBN growth on graphene surfaces. This could be achieved by using exfoliated graphite flakes on sapphire surfaces and work is already planned to address this. In addition, attempts to grow hBN directly on the sapphire surface are ongoing which will remove the need to use exfoliated hBN substrates.

Chapter 7

Bibliography

[1] G. Binnig and H. Rohrer, "Scanning tunneling microscopy," *Surf. Sci.*, vol. 126, no. 126, pp. 236–244, 1982.

[2] G. Binnig, H. Rohrer, C. Gerber, and E. Weibel, "7 x 7 Reconstruction on Si(111) Resolved in Real Space," *Phys. Rev. Lett.*, vol. 50, pp. 120–123, jan 1983.

[3] D. K. Schweizer and E. K. Eigler, "Positioning single atoms with a scanning tunneling microscop," *Nature*, vol. 344, pp. 524–525, 1990.

[4] M. F. Crommie, C. P. Lutz, and D. M. Eigler, "Confinement of electrons to quantum corrals on a metal surface.," *Science*, vol. 262, no. 5131, pp. 218–220, 1993.

[5] R. P. Feynman, "There's plenty of room at the bottom," *Eng. Sci.*, vol. 23, no. 5, pp. 22–36, 1960.

[6] V. V. Korolkov, S. A. Svatek, A. Summerfield, J. Kerfoot, L. Yang, T. Taniguchi, K. Watanabe, N. R. Champness, N. A. Besley, and P. H. Beton, "Van der Waals-induced chromatic shifts in hydrogen-bonded two-dimensional porphyrin arrays on boron nitride," *ACS Nano*, vol. 9, no. 10, pp. 10347–10355, 2015.

[7] M. Lackinger, S. Griessl, W. A. Heckl, M. Hietschold, and G. W. Flynn, "Self-assembly of trimesic acid at the liquid-solid interface - a study of solvent-induced polymorphism," *Langmuir*, vol. 21, no. 11, pp. 4984–4988, 2005.

[8] S. Griessl, M. Lackinger, M. Edelwirth, M. Hietschold, and W. M. Heckl, "Self-assembled two-dimensional molecular host-guest architectures from trimesic acid," *Single Mol.*, vol. 3, no. 1, pp. 25–31, 2002.

[9] J. P. Garrahan, A. Stannard, M. O. Blunt, and P. H. Beton, "Molecular random tilings as glasses," *PNAS*, vol. 106, pp. 15209–15213, sep 2009.

[10] T. Lin, G. Kuang, X. S. Shang, P. N. Liu, and N. Lin, "Self-assembly of metalorganic coordination networks using on-surface synthesized ligands," *Chem. Commun.*, vol. 50, no. 97, pp. 15327–15329, 2014.

[11] M. O. Blunt, J. C. Russell, N. R. Champness, and P. H. Beton, "Templating molecular adsorption using a covalent organic framework," *Chem. Commun.*, vol. 46, no. 38, pp. 7157–7159, 2010.

[12] O. Shekhah, H. Wang, S. Kowarik, F. Schreiber, M. Paulus, M. Tolan, C. Sternemann, F. Evers, D. Zacher, R. A. Fischer, and C. Wöll, "Step-by-step route for the synthesis of metal-organic frameworks.," *J. Am. Chem. Soc.*, vol. 129, pp. 15118–9, dec 2007.

[13] M. Hoffmann, C. J. Wilson, B. Odell, and H. L. Anderson, "Template-directed synthesis of a π;-conjugated porphyrin nanoring," *Angew. Chemie - Int. Ed.*, vol. 46, no. 17, pp. 3122–3125, 2007.

[14] M. Hoffmann, J. Kärnbratt, M.-H. Chang, L. M. Herz, B. Albinsson, and H. L. Anderson, "Enhanced pi conjugation around a porphyrin[6] nanoring.," *Angew. Chem*, vol. 47, pp. 4993–6, jan 2008.

[15] C.-K. Yong, P. Parkinson, D. V. Kondratuk, W.-H. Chen, A. Stannard, A. Summerfield, J. K. Sprafke, M. C. O'Sullivan, P. H. Beton, H. L. Anderson, and L. M. Herz, "Ultrafast delocalization of excitation in synthetic light-harvesting nanorings," *Chem. Sci.*, vol. 6, pp. 181–189, sep 2015.

[16] P. Parkinson, D. V. Kondratuk, C. Menelaou, J. Q. Gong, H. L. Anderson, and L. M. Herz, "Chromophores in Molecular Nanorings: When Is a Ring a Ring?," *J. Phys. Chem. Lett.*, vol. 5, pp. 4356–4361, nov 2014.

[17] K. S. Novoselov, A. K. Geim, S. V. Morozov, D. Jiang, Y. Zhang, S. V. Dubonos, I. V. Grigorieva, and A. A. Firsov, "Electric field effect in atomically thin carbon films.," *Science*, vol. 306, no. 5696, pp. 666–669, 2004.

[18] X. Li, W. Cai, J. An, S. Kim, J. Nah, D. Yang, R. Piner, A. Velamakanni, I. Jung, E. Tutuc, S. K. Banerjee, L. Colombo, and R. S. Ruoff, "Large-area synthesis of high-quality and uniform graphene films on copper foils.," *Science*, vol. 324, no. 5932, pp. 1312–1314, 2009.

[19] C. R. Dean, A. F. Young, I. Meric, C. Lee, L. Wang, S. Sorgenfrei, K. Watanabe, T. Taniguchi, P. Kim, K. L. Shepard, and J. Hone, "Boron nitride substrates for high-quality graphene electronics.," *Nat. Nanotechnol.*, vol. 5, no. 10, pp. 722–726, 2010.

[20] H. Ohtani, R. J. Wilson, S. Chiang, and C. M. Mate, "Scanning Tunneling Microscopy Observations of Benzene Molecules on the Rh(111)-(33) (C6H6 + 2CO) Surface," *Phys. Rev. Lett.*, vol. 60, no. 23, pp. 2398–2401, 1988.

[21] Nobelprize.org, "Press Release: The 1986 Nobel Prize in Physics," 1986.

[22] C. J. Chen, "Introduction to Scanning Tunneling Microscopy Second Edition," *Oxford Univ. Press*, 2008.

[23] R. Wiesendanger, *Scanning Probe Microscopy and Spectroscopy: Methods and Applications*. Cambridge: Cambridge University Press, first ed., 1994.

[24] J. Tersoff and D. R. Hamann, "Theory of the scanning tunneling microscope," *Phys. Rev. B*, vol. 31, pp. 805–813, jan 1985.

[25] J. Bardeen, "Tunnelling from a Many-Particle Point of View," *Phys. Rev. Lett.*, vol. 6, no. 2, pp. 57–59, 1961.

[26] Bonnell, *Scanning Probe Microscopy and Spectroscopy: Theory, Techniques, and Applications, 2nd Edition*. 2 ed., 2001.

[27] R. Feenstra, J. Stroscio, J. Tersoff, and A. Fein, "Atom-selective imaging of the GaAs(110) surface.," *Phys. Rev. Lett.*, vol. 58, pp. 1192–1195, mar 1987.

[28] J. Repp, G. Meyer, S. M. Stojković, A. Gourdon, and C. Joachim, "Molecules on insulating films: Scanning-tunneling microscopy imaging of individual molecular orbitals," *Phys. Rev. Lett.*, vol. 94, no. 2, pp. 1–4, 2005.

[29] L. Gross, "Recent advances in submolecular resolution with scanning probe microscopy," *Nat. Chem.*, vol. 3, no. 4, pp. 273–278, 2011.

[30] J. Stirling, *Scanning Probe Microscopy from the Perspective of the Sensor*. Phd thesis, Nottingham, 2014.

[31] G. Binnig and C. F. Quate, "Atomic Force Microscope," *Phys. Rev. Lett.*, vol. 56, no. 9, pp. 930–933, 1986.

[32] J. E. Jones, "On the Determination of Molecular Fields. II. From the Equation of State of a Gas," *Proc. R. Soc. A Math. Phys. Eng. Sci.*, vol. 106, no. 738, pp. 463–477, 1924.

[33] A. Bridgwater, "http://www.computerweekly.com/blogs/open-source-insider/2015/11/chef-beefs-up-for-regulatory-compliance.html," 2015.

[34] T. Ladnorg, A. Welle, S. Heißler, C. Wöll, and H. Gliemann, "Site-selective growth of surface-anchored metal-organic frameworks on self-assembled monolayer patterns prepared by AFM nanografting.," *Beilstein J. Nanotechnol.*, vol. 4, pp. 638–48, jan 2013.

[35] Y. Martin and H. K. Wickramasinghe, "Magnetic imaging by "force microscopy" with 1000 Å resolution," *Appl. Phys. Lett.*, vol. 50, no. 20, pp. 1455–1457, 1987.

[36] B. S. Swartzentruber, "Direct Measurement of Surface Diffusion Using Atom-Tracking Scanning Tunneling Microscopy," *Phys. Rev. Lett.*, vol. 76, no. 3, pp. 459–462, 1996.

[37] P. Rahe, J. Schtte, W. Schniederberend, M. Reichling, M. Abe, Y. Sugimoto, and A. Khnle, "Flexible drift-compensation system for precise 3D force mapping in severe drift environments," *Rev. Sci. Instrum.*, vol. 82, no. 6, 2011.

[38] J. W. Cooley and J. W. Tukey, "An Algorithm for the Machine Computation of the Complex Fourier Series," *Math. Comput.*, vol. 19, p. 297, 1965.

[39] D. Tomnek, S. G. Louie, H. J. Mamin, D. W. Abraham, R. E. Thomson, E. Ganz, and J. Clarke, "Theory and observation of highly asymmetric atomic structure in scanning-tunneling-microscopy images of graphite," *Phys. Rev. B*, vol. 35, no. 14, pp. 7790–7793, 1987.

[40] T. Taniguchi and K. Watanabe, "Synthesis of high-purity boron nitride single crystals under high pressure by using Ba-BN solvent," *J. Cryst. Growth*, vol. 303, no. 2, pp. 525–529, 2007.

[41] L. Britnell, R. V. Gorbachev, R. Jalil, B. D. Belle, F. Schedin, A. Mishchenko, T. Georgiou, M. I. Katsnelson, L. Eaves, S. V. Morozov, N. M. R. Peres, J. Leist, A. K. Geim, K. S. Novoselov, and L. A. Ponomarenko, "Field-Effect Tunneling Transistor Based on Vertical Graphene Heterostructures," *Science*, vol. 335, no. 6071, pp. 947–950, 2012.

[42] Y. T. Kim and A. J. Bard, "Imaging and etching of self-assembled n-octadecanethiol layers on gold with the scanning tunneling microscope," *Langmuir*, vol. 8, no. 4, pp. 1096–1102, 1992.

[43] M. Hara, H. Sasabe, and W. Knoll, "Ordered nucleation of a self-assembled monolayer on Au(111) studied by scanning tunneling microscopy," *Thin Solid Films*, vol. 273, no. 95, pp. 66–69, 1996.

[44] Q. Jin, J. A. Rodriguez, C. Z. Li, Y. Darici, and N. J. Tao, "Self-assembly of aromatic thiols on Au (111)," vol. 425, no. October 1998, pp. 101–111, 1999.

[45] C. Munuera, O. Shekhah, H. Wang, C. Wöll, and C. Ocal, "The controlled growth of oriented metal-organic frameworks on functionalized surfaces as followed by scanning force microscopy.," *Phys. Chem. Chem. Phys.*, vol. 10, pp. 7257–61, dec 2008.

[46] J. Liu, O. Shekhah, X. Stammer, H. K. Arslan, B. Liu, B. Schüpbach, A. Terfort, and C. Wöll, "Deposition of Metal-Organic Frameworks by Liquid-Phase Epitaxy: The Influence of Substrate Functional Group Density on Film Orientation," *Materials*, vol. 5, pp. 1581–1592, sep 2012.

[47] S. D. Feyter and F. C. D. Schryver, "Self-Assembly at the Liquid / Solid Interface : STM Reveals," *J. Phys. Chem. B*, vol. 109, no. February, pp. 4290–4302, 2005.

[48] A. Stannard, *Pattern Formation in Nanostructured Systems*. PhD thesis, University of Nottingham, 2010.

[49] A. Summerfield and A. Allen, "Phase Transitions in Two-Dimensional Supramolecular Assemblies," project report, University of Nottingham, Nottingham, 2011.

[50] C. V. Raman, "A new radiation," *Proc. Indian Acad. Sci. - Sect. A*, vol. 37, no. 3, pp. 333–341, 1928.

[51] E. Biemmi, C. Scherb, and T. Bein, "Oriented growth of the metal organic framework Cu(3)(BTC)(2)(H(2)O)(3).xH(2)O tunable with functionalized self-assembled monolayers.," *J. Am. Chem. Soc.*, vol. 129, pp. 8054–5, jul 2007.

[52] H. K. Arslan, O. Shekhah, J. Wohlgemuth, M. Franzreb, R. A. Fischer, and C. Wöll, "High-Throughput Fabrication of Uniform and Homogenous MOF Coatings," *Adv. Funct. Mater.*, vol. 21, pp. 4228–4231, nov 2011.

[53] V. Stavila, J. Volponi, A. M. Katzenmeyer, M. C. Dixon, and M. D. Allendorf, "Kinetics and mechanism of metalorganic framework thin film growth: systematic investigation of HKUST-1 deposition on QCM electrodes," *Chem. Sci.*, vol. 3, no. 5, p. 1531, 2012.

[54] X. Lin, J. Jia, X. Zhao, K. M. Thomas, A. J. Blake, G. S. Walker, N. R. Champness, P. Hubberstey, and M. Schröder, "High H2 Adsorption by Coordination-Framework Materials," *Angew. Chem*, vol. 45, no. 44, pp. 7358–7364, 2006.

[55] H. Li, M. Eddaoudi, M. O'Keeffe, and O. M. Yaghi, "Design and synthesis of an exceptionally stable and highly porous metal-organic framework," vol. 402, pp. 276–279, nov 1999.

[56] A. U. Czaja, N. Trukhan, and U. Müller, "Industrial applications of metal-organic frameworks.," *Chem. Soc. Rev.*, vol. 38, pp. 1284–93, may 2009.

[57] A. P. Nelson, O. K. Farha, K. L. Mulfort, and J. T. Hupp, "Supercritical processing as a route to high internal surface areas and permanent microporosity in metal-organic framework materials.," *J. Am. Chem. Soc.*, vol. 131, pp. 458–60, jan 2009.

[58] O. Shekhah, H. Wang, T. Strunskus, P. Cyganik, D. Zacher, R. A. Fischer, and C. Wöll, "Layer-by-layer growth of oriented metal organic polymers on a functionalized organic surface.," *Langmuir*, vol. 23, pp. 7440–2, jul 2007.

[59] D. Zacher, K. Yusenko, A. Bétard, S. Henke, M. Molon, T. Ladnorg, O. Shekhah, B. Schüpbach, T. de los Arcos, M. Krasnopolski, M. Meilikhov, J. Winter, A. Terfort, C. Wöll, and R. A. Fischer, "Liquid-phase epitaxy of multicomponent layer-based porous coordination polymer thin films of [M(L)(P)0.5] type: importance of deposition sequence on the oriented growth.," *Chem. - A Eur. J.*, vol. 17, pp. 1448–55, feb 2011.

[60] J.-R. Li, R. J. Kuppler, and H.-C. Zhou, "Selective gas adsorption and separation in metal-organic frameworks.," *Chem. Soc. Rev.*, vol. 38, pp. 1477–504, may 2009.

[61] L. J. Murray, M. Dinc, and J. R. Long, "Hydrogen storage in metal-organic frameworks.," *Chem. Soc. Rev.*, vol. 38, pp. 1294–314, may 2009.

[62] M. D. Allendorf, A. Schwartzberg, V. Stavila, and A. A. Talin, "A roadmap to implementing metal-organic frameworks in electronic

devices: challenges and critical directions.," *Chemistry*, vol. 17, pp. 11372–88, oct 2011.

[63] O. Shekhah, J. Liu, R. A. Fischer, and C. Wöll, "MOF thin films: existing and future applications.," *Chem. Soc. Rev.*, vol. 40, pp. 1081–106, feb 2011.

[64] M. Meilikhov, S. Furukawa, K. Hirai, R. A. Fischer, and S. Kitagawa, "Binary Janus porous coordination polymer coatings for sensor devices with tunable analyte affinity.," *Angew. Chem*, vol. 52, pp. 341–5, jan 2013.

[65] J. Goldsmith, A. G. Wong-Foy, M. J. Cafarella, and D. J. Siegel, "Theoretical Limits of Hydrogen Storage in MetalOrganic Frameworks: Opportunities and Trade-Offs," *Chem. Mater.*, vol. 25, no. 16, pp. 3373–3382, 2013.

[66] Y. Yan, S. Yang, A. J. Blake, W. Lewis, E. Poirier, S. a. Barnett, N. R. Champness, and M. Schröder, "A mesoporous metal-organic framework constructed from a nanosized C(3)-symmetric linker and [Cu(24)(isophthalate)(24)] cuboctahedra.," *Chem. Commun.*, vol. 47, pp. 9995–9997, sep 2011.

[67] Y. Yan, X. Lin, S. Yang, A. J. Blake, A. Dailly, N. R. Champness, P. Hubberstey, and M. Schröder, "Exceptionally high H2 storage by a metal-organic polyhedral framework.," *Chem. Commun.*, pp. 1025–1027, mar 2009.

[68] A. Stannard, M. O. Blunt, P. H. Beton, and J. P. Garrahan, "Entropically stabilized growth of a two-dimensional random tiling," *Phys. Rev. E*, vol. 82, p. 41109, oct 2010.

[69] A. Stannard, J. C. Russell, M. O. Blunt, C. Salesiotis, M. d. C. Giménez-López, N. Taleb, M. Schröder, N. R. Champness, J. P. Garrahan, and P. H. Beton, "Broken symmetry and the variation of critical properties in the phase behaviour of supramolecular rhombus tilings.," *Nat. Chem.*, vol. 4, pp. 112–7, feb 2012.

[70] H. Deng, S. Grunder, K. E. Cordova, C. Valente, H. Furukawa, M. Hmadeh, F. Gándara, A. C. Whalley, Z. Liu, S. Asahina, H. Kazumori, M. O'Keeffe, O. Terasaki, J. F. Stoddart, and O. M. Yaghi, "Large-pore apertures in a series of metal-organic frameworks.," *Science*, vol. 336, pp. 1018–23, may 2012.

[71] C. G. Silva, A. Corma, and H. García, "Metalorganic frameworks as semiconductors," *J. Mater. Chem.*, vol. 20, no. 16, p. 3141, 2010.

[72] L. Ma, C. Abney, and W. Lin, "Enantioselective catalysis with homochiral metal-organic frameworks.," *Chem. Soc. Rev.*, vol. 38, pp. 1248–56, may 2009.

[73] K. M. Choi, H. M. Jeong, J. H. Park, Y.-B. Zhang, J. K. Kang, and O. M. Yaghi, "Supercapacitors of Nanocrystalline Metal-Organic Frameworks.," *ACS Nano*, vol. 8, pp. 7451–7, jul 2014.

[74] A. A. Talin, A. Centrone, A. C. Ford, M. E. Foster, V. Stavila, P. Haney, R. A. Kinney, V. Szalai, F. El Gabaly, H. P. Yoon, F. Léonard, and M. D. Allendorf, "Tunable electrical conductivity in metal-organic framework thin-film devices.," *Science*, vol. 343, pp. 66–9, dec 2014.

[75] S. M. Yoon, S. C. Warren, and B. A. Grzybowski, "Storage of electrical information in metal-organic-framework memristors.," *Angew. Chem*, vol. 53, pp. 4437–41, apr 2014.

[76] E. Redel, Z. Wang, S. Walheim, J. Liu, H. Gliemann, and C. Wöll, "On the dielectric and optical properties of surface-anchored metal-organic frameworks: A study on epitaxially grown thin films," *Appl. Phys. Lett.*, vol. 103, no. 9, pp. 14–19, 2013.

[77] S. Hermes, D. Zacher, A. Baunemann, C. Wöll, and R. A. Fischer, "Selective growth and MOCVD loading of small single crystals of MOF-5 at alumina and silica surfaces modified with organic self-assembled monolayers," *Chem. Mater.*, no. 9, pp. 2168–2173, 2007.

[78] S. Hermes, F. Schröder, R. Chelmowski, C. Wöll, and R. A. Fischer, "Selective nucleation and growth of metal-organic open framework thin films on patterned COOH/CF3-terminated self-assembled monolayers on Au(111).," *J. Am. Chem. Soc.*, vol. 127, pp. 13744–5, oct 2005.

[79] D. Bradshaw, A. Garai, and J. Huo, "Metal-organic framework growth at functional interfaces: thin films and composites for diverse applications.," *Chem. Soc. Rev.*, vol. 41, pp. 2344–81, mar 2012.

[80] D. Zacher, A. Baunemann, S. Hermes, and R. A. Fischer, "Deposition of microcrystalline [Cu3(btc)2] and [Zn2(bdc)2(dabco)] at alumina and silica surfaces modified with patterned self assembled organic monolayers: evidence of surface selective and oriented growth," *J. Mater. Chem.*, vol. 17, no. 27, p. 2785, 2007.

[81] P. Falcaro, R. Ricco, C. M. Doherty, K. Liang, A. J. Hill, and M. J. Styles, "MOF positioning technology and device fabrication.," *Chem. Soc. Rev.*, vol. 43, no. 16, pp. 5513–5560, 2014.

[82] K. Szelagowska-Kunstman, P. Cyganik, M. Goryl, D. Zacher, Z. Puterova, R. A. Fischer, and M. Szymonski, "Surface structure of metal-organic framework grown on self-assembled monolayers revealed by high-resolution atomic force microscopy.," *J. Am. Chem. Soc.*, vol. 130, pp. 14446–7, nov 2008.

[83] D. Zacher, O. Shekhah, C. Wöll, and R. A. Fischer, "Thin films of metal-organic frameworks.," *Chem. Soc. Rev.*, vol. 38, pp. 1418–29, may 2009.

[84] H. Gliemann and C. Wöll, "Epitaxially grown metal-organic frameworks," *Mater. Today*, vol. 15, pp. 110–116, mar 2012.

[85] O. Shekhah, K. Hirai, H. Wang, H. Uehara, M. Kondo, S. Diring, D. Zacher, R. A. Fischer, O. Sakata, S. Kitagawa, S. Furukawa, and C. Wöll, "MOF-on-MOF heteroepitaxy: perfectly oriented [Zn2(ndc)2(dabco)]n grown on [Cu2(ndc)2(dabco)]n thin films.," *Dalton Trans.*, vol. 40, pp. 4954–8, may 2011.

[86] L. Heinke, M. Cakici, M. Dommaschk, S. Grosjean, R. Herges, S. Bräse, and C. Wöll, "Photoswitching in two-component surface-mounted metal-organic frameworks: optically triggered release from a molecular container," *ACS Nano*, vol. 8, pp. 1463–1467, jan 2014.

[87] M. Tu and R. A. Fischer, "Heteroepitaxial growth of surface mounted metalorganic framework thin films with hybrid adsorption functionality," *J. Mater. Chem. A*, vol. 2, no. 7, pp. 2018–2022, 2014.

[88] K. Otsubo, T. Haraguchi, O. Sakata, A. Fujiwara, and H. Kitagawa, "Step-by-step fabrication of a highly oriented crystalline three-dimensional pillared-layer-type metal-organic framework thin film confirmed by synchrotron X-ray diffraction.," *J. Am. Chem. Soc.*, vol. 134, pp. 9605–8, jun 2012.

[89] O. Shekhah, H. K. Arslan, K. Chen, M. Schmittel, R. Maul, W. Wenzel, and C. Wöll, "Post-synthetic modification of epitaxially grown, highly oriented functionalized MOF thin films.," *Chem. Commun.*, vol. 47, pp. 11210–2, oct 2011.

[90] B. Liu, M. Ma, D. Zacher, A. Bétard, K. Yusenko, N. Metzler-Nolte, C. Wöll, and R. A. Fischer, "Chemistry of SURMOFs: layer-selective installation of functional groups and post-synthetic covalent modification probed by fluorescence microscopy.," *J. Am. Chem. Soc.*, vol. 133, pp. 1734–7, feb 2011.

[91] O. Shekhah, "Layer-by-Layer Method for the Synthesis and Growth of Surface Mounted Metal-Organic Frameworks (SURMOFs)," *Materials*, vol. 3, pp. 1302–1315, feb 2010.

[92] O. Shekhah, H. Wang, D. Zacher, R. A. Fischer, and C. Wöll, "Growth mechanism of metal-organic frameworks: insights into the nucleation by employing a step-by-step route.," *Angew. Chem*, vol. 48, pp. 5038–41, jan 2009.

[93] C. Shen, I. Cebula, C. Brown, J. Zhao, M. Zharnikov, and M. Buck, "Structure of isophthalic acid based monolayers and its relation to the initial stages of growth of metalorganic coordination layers," *Chem. Sci.*, vol. 3, no. 6, p. 1858, 2012.

[94] S. S. Chui, S. M. F. Lo, J. P. H. Charmant, A. G. Orpen, and I. D. Williams, "A Chemically Functionalizable Nanoporous Material [Cu3(TMA)2(H2O)3]n," *Science*, vol. 283, pp. 1148–1150, feb 1999.

[95] F. H. Allen, "The Cambridge Structural Database: a quarter of a million crystal structures and rising," *Acta Crystallogr. Sect. B*, vol. 58, pp. 380–388, jun 2002.

[96] A. Kumar and G. M. Whitesides, "Features of gold having micrometer to centimeter dimensions can be formed through a combination of stamping with an elastomeric stamp and an alkanethiol "ink" followed by chemical etching," *Appl. Phys. Lett.*, vol. 63, no. 14, pp. 2002–2004, 1993.

[97] R. Thakar and L. A. Baker, "Lithography-free production of stamps for microcontact printing of arrays," *Anal. Methods*, vol. 2, no. 8, p. 1180, 2010.

[98] Y. Xia and G. M. Whitesides, "Self-assembled Monolayer Films: Microcontact Printing," *Encycl. Mater. Sci. Technol.*, pp. 8309–8315, 1998.

[99] I. Cebula, C. Shen, and M. Buck, "Isophthalic acid: a basis for highly ordered monolayers.," *Angew. Chem*, vol. 49, pp. 6220–3, aug 2010.

[100] C. Carbonell, I. Imaz, and D. Maspoch, "Single-crystal metal-organic framework arrays.," *J. Am. Chem. Soc.*, vol. 133, pp. 2144–7, feb 2011.

[101] S. Li, W. Shi, G. Lu, S. Li, S. C. J. Loo, and F. Huo, "Unconventional nucleation and oriented growth of ZIF-8 crystals on non-polar surface," *Adv. Mater.*, vol. 24, pp. 5954–5958, aug 2012.

[102] J.-L. Zhuang, D. Ceglarek, S. Pethuraj, and A. Terfort, "Rapid Room-Temperature Synthesis of Metal-Organic Framework HKUST-1 Crystals in Bulk and as Oriented and Patterned Thin Films," *Adv. Funct. Mater.*, vol. 21, pp. 1442–1447, apr 2011.

[103] D. G. T. Strange and M. L. Oyen, "Biomimetic bone-like composites fabricated through an automated alternate soaking process.," *Acta Biomater.*, vol. 7, pp. 3586–94, oct 2011.

[104] P. Falcaro, D. Buso, A. J. Hill, and C. M. Doherty, "Patterning techniques for metal organic frameworks.," *Adv. Mater.*, vol. 24, pp. 3153–68, jun 2012.

[105] A. Summerfield, I. Cebula, M. Schröder, and P. H. Beton, "Nucleation and Early Stages of Layer-by-Layer Growth of Metal Organic Frameworks on Surfaces," *J. Phys. Chem. C*, vol. 119, pp. 23544–23551, oct 2015.

[106] D. Zacher, R. Schmid, C. Wöll, and R. A. Fischer, "Surface chemistry of metal-organic frameworks at the liquid-solid interface.," *Angew. Chem*, vol. 50, pp. 176–99, jan 2011.

[107] M. W. Anderson, N. S. John, C. Scherb, M. Sho, M. P. Attfield, T. Bein, and M. Shöâeè, "Single layer growth of sub-micron metal-organic framework crystals observed by in situ atomic force microscopy.," *Chem. Commun.*, vol. 2, pp. 6294–6, dec 2009.

[108] S. Amirjalayer, M. Tafipolsky, and R. Schmid, "Surface Termination of the Metal-Organic Framework HKUST-1: A Theoretical Investigation," *J. Phys. Chem. Lett.*, vol. 5, no. 18, pp. 3206–3210, 2014.

[109] M. L. Ohnsorg, C. K. Beaudoin, and M. E. Anderson, "Fundamentals of MOF Thin Film Growth via Liquid-Phase Epitaxy: Investigating the Initiation of Deposition and the Influence of Temperature," *Langmuir*, vol. 31, no. 22, pp. 6114–6121, 2015.

[110] S. Bundschuh, O. Kraft, H. K. Arslan, H. Gliemann, P. G. Weidler, and C. Wöll, "Mechanical properties of metal-organic frameworks: An indentation study on epitaxial thin films," *Appl. Phys. Lett.*, vol. 101, no. 10, pp. 1–5, 2012.

[111] G. W. Mudd, S. A. Svatek, L. Hague, O. Makarovsky, Z. R. Kudrynskyi, C. J. Mellor, P. H. Beton, L. Eaves, K. S. Novoselov, Z. D. Kovalyuk, E. E. Vdovin, A. J. Marsden, N. R. Wilson, and A. Patanè, "High Broad-Band Photoresponsivity of Mechanically Formed InSeGraphene van der Waals Heterostructures," *Adv. Mater.*, vol. 27, no. 25, pp. 3760–3766, 2015.

[112] F. Moreau, T. L. Easun, A. Dailly, M. Lennox, W. Lewis, A. J. Blake, E. Bichoutskaia, and M. Schroder, "Engineering porosity and gas uptake in a series of octacarboxylate based Metal-Organic Frameworks," *Prep.*, 2015.

[113] S. R. Batten and R. Robson, "Interpenetrating Nets: Ordered, Periodic Entanglement," *Angew. Chem*, vol. 37, no. 11, pp. 1460–1494, 1998.

[114] R. Haldar, N. Sikdar, and T. K. Maji, "Interpenetration in coordination polymers: Structural diversities toward porous functional materials," 2015.

[115] O. M. Yaghi, M. O'Keeffe, N. W. Ockwig, H. K. Chae, M. Eddaoudi, and J. Kim, "Reticular synthesis and the design of new materials.," *Nature*, vol. 423, no. 6941, pp. 705–714, 2003.

[116] C. Wiktor, S. Turner, D. Zacher, R. A. Fischer, and G. V. Tendeloo, "Imaging of intact MOF-5 nanocrystals by advanced TEM at liquid nitrogen temperature," *Microporous Mesoporous Mater.*, vol. 162, pp. 131–135, 2012.

[117] S. Turner, O. I. Lebedev, F. Schro, D. Esken, and R. a. Fischer, "Direct Imaging of Loaded Metal-Organic Framework Materials (Metal @ MOF-5)," *Framework*, no. 12, pp. 5622–5627, 2008.

[118] R. J. T. Houk, B. W. Jacobs, F. El Gabaly, N. N. Chang, A. A. Talin, D. D. Graham, S. D. House, I. M. Robertson, M. D. Allendorf, and F. E. Gabaly, "Silver cluster formation, dynamics, and chemistry in metal-organic frameworks.," *Nano Lett.*, vol. 9, no. 10, pp. 3413–8, 2009.

[119] Z. Wei, W. Lu, H.-l. Jiang, and H.-c. Zhou, "A Route to Metal Organic Frameworks through Framework Templating," vol. 4, pp. 2012–2014, 2013.

[120] S. Rode, N. Oyabu, K. Kobayashi, H. Yamada, and A. Kühnle, "True atomic-resolution imaging of (1014) calcite in aqueous solution by frequency modulation atomic force microscopy," *Langmuir*, vol. 25, no. 5, pp. 2850–2853, 2009.

[121] H. L. Anderson, "Building molecular wires from the colours of life: conjugated porphyrin oligomers," *Chem. Commun.*, no. 23, pp. 2323–2330, 1999.

[122] P. Rothemund, "Formation of Porphyrins from Pyrrole and Aldehydes," *J. Am. Chem. Soc.*, vol. 57, no. 10, pp. 2010–2011, 1935.

[123] P. Rothemund, "A New Porphyrin Synthesis. The Synthesis of Porphin 1," *J. Am. Chem. Soc.*, vol. 58, no. 4, pp. 625–627, 1936.

[124] A. D. Adler, F. R. Longo, J. D. Finarelli, J. Goldmacher, J. Assour, and L. Korsakoff, "A simplified synthesis for meso-tetraphenylporphine," *J. Org. Chem.*, vol. 32, no. 2, p. 476, 1967.

[125] J. S. Lindsey, I. C. Schreiman, H. C. Hsu, P. C. Kearney, and A. M. Marguerettaz, "Rothemund and Adler-Longo reactions revisited: synthesis of tetraphenylporphyrins under equilibrium conditions," *J. Org. Chem.*, vol. 52, no. 5, pp. 827–836, 1987.

[126] E. Hückel, "Quantentheoretische Beiträge zum Problem der aromatischen und ungesättigten Verbindungen. III," *Zeitschrift für Phys.*, vol. 76, pp. 628–648, sep 1932.

[127] C. Soret, "Ueber ein Refractometer zur Messung der Brechungsexponentenund der Dispersion fester Körper," *Zeitschrift für Krist. - Cryst. Mater.*, vol. 7, jan 1883.

[128] J. S. Baskin, H. Z. Yu, and A. H. Zewail, "Ultrafast dynamics of porphyrins in the condensed phase: I. Free base tetraphenylporphyrin," *J. Phys. Chem. A*, vol. 106, no. 42, pp. 9837–9844, 2002.

[129] M. Gouterman, "Spectra of porphyrins," *J. Mol. Spectrosc.*, vol. 6, pp. 138–163, jan 1961.

[130] L. R. Milgrom, *The colours of life : an introduction to the chemistry of porphyrins and related compounds.* Oxford [etc.]: Oxford University Press, 1997.

[131] T. Tanaka and A. Osuka, "Conjugated porphyrin arrays: synthesis, properties and applications for functional materials.," *Chem. Soc. Rev.*, vol. 44, pp. 943–969, 2014.

[132] G. McDermott, S. M. Prince, A. A. Freer, A. M. Hawthornthwaite-Lawless, M. Z. Papiz, R. J. Cogdell, and N. W. Isaacs, "Crystal structure of an integral membrane light-harvesting complex from photosynthetic bacteria," 1995.

[133] S. Scheuring, F. Reiss-Husson, A. Engel, J. L. Rigaud, and J. L. Ranck, "High-resolution AFM topographs of Rubrivivax gelatinosus light-harvesting complex LH2," *EMBO J.*, vol. 20, no. 12, pp. 3029–3035, 2001.

[134] S. Scheuring, J. Seguin, S. Marco, D. Lévy, B. Robert, and J.-L. Rigaud, "Nanodissection and high-resolution imaging of the Rhodopseudomonas viridis photosynthetic core complex in native membranes by AFM," *Proc. Natl. Acad. Sci.*, vol. 100, no. 4, pp. 1690–1693, 2003.

[135] S. Scheuring, T. Boudier, and J. N. Sturgis, "From high-resolution AFM topographs to atomic models of supramolecular assemblies," *J. Struct. Biol.*, vol. 159, no. 2, pp. 268–276, 2007.

[136] S. Scheuring and J. N. Sturgis, "Atomic force microscopy of the bacterial photosynthetic apparatus: Plain pictures of an elaborate machinery," *Photosynth. Res.*, vol. 102, no. 2, pp. 197–211, 2009.

[137] L.-N. Liu and S. Scheuring, "Investigation of photosynthetic membrane structure using atomic force microscopy.," *Trends Plant Sci.*, vol. 18, no. 5, pp. 277–86, 2013.

[138] M. U. Winters, E. Dahlstedt, H. E. Blades, C. J. Wilson, M. J. Frampton, H. L. Anderson, and B. Albinsson, "Probing the efficiency of electron transfer through porphyrin-based molecular wires.," *J. Am. Chem. Soc.*, vol. 129, no. 14, pp. 4291–7, 2007.

[139] A. Saywell, J. K. Sprafke, L. J. Esdaile, A. J. Britton, A. Rienzo, H. L. Anderson, J. N. O'Shea, and P. H. Beton, "Conformation and packing of porphyrin polymer chains deposited using electrospray on a gold surface.," *Angew. Chem*, vol. 49, pp. 9136–9, nov 2010.

[140] H. L. Anderson, S. J. Martin, and D. D. C. Bradley, "Synthesis and Third-Order Nonlinear Optical Properties of a Conjugated Porphyrin Polymer," *Angew. Chemie Int. Ed. English*, vol. 33, no. 6, pp. 655–657, 1994.

[141] S. Anderson, H. L. Anderson, and J. K. M. Sanders, "Template-directed synthesis of linear and cyclic butadiyne-linked porphyrin oligomers up to a linear octamer," *J. Chem. Soc. Perkin Trans. 1*, vol. 2, no. 18, p. 2247, 1995.

[142] C. Glaser, "Beiträge zur Kenntniss des Acetenylbenzols," *Berichte der Dtsch. Chem. Gesellschaft*, vol. 2, no. 1, pp. 422–424, 1869.

[143] A. Hay, "Oxidative Coupling of Acetylenes. II1," *J. Org. Chem.*, no. Ii, pp. 3–4, 1962.

[144] H. L. Anderson and J. K. M. Sanders, "Synthesis of a cyclic porphyrin trimer with a semi-rigid cavity," *J. Chem. Soc. Chem. Commun.*, no. 22, p. 1714, 1989.

[145] M. C. O'Sullivan, J. K. Sprafke, D. V. Kondratuk, C. Rinfray, T. D. W. Claridge, A. Saywell, M. O. Blunt, J. N. O'Shea, P. H. Beton, M. Malfois, and H. L. Anderson, "Vernier templating and synthesis of a 12-porphyrin nano-ring.," *Nature*, vol. 469, pp. 72–5, jan 2011.

[146] D. V. Kondratuk, L. M. A. Perdigão, A. M. S. Esmail, J. N. O'Shea, P. H. Beton, and H. L. Anderson, "Supramolecular nesting of cyclic polymers," *Nat. Chem.*, vol. 7, no. April, pp. 317–322, 2015.

[147] O. V. Salata, "Tools of Nanotechnology: Electrospray," *Curr. Nanosci.*, vol. 1, no. 1, pp. 25–33, 2005.

[148] J. N. O'Shea, J. B. Taylor, J. C. Swarbrick, G. Magnano, L. C. Mayor, and K. Schulte, "Electrospray deposition of carbon nanotubes in vacuum.," *Nanotechnology*, vol. 18, no. 3, p. 035707, 2007.

[149] L. C. Mayor, A. Saywell, G. Magnano, C. J. Satterley, J. Schnadt, and J. N. O'Shea, "Adsorption of a Ru(II) dye complex on the Au(111) surface: Photoemission and scanning tunneling microscopy," *J. Chem. Phys.*, vol. 130, no. 16, 2009.

[150] D. V. Kondratuk, L. M. A. Perdigão, M. C. O'Sullivan, S. Svatek, G. Smith, J. N. O'Shea, P. H. Beton, and H. L. Anderson, "Two Vernier-templated routes to a 24-porphyrin nanoring.," *Angew. Chem*, vol. 51, pp. 6696–9, jul 2012.

[151] S. A. Svatek, L. M. A. Perdigão, A. Stannard, M. B. Wieland, D. V. Kondratuk, H. L. Anderson, J. N. O'Shea, and P. H. Beton, "Mechanical stiffening of porphyrin nanorings through supramolecular columnar stacking," *Nano Lett.*, vol. 13, pp. 3391–3395, jun 2013.

[152] D. V. Kondratuk, J. K. Sprafke, M. C. O'Sullivan, L. M. A. Perdigão, A. Saywell, M. Malfois, J. N. O'Shea, P. H. Beton, A. L. Thompson, and H. L. Anderson, "Vernier-Templated Synthesis, Crystal Structure, and Supramolecular Chemistry of a 12-Porphyrin Nanoring," *Chem. - A Eur. J.*, vol. 20, no. 40, pp. 12826–12834, 2014.

[153] N. Metropolis, A. W. Rosenbluth, M. N. Rosenbluth, A. H. Teller, and E. Teller, "Equation of State Calculations by Fast Computing Machines," *J. Chem. Phys.*, vol. 21, no. 6, pp. 1087–1092, 1953.

[154] R. M. Stallman, "Using the GNU Compiler Collection," 2012.

[155] M. Kasha, "Energy Transfer Mechanisms and the Molecular Exciton Model for Molecular Aggregates," *Radiat. Res.*, vol. 20, pp. 55–70, 1963.

[156] M. Kasha, H. R. Rawls, and M. Ashraf El-Bayoumi, "The exciton model in molecular spectroscopy," *Pure Appl. Chem.*, vol. 11, no. 3-4, pp. 371–392, 1965.

[157] M. H. Chang, M. Hoffmann, H. L. Anderson, and L. M. Herz, "Dynamics of excited-state conformational relaxation and electronic delocalization in conjugated porphyrin oligomers," *J. Am. Chem. Soc.*, vol. 130, no. 31, pp. 10171–10178, 2008.

[158] M. H. Chang, F. J. M. Hoeben, P. Jonkheijm, a. P. H. J. Schenning, E. W. Meijer, C. Silva, and L. M. Herz, "Influence of mesoscopic ordering on the photoexcitation transfer dynamics in supramolecular assemblies of oligo-p-phenylenevinylene," *Chem. Phys. Lett.*, vol. 418, no. 1-3, pp. 196–201, 2006.

[159] S. Whitelam, I. Tamblyn, J. P. Garrahan, and P. H. Beton, "Emergent rhombus tilings from molecular interactions with m-fold rotational symmetry," *Phys. Rev. Lett.*, vol. 114, no. 11, pp. 1–5, 2015.

[160] C. R. Woods, L. Britnell, A. Eckmann, R. S. Ma, J. C. Lu, H. M. Guo, X. Lin, G. L. Yu, Y. Cao, R. V. Gorbachev, A. V. Kretinin, J. Park, L. A. Ponomarenko, M. I. Katsnelson, Y. N. Gornostyrev, K. Watanabe, T. Taniguchi, C. Casiraghi, H.-j. Gao, A. K. Geim, and K. S. Novoselov, "Commensurate incommensurate transition in graphene on hexagonal boron nitride," *Nat. Phys.*, vol. 10, no. June, pp. 1–6, 2014.

[161] Nobelprize.org, "The 2010 Nobel Prize in Physics - Press Release," 2010.

[162] K. S. Novoselov, V. I. Fal'ko, L. Colombo, P. R. Gellert, M. G. Schwab, and K. Kim, "A roadmap for graphene," *Nature*, vol. 490, no. 7419, pp. 192–200, 2012.

[163] J. Hedberg, "Images of C60 and carbon nanotubes," *www.jameshedberg.com*, 2015.

[164] E. Wieser, "Rendering of a Multi-walled carbon nanotube," *Wikimedia Commons wikimedia.org/wiki/File:Multi-walled_Carbon_Nanotube.png*, 2010.

[165] A. H. Castro Neto, N. M. R. Peres, K. S. Novoselov, A. K. Geim, F. Guinea, and A. Neto, "The electronic properties of graphene," *Rev. Mod. Phys.*, vol. 81, no. 1, pp. 109–162, 2009.

[166] P. R. Wallace, "The band theory of graphite," *Phys. Rev.*, vol. 71, no. 9, pp. 622–634, 1947.

[167] A. K. Geim, K. S. Novoselov, Geim A. K., and Novoselov K. S., "The rise of graphene.," *Nat. Mater.*, pp. 183–191, 2007.

[168] A. S. Mayorov, R. V. Gorbachev, S. V. Morozov, L. Britnell, R. Jalil, L. A. Ponomarenko, P. Blake, K. S. Novoselov, K. Watanabe, T. Taniguchi, and A. K. Geim, "Micrometer-scale ballistic transport in encapsulated graphene at room temperature," *Nano Lett.*, vol. 11, no. 6, pp. 2396–2399, 2011.

[169] K. S. Novoselov, A. K. Geim, S. V. Morozov, D. Jiang, M. I. Katsnelson, I. V. Grigorieva, S. V. Dubonos, and A. A. Firsov, "Two-dimensional gas of massless Dirac fermions in graphene.," *Nature*, vol. 438, pp. 197–200, nov 2005.

[170] K. S. Novoselov, Z. Jiang, Y. Zhang, S. V. Morozov, H. L. Stormer, U. Zeitler, J. C. Maan, G. S. Boebinger, P. Kim, and A. K. Geim, "Room-temperature quantum Hall effect in graphene.," *Science*, vol. 315, p. 1379, mar 2007.

[171] C. Lee, X. Wei, J. W. Kysar, and J. Hone, "Measurement of the Elastic Properties and Intrinsic Strength of Monolayer Graphene," *Science*, vol. 321, no. 18 July 2008, pp. 385–388, 2008.

[172] A. A. Balandin, "Thermal properties of graphene and nanostructured carbon materials.," *Nat. Mater.*, vol. 10, no. 8, pp. 569–581, 2011.

[173] R. R. Nair, A. N. Grigorenko, P. Blake, K. S. Novoselov, T. J. Booth, N. M. R. Peres, T. Stauber, and A. K. Geim, "Fine structure constant defines visual transparency of graphene.," *Science*, vol. 320, no. 5881, p. 1308, 2008.

[174] A. C. Ferrari, J. C. Meyer, V. Scardaci, C. Casiraghi, M. Lazzeri, F. Mauri, S. Piscanec, D. Jiang, K. S. Novoselov, S. Roth, and A. K. Geim, "Raman Spectrum of Graphene and Graphene Layers," *Phys. Rev. Lett.*, vol. 97, no. 18, p. 187401, 2006.

[175] Y. Y. Wang, Z. H. Ni, T. Yu, Z. X. Shen, H. M. Wang, Y. H. Wu, W. Chen, and A. T. Shen Wee, "Raman Studies of Monolayer Graphene: The Substrate Effect," *J. Phys. Chem. C*, vol. 112, pp. 10637–10640, jul 2008.

[176] A. C. Ferrari and D. M. Basko, "Raman spectroscopy as a versatile tool for studying the properties of graphene," *Nat. Nanotechnol.*, vol. 8, no. 4, pp. 235–246, 2013.

[177] D. Vignaud and E. Moreau, "Graphene growth by molecular beam epitaxy," in *Mol. Beam Ep.* (M. Henini, ed.), ch. 23, pp. 547–557, Elsevier, 1 ed., 2012.

[178] P. H. Tan, W. P. Han, W. J. Zhao, Z. H. Wu, K. Chang, H. Wang, Y. F. Wang, N. Bonini, N. Marzari, N. Pugno, G. Savini, A. Lombardo, and A. C. Ferrari, "The shear mode of multilayer graphene," *Nat. Mater.*, vol. 11, no. 4, pp. 294–300, 2012.

[179] T. M. G. Mohiuddin, A. Lombardo, R. R. Nair, A. Bonetti, G. Savini, R. Jalil, N. Bonini, D. M. Basko, C. Galiotis, N. Marzari, K. S. Novoselov, A. K. Geim, and A. C. Ferrari, "Uniaxial strain in graphene by Raman spectroscopy: G peak splitting, Grüneisen parameters, and sample orientation," *Phys. Rev. B - Condens. Matter Mater. Phys.*, vol. 79, no. 20, pp. 1–8, 2009.

[180] A. J. Pollard and D. Roy, "Graphene characterisation and standardisation via Raman spectroscopy," *Spectrosc. Eur.*, vol. 27, no. 5, pp. 9–12, 2015.

[181] L. Malard, M. Pimenta, G. Dresselhaus, and M. Dresselhaus, "Raman spectroscopy in graphene," *Phys. Rep.*, vol. 473, no. 5-6, pp. 51–87, 2009.

[182] J. W. Suk, A. Kitt, C. W. Magnuson, Y. Hao, S. Ahmed, J. An, A. K. Swan, B. B. Goldberg, and R. S. Ruoff, "Transfer of CVD-Grown Monolayer Graphene onto Arbitrary Substrates," no. 9, 2011.

[183] W. Yang, G. Chen, Z. Shi, C.-C. Liu, L. Zhang, G. Xie, M. Cheng, D. Wang, R. Yang, D. Shi, K. Watanabe, T. Taniguchi, Y. Yao, Y. Zhang, and G. Zhang, "Epitaxial growth of single-domain graphene on hexagonal boron nitride.," *Nat. Mater.*, vol. 12, no. 9, pp. 792–7, 2013.

[184] A. Eckmann, J. Park, H. Yang, D. Elias, A. S. Mayorov, G. Yu, R. Jalil, K. S. Novoselov, R. V. Gorbachev, M. Lazzeri, A. K. Geim, and C. Casiraghi, "Raman fingerprint of aligned graphene/h-BN superlattices," *Nano Lett.*, vol. 13, pp. 5242–5246, 2013.

[185] T. Georgiou, R. Jalil, B. B. D. Belle, L. Britnell, R. V. Gorbachev, S. V. Morozov, Y.-J. Kim, A. Gholinia, S. J. Haigh, O. Makarovsky, L. Eaves, L. a. Ponomarenko, A. K. Geim, K. S. Novoselov, and A. Mishchenko, "Vertical field-effect transistor based on graphene-WS2 heterostructures for flexible and transparent electronics," *Nat. Nanotechnol.*, vol. 8, pp. 100–3, feb 2013.

[186] L. Wang, I. Meric, P. Y. Huang, Q. Gao, Y. Gao, H. Tran, T. Taniguchi, K. Watanabe, L. M. Campos, D. A. Muller, J. Guo, P. Kim, J. Hone, K. L. Shepard, and C. R. Dean, "One-dimensional electrical contact to a two-dimensional material.," *Science*, vol. 342, pp. 614–7, nov 2013.

[187] A. Mishchenko, J. S. Tu, Y. Cao, R. V. Gorbachev, J. R. Wallbank, M. T. Greenaway, V. E. Morozov, S. V. Morozov, M. J. Zhu, S. L. Wong, F. Withers, C. R. Woods, Y.-J. Kim, K. Watanabe, T. Taniguchi, E. E. Vdovin, O. Makarovsky, T. M. Fromhold, V. I. Fal'ko, A. K. Geim, L. Eaves, and K. S. Novoselov, "Twist-controlled resonant tunnelling in graphene/boron nitride/graphene heterostructures.," *Nat. Nanotechnol.*, vol. 9, no. 10, pp. 808–13, 2014.

[188] S. Tang, H. Wang, Y. Zhang, A. Li, H. Xie, X. Liu, L. Liu, T. Li, F. Huang, X. Xie, and M. Jiang, "Precisely aligned graphene grown on hexagonal boron nitride by catalyst free chemical vapor deposition.," *Sci. Rep.*, vol. 3, p. 2666, 2013.

[189] S. Tang, H. Wang, H. S. Wang, Q. Sun, X. Zhang, C. Cong, H. Xie, X. Liu, X. Zhou, F. Huang, X. Chen, T. Yu, F. Ding, X. Xie, and M. Jiang, "Silane-catalysed fast growth of large single-crystalline graphene on hexagonal boron nitride," *Nat. Commun.*, vol. 6, p. 6499, 2015.

[190] F. Guinea, M. I. Katsnelson, and A. K. Geim, "Energy gaps and a zero-field quantum Hall effect in graphene by strain engineering," *Nat. Phys.*, vol. 6, no. 1, pp. 30–33, 2010.

[191] F. Guinea, "Strain engineering in graphene," *Solid State Commun.*, vol. 152, no. 15, pp. 1437–1441, 2012.

[192] S.-M. Choi, S.-H. Jhi, and Y.-W. Son, "Effects of strain on electronic properties of graphene," *Phys. Rev. B*, vol. 81, no. 8, p. 081407, 2010.

[193] B. Hunt, T. Taniguchi, P. Moon, M. Koshino, and R. C. Ashoori, "Massive Dirac Fermions and," *Science*, vol. 340, no. June, pp. 1427–1431, 2013.

[194] J. R. Wallbank, M. Mucha-Kruczyski, X. Chen, and V. I. Fal'ko, "Moiré superlattice effects in graphene/boron-nitride van der Waals heterostructures," *Ann. Phys.*, vol. 527, no. 5-6, pp. 359–376, 2015.

[195] J. Jung, A. M. DaSilva, A. H. MacDonald, and S. Adam, "Origin of band gaps in graphene on hexagonal boron nitride.," *Nat. Commun.*, vol. 6, p. 6308, 2015.

[196] M. Neek-Amal and F. M. Peeters, "Graphene on hexagonal lattice substrate: Stress and pseudo-magnetic field," *Appl. Phys. Lett.*, vol. 104, no. 17, pp. 0–5, 2014.

[197] M. Neek-Amal and F. M. Peeters, "Graphene on boron-nitride: Moiré pattern in the van der Waals energy," *Appl. Phys. Lett.*, vol. 104, no. May 2015, p. 041909, 2014.

[198] G. Tsoukleri, J. Parthenios, K. Papagelis, R. Jalil, A. C. Ferrari, A. K. Geim, K. S. Novoselov, and C. Galiotis, "Subjecting a graphene monolayer to tension and compression," *Small*, vol. 5, no. 21, pp. 2397–2402, 2009.

[199] H. Shioya, M. F. Craciun, S. Russo, M. Yamamoto, and S. Tarucha, "Straining Graphene Using Thin Film Shrinkage Methods," *Nano Lett.*, pp. 10–15, 2014.

[200] S. T. Gill, J. H. Hinnefeld, S. Zhu, W. J. Swanson, T. Li, and N. Mason, "Mechanical control of graphene on engineered pyramidal strain arrays," *ACS Nano*, vol. 9, no. 6, pp. 5799–5806, 2015.

[201] N. Levy, S. A. Burke, K. L. Meaker, M. Panlasigui, A. Zettl, F. Guinea, A. H. Castro Neto, and M. F. Crommie, "Strain-induced pseudo-magnetic fields greater than 300 tesla in graphene nanobubbles.," *Science*, vol. 329, no. 5991, pp. 544–547, 2010.

[202] Z. Yan, Z. Peng, G. Casillas, J. Lin, C. Xiang, H. Zhou, Y. Yang, G. Ruan, A.-R. O. Raji, E. L. G. Samuel, R. H. Hauge, M. J. Yacaman, and J. M. Tour, "Rebar graphene.," *ACS Nano*, vol. 8, no. 5, pp. 5061–8, 2014.

[203] A. Cho and J. Arthur, "Molecular beam epitaxy," *Prog. Solid State Chem.*, vol. 10, pp. 157–191, jan 1975.

[204] M. Henini, ed., *Molecular Beam Epitaxy: From Research to Mass Production*. Elsevier, 1 ed., 2012.

[205] J. Park, W. C. Mitchel, L. Grazulis, H. E. Smith, K. G. Eyink, J. J. Boeckl, D. H. Tomich, S. D. Pacley, and J. E. Hoelscher, "Epitaxial graphene growth by Carbon Molecular Beam Epitaxy (CMBE)," *Adv. Mater.*, vol. 22, no. 37, pp. 4140–4145, 2010.

[206] G. Lippert, J. Dabrowski, Y. Yamamoto, F. Herziger, J. Maultzsch, J. Baringhaus, C. Tegenkamp, M. C. Lemme, W. Mehr, and G. Lupina, "Molecular beam epitaxy of graphene on mica," *Phys. Status Solidi Basic Res.*, vol. 249, no. 12, pp. 2507–2510, 2012.

[207] J. M. Garcia, U. Wurstbauer, A. Levy, L. N. Pfeiffer, A. Pinczuk, A. S. Plaut, L. Wang, C. R. Dean, R. Buizza, A. M. Van Der Zande, J. Hone, K. Watanabe, and T. Taniguchi, "Graphene growth on h-BN by molecular beam epitaxy," *Solid State Commun.*, vol. 152, no. 12, pp. 975–978, 2012.

[208] S. Wang, L. Fernandes dos Santos, U. Wurstbauer, L. Wang, L. N. Pfeiffer, J. Hone, J. M. Garcia, and A. Pinczuk, "Single- and bi-layer graphene grown on sapphire by molecular beam epitaxy," *Solid State Commun.*, vol. 189, no. June 2015, pp. 15–20, 2014.

[209] A. Van Bommel, J. Crombeen, and A. Van Tooren, "LEED and Auger electron observations of the SiC(0001) surface," *Surf. Sci.*, vol. 48, pp. 463–472, mar 1975.

[210] W. A. de Heer, C. Berger, X. Wu, P. N. First, E. H. Conrad, X. Li, T. Li, M. Sprinkle, J. Hass, M. L. Sadowski, M. Potemski, and G. Martinez, "Epitaxial graphene," *Solid State Commun.*, vol. 143, no. 1-2, pp. 92–100, 2007.

[211] M. Yankowitz, J. Xue, D. Cormode, J. D. Sanchez-Yamagishi, K. Watanabe, T. Taniguchi, P. Jarillo-Herrero, P. Jacquod, and B. J. LeRoy, "Emergence of superlattice Dirac points in graphene on hexagonal boron nitride," *Nat. Phys.*, vol. 8, no. 5, pp. 382–386, 2012.

[212] J. Dabrowski, G. Lippert, T. Schroeder, and G. Lupina, "Role of defects in the process of graphene growth on hexagonal boron nitride from atomic carbon," *Appl. Phys. Lett.*, vol. 105, p. 191610, 2014.

[213] T. S. Cheng, A. Davies, A. Summerfield, Y. Cho, I. Cebula, C. J. Mellor, A. N. Khlobystov, T. Taniguchi, K. Watanabe, P. H. Beton, T. C. Foxon, L. Eaves, and S. V. Novikov, "High temperature MBE of graphene on sapphire and h-BN flakes on sapphire," *Submitted*, 2015.

[214] A. J. Marsden, M. Phillips, and N. R. Wilson, "Friction force microscopy: a simple technique for identifying graphene on rough substrates and mapping the orientation of graphene grains on copper.," *Nanotechnology*, vol. 24, no. 25, p. 255704, 2013.

[215] W. Bao, F. Miao, Z. Chen, H. Zhang, W. Jang, C. Dames, and C. N. Lau, "Controlled ripple texturing of suspended graphene and ultrathin graphite membranes," *Nat. Nanotechnol.*, vol. 4, no. 9, pp. 562–566, 2009.

[216] D. Yoon, Y.-W. Son, and H. Cheong, "Negative thermal expansion coefficient of graphene measured by Raman spectroscopy.," *Nano Lett.*, vol. 11, no. 8, pp. 3227–31, 2011.

[217] S. Linas, Y. Magnin, B. Poinsot, O. Boisron, V. Martinez, R. Fulcrand, F. Tournus, V. Dupuis, F. Rabilloud, L. Bardotti, Z. Han, D. Kalita, V. Bouchiat, and F. Calvo, "Interplay between Raman shift and thermal expansion in graphene: Temperature-dependent measurements and analysis of substrate corrections," *Phys. Rev. B*, vol. 91, no. 075426, pp. 1–5, 2015.

[218] A. Dragässer, O. Shekhah, O. Zybaylo, C. Shen, M. Buck, C. Wöll, and D. Schlettwein, "Redox mediation enabled by immobilised centres in the pores of a metalorganic framework grown by liquid phase epitaxy," *Chem. Commun.*, vol. 48, p. 663, 2012.

Chapter 8

Appendix

8.1 Nanoring Distortion Model

Derivation of equation 4.8 in terms of the connecting vectors from section 4.6.

Starting from the sine rule;

$$2R = \frac{a}{\sin A} = \frac{b}{\sin B} = \frac{c}{\sin C} \tag{8.1}$$

since,

$$C = \frac{1}{R} \Rightarrow C = \frac{2 \sin A}{a} \tag{8.2}$$

and from inspection of Fig 4.25,

$$C_i = \frac{2 \sin \phi_i}{\|\vec{s}_i + \vec{s}_{i+1}\|} \tag{8.3}$$

since $\phi_i = \pi - \theta_i \Rightarrow 4\sin^2\theta_i = 4\sin^2\phi_i$ as $\sin(\pi - x) = \sin x$

$$\Rightarrow C_i^2 = \left(\frac{2\sin\phi_i}{|\vec{s}_i + \vec{s}_{i+1}|}\right)^2 = \frac{4\sin^2\theta_i}{|\vec{s}_i + \vec{s}_{i+1}|} = \frac{4(1-\cos^2\theta_i)}{|\vec{s}_i + \vec{s}_{i+1}|} \tag{8.4}$$

Using the vector relation $\cos\theta = \dfrac{\vec{r}_1 \cdot \vec{r}_1}{|\vec{r}_1||\vec{r}_2|}$ where θ is the angle between two arbitrary vectors $\vec{r}_1$ and $\vec{r}_2$;

$$\Rightarrow C_i^2 = \frac{4\left(1 - \left(\dfrac{\vec{s}_i \cdot \vec{s}_{i+1}}{|\vec{s}_i||\vec{s}_{i+1}|}\right)^2\right)}{|\vec{s}_i + \vec{s}_{i+1}|^2} \tag{8.5}$$

and given that the segment length at the i^{th} monomer can be written as;

$$\Delta\vec{s}_i = \frac{|\vec{s}_i| + |\vec{s}_{i+1}|}{2} \tag{8.6}$$

Therefore the total energy of the system can be written entirely in terms of the $\vec{s}$ vectors between each bending position;

$$U_{tot} = \underbrace{\epsilon_b \sum_{i=1}^{N} \frac{\left(1 - \left(\frac{\vec{s}_i \cdot \vec{s}_{i+1}}{|\vec{s}_i||\vec{s}_{i+1}|}\right)^2\right)(|\vec{s}_i| + |\vec{s}_{i+1}|)}{|\vec{s}_i + \vec{s}_{i+1}|^2}}_{\text{Energy due to bond bending}} + \underbrace{\epsilon_s \sum_{i=1}^{N} (1 - |\vec{s}_i|)^2}_{\text{Energy due to bond stretching}} \tag{8.7}$$